UNIVERSITY OF CALIFORNIA, MERCED

Photo-Thermo-Mechanical Analysis and Control for High-brightness and High-repetition-rate X-ray Optics

by

Zhengxian Qu

A dissertation submitted in partial satisfaction of the
requirements for the degree of
Doctor of Philosophy

in

Mechanical Engineering

Committee in charge:
Professor Min Hwan Lee, Chair
Professor Yanbao Ma
Doctor Juhao Wu
Professor James W. Palko

Spring 2020

The dissertation of Zhengxian Qu is approved:

Min Hwan Lee, Chair	Date
Yanbao Ma	Date
Juhao Wu	Date
James W. Palko	Date

University of California, Merced

Let there be light.

Acknowledgments

Without light, none of us can ever survive. The light is the key to understand everything, from huge astronomical objects to the tiny structure of the atomic nucleus. With the light, we may see them for real. It's that simple. But it is such an unexpectedly long journey to access the light. Fortunately, I am not alone in this journey. Many people have guided, supported, and stimulated me to keep going and achieve success. Here I would like to take this change and gratefully acknowledge their help.

In the first place, I want to thank my parents and my wife, for their constant and continuing support, especially during this special period with COVID-19. Same appreciation for my advisor, Prof. Yanbao Ma, and my advisor at SLAC, Dr. Juhao Wu, as they provided me opportunity that I never could imagine. Without their help, I will never be able to build up expertise in this new field, and apply what I have mastered to contribute to the world leading project. I also owe my thanks to my committee members, Prof. Min Hwan Lee and Prof. James W. Palko from Department of Mechanical Engineering, for their time, invaluable feedback on this work, and constructive guidance on both my coursework and research skills.

Furthermore, I also want to extend my gratitude to all my coworkers in an integrated teamwork environment. Dr. Guanqun Zhou offered me help all the time, with whom I coauthored several manuscripts. Dr. Wu, Dr. Franz-Josef Decker, Dr. Alberto Lutman, Dr. Diling Zhu, Dr. Lin Zhang, Dr. Matthew Seaberg, Dr. Zhirong Huang, and many other senior scientists in SLAC, as well as Dr. Bo Yang, Dr. Yongqiang Qiu and Mr. Ye Hong in the team, are all greatly appreciated. I am very lucky to receive all the guidance and instructive suggestions from them.

Last but not least, I want to address my thanks to all the people who kindly advised me at University of California, Merced. Our Designated School Official, Ms. Becky Miraz, School of Engineering faculty Dr. Gerardo Diaz, Dr. Jian-Qiao Sun, and SoE staffs or former staffs Ms. Tamika Hankston, Ms. Tomiko Hale, and all others. My deep appreciation for your support throughout my journey here over the years.

Curriculum Vitae

Education

- M.S. in Mechanical Engineering. University of California, Merced (UCM). Merced, CA, USA, Aug. 2013 - May. 2016
- B.S. in Thermal Sciences and Energy Engineering, University of Science and Technology of China, Hefei, China, Sep. 2009 - Jul. 2013

Publications & Patent

1. Wang, D., Qu, Z., Guo, L., Ma, Y. Study of Electron Relaxation in Gold Films from Intraband to Interband Transitions Regime. *Journal of Applied Physics*, in preparation
2. Qu, Z., Wang, D., Ma, Y. Predicting the Failure of Fourier's law: Criterion of Nondiffusive Thermal Transport in Laser-induced Experiments. *Journal of Applied Physics*, in preparation
3. Qu, Z., Ma, Y., Zhou, G., Wu, J. A Comparative Study of Different Monochromators Performance at Quasi-Steady State Operation of Self-Seeded X-ray Free Electron Laser. *Journal of Synchrotron Radiation*, in preparation
4. Qu, Z. et al. Quantitatively Characterizing the Monochromator Performance Degradation under the Thermal Load from High-Brightness Free-Electron Lasers. *Nature Communications*, in preparation
5. Qu, Z., Yuan, P., Ma, Y. A Wave-Diffusive Model for Thermal Waves at Cryogenic Temperatures. *International Journal of Heat and Mass Transfer*, ready for submission
6. Qu, Z., Ma, Y., Zhou, G., Wu, J. (2020). An Analytical Model for Monochromator Performance Characterizations under Thermal Load. *Optics Express*, under review
7. Qu, Z., Ma, Y., Zhou, G., Wu, J. (2020). Dynamic Pulse-to-pulse Thermal Load Effects in Self-seeded X-ray Free Electron Laser operated in Pulse Train Mode. *Journal of Synchrotron Radiation*, under review
8. Zhou, G., Qu, Z., Ma, Y., Corbett, W., Jiao, Y., Raubenheimer, T., Wang, J., Wu, J. (2020). Two-stage reflective self-seeding scheme for high repetition rate X-ray free-electron lasers. *Journal of Synchrotron Radiation*, under review
9. Qu, Z., Ma, Y., Zhou, G., Wu, J. (2020). Thermal Loading on Self-Seeding Monochromators in X-Ray Free Electron Lasers. *Nuclear Instruments and Methods in Physics Research, A*, Accepted
10. Qu, Z., Wang, D., & Ma, Y. Nondiffusive thermal transport and prediction of the breakdown of Fourier's law in nanograting experiments. *AIP Advances*, 7(1), 015108.

11. Qu, Z., Ma, Y. (2016). A Unified Diffusive-nondiffusive Two Parameter Heat Condcution Model. In *Multiscale Thermal Transport in Energy Systems*. Hauppauge, NY: Nova Science Publishers, Inc.

12. Wang, D., Qu, Z., & Ma, Y. (2016). An enhanced Gray model for nondiffusive heat conduction solved by implicit lattice Boltzmann method. *International Journal of Heat and Mass Transfer, 94*, 411-418.

13. Qu, Z., Liu, Z., Wang, X., & Zhao, P. (2014). Finite analytic numerical method for solving two-dimensional quasi-Laplace equation. *Numerical Methods for Partial Differential Equations, 30*(6), 1755-1769.

14. Qu, Z.. Motor Vehicle Seat with Ventilation Adjusting Temperature. CN, ZL 201220473635.X, filed Sept. 05, 2012, issued May 29, 2013.

Contents

List of Figures

List of Tables

Nomenclature and Acronyms

Roman Letters

ΔT	temperature change, K
Δt	temporal step, s
$\Delta x, \Delta y, \Delta z$	spatial step, m
$\hat{\mathbf{s}}$	unit directional vector (vector), 1
$\hat{\mathbf{x}}, \hat{\mathbf{y}}, \hat{\mathbf{z}}$	unit directional vector (vector) for x, y, z respectively, 1
$\vec{B}_u$	magnetic filed of undulator, T
$\vec{E}$	electric field, V/m
$\vec{h}$	vector of the reciprocal lattice, 1/m
$\vec{p}$	momentum, kgm/s^2
$\vec{q}$	heat flux (vector), W/m^2
$\vec{v}$	velocity, m/s
c	speed of light, m/s
c_l	longitudinal wave speed, m/s
c_p	heat capacity, kg/m^{3}K
c_s	Debye velocity, m/s
c_t	transverse wave speed, m/s
c_v	volumetric specific heat, J/m^{3}K
d	interplanar distance, m
e	elementary charge, C
E_c	central photon energy, eV

f repetition rate, Hz

H Hamiltonian, J

h crystal thickness, m

I light intensity, $\mathrm{W/m^2}$

I_0 pulse energy, J

K nondimensional parameter of the undulator, 1

Kn Knudsen number, 1

L length, m

L_c system characteristic length, m

m mass, kg

N_A Avogadro's number, 1

n_e electron beam density, 1

T temperature, K

T_∞ environmental temperature, K

u, v, w displacement in x, y, z direction, respectively, m

x, y, z spatial coordinates, m

c speed of sound, m/s

v_p group velocity, m/s

E volumetric energy density, $\mathrm{J/m^3}$

Kn Knudsen number, 1

Greek Letters

α_T linear thermal expansion coefficient, $\mathrm{K^{-1}}$

β ratio between the speed of electrons and light, 1

$\Delta\Omega$ deviation parameter, Hz

γ Lorentz factor, 1

κ thermal conductivity, $\mathrm{Wm^{-1}K^{-1}}$

Λ mean free path, m/s

λ_r radiation wavelength, m

ν_s Poisson ratio, 1

Ω deviational angular frequency, Hz

ω_0 central angular frequency, Hz

ω_p plasma frequency, 1/s

ϕ phase, rad

ρ mass density, kg/m^3

σ_{ij} i, j stress component, Pa

τ_N relaxation time for N-process, s

τ_R relaxation time for R-process, s

θ_B Bragg angle, rad

Θ_D Debye temperature, K

ε_{ij} i, j strain component, 1

φ phase, rad

ζ nondimensional number that characterizes the nondiffusive effects, 1

β nonequilibrium absolute temperature, K

Λ_B ballistic phonon mean free path, m

Λ_D diffusive phonon mean free path, m

τ_B ballistic phonon lifetime s

τ_D diffusive phonon lifetime, s

Subscripts

$\perp$ transverse component

$\parallel$ longitudinal component

Abbreviations

1D one-dimensional

2D two-dimensional

3D three-dimensional

CFL Courant-Friedrichs-Lewy number

CRLs Compound refractive lenses

CVD Chemical Vapor Deposition

EuXFEL European X-ray free-electron laser

FD finite difference

FELs free-electron lasers

FWHM full width half maximum

KB Kirkpatrick-Baez

LCLS Linac Coherent Light Source

LHS left hand side

Linac linear accelerator

MFP mean free path

PAL-XFEL Pohang Accelerator Laboratory X-ray Free Electron Laser

RHS right hand side

SACLA SPring-8 Angstrom Compact free electron LAser

SASE self-amplified spontaneous emission

SR synchrotron radiation

TDTR time-domain thermoreflectance

TTG transient thermal grating

XFEL X-ray free-electron lasers

XFELO X-ray free-electron lasers oscillator

ZGV zero group velocity

ZPs zone plates

Abstract

Photo-Thermo-Mechanical Analysis and Control for High-brightness and High-repetition-rate X-ray Optics
by
Zhengxian Qu
Doctor of Philosophy
in
Mechanical Engineering
University of California, Merced
Professor Yanbao Ma, Advisor

X-ray optics has been serving the exploration of nature in synchrotron radiation for many decades. In recent years, X-ray free-electron lasers (XFELs) open a new era of X-ray based research by generating extremely intense X-ray flashes. The outstanding properties including extremely high brightness enable unprecedent discoveries in many research fields, such as structural biology, photochemistry, atomic, molecular and cluster physics. To assist research, the X-ray optics used in synchrotron radiation are either directly employed or modified for their utilizations in XFEL. One emerging challenge for the implementation of X-ray optics in XFEL is that the extremely bright photon beam introduces highly localized and strong thermal load on the X-ray optics, especially at high repetition rates. The thermal load induces severe non-uniform thermal deformation of the optics, degrading their ability to preserve the superior XFEL beam quality, such as high brightness and outstanding coherence.

To understand the thermal load effects and provide design principles to minimize these effects, in this study, we carry out coupled photo-thermal-mechanical analyses. We first provide necessary background and review of current studies on thermal load in X-ray optics. Next, we derive an analytical model to yield qualitative understanding on thermal load. According to the analytical model, the thermal load effects can be decomposed into two parts: the tunable part (due to the overall strain increase) and untunable part (due to the strain and surface slope inhomogeneity). We then further investigate and quantitatively evaluate the performance degradation of the optics due to thermal load in practical operating modes: pump-probe mode, pulse train mode and quasi-steady state. In pump-probe mode, the tunable part is invisible due to the limited amount of energy deposited, while the untunable part results in significant performance reduction for short delay time between the two pulses. For beamline monochromator, additional effects such as laser footprint distortion and tranverse coherence degradation are also harmful for photon science experiments. In pulse train mode where more than two pulses are incident, thermal load accumulates pulse by pulse. Both tunable and untunable parts are observable. The optics performance degrades dynamically due to continuing thermal load accumulation. Accordingly, the tuning needs to follow this dynamic behavior to recover the central photon energy shift and align the spectrum if multiple monochromators are cooperating in the system. At quasi-steady state, the performance is constantly affected and necessary design is needed to refrain the thermal load. Three designs of monochromators are proposed and analyzed for different repetition rate at different cooling temperatures. Critical repetition rate

is accordingly determined. One desirable way to improve the thermal load tolerance of the X-ray optics is to operate them at cryogenic temperature, as confirmed by simulation. However, at cryogenic temperature, the emerging unconventional nondiffusive heat transfer phenomena may result in the performance deviation from designed status. We introduce and propose simplified nondiffusive models to characterize these new features and prepare for the experimental analysis with cryogenic cooling. Based on this study, the thermal load effects are be better understood. Design insights including geometry design and operation condition are also provided, contributing to the preparation for practical experimental test and maintaining the X-ray optics performance at high-brightness and high-repetition-rates.

Chapter 1

Introduction

Thanks to the development of third generation of light source, the dedicated synchrotron radiation sources, a lot of new physics and mechanisms in wide research fields are uncovered and understood. To appropriately handle the X-ray, substantial research and development of instrumentation has been carried out. On synchrotron beamline, many types of X-ray optics are employed. Classified by the physical effect used, the X-ray optics can be divided into four major types as listed in the table below.

Physical effect	**Optics**
Reflection	Kirkpatrick-Baez (KB) mirror, capillary optics
Diffraction	Fresnel zone plates (ZPs), multilayer Laue lenses
Refraction	Compound refractive lenses (CRLs)
Absorption	Windows, filters, pin holes, coded mask telescopes

Table 1.1: Types of X-ray optics on beamline.

However, in modern storage rings, boosted number of available photons can pose significant heat load on the optics. The heat load is deposited into the optics due to X-ray-matter interactions, and results in inhomogeneity and reduction of the optical performance. An order of magnitude estimation for thermal power densities of focused white radiation beams can be in 100 Wmm^2 range [1]. This is detrimental to beamline X-ray optics and should be compensated by specifically designed optics geometry and engineered materials, or by implementation of cooling schemes.

1.1 Cooling techniques for beamline optics

For common type of cooled beamline optics, such as mirror or monochromator, analytical treatment based on conventional heat transfer theory is briefly presented here as background information. Here we take mirror as an example, as it is one most intensely studied optics with cooling.

For mirror optics, the distortion due to thermal load can usually be categorized into two types: 1) the gross bending of the whole mirror and 2) the mapping distortion [2].

The gross bending of the whole mirror refers to the distortion of the mirror due to the temperature difference between the irradiated and cooled surfaces. This can be illustrated by an unconstrained block. Assuming that the top surface of the block is exposed to beamline radiation,

while the bottom surface is cooled, there exists a temperature difference ΔT. Consequently, the top surface with length L, due to the thermal expansion, is elongated by $L\alpha\Delta T$. If the thickness of the block is d, this elongation results in a bending with radius $t/\alpha\Delta T$. With this curvature, the pointing and other optical performance of this mirror are deviating from designed status. The mapping distortion refers to the local swelling due to direct expansion of the heated material normal to the heated surface which leads to a distortion which "maps" the power density distribution [2]. This is usually triggered by non-uniform irradiation from the photon beams. For reflective monochromator that consists of two parallel crystal mirror, this could cause severe degradation of performance due to the mismatch in lattice spacing between the two surfaces [3].

Generally, it is desirable to design the cooling location as close as possible to the heat load location, for example just under the surface with enough material thickness to allow required mechanical strength. The thermal load comes in at the reflection surface; it is then dissipated through heat conduction to the thin layer above the cooled surface known as "hot wall", and extracted through designed cooling method, usually convection. However, if the heat load is not uniform as in mapping distortion cases, there exists local surface slope called *slope error*, which needs to be characterized and minimized.

Typical cooling schemes in existing beamline physics are based on indirect convective cooling, which employs the base cooling plate and channel to duct the flow of the working fluid. Depending on the design operating condition and the thermal load, the working fluid could be water, liquid nitrogen or even liquid helium. The cooling mechanisms are based on channel flow convective heat transfer with possibly extended surface such as fins. The design theoretical fundamentals are the engineering convective heat transfer correlation with Nusselt number and Reynolds number and the fin efficiency calculation. A comprehensive derivation and collection of the relevant formulas can be found in a mechanical engineering textbook [4].

1.2 New challenges in free-electron laser optics

X-ray free-electron laser (XFEL) provides unprecedently high brightness X-ray compared to other X-ray sources. It also offers pulse with duration time down to femtoseconds or even attoseconds. The superior properties introduce two fundamental XFEL photonics properties for XFEL design [5]: 1) extremely high peak intensity due to the large number of X-ray photons ($> 10^{12}$) in a very short pulse duration ($< 100\,\mathrm{fs}$); 2) excellent transverse beam coherence. Although the general requirements for XFEL optics are similar to that for storage rings, the different beam properties still pose different requirements for design of optics.

One challenge that is closely related to thermal load is the small high-brightness XFEL spot size on optical elements, due to the low source divergence [5]. Consider that the pulse duration of XFEL is typically very short, the thermal load in this case can be significantly higher than in storage ring in terms of heat flux. For example, in Linac Coherent Light Source (LCLS) of SLAC National Accelerator Laboratory, a typical XFEL has pulse energy about $100\,\mu\mathrm{J}$, transverse spot size about $20\,\mu\mathrm{m}$ and pulse duration about $100\,\mathrm{fs}$. The averaged absorbed heat flux during the XFEL pulse can be calculated as $4 \times 10^{17}\,\mathrm{W/m^2}$. This high heat flux, confined by small space and short time, generates large local temperature increase and strong strain within the XFEL footprint, contributing to the mapping distortion of the optics. In extreme cases, the high heat flux may even damage the optics. This high local thermal load becomes more severe when the repetition rate of the XFEL

pulse is high. Short pulse-to-pulse time restricts the thermal relaxation time, so that the thermal load is accumulating and finally may even lead to the damage of the optics. Even below the damage threshold, the optical performance of the optics could also be significantly degraded.

Another challenge is that, when transmissive monochromator [6] is using, a thin plate of crystal is employed. The thin crystal plate must maintain its transparency while remain strain-free status. These requirements rule out the possibility to design cooling scheme right underneath the surface, and introduce strict condition for side surface cooling: the cooling device must be 1) integrated with the monochromator in a strain-free manner and 2) able to dissipate enough power with given small side surface area.

For monochromators, one more challenge emerges as the strain in the monochromator needs to be considered and refrained. When stimulated by short and intense thermal load, strong thermal stress could be generated and propagating as strain waves, which further complicates the situation.

The free-electron laser, unlike a conventional laser, employs the free electrons that are not bounded within discrete energy states in a gain medium. By tuning the electron beam or other components, the FEL is smoothly tunable and scalable. In FEL, the laser originates from the spontaneous emission of the electron beams and is exponentially amplified due to the positive feedback in the interactions between the electron beams and radiation, which is also a unique feature. Here, we briefly outline the theoretical fundamentals of FEL to introduce the output photon beam properties, which, to a large extent, determines the thermal load on the crystal FEL optics.

1.3 Free-electron laser

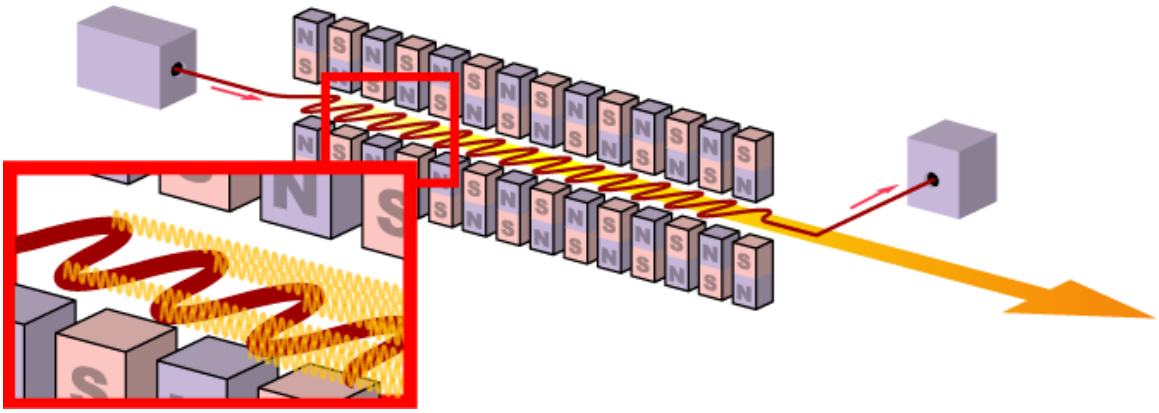

Figure 1.1: Illustration of the free-electron laser [7]

To obtain FEL, the electron beam is generated and accelerated by the accelerators (including microtrons, electron storage rings, electrostatic accelerators, room temperature and superconducting radio frequency linear accelerator [8]) to a very high energy with its speed almost being the light speed. The electrons, after going through necessary components such as beam compressor, are then guiding through the undulator, which is an array of alternating polarity dipole magnets. The electrons then pass through the undulator along a sinusoidal-like trajectory in a plane perpendicular to the magnetic field direction. During their passing process, the electrons emit synchrotron radiation

(SR) due to their transverse acceleration and follows the SR very closely. The propagation of the radiation ahead of the electrons is termed "slippage" [5]. When the amount of slippage matches with the period of the undulator through some condition, the SR will be magnified, as will be illustrated in details in below sub-section.

1.3.1 Single electron in the undulator

Compared to the undulator magnetic field, the influence that one electron receives from all other electrons in the beam (space charge effects) can be ignored, so that we only consider single electron motion in the undulator. There are typically two types of undulator in use for FEL. One is a planar undulator, the other is a helical or elliptical undulator. Here we take planar undulator as an example. In planar undulator, we can introduce the Hamiltonian

$$H = \sqrt{\left(\vec{p} - e\vec{A}\right)^2 c^2 + m^2 c^4}, \tag{1.1}$$

where the vector potential $\vec{A} = A_u \hat{x} \cos(k_u z)$. The x and y are transverse direction of the undulator and z is the axial direction of the undulator. The magnetic field can be written as

$$\overrightarrow{B}_u = -A_u k_u \sin(k_u z)\, \hat{y}. \tag{1.2}$$

For the Hamiltonian given by Eq. (1.1), we obtain

$$\dot{p}_x = \frac{\partial H}{\partial x} = 0, \tag{1.3}$$

so that the x direction momentum $p_x = 0$. For single electron, by omitting the influence of the emitted radiation, the dynamic equation can be written as

$$m\gamma v_x = p_x - eA_x = -eA_u \cos(k_u z), \tag{1.4}$$

where γ is Lorentz factor, β is the ratio between the speed of the electron and the speed of light, $k_u = 2\pi/\lambda_u$ is the wavenumber of the undulator, and an important nondimensional parameter of the undulator, K, is defined as

$$K \equiv \frac{eB_u}{mck_u}, \tag{1.5}$$

where e is elementary charge, m is the mass of electron and c is the speed of light. For the undulator in FEL application, $K \approx 1$, while for synchrotron radiation in storage rings, the undulator is usually called wiggler with $K \gg 1$.

Solving Eq. (1.5) yields

$$v_x = \frac{Kc}{\gamma} \cos(k_u z). \tag{1.6}$$

When the speed of the electron is very close to the speed of light (several GeV for hard X-ray), the z position of the electron can be approximated as $z = ct$, so that z direction velocity can then be

determined as

$$v_z = \sqrt{v^2 - v_x^2} \approx c\left[1 - \frac{1 + K^2/2}{2\gamma^2} - \frac{K^2}{4\gamma^2}\cos\left(2k_u z\right)\right]. \tag{1.7}$$

From Eq. (1.7), one may notice that the z velocity component of the electron can be expressed as a superposition of two terms: one is the average z velocity written as

$$\bar{v}_z = c\left(1 - \frac{1 + K^2/2}{2\gamma^2}\right), \tag{1.8}$$

and the other is the oscillating component.

To enable the interaction between the radiation and the electron, resonance condition needs to be satisfied.

1.3.2 Resonance condition

For a co-propagating radiation field, $E_x = E\left(z,t\right)e^{i(k_r z - \omega_r t)} + E^*\left(z,t\right)e^{-i(k_r z - \omega_r t)}$, with slow varying amplitude $E\left(z,t\right)$, the energy conservation yields

$$mc^2\dot{\gamma} = ev_x E_x. \tag{1.9}$$

Plug the radiation field we have the energy change

$$\frac{d\gamma}{dz} = -e\frac{K}{\gamma}\frac{E}{mc^2}\cos\left(k_u z\right)e^{i(k_r z - \omega_r t)} - e\frac{K}{\gamma}\frac{E^*}{mc^2}\cos\left(k_u z\right)e^{-i(k_r z - \omega_r t)}. \tag{1.10}$$

The phase can be defined as

$$\phi = \left(k_u + k_r\right)z - \omega_r t, \tag{1.11}$$

so that its gradient in z direction is

$$\frac{d\phi}{dz} = k_u + k_r - \frac{\omega_r}{dz/dt} = k_u + k_r - k_r\beta_{\parallel}^{-1}. \tag{1.12}$$

Here, the longitudinal velocity is

$$\begin{aligned}\beta_{\parallel}^{-1} &= \left(\beta^2 - \beta_{\perp}^2\right)^{-1/2} = \left[1 - \frac{1}{\gamma^2} - \frac{K^2}{\gamma^2}\cos^2\left(k_u z\right)\right]^{-1/2} \\ &\approx 1 + \frac{1 + K^2\cos^2\left(k_u z\right)}{2\gamma^2}.\end{aligned} \tag{1.13}$$

For one undulator period, averaged $\beta_{\parallel}^{-1}$ is

$$\overline{\beta}_{\parallel}^{-1} = 1 + \frac{1 + K^2/2}{2\gamma^2}. \tag{1.14}$$

The resonance condition is

$$k_u + k_r - k_r \overline{\beta}_{\parallel}^{-1} = 0. \tag{1.15}$$

Once this condition is satisfied, ϕ does not change after one period. Introduce a resonance energy γ_0 and plug Eq. (1.14) into Eq. (1.15) to obtain

$$k_u = k_r \frac{1 + K^2/2}{2\gamma_0^2}. \tag{1.16}$$

This is the important resonance condition in undulator. The phase ϕ can then be rewritten as

$$\phi = \theta - b \sin(2k_u z), \tag{1.17}$$

where $\theta \equiv \int k_u \left(1 - \frac{\gamma_0^2}{\gamma^2}\right) dz$ is a slow varying phase and $b \equiv \frac{K^2/4}{1+K^2/2}$.

1.3.3 Pendulum model & micro-bunching

Expanding the exponential term in Eq. (1.10) yields

$$\cos(k_u z)\, e^{i(k_r z - \omega_r t)} = \frac{1}{2}\left[e^{i\phi} + e^{i(\phi - 2k_u z)}\right] \approx \frac{e^{i\theta}}{2}\left[J_0(b) - J_1(b)\right] \tag{1.18}$$

Plug Eq. (1.18) back into Eq. (1.10) to obtain

$$\frac{d\gamma}{dz} = -\frac{k_u D_2}{\gamma_0}\left(E e^{i\theta} + E^* e^{-i\theta}\right), \tag{1.19}$$

where

$$D_2 = \frac{eK[JJ]}{2k_u mc^2}. \tag{1.20}$$

For slow varying phase, Eq. (1.12) can be rewritten as

$$\frac{d\theta}{dz} = k_u \left(1 - \frac{\gamma_0^2}{\gamma^2}\right) \approx \frac{2k_u(\gamma - \gamma_0)}{\gamma_0}. \tag{1.21}$$

We can define the dimensionless variable $Z = k_u z$ and $\eta = 2\frac{\gamma - \gamma_0}{\gamma_0}$, so that Eq. (1.21) can be rewritten as

$$\frac{d\theta}{dZ} = \eta. \tag{1.22}$$

Combine Eq. (1.22) with Eq. (1.19) to obtain

$$\frac{d^2\theta}{dZ^2} + \frac{2D_2}{\gamma_0^2}\left(E e^{i\theta} + E^* e^{-i\theta}\right) = 0. \tag{1.23}$$

If E is assumed constant (in low-gain FEL where the energy transfer between the electron and radiation is negligible), Eq. (1.23) becomes the pendulum equation:

$$\frac{d^2\theta}{dZ^2} + \frac{4D_2}{\gamma_0^2} E \sin\theta = 0. \tag{1.24}$$

In longitudinal phase space, the electrons initially with $\theta \in (-\pi, 0)$ gain energy while the electrons with $\theta \in (0, \pi)$ lose energy. This gives rise to an energy modulation, which will be turned into an electron density modulation since the higher energy electrons advance in phase while the lower energy electrons retard. This density modulation is termed the FEL micro-bunching.

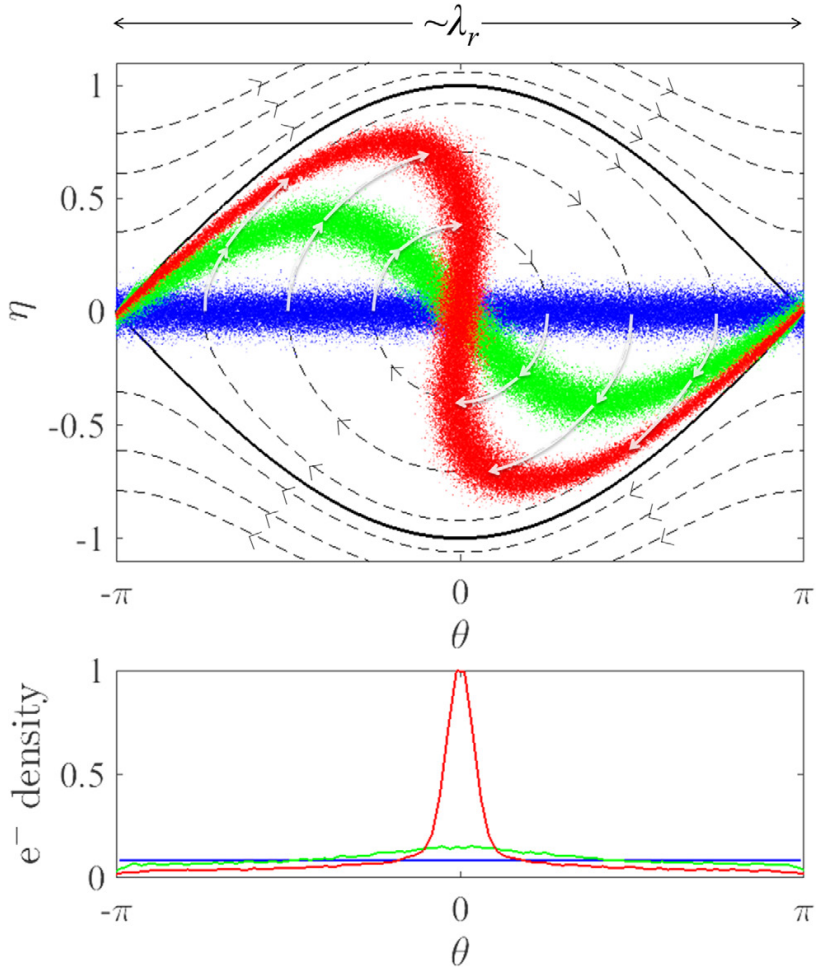

Figure 1.2: Electron motion in phase space. Starting with the blue dots, the electron beam evolves to green dots and finally red dots, forming the micro-bunching. The black solid line represents the separatrix [5].

For high-gain FEL, we skip the derivation but provide an illustration. The fixed radiation amplitude E can evolve so that coupled Vlasov equation and Maxwell equation need to be solved. In Fig. 1.3, initially the electron beam distributes like in Fig. 1.3 (a), then it starts evolving as

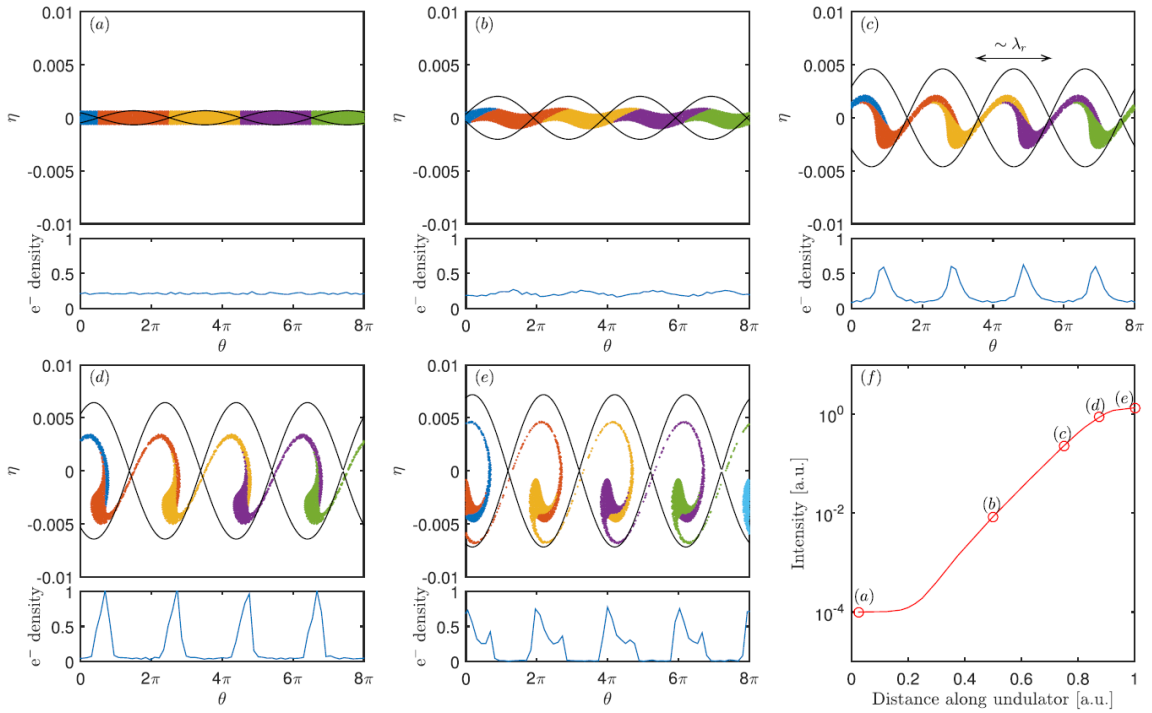

Figure 1.3: Longitudinal phase space evolution in high-gain FEL [5].

described in low-gain FEL pendulum model. As the micro-bunching forms in Fig. 1.3 (b) and (c), the radiation enters the exponential growth stage, and reaches maximally bunched status in (d). This is where the saturation stage starts, as the micro-bunches continues evolving but no significant power increase in radiation.

1.3.4 Output properties of SASE FEL

As stated in previous sub-sections, the radiation is emitted by the electron beam and amplified by the electron beam as well. This is called self-amplified spontaneous emission (SASE). The SASE mode is the most fundamental operating mode of X-ray FEL.

Temporal structure In SASE mode, due to the intrinsic initial local bunching of the electron beam when entering the undulator (termed shot noise), the radiation pulse can be showed to consist of a random superposition of many spikes in temporal domain [9]. Each of these spikes follows the Gaussian distribution because the energy spread of the electron beam follows the Gaussian distribution. The phases of these spikes are uncorrelated because the shot noise at different locations of the electron beams are usually independent. However, the overall average temporal profile is usually Gaussian. This is due to the long total length of the electron beam compared to the micro-bunching length: a large number of micro-bunching emission (typically several thousand or more) follows the law of large numbers so that their amplitudes also follow Gaussian distribution.

Overall, statistically for many shots, the SASE temporal profile can be approximated as a Gaussian if these conditions are satisfied, so is its spectrum.

Bandwidth Although many spikes in temporal domain exists, they all approximately share the same bandwidth, which is gain bandwidth of the FEL system, making the SASE pulse bandwidth about the same as the gain bandwidth. The gain bandwidth can be derived analytically [5] and grows narrower in relative value with the propagation distance in the undulator as $\sigma_\lambda \approx 2\rho\sqrt{\pi/\bar{z}}$, where ρ is the Pierce parameter of FEL defined as

$$\rho = \frac{\left(a_u\omega_p/4ck_u\right)^{2/3}}{\gamma}, \tag{1.25}$$

where $a_u^2 = K^2/2$ is the RMS undulator parameter, $\omega_p = \sqrt{4\pi e^2 n_e/m}$ is the plasma frequency, n_e is the electron beam density. After saturation length, the bandwidth roughly remains unchanged. For short-wavelength high-gain FEL, ρ is typically $10^{-4} - 10^{-3}$, so that the relative bandwidth of SASE at saturation is about $10^{-4} - 10^{-3}$.

Peak power At saturation, the peak radiation power is proportional to the electron beam peak power with a slope of ρ, which further depends on the peak current and electron energy. For short-wavelength high-gain FEL, the electron beam energy is about tens of GeV and the peak current is a few kA, leading to a peak power of tens of GW.

In theory, the power scales with n_e^2 if the electron beam is fully pre-bunched, or scales with n_e if the electron beam is unbunched [10]. However, in reality, the electron beam is neither fully pre-bunched nor unbunched so that the power usually scales with $n_e^{4/3}$ [5].

Pulse energy The total photon energy in a pulse photon beam is the pulse energy. Given the previously estimated peak power of tens of GW and the pulse durations of 10-100 fs, the pulse energy can be calculated as sub-mJ to mJ level. Accordingly, the total number of photons can also be obtained as $10^{10} - 10^{11}$.

Waist size The waist size of SASE is determined by the waist size of the electron beam, which originates from the electron emittance of the cathode and the beta function (β_x) of the lattice (an array of electron optics which is adjustable). In practical operation, the waist size of the electron beam is usually adjusted to remain approximately unchanged. An example calculation for 4 GeV electron beam with $\beta_x = 20$ gives a waist size of 31.62 μm for the Gaussian photon beam.

Brightness One important metric for the output photon beam is the brightness, which is defined as the energy flux per bandwidth per solid angle. Due to its narrow bandwidth, small radiation opening angle and high peak power, the brightness of FEL can be at least eight orders of magnitude higher than the source from storage ring for short-wavelength radiation (wavelength about 0.1 nm) [5].

1.4 Further improvement on coherence

Although SASE FEL already has very narrow bandwidth, the temporal coherence of SASE can be further improved by several method towards the achievement of fully coherent FEL. The most direct way is to insert a monochromator on downstream to select the frequency range of interest. In addition, various SASE-based, external seeding-based and oscillator-based techniques have been proposed and partially demonstrated in recent years [11], including self-seeding and cavity-based XFEL, such as XFEL oscillator (XFELO).

1.4.1 Self-seeding

Self-seeding technique [12] can significantly improve the temporal coherence of SASE. This technique has been experimentally demonstrated in LCLS [6]. Figure 2.3 shows the schematic of self-seeding technique.

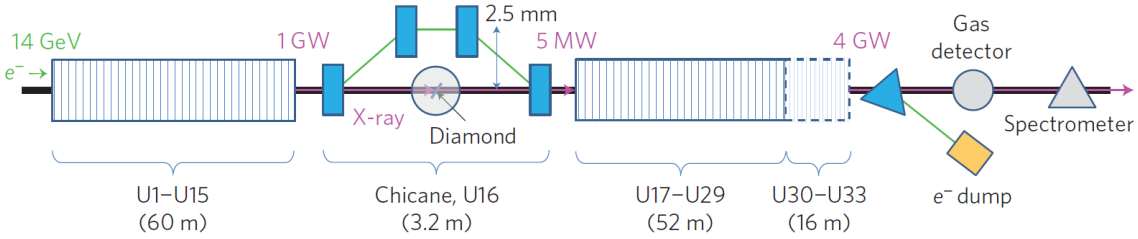

Figure 1.4: Layout of the LCLS hard X-ray self-seeding system [6].

In self-seeding mode, the undulators are divided into two sessions, with one monochromator inserted between the two sessions. The SASE obtained in the first session passes the monochromator and generates a purified wake "seed". This seed is then amplified in the second session of undulator to allow an intense coherent XFEL pulse as output. During the seeding process, the electron beam is directed to a chicane to be delayed so that it can meet the seed in the second session of undulator. The microbunching formed in the first session can also be washed out.

Figure 1.5 shows the comparison between the spectrum of SASE and self-seeded XFEL. The bandwidth is reduced by 50 folds and the brightness is significantly improved.

Further advancement of self-seeding mode towards high repetition rate leads to the dramatic increase of the thermal load deposited from SASE pulses to the crystal monochromator, which is also one major concern in this dissertation. To mitigate the thermal load effects, the cascading self-seeding scheme was proposed [13] and numerically analyzed [14].

1.4.2 Cavity-based XFEL

The concept of XFELO was proposed as early as SASE was. However, due to the lack of perfect crystal mirrors, it has not received much attention until recent years. The demonstration of high-reflectivity Bragg diffraction at diamond crystal [15] prepares the potential candidate for the crystal mirrors in XFELO. The schematic of XFELO [16] is given in Fig. 1.6.

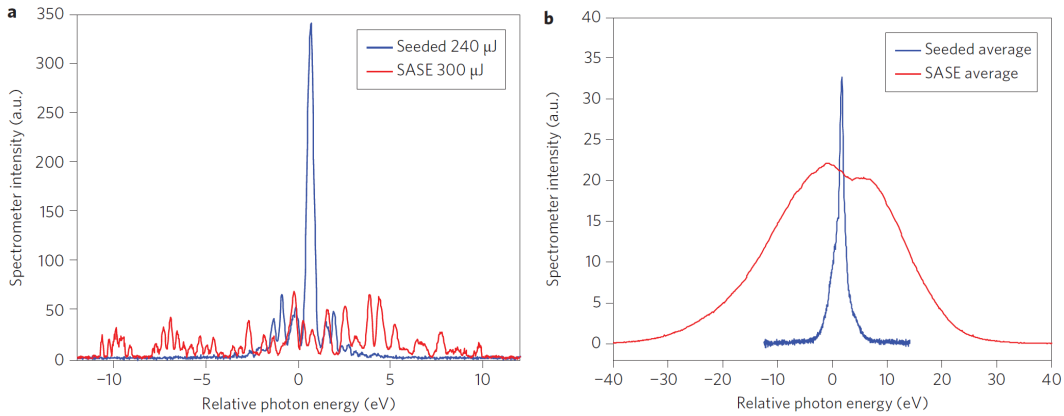

Figure 1.5: Output X-ray spectra for (a) single shot and (b) averaged in SASE mode (red line) and self-seeding mode (blue) [6]. The FWHM of single shot SASE is about 20 eV, as compared to seeded pulse of 0.4 eV.

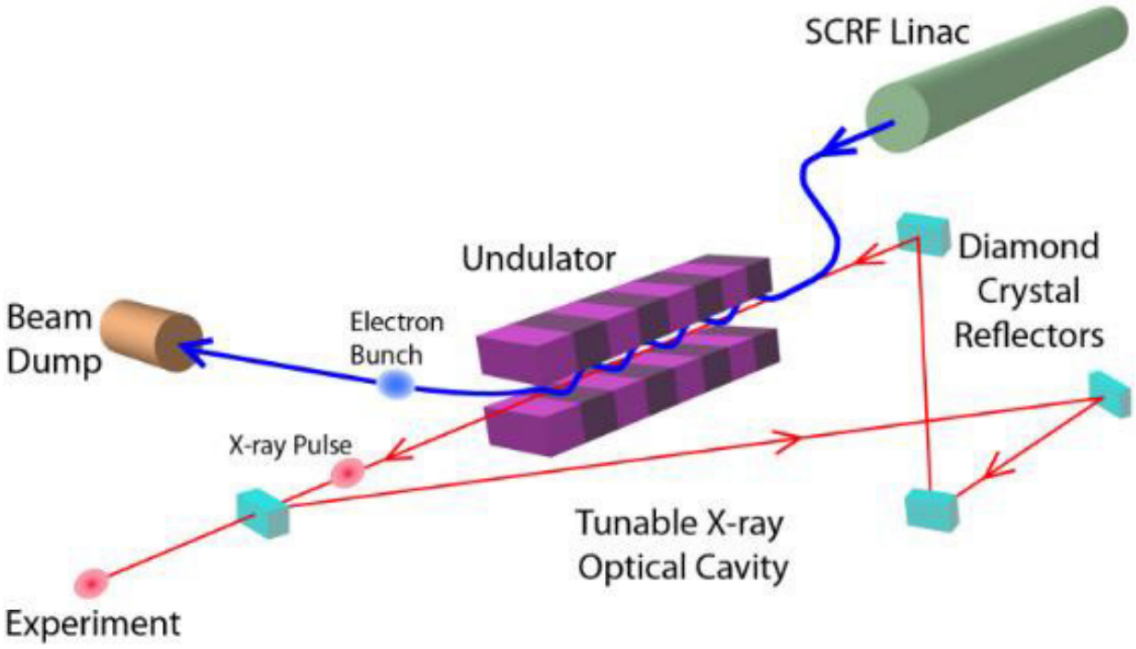

Figure 1.6: Schematic of XFELO [16].

The cavity consists of four crystal mirrors with one segment of undulator inside. The leading electron bunch produces the first SASE pulse in the undulator. The SASE will be amplified exponentially if its gain exceeds loss. XFELO works in a low gain regime so that it requires a large number of round trips in the cavity to reach saturation. The output photon beam is coupled out through crystal mirror transmission.

XFELO is able to produce fully coherent X-ray pulses at very high repetition rate (1 – 100 MHz) with large numbers of photons (10^9 – 10^{11}). This is very attractive for photon sciences.

However, thermal load issue in XFELO also exists as in self-seeding. The multiple reflections during the round trip of the X-ray requires a minimization of the loss, which poses possibly an even lower tolerance. Moreover, the mapping distortion and pointing error due to thermal load should also be mitigated to allow the production of high-quality photon beam.

1.5 Remaining challenges & objectives

In previous sections, we have presented the necessary FEL theory as well as the output properties of the SASE FEL. The background information given here serves as the input for the thermal load on both beamline optics in FEL and other optics employed in different FEL schemes, such as self-seeding and XFELO. Given the unprecedentedly high brightness of the photon beam, the thermal load also becomes more challenging as discussed previously.

For multi-bounce reflective monochromator in XFEL beamline, thermal load leads to footprint and wavefront distortion. This distortion could result in multiple problems. For example, the distortion leads to very limited overlapping area between the leading and trailing pulses, significantly limiting the flexibility for pump-probe type experiments, as the sample has to be extremely carefully aligned. On the other hand, the suppression of the peak intensity also undermines the quality of the measurement due to the decreasing number of photons.

Furthermore, for other FEL applications, such as self-seeding and XFELO, more requirements on the output beam properties exist. In self-seeding XFEL, for example, the wake seed power could be significantly suppressed due to thermal load. When this seed is not strong enough to dominate the shot noise, the self-seeding fails. XFELO, on the other hand, has even more strict requirement, such as nano-radian level surface slope.

Based on the background review, the overall objective of the dissertation is to characterize the thermal load effects on crystal optics performance (including reflective and transmissive type) at high repetition rate, and provide general principles for the compensation actions. More specifically, thermal load in several different situations, such as pump-probe mode, will be studied both analytically and numerically. With the characterized thermal load, the diffraction study will be conducted to evaluate the degradation of the output photon beam to provide both prediction and guidance to determine critical operation parameters.

The itemized objectives are listed as below:

1. Provide qualitative and quantitative understanding of how the thermal load affects the performance of X-ray optics for
   (a) Reflective monochromator
   (b) Transmissive monochromator
2. Develop coupled photo-thermal-mechanical tools to quantitatively evaluate the thermal load effects on the optical performance of X-ray optics in
   (a) Pump-probe mode XFEL
   (b) Pulse train mode XFEL
   (c) Quasi-steady XFEL

3. Provide design principles for

   (a) Geometric design of X-ray optics

   (b) Critical operation parameter determination

1.6 Outline

- In Chapter 1, necessary information about free-electron laser is presented as an introduction of the input thermal load power for the optics. In addition, the related output beam properties are also introduced.

- In Chapter 2, the involved physical processes will be listed and discussed to simplify the analysis. Based on the simplification, an analytical model is derived and validated, to evaluate and understand the thermal load effects.

- In Chapter 3, the thermal load effects on monochromator in pump-probe mode will be studied. Footprint and wavefront distortion, peak intensity suppression and thermal distortion of the rocking curves will be characterized. The transient elastic waves effects, which is not analytically accessible, will also be evaluated.

- In Chapter 4, the thermal load effects in multi-pulse situations at high repetition rate will be studied. The dynamic pulse-to-pulse variation of the output photon beam properties will be shown and characterized. Furthermore, the critical operation parameters will be determined accordingly when the pulse-to-pulse variation vanishes and the system reaches a quasi-steady state. The benefits of operating the monochromator at cryogenic temperatures will also be discussed.

- In Chapter 5, the emerging nondiffusive heat transfer phenomena at cryogenic temperature will be studied. Based on the two parameter heat conduction model, a nondimensional parameters characterizing the significance of the nondiffusive effects will be presented. In the cases where nondiffusive effects are very strong and wave-like heat transport behavior emerges, a simplified wave-diffusive model will be proposed to characterize the heat dissipation.

- In Chapter 6, a summary for this thesis is given and future work is suggested.

Chapter 2

Analytical analysis for thermal load

In this chapter, we first briefly introduce the physical processes involved in the photon-crystal interactions. The time scale for these physical processes differs significantly, making this study a multiscale problem. Given the time scale of interest, we introduce some assumptions to simplify the analysis. With these assumptions, we deliver an analytical model to illustrate the thermal load effects and provide quick estimation tool for practical applications.

2.1 Bragg condition and dynamic diffraction

Proposed by Lawrence Bragg and his father William Henry Bragg in 1913 [17], Bragg diffraction describes the reflection of X-ray on crystalline solids. In Bragg's model, the crystal is depicted as a set of discrete parallel planes separated by a constant parameter d. When the incident X-ray with incident angle θ and wavelength λ satisfies certain condition (n is an integer)

$$n\lambda = 2d \sin\theta, \tag{2.1}$$

the reflected intensity peaks (Fig. 2.1). This discovery equally applies to neutron and electron diffraction; it also provides direct evidence for the periodic atomic structure of crystal postulated for several centuries. Based on this important formula, the work determining crystal structures by the Braggs leads to their awarded the Nobel Prize in physics in 1915.

In Eq. (2.1), the periodic structure of the atoms in crystal is assumed to be uniform without any defects or deformation. Further development of dynamic diffraction theory was derived by Darwin by considering multiple scattering effects [19] and by Ewald [20], the latter treated the crystal as an infinite periodic lattice of point scatterers. After reformulated and extended by von Laue [21] and other researchers [22–26], the dynamic diffraction theory became applicable for calculating and explaining the physical effects of the plane waves. However, some practical issues such as the other types of incident waves and lattice deformations due to bending or defects, were still not included. To consider these issues, Takagi [27] and Taupin [28] independently derived, from the basic equations of classical electrodynamics, a general theory for arbitrary incident X-ray wave propagation in distorted crystal. However, due to the complexity of the equations, the analytical solutions are only limited to some simple cases such as uniform strain gradient and a crystal with a transition layer. Numerical solutions of the Takagi-Taupin equation assist interpretations of X-ray propagation in distorted crystals [29].

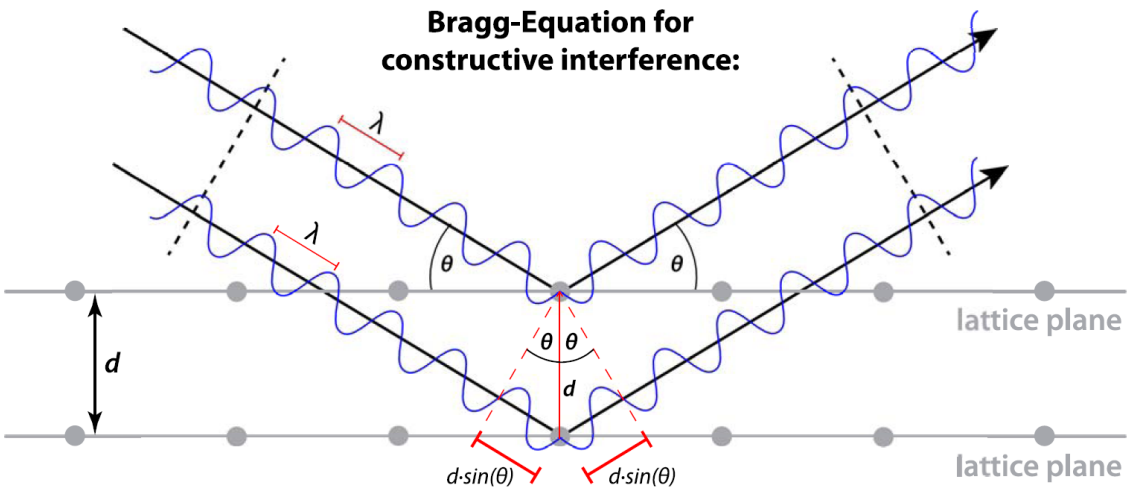

Figure 2.1: The illustration of Bragg's law [18]

By applying the theory of X-ray diffraction based on Bragg condition, the photon absorption, reflection and transmission can be captured. The time scale for diffraction is around femtosecond, which is at least 3 orders of magnitude shorter than other physics discussed later. Therefore, this process can be viewed as instantaneous by other physical processes, and the effects of other physical processes can be "frozen" for diffraction.

2.2 Energy absorption

After the interactions between incident X-ray and the crystal, some energy is deposited into the crystal by absorption. The major absorption mechanism from visible light to hard X-ray (~ 50 keV) regime can be described as the photoelectric effect, which can be further divided into the inner and the outer photoelectric effects. The inner photoelectric effect refers to the excitation of electrons by photon from the valence band (VB) or atomic inner shells to the conduction band (CB). The outer photoelectric effect, on the other hand, happens when the energy transfer from photon to the electron exceeds the work function: the electron is able to escape from the surface.

In diamond, the thermalized electrons in the conduction band, either from valence band or inner shell, excite more electrons from valence band through the electron impact ionization. Meanwhile, they also interact with each other. Consequently, a fast thermalization of the conduction band electrons is achieved, typically in few tens of femtoseconds (at most 200 fs).

Between the electrons and lattice, energy exchange starts as soon as the first photoelectrons appear. The recombination process, both radiative recombination and non-radiative recombination, leads to local thermal equilibrium and emission of phonons. The timescale for local electron-lattice thermal equilibrium typically ranges from tens of picoseconds [31] hundreds of nanoseconds [32] depending on various conditions (such as nitrogen content).

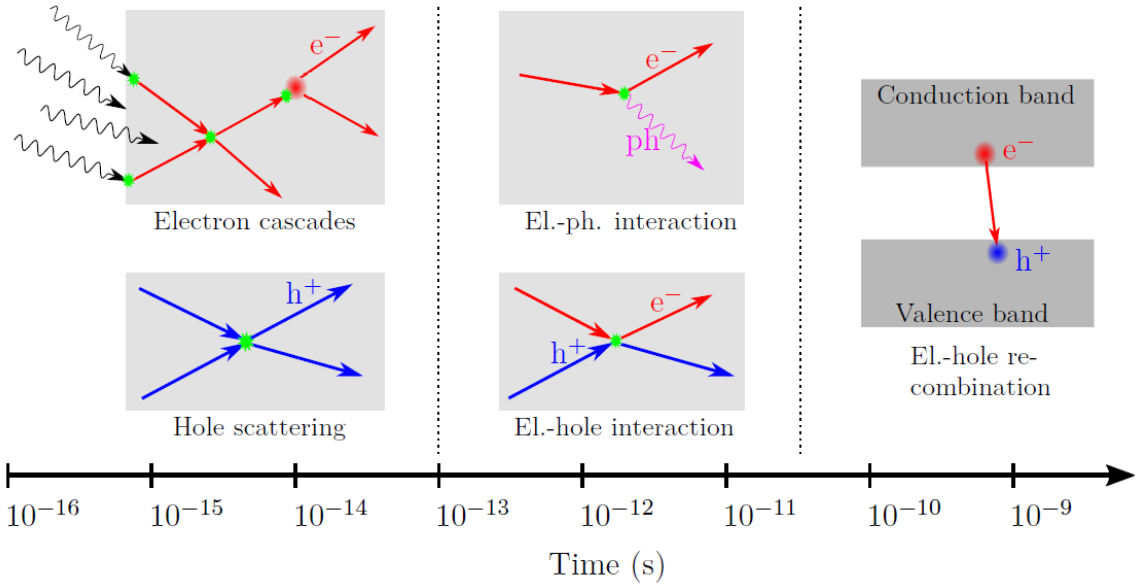

Figure 2.2: The timescales for photon-crystal excitation and relaxation [30]

2.2.1 Instantaneous strain generation

The temperature rise due to the energy deposition introduces thermal stress to the crystal. Lattice strain is generated mainly at the surface as there is traction-free condition and no confinement in surface normal direction [33]. It then propagates as compression elastic waves into the thickness and starts to bounce back and forth on the top and bottom traction-free boundaries. Thomsen et al. showed that the stress generation and propagation is well described by the thermoelastic model [34], confirmed by the experimental measurement on diamond by Stoupin et al. [35]. An illustration of generated strain waves is shown in Fig. 2.3.

In 3D, the transient thermoelastic model can be given by [36] without the hot electron blast effects in strain generation

$$\rho\frac{\partial^2 u}{\partial t^2} = \frac{\partial \sigma_x}{\partial x} + \frac{\partial \sigma_{xy}}{\partial y} + \frac{\partial \sigma_{xz}}{\partial z}, \tag{2.2}$$

$$\rho\frac{\partial^2 v}{\partial t^2} = \frac{\partial \sigma_{xy}}{\partial x} + \frac{\partial \sigma_y}{\partial y} + \frac{\partial \sigma_{yz}}{\partial z}, \tag{2.3}$$

$$\rho\frac{\partial^2 w}{\partial t^2} = \frac{\partial \sigma_{xz}}{\partial x} + \frac{\partial \sigma_{yz}}{\partial y} + \frac{\partial \sigma_z}{\partial z}, \tag{2.4}$$

$$\sigma_x = \lambda\left(\varepsilon_x + \varepsilon_y + \varepsilon_z\right) + 2\mu\varepsilon_x - (3\lambda + 2\mu)\,\alpha_T\,(T - T_{\text{ref}})\,, \tag{2.5}$$

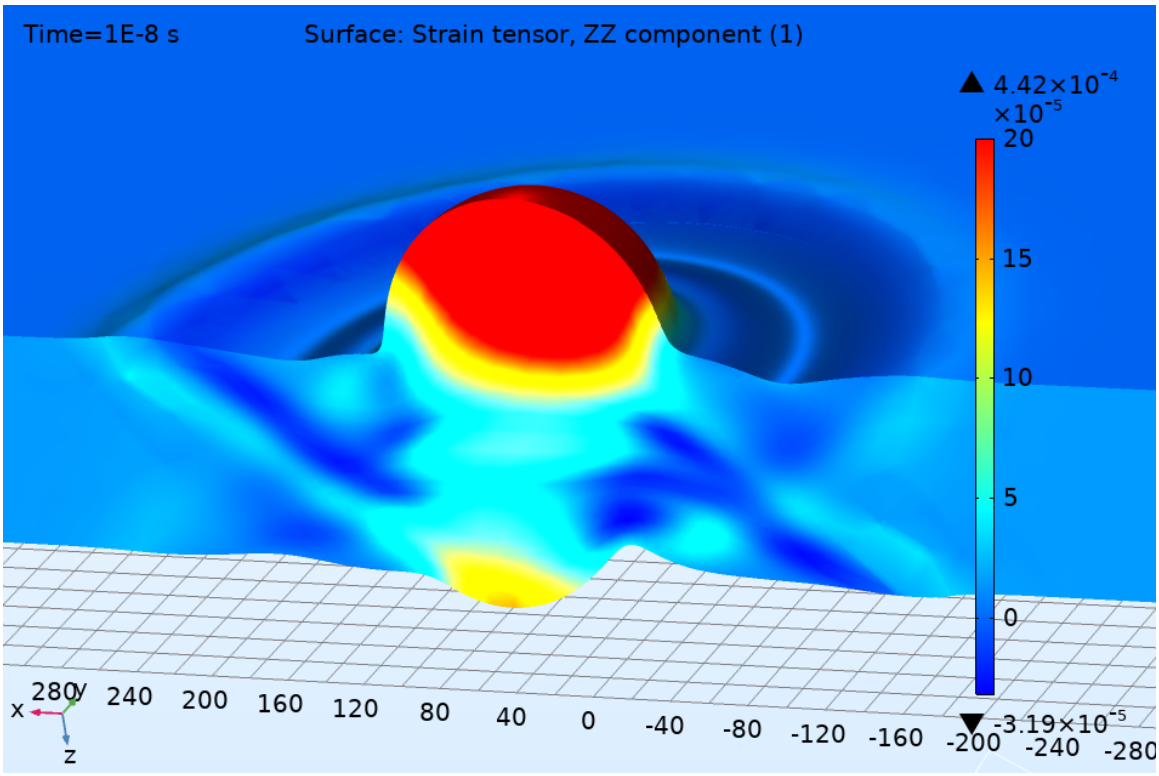

Figure 2.3: An example of generated strain waves propagation in diamond, simulated by COMSOL.

$$\sigma_y = \lambda\left(\varepsilon_x + \varepsilon_y + \varepsilon_z\right) + 2\mu\varepsilon_y - (3\lambda + 2\mu)\,\alpha_T\,(T - T_{\text{ref}})\,, \tag{2.6}$$

$$\sigma_z = \lambda\left(\varepsilon_x + \varepsilon_y + \varepsilon_z\right) + 2\mu\varepsilon_z - (3\lambda + 2\mu)\,\alpha_T\,(T - T_{\text{ref}})\,, \tag{2.7}$$

$$\sigma_{xy} = \mu\gamma_{xy}, \quad \sigma_{xy} = \mu\gamma_{xy}, \quad \sigma_{xy} = \mu\gamma_{xy}, \tag{2.8}$$

$$\varepsilon_x = \frac{\partial u}{\partial x}, \quad \varepsilon_y = \frac{\partial v}{\partial y}, \quad \varepsilon_z = \frac{\partial w}{\partial z}, \tag{2.9}$$

$$\gamma_{xy} = \frac{\partial u}{\partial y} + \frac{\partial v}{\partial x}, \quad \gamma_{xz} = \frac{\partial u}{\partial z} + \frac{\partial w}{\partial x}, \quad \gamma_{yz} = \frac{\partial v}{\partial z} + \frac{\partial w}{\partial y}, \tag{2.10}$$

where u, v, w are the displacements in the x, y, z directions, respectively; ε_x, ε_y, ε_z are the normal strains in the x, y, z directions, respectively; γ_{xy} is the shear strain in the xy direction, γ_{xz} is the shear strain in the xz direction, γ_{yz} is the shear strain in the yz direction; σ_x, σ_y, σ_z are the normal stresses in the x, y, z directions, respectively; σ_{xy} is the shear stress in the xy direction, σ_{xz} is the shear stress in the xz direction, σ_{yz} is the shear stress in the yz direction; T is the temperature; T_{ref} is the reference temperature; ρ is density; $\lambda = K - \frac{2}{3}\mu$ and μ are Lame's coefficients; and α_T is the

thermal expansion coefficient.

The timescale for this thermomechanical transient strain waves propagation can last for microseconds or longer. Depending to the excitation modes, the timescale may even extend to millisecond or longer, as will be shown in later chapter. This is due to the high quality factor of diamond.

In timescale larger than about 100 ns level, the multidimensional effects already merged and need to be considered. Figure 3.3 shows the comparison between the experimental and analytical work by Stoupin et al. [35] and the 2D axisymmetric finite element analysis results simulated by COMSOL. A clear decay in strain waves amplitude can be observed, which is due to the strain wave propagation in radial direction. In diamond thin plate, the generated acoustic waves initially propagate as bulk longitudinal and transverse waves, but after multiple reflections at the surface, they interfere and develop into new modes. This is Lamb wave. We will introduce and discuss about it in later chapter.

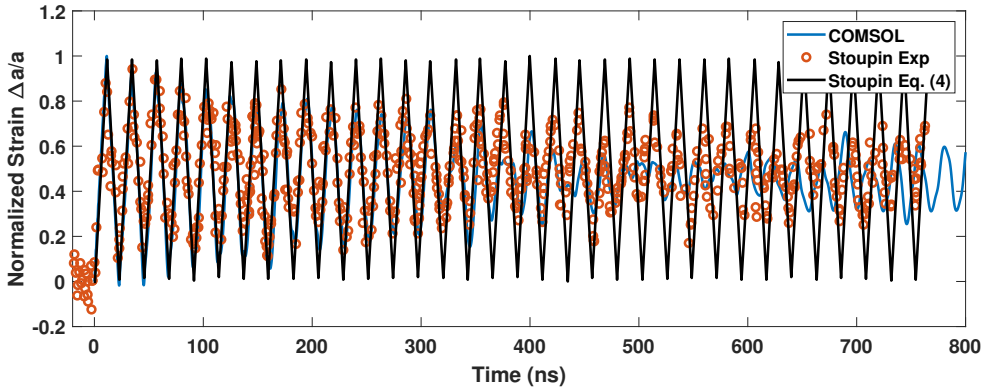

Figure 2.4: Figure 3.2 The comparison between the experimental and analytical results by Stoupin et al. [35] and the axisymmetric results by COMSOL.

The propagating or non-propagating strain waves pose a potential issue for the diffraction: if the repetition rate does not synchronize with the strain wave frequency, the incident light will see different strain fields from pulse to pulse, leading to seemingly random output light. On the other hand, if the repetition rate does synchronize with the strain wave frequency, resonance condition could be satisfied, triggering even worse instability. These issues will also be addressed in later chapters.

2.2.2 Thermal dissipation

After the thermalization of phonon, the thermal transport can be described by tradition thermal conduction equation:

$$\rho c_p \frac{\partial T}{\partial t} = \frac{\partial}{\partial x}\left(\kappa \frac{\partial T}{\partial x}\right) + \frac{\partial}{\partial y}\left(\kappa \frac{\partial T}{\partial y}\right) + \frac{\partial}{\partial z}\left(\kappa \frac{\partial T}{\partial z}\right) + \dot{q}''', \tag{2.11}$$

where T refers to temperature, t refers to time, c_p is the specific heat, κ is thermal conductivity, and $\dot{q}'''$ is the volumetric heat generation.

Accordingly, a thermal diffusion characteristic time can be defined as

$$\tau = \frac{L_c^2 \rho c_p}{\kappa}, \tag{2.12}$$

where L_c is the characteristic length of thermal diffusion. For diamond at room temperature (300 K), the density ρ is $3520\,\mathrm{kg/m^3}$, thermal diffusivity is $10.83\,\mathrm{cm^2/s}$. If the characteristic length of thermal diffusion is $100\,\mu\mathrm{m}$, the thermal diffusion characteristic time can be calculated as $9.23\,\mu\mathrm{s}$. This thermal diffusion time is comparable with the repetition rate timescale of interest. Heat conduction should be considered as dynamic.

However, the traditional thermal conduction theory relies on a strong assumption: the collisions between the thermal energy carriers happen everywhere at any moment. In other words, the mean free path (MFP) of the heat carriers are much smaller than the characteristic length. An important nondimensional parameter describing this is the Knudsen number

$$\mathrm{Kn} = \frac{\Lambda}{L_c}, \tag{2.13}$$

where Λ is the MFP of the heat carriers. In macroscopy or at high temperature, this assumption is valid. However, for thin film with small thickness or at cryogenic temperature, Knudsen number may increase to even larger than unity. In these situation, nondiffusive heat transfer phenomena merge and traditional heat diffusion theory does not offer correct description and prediction.

In nondiffusive regime, there are several distinctive thermal transport behaviors. The most relevant ones to this study are 1) the thickness-dependent thermal conductivity, 2) the size-dependent heat dissipation and 3) the wave-like thermal transport. The first two modify the heat dissipation rate predicted by diffusive heat transfer and result in inaccuracy in the prediction, while the last one could introduce further influence. We will discuss this in later chapters.

2.3 Strain & surface slope effects: an analytical thermal load model

Although we have introduced all the physical processes in the X-ray-crystal interaction process under high repetition rate XFEL, it is the coupling and resultant effects that alter the properties of the output light from the optics. Here, based on the thermally induced strain and surface slope field, an analytical model is derived below to reveal clear physics picture of how the output photon will be affected due to the thermal load.

2.3.1 Non-uniform thermal distortion

The successful operation [37–40] of the fourth generation of light source, the X-ray free-electron laser (XFEL), enables the experimental explorations and measurements in a wide range of fields, such as chemistry [41], life sciences [42] and material sciences [43]. The superior properties of XFEL beam, such as ultra-short duration [44], high transverse coherence [45] and unprecedentedly high spectral brightness [37], make it possible to probe structures and dynamics [46] in very small scale, such as single molecule imaging. Compared to the third generation of light source, the synchrotron sources, the XFEL delivers relatively low total power but extreme flux due to small angular divergence. The extreme flux generates a local hot spot (or thermal bump) at its footprint

due to the X-ray-matter interactions, triggering local disturbance from the Bragg condition. This thermally induced deviation from Bragg condition is known as thermal load.

Thermal load has been an issue in X-ray optics for several decades [47]. For the X-ray optics serving on synchrotron beamlines, such as mirrors and monochromators, one fundamental requirement is that, the beam quality should be preserved. However, thermal load results in disturbance (such as thermally induced surface slope and strain) from the Bragg condition. The disturbance is usually non-uniform and leads to the distortion of crystal rocking curve: its central frequency may shift and its band width may be broadened. Thus thermal load causes degradation of the beam quality. Existing solutions to mitigate thermal load are appropriately designed cooling and stiffening strategies [2]. These solutions are proved successful to suppress the thermal load effects to an acceptable degree [48] for X-ray optics in synchrotron beamline. However, the extreme flux provided by XFEL challenges the existing solutions. Compared to synchrotron light sources, the heat flux deposited by XFEL pulses can be several orders of magnitude higher. For example, in Linac Coherent Light Source (LCLS) of SLAC National Accelerator Laboratory, a typical XFEL has pulse energy about 2 mJ, transverse spot size about 150 μm and pulse duration about 100 fs. The averaged absorbed heat flux during the XFEL pulse can be calculated as 4×10^{13} W/m^2. With this extremely high heat flux, the existing cooling techniques may not be sufficient to extract the residual heat within the XFEL footprint. The requirements for cooling also become more strict for applications such as self-seeding [6] and X-ray free-electron laser oscillator (XFELO) [49], where the spot size is even smaller or the relaxation time for the crystal is very limited (at high repetition rate). Moreover, in pump-probe mode, the cooling may not work at all due to the short delay time (tens or hundreds of nanoseconds) between the two pulses.

Therefore, it is crucial to characterize thermal load for better solutions. At present, only incomplete qualitative estimation of thermal load is available. For example, the central frequency shift is usually estimated by the maximal thermal strain. However, there is no simple estimation available for band broadening, even though it is known to be caused by non-uniformity of the thermal load. The exists very limited number of studies that quantitatively describe the thermal load effects. Bushuev [50, 51] showed that the rocking curves can be strongly distorted by thermal load, but no separate assessment on how different factors of thermal load (such as maximal strain and the non-uniformity of the thermal load) contribute to this distortion was provided. In this study, we derive an analytical model to quantitatively describe the thermal load effects on the distortion of the rocking curve. We show that the central frequency shift and distortion of the rocking curve can be attributed to different factors. The central frequency shift is mainly due to the overall disturbance of the crystal under thermal load, while the rocking curve distortion is caused by the non-uniformity of the thermal load. These effects are assessed individually and quantitatively by the analytical model, providing potential directions for designing the monochromator and corresponding cooling schemes.

2.3.2 Analytical model derivation

For a perfect crystal without any strain and deformation, the rocking curve is accessible through multiple methods, such as the response function method by Shvyd'ko and Lindberg [52]. When small perturbation is present (such as weak strain and deformation), a parameter α can be

defined [50–52] to account for local deviation from the exact Bragg condition

$$\alpha \equiv \frac{k^2 - \left(\vec{h} + \vec{k}\right)^2}{k^2}, \tag{2.14}$$

where $\vec{k}$ is the wavevector, $\vec{h}$ is the vector of the reciprocal lattice. Bushuev [50] showed that α can be expressed as

$$\alpha = 2\sin(2\theta_B)\left[\delta\theta + \left(\frac{\Omega}{\omega_0} + \frac{\delta d}{d}\right)\tan\theta_B\right], \tag{2.15}$$

where θ_B is the Bragg angle, $\delta\theta$ is the local incident angle deviation from Bragg angle, $\Omega = \omega - \omega_0$ is the deviation of angular frequency ω from the central angular frequency ω_0 of Bragg condition, and d is the interplanar distance. The relative change of the interplanar distance is characterized by strain $\varepsilon \equiv \delta d/d$. The parameter α indicates that, an effective frequency disturbance can be defined as

$$\frac{\Omega_{\text{eff}}}{\omega_0} = \frac{\Omega}{\omega_0} + \cot\theta_B\delta\theta + \varepsilon = \frac{\Omega + \Delta\Omega}{\omega_0}. \tag{2.16}$$

This effective frequency disturbance Ω_{eff} causes the same disturbance around Bragg condition without $\delta\theta$ and ε as an Ω with $\delta\theta$ and ε can. $\Delta\Omega$ is the deviation parameter defined as

$$\frac{\Delta\Omega}{\omega_0} \equiv \cot\theta_B\delta\theta + \varepsilon. \tag{2.17}$$

Thus, the local deviation from Bragg condition due to thermal load is conjointly introduced to the rocking curve as a local effective deviation angular frequency. The rocking curve now is spatial dependent.

However, if a full three-dimensional spatial-dependent local deviation is considered, an explicit analytical solution is almost impossible. To proceed, we assume that the local deviation is two-dimensional (2D). This assumption is applicable in many situations. One example is the transmissive monochromator in hard X-ray self-seeding mode. It is usually a thin CVD diamond plate. The thermal strain variation in thickness direction can be omitted so that the thermal strain field is reduced to 2D [51], especially when the X-ray penetration depth is much larger than the crystal thickness. Another example is a typical silicon reflective monochromator in beamline: when the extinction length of the incident pulse is very small compared to strain variation in thickness direction, only thermal slope and strain field on the surface need to be considered.

We start with a typical SASE pulse with M modes

$$E_\omega(x,y) = \sqrt{\frac{I_0}{\pi r_x r_y}}\exp\left(-\frac{x^2}{2r_x^2} - \frac{y^2}{2r_y^2}\right)\sum_{j=1}^{M}\sqrt{\frac{1}{M\sqrt{2\pi}\sigma_{\omega,j}}}\exp\left[-\left(\frac{\omega - \omega_{0,j}}{2\sigma_{\omega,j}}\right)^2 + i\varphi_j\right], \tag{2.18}$$

where I_0 is the incident SASE pulse energy, $\sigma_{\omega,j}$ is the SASE bandwidth in RMS, r_x and r_y are intensity radius in x and y direction, respectively. The phase for j^{th} mode, φ_j, is random and assumed not spatial-dependent (due to good transverse coherence [44, 45]). Therefore, Eq. (2.18) can be processed mode by mode and superimposed in the end. For simplicity and without the loss of generality, we select a single mode Gaussian envelope SASE with the same thermal load as a

typical multi-mode SASE:

$$E_\omega(x,y) = \sqrt{\frac{I_0}{\sqrt{2\pi}\sigma_\omega \pi r_x r_y}} \exp\left[-\frac{x^2}{2r_x^2} - \frac{y^2}{2r_y^2} - \left(\frac{\omega-\omega_0}{2\sigma_\omega}\right)^2 + i\varphi\right]. \tag{2.19}$$

The intensity distribution can be calculated as

$$I_\omega(x,y) = \frac{I_0}{\sqrt{2\pi}\sigma_\omega \pi r_x r_y} \exp\left[-\frac{x^2}{r_x^2} - \frac{y^2}{r_y^2} - \left(\frac{\omega-\omega_0}{\sqrt{2}\sigma_\omega}\right)^2\right]. \tag{2.20}$$

For simplification, we normalize the equation by $x^* = x/r_x$,$y^* = y/r_y$ and $\Omega^* = \Omega/\omega_0$. Thus, Eq. (2.20) can be written as

$$I_\omega(x,y) = \frac{I_0}{\sqrt{2\pi}\sigma_\omega \pi r_x r_y} \exp\left(-x^2 - y^2 - \frac{\Omega}{\sqrt{2}\sigma_\omega^2/\omega_0^2}\right), \tag{2.21}$$

where the superscript star has been dropped without confusion.

The overall reflectance R (or transmittance T) is defined as the weighted average of the local reflectance (or transmittance) of the whole field (according to Bushuev [50])

$$\begin{aligned}
\bar{R} &\equiv \frac{\iint_{-\infty}^{+\infty} R\left[\Omega + \Delta\Omega(x,y)\right] I_\omega dxdy}{\iint_{-\infty}^{+\infty} I_\omega dxdy} \\
&= \frac{1}{\pi}\iint_{-\infty}^{+\infty} R\left[\Omega + \Delta\Omega(x,y)\right] \exp\left(-x^2 - y^2\right) dxdy \\
&= \frac{1}{\pi}\int_{-\infty}^{+\infty} \exp\left(-y^2\right) dy \int_{-\infty}^{+\infty} R\left[\Omega + \Delta\Omega(x,y)\right] \exp\left(-x^2\right) dx.
\end{aligned} \tag{2.22}$$

The reflectance R is interchangeable with transmittance T. Here we take R as an example.

Integrating Eq. (2.22) by parts yields

$$\begin{aligned}
\bar{R} &= \frac{1}{\pi}\int_{-\infty}^{\infty} \exp\left(-y^2\right)\left[\frac{\sqrt{\pi}}{2}\operatorname{erf}(x) R(\Omega + \Delta\Omega)\Big|_{-\infty}^{\infty} - \frac{\sqrt{\pi}}{2}\int_{-\infty}^{\infty}\frac{\partial R}{\partial x}\operatorname{erf}(x)\, dx\right] dy \\
&= \frac{1}{\sqrt{\pi}}\int_{-\infty}^{\infty} \exp\left(-y^2\right)\left[R(\Omega + \Delta\Omega_{\infty,x}) - \frac{1}{2}\int_{-\infty}^{\infty}\frac{\partial R}{\partial x}\operatorname{erf}(x)\, dx\right] dy \\
&= \frac{1}{\sqrt{\pi}}\int_{-\infty}^{\infty} R(\Omega + \Delta\Omega_{\infty,x}) \exp\left(-y^2\right) dy - \frac{1}{2\sqrt{\pi}}\iint_{-\infty}^{\infty}\frac{\partial R}{\partial x}\operatorname{erf}(x) \exp\left(-y^2\right) dxdy.
\end{aligned} \tag{2.23}$$

Here, $\Delta\Omega_{\infty,x}$ means the $\Delta\Omega$ evaluated at $y \to \infty$. One should realize that, it is not necessarily zero, as this infinity is defined based on intensity distribution length scale (transverse spot size of the

SASE pulse). Thermal dissipation has a different length scale (usually much larger depending on relaxation time). Therefore, even at the location that's nearly infinitely away for intensity, thermal dissipation may still affect this location. Thus, the thermally induced strain field is not necessarily vanishing, especially for quasi-steady state in uniform pulsed mode where an overall temperature increase constantly exists throughout the domain.

Integrating by parts again yields

$$\begin{aligned}
\bar{R} &= \left[\frac{1}{2} \operatorname{erf}(y) R\left(\Omega + \Delta\Omega_{\infty,x}\right) \Big|_{-\infty}^{\infty} - \frac{1}{2} \int_{-\infty}^{\infty} \frac{\partial R\left(\Omega + \Delta\Omega_{\infty,x}\right)}{\partial y} \operatorname{erf}(y)\, dy \right] \\
&- \frac{1}{2\sqrt{\pi}} \iint_{-\infty}^{\infty} \frac{\partial R}{\partial x} \operatorname{erf}(x) \exp\left(-y^2\right) dxdy \\
&= R\left(\Omega + \Delta\Omega_{\infty}\right) - \frac{1}{2} \int_{-\infty}^{\infty} \frac{\partial R\left(\Omega + \Delta\Omega_{\infty,x}\right)}{\partial y} \operatorname{erf}(y)\, dy \\
&- \frac{1}{2\sqrt{\pi}} \iint_{-\infty}^{\infty} \frac{\partial R}{\partial x} \operatorname{erf}(x) \exp\left(-y^2\right) dxdy
\end{aligned} \tag{2.24}$$

Integrating by parts one more time yields

$$\begin{aligned}
\bar{R} &= R\left(\Omega + \Delta\Omega_{\infty}\right) - \frac{1}{2} \int_{-\infty}^{\infty} \frac{\partial R\left(\Omega + \Delta\Omega_{\infty,x}\right)}{\partial y} \operatorname{erf}(y)\, dy \\
&- \frac{1}{4} \left[\int_{-\infty}^{\infty} \frac{\partial R}{\partial x} \operatorname{erf}(x)\, dx \operatorname{erf}(y) \Big|_{-\infty}^{\infty} - \iint_{-\infty}^{\infty} \frac{\partial^2 R}{\partial x \partial y} \operatorname{erf}(x) \operatorname{erf}(y)\, dxdy \right] \\
&= R\left(\Omega + \Delta\Omega_{\infty}\right) - \frac{1}{2} \int_{-\infty}^{\infty} \frac{\partial R}{\partial x}\Big|_{y\to\infty} \operatorname{erf}(x)\, dx - \frac{1}{2} \int_{-\infty}^{\infty} \frac{\partial R\left(\Omega + \Delta\Omega_{\infty,x}\right)}{\partial y} \operatorname{erf}(y)\, dy \\
&+ \frac{1}{4} \iint_{-\infty}^{\infty} \frac{\partial^2 R}{\partial x \partial y} \operatorname{erf}(x) \operatorname{erf}(y)\, dxdy.
\end{aligned} \tag{2.25}$$

Applying chain rule:

$$\begin{aligned}
\bar{R} &= R\left(\Omega + \Delta\Omega_{\infty}\right) - \frac{1}{2} \int_{-\infty}^{\infty} \frac{\partial R}{\partial \Delta\Omega} \frac{\partial \Delta\Omega}{\partial x}\Big|_{y\to\infty} \operatorname{erf}(x)\, dx - \frac{1}{2} \int_{-\infty}^{\infty} \frac{\partial R}{\partial \Delta\Omega} \frac{\partial \Delta\Omega}{\partial y}\Big|_{x\to\infty} \operatorname{erf}(y)\, dy \\
&+ \frac{1}{4} \iint_{-\infty}^{\infty} \frac{\partial}{\partial x} \left(\frac{\partial R}{\partial \Delta\Omega} \frac{\partial \Delta\Omega}{\partial y} \right) \operatorname{erf}(x) \operatorname{erf}(y)\, dxdy.
\end{aligned} \tag{2.26}$$

Finally, we have the expression for general 2D cases

$$\overline{R} = R\left(\Omega + \Delta\Omega_\infty\right) - \frac{1}{2}\int_{-\infty}^{\infty} \frac{\partial R}{\partial \Delta\Omega}\frac{\partial \Delta\Omega}{\partial x}\bigg|_{y\to\infty} \operatorname{erf}(x)\, dx - \frac{1}{2}\int_{-\infty}^{\infty} \frac{\partial R}{\partial \Delta\Omega}\frac{\partial \Delta\Omega}{\partial y}\bigg|_{x\to\infty} \operatorname{erf}(y)\, dy + \frac{1}{4}\iint_{-\infty}^{\infty}\left[\frac{\partial^2 R}{\partial\left(\Delta\Omega\right)^2}\frac{\partial \Delta\Omega}{\partial x}\frac{\partial \Delta\Omega}{\partial y} + \frac{\partial R}{\partial \Omega}\frac{\partial^2 \Delta\Omega}{\partial x \partial y}\right]\operatorname{erf}(x)\operatorname{erf}(y)\, dxdy. \tag{2.27}$$

Here, $\Delta\Omega_\infty$ means the $\Delta\Omega$ evaluated at infinity. If $\Delta\Omega_{\infty,x}$, $\Delta\Omega_{\infty,y}$ and $\Delta\Omega_\infty$ are all constant that does not depend on y, then Eq. (2.27) can be re-written as

$$\bar{R} = R\left(\Omega + \Delta\Omega_\infty\right) + \frac{1}{4}\iint_{-\infty}^{\infty}\left[\frac{\partial^2 R}{\partial(\Delta\Omega)^2}\frac{\partial \Delta\Omega}{\partial x}\frac{\partial \Delta\Omega}{\partial y} + \frac{\partial R}{\partial \Delta\Omega}\frac{\partial^2 \Delta\Omega}{\partial x \partial y}\right]\operatorname{erf}(x)\operatorname{erf}(y)\, dxdy. \tag{2.28}$$

However, one should be reminded that, unfortunately, $\Delta\Omega_\infty$ might not vanish, as this infinity is defined based on intensity distribution length scale. Thermal load typically has a much larger length scale, so that the strain field is not vanishing. Especially, for the situations where a quasi-steady state can be reached, a non-zero temperature increase constantly exists everywhere.

2.3.3 Validations

Bushuev [50,51] analytically solved the temperature field for a thin infinite crystal with multi-pulse incident SASE and provided the thermally distorted rocking curves. Here, we combine our analytical model with this analytically solved temperature and compare the results as validation.

In his analytical solution, Bushuev [50] considered a 2D infinite domain ($-\infty < x, y < \infty$) with constant thermal properties. After n incident SASE pulses, the temperature rise field $\Delta T\left(x, y, t\right)$ can be analytically solved as

$$\Delta T\left(x, y, t\right) = \sum_{i=0}^{n} \Delta T\left(x, y, t - t_i\right) = \sum_{i=0}^{n} \frac{\Delta T_i}{\sqrt{\beta_{x,i}\beta_{y,i}}} \exp\left(-\frac{x^2}{\beta_{x,i}} - \frac{y^2}{\beta_{y,i}}\right), \tag{2.29}$$

where $\beta_{x,i} = 1 + \gamma_0^2 \frac{t-t_i}{\tau_T}$, $\beta_{y,i} = 1 + \frac{t-t_i}{\tau_T}$, $\Delta T_1 = \frac{\mu Q_p}{\pi \rho c_p r_1^2}$, $r_x = r_1/\gamma_0$, $r_y = r_1$, $r_1 \approx 0.6 r_p = 0.6 r_s M = 0.6 r_s \sqrt{(1+\alpha_s D)^2 + D^2}$, $\gamma_0 = \sin\theta_B$, $\tau_T = r_1^2 c_p \rho / 4\kappa$. All the parameters can be found in Ref. [50]. In Ref. [50], the deviation parameter can be defined as

$$\Delta\Omega = \varepsilon_{\text{thermal}} = \sum_{i=1}^{n} \alpha_T \Delta T\left(x, y, t - t_i\right) = \sum_{i=1}^{n} \Delta\Omega_i, \tag{2.30}$$

where $\Delta\Omega_i$ is defined as

$$\Delta\Omega_i = \frac{\alpha_T \Delta T_i}{\sqrt{\beta_{x,i}\beta_{y,i}}} \exp\left(-\frac{x^2}{\beta_{x,i}} - \frac{y^2}{\beta_{y,i}}\right). \tag{2.31}$$

The derivatives can be calculated as

$$\begin{aligned}\frac{\partial \Delta\Omega}{\partial x} &= \sum_{i=1}^{n} \frac{\alpha_T \Delta T_i}{\sqrt{\beta_{x,i}\beta_{y,i}}} \frac{\partial}{\partial x}\left[\exp\left(-\frac{x^2}{\beta_{x,i}} - \frac{y^2}{\beta_{y,i}}\right)\right] \\ &= \sum_{i=1}^{n} \frac{\alpha_T \Delta T_i}{\sqrt{\beta_{x,i}\beta_{y,i}}} \left(-\frac{2x}{\beta_{x,i}}\right) \exp\left(-\frac{x^2}{\beta_{x,i}} - \frac{y^2}{\beta_{y,i}}\right) \\ &= -\sum_{i=1}^{n} \frac{2x}{\beta_{x,i}} \Delta\Omega_i. \end{aligned} \tag{2.32}$$

Similarly,

$$\begin{aligned}\frac{\partial \Delta\Omega}{\partial y} &= \sum_{i=1}^{n} \frac{\alpha_T \Delta T_i}{\sqrt{\beta_{x,i}\beta_{y,i}}} \frac{\partial}{\partial y}\left[\exp\left(-\frac{x^2}{\beta_{x,i}} - \frac{y^2}{\beta_{y,i}}\right)\right] \\ &= \sum_{i=1}^{n} \frac{\alpha_T \Delta T_i}{\sqrt{\beta_{x,i}\beta_{y,i}}} \left(-\frac{2y}{\beta_{y,i}}\right) \exp\left(-\frac{x^2}{\beta_{x,i}} - \frac{y^2}{\beta_{y,i}}\right) \\ &= -\sum_{i=1}^{n} \frac{2y}{\beta_{y,i}} \Delta\Omega_i. \end{aligned} \tag{2.33}$$

Moreover, for cross derivative terms

$$\begin{aligned}\frac{\partial^2 \Delta\Omega}{\partial x \partial y} &= \sum_{i=1}^{n} \frac{\alpha_T \Delta T_i}{\sqrt{\beta_{x,i}\beta_{y,i}}} \left(\frac{4xy}{\beta_{x,i}\beta_{y,i}}\right) \exp\left(-\frac{x^2}{\beta_{x,i}} - \frac{y^2}{\beta_{y,i}}\right) \\ &= \sum_{i=1}^{n} \frac{4xy}{\beta_{x,i}\beta_{y,i}} \Delta\Omega_i. \end{aligned} \tag{2.34}$$

We can plug Eqs. (2.32)-(2.34) into Eq. (2.27) to obtain

$$\begin{aligned}\overline{R} =& R\left(\Omega + \Delta\Omega_\infty\right) + \int_{-\infty}^{\infty} \frac{\partial R}{\partial \Delta\Omega} \left(\sum_{j=0}^{n} \frac{\Delta\Omega_j|_{y\to\infty}}{\beta_{x,j}}\right) x \operatorname{erf}(x)\, dx \\ &+ \int_{-\infty}^{\infty} \frac{\partial R}{\partial \Delta\Omega} \left(\sum_{j=0}^{n} \frac{\Delta\Omega_j|_{x\to\infty}}{\beta_{y,j}}\right) y \operatorname{erf}(y)\, dy \\ &+ \iint_{-\infty}^{\infty} \frac{\partial^2 R}{\partial \left(\Delta\Omega\right)^2} \left(\sum_{j=0}^{n} \frac{\Delta\Omega_j}{\beta_{x,j}}\right)\left(\sum_{j=0}^{n} \frac{\Delta\Omega_j}{\beta_{y,j}}\right) xy \operatorname{erf}(x) \operatorname{erf}(y)\, dxdy \\ &+ \iint_{-\infty}^{\infty} \frac{\partial R}{\partial \Delta\Omega} \left(\sum_{j=0}^{n} \frac{\Delta\Omega_j}{\beta_{x,j}\beta_{y,j}}\right) xy \operatorname{erf}(x) \operatorname{erf}(y)\, dxdy. \end{aligned} \tag{2.35}$$

Eq. (2.35) is now ready to compare with Figs. 5 and 6 in Ref. [50] for validation, as plotted in Fig. 2.5. In Fig. 2.5, the numerical results represents our calculation that exactly follows the process specified in Ref. [50]. Our numerical results strictly overlaps with our analytical results by

Eq. (2.35). Also, an excellent agreement is observed in the comparison between our results and Bushuev's.

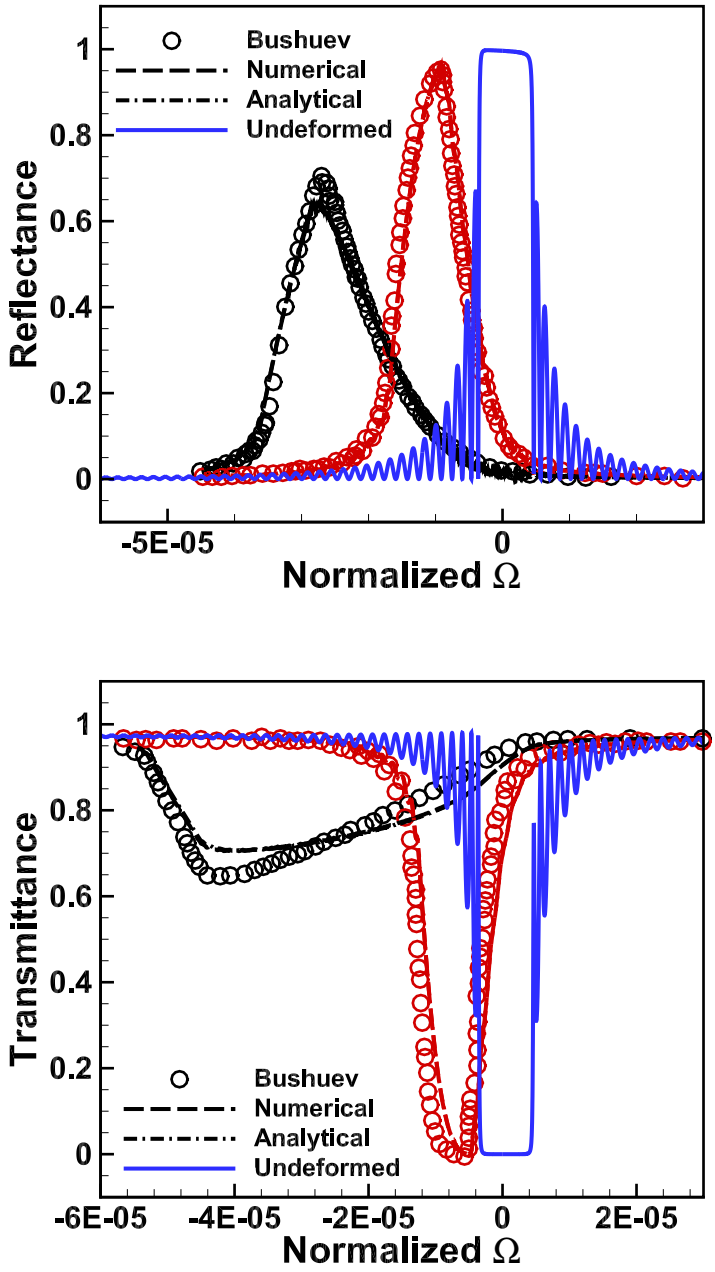

Figure 2.5: Comparison between the results by Eq. (2.35), our numerical calculation and by Bushuev [50].

As shown in Fig. 2.5, thermal load significantly distorts the rocking curve. Severe central

frequency shift and distortion can be observed due to thermal load. The peak reflectance is also suppressed, indicating a suppression in peak reflected beam intensity. All these effects are captured by Eq. (2.27). However, even though Eq. (2.27) predicts the effects of thermal load in many situations where the assumptions fit, its complicated form still obscures some direct and clear contributions from different factors of the thermal load, as addressed in introduction. To further reveal a clear picture of the thermal load effects, we present an axisymmetric (1D) case.

2.3.4 Clear physical insights: an axisymmetric case

In an axisymmetric case, the complicated form of Eq. (2.27) can be greatly simplified. We start by presenting the 1D axisymmetric form of Eq. (2.22)

$$\begin{aligned}\bar{R} &\equiv \frac{\int_0^\infty R I_\omega 2\pi r dr}{\int_0^\infty I_\omega 2\pi r dr} \\ &= \frac{\frac{I_0}{\sqrt{2\pi}\sigma_\omega \pi}\exp\left(-\frac{\Omega^2}{2\sigma_\omega^2/\omega_0^2}\right)\int_0^\infty R\left(\Omega+\Delta\Omega\right)\exp\left(-r^2\right)2\pi r dr}{\frac{I_0}{\sqrt{2\pi}\sigma_\omega}\exp\left(-\frac{\Omega^2}{2\sigma_\omega^2/\omega_0^2}\right)} \\ &= 2\int_0^\infty R\left(\Omega+\Delta\Omega\right)\exp\left(-r^2\right) r dr. \end{aligned} \tag{2.36}$$

Similarly, we integrate by parts

$$\begin{aligned}\bar{R} =& -R\left(\Omega+\Delta\Omega\right)\exp\left(-r^2\right)\Big|_0^\infty + \int_0^\infty \frac{\partial}{\partial r} R\left(\Omega+\Delta\Omega\right)\exp\left(-r^2\right) dr \\ =& -R\left(\Omega+\Delta\Omega\right)\exp\left(-r^2\right)\Big|_0^\infty + \int_0^\infty \frac{\partial R}{\partial \Delta\Omega}\frac{\partial \Delta\Omega}{\partial r}\exp\left(-r^2\right) dr. \end{aligned} \tag{2.37}$$

Therefore, we have

$$\bar{R} = R\left(\Omega+\Delta\Omega|_{r=0}\right) + \int_0^\infty \frac{\partial R}{\partial \Delta\Omega}\frac{\partial \Delta\Omega}{\partial r}\exp\left(-r^2\right) dr. \tag{2.38}$$

Compared to Eq. (2.27), Eq. (2.38) is simple, and it offers several straightforward and clear points. The central wavelength shift is strongly related to maximal deviation, as suggested by the first term of Eq. (2.38). In axisymmetric case, the maximal deviation is essentially the strain at the center of the footprint. The distortion is caused by the gradient, or non-uniformity, of the deviation, as suggested by the second term of Eq. (2.38). For narrow rocking (high order diffraction or better materials), the first derivative term $\partial R/\partial\Delta\Omega$ is larger, indicating that the Darwin width will be more sensitive to the thermal load.

Therefore, the maximal disturbance (estimated by $\alpha\Delta T_{\max}$, if only thermal strain is considered) is usually a reliable qualitative indicator of the frequency shift [50], though a minor contribution may also come from the second term of Eq. (2.38). This indicator has been successfully used

in the community for quite a long time. On the other hand, it has long been realized [2, 47] that the non-uniformity of temperature rise results in "mapping" error. Here, Eq. (2.38) quantifies this effect.

Furthermore, Eq. (2.38) also suggests that the frequency shift due to thermal load can be compensated by re-orienting the crystal with a small angle

$$\delta\theta_{\text{tuning}} = -\Delta\Omega|_{r=0}. \tag{2.39}$$

However, the distortion due to thermal load can only be minimized by suppressing the non-uniformity. To suppress the non-uniformity, one may implement optimal geometric design, or cooling or even compensated heating.

2.3.5 Comparison with numerical simulation

To provide a quantitative comparison, we investigate one special axisymmetric case. In this case, we consider incident SASE pulses at 9.83 keV with relative bandwidth (FWHM) of 1.18×10^{-3}, spot size (FWHM) of 47 um and pulse energy of 100 µJ. A 110-µm-thick diamond plate with (4 4 0) orientation is used as the monochromator to produce the seed pulse in self-seeding mode. The pulse repetition rate is 400 kHz. The Bragg angle here is 90°, and the absorption length is 1518.3 µm. Consequently, the 1D axisymmetric assumption is appropriate here because the incidence is normal and the absorption length is much larger than the crystal thickness.

In 1D axisymmetric case, Eq. (2.31) can be rewritten as

$$\Delta\Omega = \alpha_T \sum_{j=0}^{n} \frac{\Delta T_j}{\beta_{r,j}} \exp\left(-\frac{r^2}{\beta_{r,j}}\right). \tag{2.40}$$

where $r = \sqrt{x^2 + y^2}$ and $\beta_{r,j} = 1 + \frac{t-t_j}{\tau_T}$. In this case, due to normal incidence of SASE, the thermal slope is not present in the deviation parameter ($\cot\theta_B = 0$) given in Eq. (2.16). The elastic strain component is omitted for now but further discussion will be provided later. Eq. (2.40) also indicates that a quasi-steady state can never be reached because of its harmonic series behavior.

According to Eq. (2.16), we have

$$\Delta\Omega = \cot\theta_B\delta\theta + \varepsilon = \varepsilon. \tag{2.41}$$

When the elastic strain component is omitted, Eq. (2.41) leads to

$$\Delta\Omega = \varepsilon_{\text{thermal}} = \sum_{j=0}^{n} \frac{\alpha_T\Delta T_j}{\beta_{r,j}} \exp\left(-\frac{r^2}{\beta_{r,j}}\right). \tag{2.42}$$

Plug it into Eq. (2.38) to obtain

$$\bar{R} = R\left(\Omega + \alpha_T \sum_{j=0}^{n} \frac{\Delta T_j}{\beta_{r,j}}\right) - 2\int_0^{\infty} \frac{\partial R}{\partial\Delta\Omega}\left[\sum_{j=0}^{n} \frac{\alpha_T\Delta T_j}{\beta_{r,j}^2} \exp\left(-\frac{r^2}{\beta_{r,j}}\right)\right] \exp\left(-r^2\right) r dr. \tag{2.43}$$

For forward Bragg diffraction as in self-seeding case [6], the transmittance T is considered. The

same formula can be obtained for the transmittance:

$$\bar{T} = T\left(\Omega + \alpha_T \sum_{j=0}^{n} \frac{\Delta T_j}{\beta_{r,j}}\right) - 2\int_0^{\infty} \frac{\partial T}{\partial \Delta\Omega}\left[\sum_{j=0}^{n} \frac{\alpha_T \Delta T_j}{\beta_{r,j}^2} \exp\left(-\frac{r^2}{\beta_{r,j}}\right)\right] \exp\left(-r^2\right) r dr. \tag{2.44}$$

To provide a concrete comparison and characterize the applicability of our analytical model, we conduct finite element analysis (FEA) using COMSOL with the same SASE properties and crystal orientation and thickness. The crystal we consider is a 110-μm-thick 2 mm by 2 mm square plate. More details of numerical simulation will be described in Chapter 3. The temperature on one side surface is fixed at 300 K to enable a quasi-steady state, where the system behavior is periodic in time. After around 5000 incident pulses, the system approaches this quasi-steady state. In numerical simulation, the temperature-dependent thermal properties [53] and the boundary effects are both included. In addition, the elastic strain component effect can be quantified by comparing the results with or without it. With all these effects accounted, we export the strain field obtained by FEA and calculate the field of $\Delta\Omega(x, y)$ through Eq. (2.16), and feed it into Eq. (2.27) to evaluate the rocking curves under thermal load. The details of the numerical simulation were discussed in somewhere else.

Figure 2.6(a) shows the transmittance curves for the 1st, 10th, 200th and 5000th pulse. A significant shift can be observed here, but no significant band broadening is captured. However, the transmittance curve deforms noticeably, as the oscillating behavior near the fast-decreasing edges is suppressed when thermal load is present. This suppression can results in the seed pulse energy reduction for self-seeding, as shown in supplementary materials.

On the other hand, Fig. 2.6(b) summarizes the central frequency shift of the transmittance curve. The central frequency shift is calculated as the deviation of the rocking curve peak location from the designed value. This deviation can be predicted by Eq. (2.44) as $-\alpha_T \Delta T_{\max}$ when normalized. To show this, we analytically calculate the thermally distorted rocking curve using Eq. (2.44) and extract its central frequency shift. An outstanding agreement is observed between this calculated deviation (green square line) and $-\alpha_T \Delta T_{\max}$ (red triangle line). These two lines both grow logarithmically, as suggested by the harmonic series of Eq. (2.40). The other two lines stand for the central frequency shift calculated from the numerical results without the elastic strain (blue diamond line) and with the elastic strain (violet circle line). These two line both converge, indicating the existence of the quasi-steady state. The difference between these two lines is the presence of the elastic strain component. The elastic strain component results in only about 10% difference, as its magnitude is only about 10% of the thermal strain component.

The numerical result without elastic strain is overlapped with the curve of $-\alpha_T \Delta T_{\max}$ in first 300 pulses. A minor discrepancy between these two curves is due to the temperature-dependence of the thermal properties, which is not considered in analytical solution. After around 400 pulses, the slope of blue diamond curve obviously changes, because thermal diffusion reaches the boundary. An estimation of thermal diffusion characteristic time (about 0.0011 second or 430 pulses) coincides with this observation. This observation indicates that, Eq. (2.44) is able to provide good estimation of beam quality degradation in pump-probe (only two pulses) experiments, or in multi-pulse situations (pulse train mode). However, one may realize that, Eq. (2.38) (or Eq. (2.27)) is still valid when equipped with appropriate surface slope and strain solution, which has been well modeled in thermoelasticity studies.

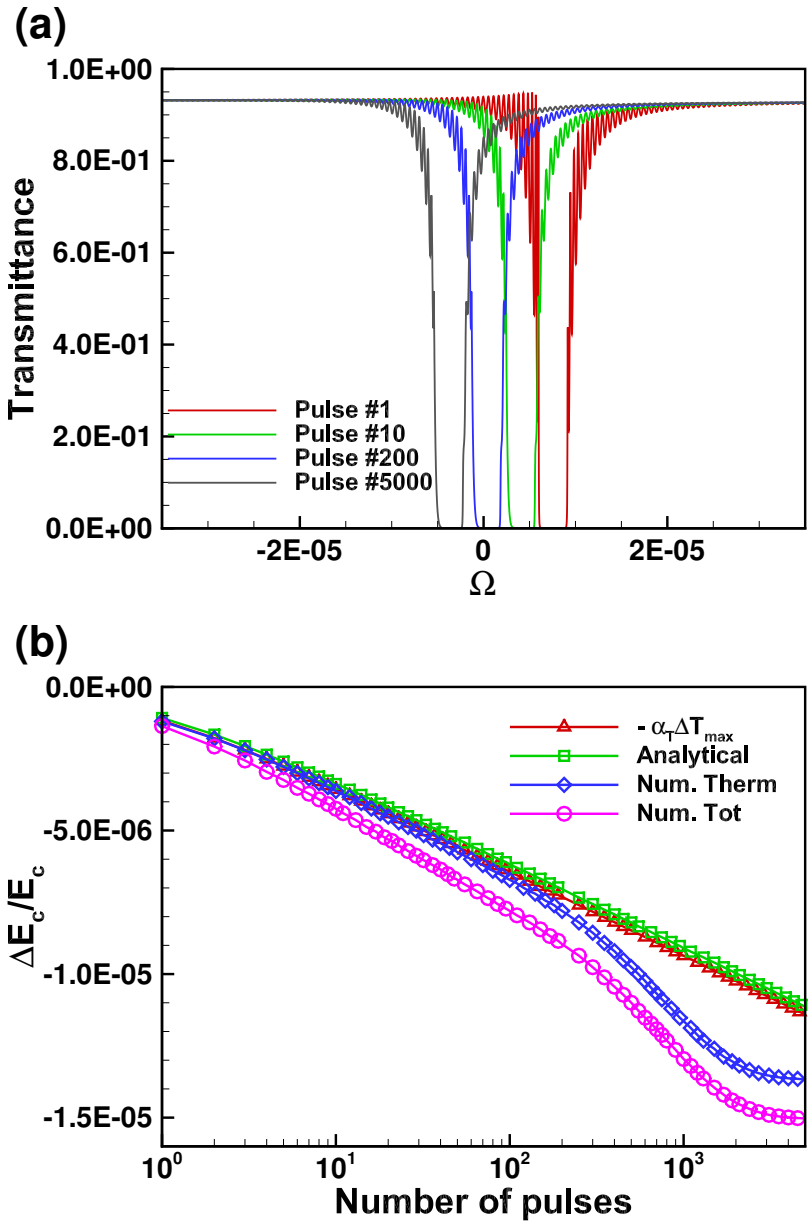

Figure 2.6: (a) The distorted transmittance curves under thermal load at different number of pulses and (b) the normalized central frequency shift history from $-\alpha_T \Delta T_{\max}$, analytical model Eq. (2.44) and numerical simulation. "Num. Therm" and "Num. Tot" represent the results that with thermal strain only and with total strain (both thermal and elastic).

2.3.6 Conclusion

In conclusion, we provide an analytical model for predicting the rocking curves under thermal load. The thermal load (surface slope and strain) can be obtained from either analytical solution with appropriate assumptions, or the numerical simulations. Based on this analytical model, differ-

ent contributions from the thermal load characteristics (such as maximal temperature increase and temperature gradient) can be quantified, as summarize below

- The maximal disturbance results in a shift in frequency.
- The gradient, or non-uniformity, of the disturbance results in the distortion of the rocking curve.
- For higher order diffraction, the narrower rocking curve suggests more significant distortion with the same thermal load.

To mitigate the thermal load effects, tuning the angle between the photon beam and crystal should eliminate the frequency shift. However, mitigating the rocking curve distortion, such as band broadening, can only be achieved through minimizing the thermal load gradient.

2.4 Summary

In this chapter, the relevant physical processes involved in the X-ray laser and crystal interaction have been discussed. The diffraction process of the X-ray in crystal happens at a time scale of femtosecond. During this process electrons and photons exchange energy. Afterwards, the electrons reach local equilibrium and interact with local lattice at a time scale of picoseconds to nanosecond depending on various conditions. These two processes, compared to the time scale of repetition rate of XFEL, can be treated as instantaneous. At the time scale of repetition rate, the thermal conduction and elastic response of the crystal are major physical processes and have been discussed in this chapter. Accordingly, an analytical model coupling the crystal response under thermal load and the diffraction has been derived. The analytical model has been validated with published study and our numerical simulation. The analytical model clearly quantitatively reveal the impacts from maximal disturbance (a commomly used metric in community) and the disturbance gradient.

Chapter 3

Thermal load in pump-probe situations

In this chapter, we study the thermal load in X-ray crystal optics in pump-probe mode. Pump-probe method is a very commonly and widely used experimental technique in many applications. This study is directly applicable for beamline photon sciences optics and is also applicable to estimate the constrains of the operation conditions. In total, three sections will be included. In the first section, a general numerical modeling of the thermal response for both reflective and transmissive monochromator will be introduced. To justify the assumptions introduced in the previous chapter (omitting transient elastic waves), in the second section, the analysis of the transient elastic waves will be conducted. The third section will present the experimental observation of thermal load on reflective monochromator in beamline, as well as the parasitic effects such as distortion of the laser footprint, wavefront and suppression of the peak intensity.

3.1 Thermal load on self-seeding monochromator

3.1.1 Interactions between XFELs & thin crystal

Synchrotron radiation sources have been extremely useful scientific tools; especially, the successful operation of X-ray free-electron lasers (XFELs) [37–39, 54] has opened the route for a new era in science ranging from chemistry, physics, material science and biology etc. To date, most of the FEL facilities operate in self-amplified spontaneous emission (SASE) [9,55] mode with very limited temporal coherence. To achieve fully coherent FEL [11], external laser-seed schemes were proposed [56, 57]. Yet, however, it is challenging for the external seed to be carried by the electron bunch down to the hard X-ray region, because of the central wavelength and intensity fluctuations of the FEL due to the imperfections of the energy distribution in the electron bunch [58]. Therefore, self-seeding schemes were proposed [6, 12, 59–61] with a crystal monochromator between two segments of undulators. Self-seeding facilities [6,61] are currently running at relatively low repetition rate. Below the damage threshold, the low repetition rate allows enough relaxation time for the monochromator to dissipate the thermal energy deposited by the leading pulse and recover to its original status before the trailing XFEL pulse arrives. However, in high repetition rate XFEL facilities [62, 63] running at MHz level, the trailing XFEL pulse will hit the monochromator before it can relax to its design parameters [64]. The residual thermally induced effect, or thermal load, has been a concern in X-ray devices used in synchrotron light sources for decades. To mitigate the thermal load problem, numerous studies have achieved significant progress [1, 65–68]. One

precedent study by Bushuev [50, 51] employed the 2D analytical solution of the heat conduction equation to evaluate the thermal strain on the beamline optics due to the SASE and showed the distorted rocking curve of the monochromator under the thermal load. However, the thermal load and its impact on the seed in self-seeding XFEL have not been well characterized yet. In this study, we provide a quantitative and comparative evaluation of the seeding performance of the transmissive [6] and the reflective [61] monochromators under the thermal load based on common representative operating parameters in self-seeding facilities. We also show the estimation of critical operation repetition for self-seeding XFEL.

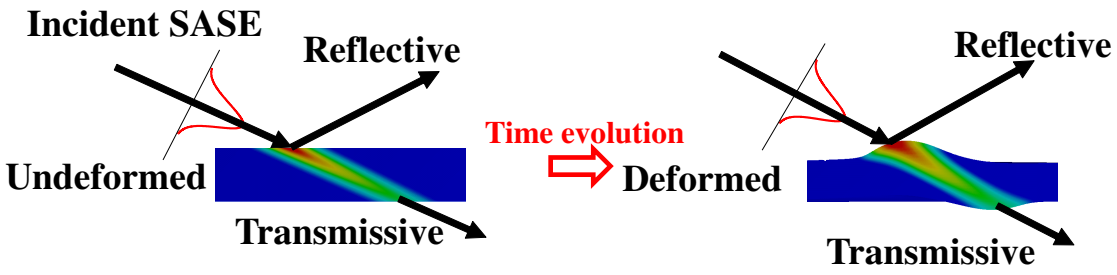

Figure 3.1: Interaction between the SASE and the monochromator.

To reduce the computational cost, we analyzed the crystal response in a pump-probe manner for the first two FEL pulses. But one should be reminded that this tool is also applicable for quasi-steady multi-pulse situation if the calculation keeps going for more XFEL pulses. The physical situation is illustrated by Fig. 3.1: the incident SASE is split into three components when it hits the crystal: reflected, transmitted and absorbed component. The reflected component is the seed for reflective monochromator, while the transmitted component contains the seed for transmissive monochromator. The absorbed component, however, is detrimental to the self-seeding process since it induces undesired non-uniform temperature increase, as shown in the left figure of Fig. 3.1. This resulted non-uniform temperature increase will then evolve into a transient deformation and strain field (right figure in Fig. 3.1, so that when the next pulse arrives, the monochromator deviates from Bragg condition and the seed is affected. This process will be repeated, and the thermal load will be accumulated till a quasi-steady being reached.

3.1.2 Simulation tools

To simulate this process, three modules are implemented iteratively: 1) diffraction, 2) transient thermal conduction and 3) static mechanical module. The diffraction module is an in-house MATLAB script based Shvyd'ko and Lindberg's method [52] for rocking curves calculation, while the thermal and mechanical modules are based on 3D finite element analysis by ANSYS to access all disturbance around Bragg condition including the thermal slope, thermal strain and quasi-static elastic response.

During the simulation process, the diffraction module is first implemented to evaluate the rocking curves based on the residual disturbance (initially all zero), and the absorptance, A, is

obtained to determine the total energy deposition (ΔU_T), which is assumed to satisfy:

$$\Delta U_T = U_{T0} \exp\left[-\left(\frac{x - z\cot\theta_B}{r_x}\right)^2 - \left(\frac{y}{r_y}\right)^2 - \frac{z}{L\sin\theta_B}\right], \tag{3.1}$$

with

$$U_{T0} = \frac{AI_0}{\pi r_x r_y L \sin\theta_B \left[1 - \exp\left(-h/L\sin\theta_B\right)\right]}, \tag{3.2}$$

where $I_0 = 100\,\mathrm{uJ}$ is the SASE pulse energy, $r_x = 20\sqrt{2}/\sin\theta_B\,\mu\mathrm{m}$ and $r_y = 20\sqrt{2}\,\mu\mathrm{m}$ are spot size in x and y direction on the crystal surface, respectively, L is the absorption length in thickness z direction, θ_B is Bragg angle, and h is the thickness of the crystal ($110\,\mu\mathrm{m}$ for transmissive monochromator and 1 mm for reflective monochromator). Based on this energy deposition distribution, an initial temperature field can be calculated accordingly using the temperature-dependent thermal properties [53]. This initial temperature field is then imported by APDL commands to the transient thermal module of ANSYS. In ANSYS transient thermal module, the boundary conditions for the simulation are set as thermal insulation for the top and bottom surfaces, and constant temperature of 300 K for the four side surfaces. To reduce the computation load, only half of the domain is simulated. When done, the temperature field at several selected moments is exported to the static structural module for deformation and strain calculation. In ANSYS static structural module, the whole domain is set free of loads, to simulate the strain free mounting in LCLS self-seeding mode. Deformation and strain fields at selected moments are simulated based on the imported "frozen" temperature field, and then exported to diffraction module for seed quality evaluation.

3.1.3 Thermal and mechanical response

An example of the thermal load for the transmissive monochromator at 8.5 keV and delay time of 1 μs is shown in Fig. 3.2. The SASE hits the crystal with incident angle of $\pi/2 - \theta_B$, so that the temperature and corresponding thermal strain field is tilted. As time goes on, this thermal load is gradually relaxed, so that the tilted thermal field evolves towards the in-plane direction (parallel to the monochromator surface). On the other hand, the strain near the free crystal surfaces is typically of higher value than inside the material due to a lack of constrain. For all incident photon energy, thermal load results in a decrease in seed central photon energy, as seen by the total derivative of Bragg condition:

$$-\frac{\delta E}{E} = \frac{\delta d}{d} + \cot\theta_B \delta\theta, \tag{3.3}$$

where E is photon energy, d is interplanar distance and θ is incident angle. Thermal load introduces the expansion of lattice constant ($\delta d > 0$), so that the photon energy should decrease ($\delta E < 0$). In addition, the lattice expansion is not uniform, translating into a broadening of the Darwin width as well as the suppression in peak value of the rocking curves. For the reflective monochromator, these effects directly cause the degradation of the seed. In diffraction module with thermal load, for all selected moments, the top surface deformation is first imported and converted into the surface slope ($\delta\theta$ in the total derivative of Bragg condition) field. However, the strain processing is different for reflective and transmissive monochromator. For reflective monochromator, the surface strain field

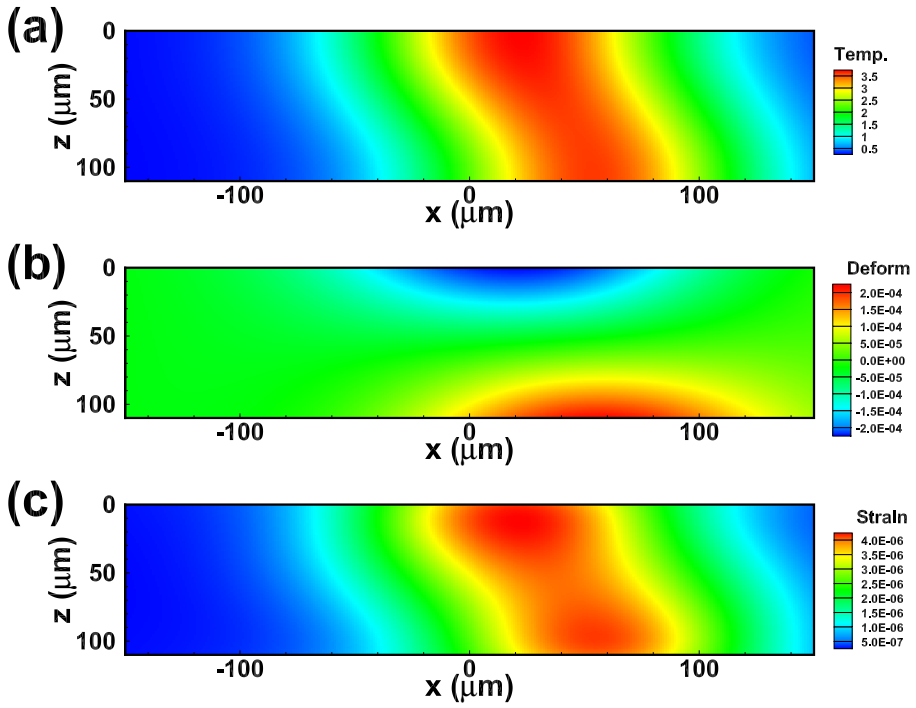

Figure 3.2: Thermal load for the transmissive monochromator with C(0 0 4) at 8.5 keV and delay time 1 μs: contours in central plane (symmetric plane) of (a) temperature increase in K, (b) deformation in μs and (c) strain.

is imported, while for transmissive monochromator, the 3D strain field is imported and averaged along the laser incident direction to obtain a 2D strain field. This is because, for this incident SASE energy, the absorption length is typically much larger than the optical path, so that the disturbance is not varying significantly across the optical path. Next, the deviation parameter α [50–52] field can be calculated. This α field is equivalently converted to ΔE so that the local reflectance and transmittance can be calculated according to the rocking curve. This reflectance or transmittance field will then be weighted averaged by the incident SASE spatial intensity distribution to finally obtain the rocking curves under thermal load. Up to now, the reflected seed spectrum is already accessible for the reflective monochromator by multiplying the incident SASE spectrum with the rocking curves. However, for the transmissive monochromator, more steps are needed to access the seed quality. First, the transmitted light is calculated by convoluting the incident SASE with the response function of the crystal (done in frequency space). The transmitted light is then inversely transformed through inverse fast Fourier transform to time domain for seed selection. After the seed is selected, it is then transformed back to frequency space using fast Fourier transform for seed quality evaluation.

3.1.4 Rocking curves and seed quality

We consider two monochromators: 1) 1-mm-thick reflective silicon (1 1 1) and 2) 110-μm-thick transmissive diamond (0 0 4) (type IIa). For the reflective monochromator, only one single

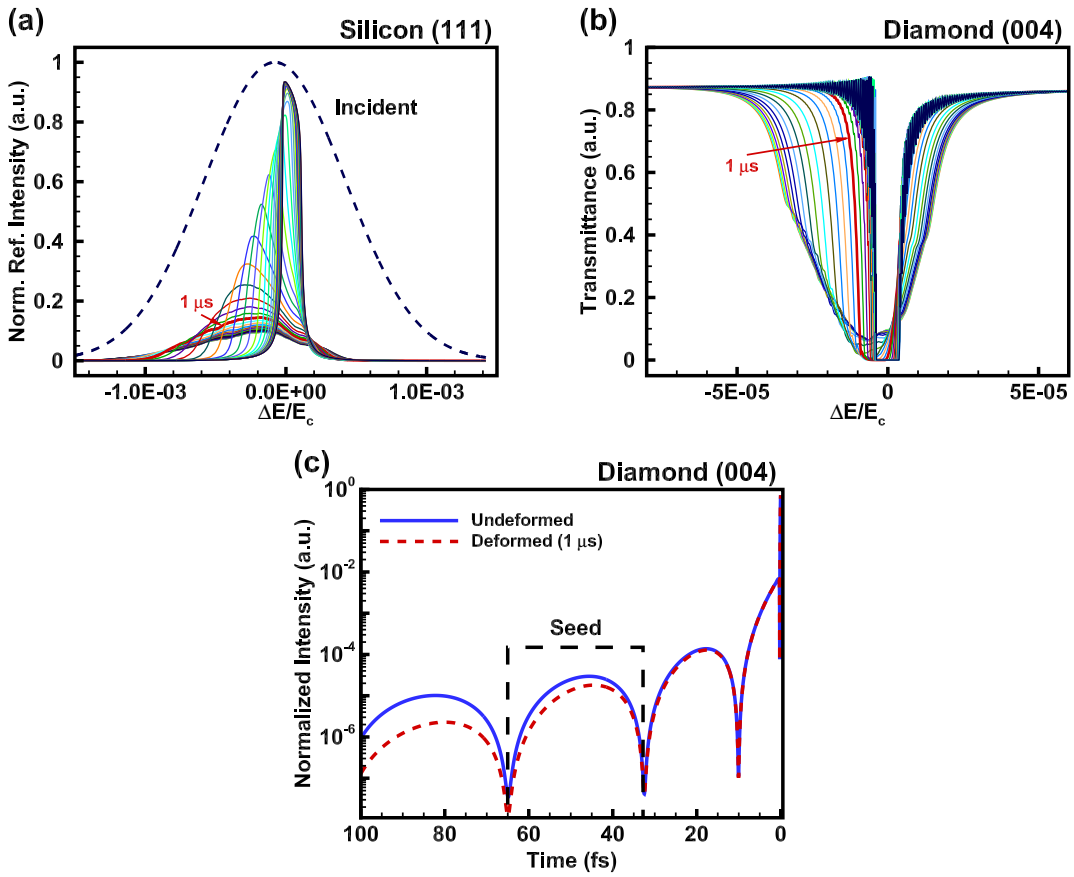

Figure 3.3: Incident 8.5 keV SASE: (a) the seed spectrum history under thermal load for reflective monochromator using Si(1 1 1). The seed spectrum at the delay time of 1 μs is marked for reference. (b) The transmittance history under thermal load for transmissive monochromator using C(0 0 4), and (c) is an example of transmitted light in time domain at the delay time of 1 μs for transmissive monochromator. The seed power downgrades to about 46% of the perfect one.

reflection is considered, as negligible thermal load is expected on the further reflections. Also, to single out the thermal load effect, in this study, we only report the X-ray properties after such a single reflection. More details will be reported in other publications regarding to different reflective monochromators. The photon energy range in consideration is 6.5 to 12.5 keV with 2 keV increment for the reflective monochromator, and 8.5 to 12.5 keV with 1 keV increment for the transmissive monochromator. The material properties including electric susceptibility and Bragg angle are obtained from database [69] through X0h website [70]. Figure 3.3 presents the history of seed spectrum for reflective monochromator for photon energy of 8.5 keV, pulse energy 100 μJ and spot size (FWHM) 47.1 μm. The relative bandwidth (FWHM) of the incident SASE is 1.3×10^{-3}. The dashed line indicates the spectrum of the incident SASE pulse, and the solid lines display the reflected seed spectrum at 40 moments of delay time uniformly distributed in logarithmic space between 10^{-8} to 10^{-3} s. At short delay time, the thermal loading effects are very significant, the reflected seed severely deviates from designed situation: its central photon energy shifts to the left compared to

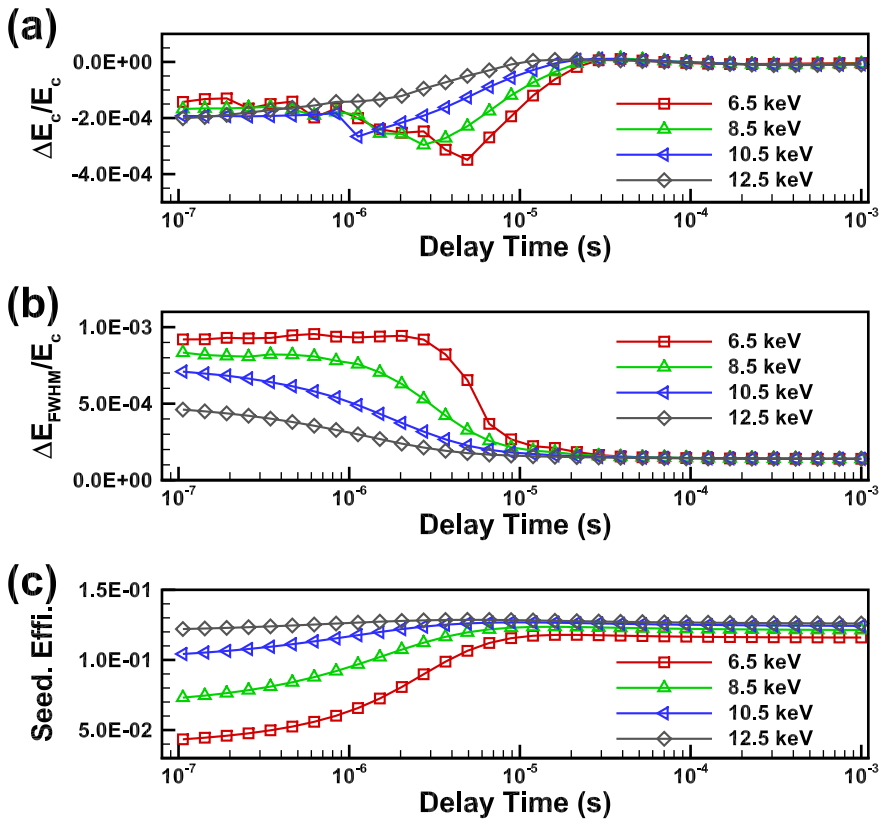

Figure 3.4: Seed quality change under thermal load for reflective monochromator Si(1 1 1): (a) seed central photon energy shift, (b) seed bandwidth (FWHM) and (c) seeding efficiency (the ratio between seed total energy and incident pulse energy).

the designed seed, and its peak intensity shrinks to about one tenth of that of the designed seed (the flat solid lines). Moreover, the seeding efficiency can be further reduced if two reflections are considered. On the other hand, the bandwidth (FWHM) of the reflected seed also increases to about six times of the designed value. As the delay time (equivalently the heat dissipation time) increases, the spectrum of reflected seed gradually approaches that of the perfect seed. However, during this process, multiple peaks may appear, leading to discontinuous change of the central photon energy. Similarly, the transmissive monochromator also suffers from the seed quality degradation. For the same incident SASE condition, the transmittance history under thermal load for transmissive monochromator is shown in Fig. 3.3(b). Totally 30 moments of delay time are selected uniformly in logarithmic space between 10^{-8} to 10^{-4}s. The transmittance of the diamond, compared to the reflectance of the silicon, recovers more quickly due to the superior thermal properties of diamond. However, an obvious seed power reduction still exists according to Fig. 3.3(c) even though the transmittance already comes very close to the undeformed case around 1 μs delay time. This can be attributed to the mechanism of the transmissive monochromator. The transmissive monochromator actually produces the monotonic "wake seed" through beating of the transmitted photons. Hence, the seed is weak and hidden in the following bumps after the SASE peak (the highest peak on the right side of Fig. 3.3(c)). Typically, the boxed bump is employed as the seed in experiments. The

farther the bump is away from the transmitted SASE, the more energy it loses due to thermal load. Therefore, the seed from transmissive monochromator is very sensitive to thermal load.

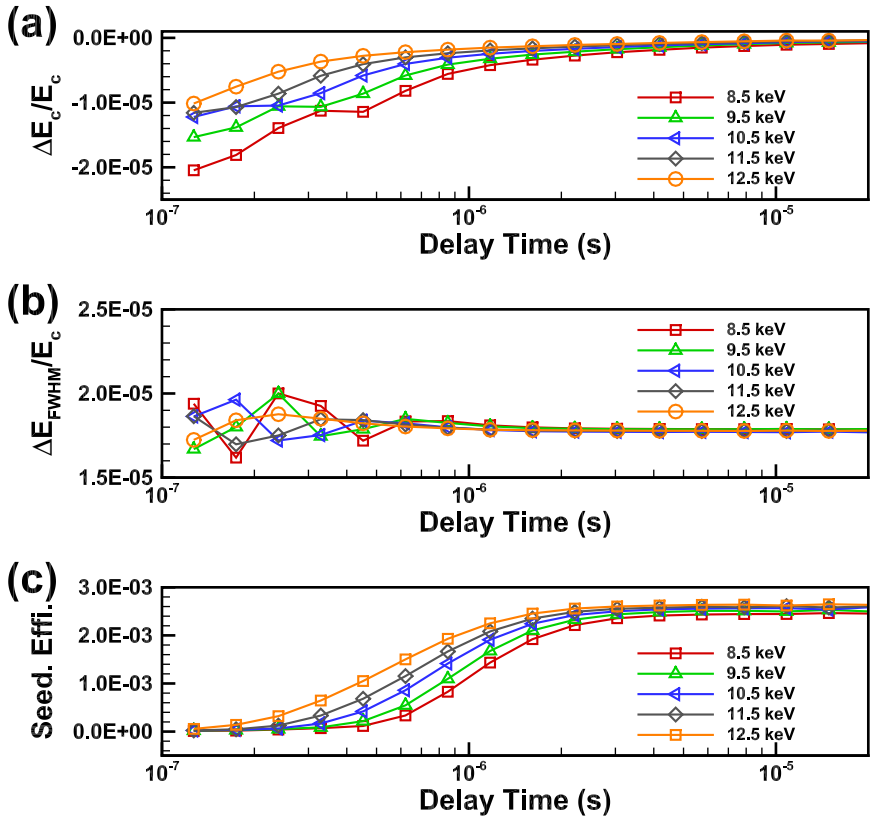

Figure 3.5: Seed quality change under thermal load for transmissive monochromator C(0 0 4): (a) seed central photon energy shift, (b) seed bandwidth (FWHM) and (c) seeding efficiency.

Figure 3.4 summarizes the reflective seed quality change as the delay time due to thermal load. All three seed quality parameters at a given delay time downgrade more for lower incident photon central photon energy due to more absorbed energy into the crystal, or equivalently stronger thermal load. On the other hand, the seed quality change history for the transmissive monochromator is shown in Fig. 3.5. The degradation behavior of the seed quality, however, is quite different for the three seed quality parameters: the seed central photon energy and bandwidth are not significantly affected, but seeding efficiency dramatically changes from very low values (i.e., 3.5×10^{-5}) to about 2.5×10^{-3} in certain delay time range (about $0.1-10\,\mu s$), due to its high sensitivity to thermal load. Experimentally, the seeding efficiency using transmissive monochromator is even considerably lower (about 10^{-4}) than the perfect seeding efficiency (2.5×10^{-3}). Similar theoretical value for perfect seeding efficiency was reported [71]. Here, we show that the seeding efficiency could reduce by 10 folds if a typical spiky SASE is considered.

Figure 3.6(a) displays the spectrum of a single-mode perfect Gaussian pulse and a multi-mode typical SASE pulse. The typical SASE is spiky with about 100 modes uniformly distributed within 3σ range. For the typical SASE pulse, the relative bandwidth (FWHM) is fixed as 1.18×10^{-4}, while the amplitude and phase are randomly taken from 0 to 2 and 0 to 2π, respectively. The absorptance

for this multi-mode SASE pulse still remains the same as the single-mode Gaussian pulse. With this SASE pulse, the seeding efficiency of the undeformed transmissive monochromator reduces to 1.2×10^{-4}. The trend of the seed quality change as a function of delay time, however, is not significantly affected by the number of modes in the SASE. In fact, only the seeding efficiency is scaled from 2.5×10^{-3} of maximal value to 1.2×10^{-4} of maximal value.

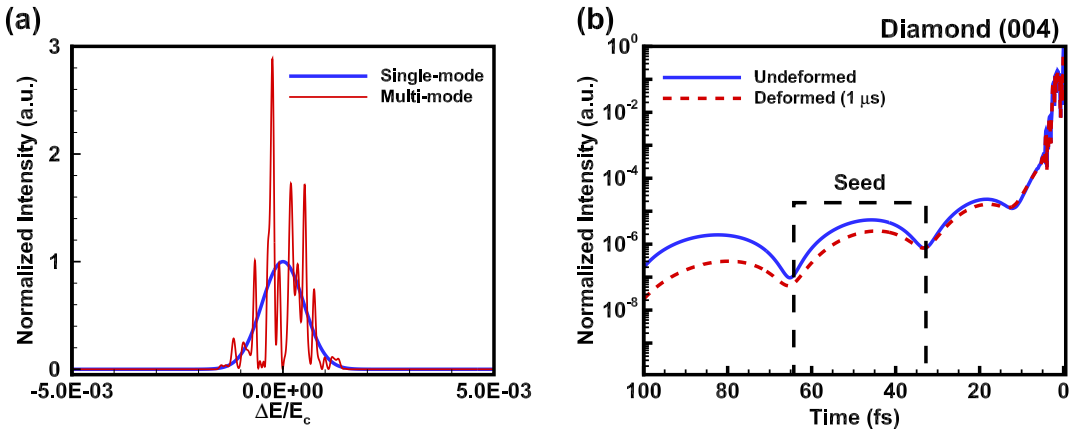

Figure 3.6: (a) The spectrum of single-mode Gaussian (blue thick line) and multi-mode SASE (red thin line). (b) The transmitted light in time domain at the delay time of 1 μs.

3.2 Transient elastic waves effects

As mentioned in Chapter 2, the thermal stress generated by XFEL pulse can excite elastic waves. The generated elastic waves, in a thin plate geometry like the transmissive monochromator, are repeatedly reflected on the two traction-free surfaces, developing new resonant acoustic excitations named Lamb waves. This was initially discovered by Horace Lamb [72] in 1917 and thus named Lamb waves. The properties of Lamb waves are quite complex, but it has found substantial practical application, especially in the field of seismology and nondestructive evaluation. In this section, we discuss how it affects the diffraction behavior of the Bragg optics in pump-probe mode, and estimate its importance for further study in multi-pulse situations.

3.2.1 Elastic waves in thin plate: Lamb waves

Lamb waves are formed through the repeated reflections of bulk longitudinal and transverse waves, as shown in Fig. 3.7. Lamb waves can be described by imposing traction-free surface boundary conditions on the equations of motion. Due to the complexity of the mode interference, the velocity is dependent on frequency or wavelength. This dependence, called dispersion relation,

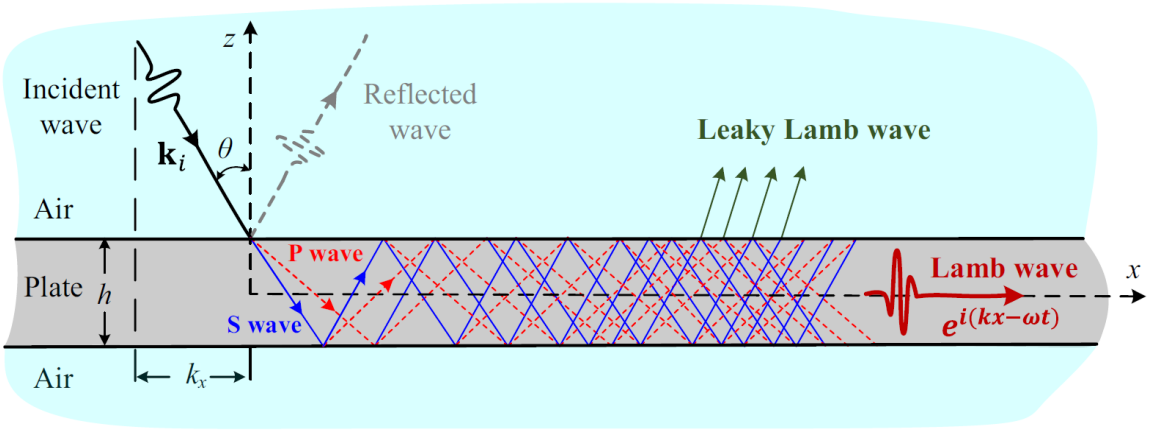

Figure 3.7: The schematic of Lamb wave formation [73].

can be obtained through Rayleigh-Lamb equation for plate with thickness d

$$\frac{\tan(\beta d/2)}{\tan(\alpha d/2)} = \frac{4\alpha\beta k^2}{(k^2+\beta^2)^2}, \tag{3.4}$$

$$\frac{\tan(\beta d/2)}{\tan(\alpha d/2)} = \frac{(k^2+\beta^2)^2}{4\alpha\beta k^2}, \tag{3.5}$$

where $\alpha^2 = k^2 - \omega^2/c_l^2$ and $\beta^2 = k^2 - \omega^2 c_t^2$. Here, ω is the angular frequency, k is the wave number, c_l and c_t are the longitudinal and shear wave velocities, respectively.

From Eqs. (3.4) and (3.5), one can see that there are two infinite sets of Lamb wave modes, as illustrated in Fig. 3.8. Eq. (3.4) denotes the symmetric modes, while Eq. (3.5) represents the anti-symmetric modes.

Thus, the dispersion can be obtained by Eqs. (3.4) and (3.5) for both symmetric and anti-symmetric modes. To obtain the dispersion, we employ a MATLAB based tool, GUIGUW [75] as our theoretical tool, and finite element analysis using ANSYS and COMSOL as our simulation tool. It is important to understand the Lamb wave dispersion for the diamond monochromator, so that the simulation parameters such as the mesh size and time step size can be determined accordingly. In addition, the non-propagating Lamb modes, as will be shown in later sections, should be found to avoid potential resonance.

3.2.2 Dispersion relationship of Lamb waves

We first validate our theoretical tool. Figure 3.9 shows a comparison between the results by GUIGUW and the results by Clorennec et al. in the literature [76]. In the figure, "A" indicates anti-symmetric mode, while "S" represents symmetric mode. Two fundamental modes, the zeroth anti-symmetric mode (A_0) and symmetric mode (S_0) have relatively low speed across the frequency range of interest. Other high order modes are also presented. The perfect agreement between GUIGUW results and literature results validates the theoretical tool.

We then validate our simulation tool by comparing our finite element results by ANSYS to

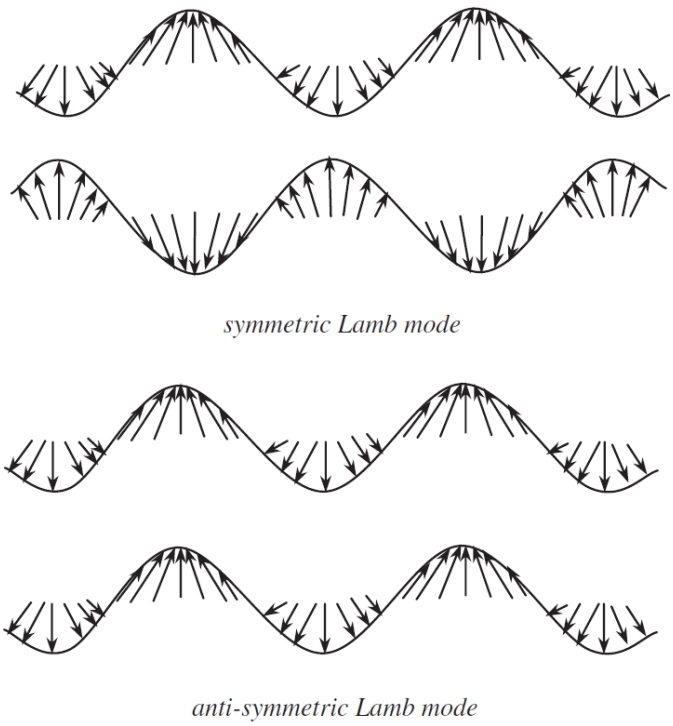

Figure 3.8: Symmetric and anti-symmetric Lamb wave modes [74].

the literature results [77]. The simulation is set up as a 2D axisymmetric case with parallelization. The initial condition is set to be all zero, and the boundary conditions are set the same as in reference [77]. A sufficiently large domain (maximal radius of 209.5 mm) is selected to represent the 1.5-mm-thick aluminum plate considered in the reference. The material properties as well as the laser heating conditions are all specified in the reference, too. To access the dispersion relation, the MATLAB script MASW, developed by Olafsdottir et al. [78], is employed. This very nice script was initially developed to extract the dispersion relation of low frequency Rayleigh waves, but is also applicable for Lamb waves. Based on multichannel analysis [79], MASW requires the displacement history of a series of detectors as input. In our simulation, the first detector is located at 50 mm. Other detectors are evenly distributed with a spacing of 0.5 mm, so that the mode with approximately 3 MHz (wavelength about 1 mm) can be captured. The raw results, together with GUIGUW results for the same material, are plotted in Fig. 3.10.

In Fig. 3.10, the numerical phase velocity results agree very well with the theoretical results by GUIGUW. However, some extra modes are also present, possibly due to numerical errors, or other wave modes such as Love modes or Rayleigh modes. The phase velocity dispersion curve is constructed by taking the maximal amplitude on the contour as a function of frequency. Based on this extracted phase velocity curve, the group velocity dispersion curve can be accessed by taking the derivative of the phase velocity curve. The calculated phase velocity and group velocity curves are both shown in Fig. 3.11 with the results by Liu and Hong [77]. A very good agreement is achieved.

In addition to the numerical results in literature, experimental results [80] of Lamb wave

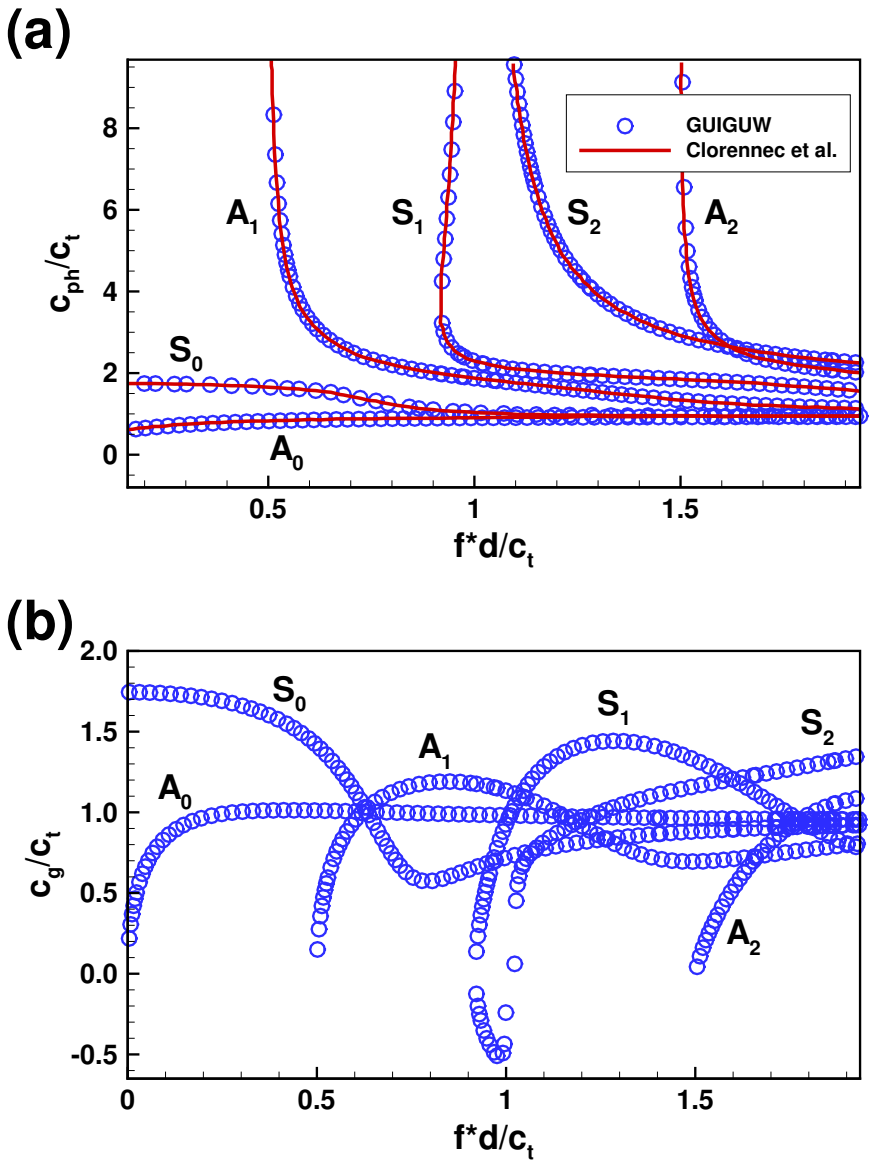

Figure 3.9: The dispersion relation of 0.49-mm-thick Duralumin [76]. (a) phase velocity and (b) group velocity.

dispersion on CVD diamond plate are also found and validated in Fig. 3.12. Good agreement on A_0 mode is observed, but no experimental measurement for S_0 mode is reported, potentially due to the minute displacement amplitude compared to A_0 mode.

Based on all the validation, the dispersion for the 110-μm-thick diamond monochromator used in LCLS is simulated and plotted in Fig. 3.13. Generally, the frequency range is pretty high (about 10 MHz) level compared to the highest repetition rate considered in this study, thanks to the superior mechanical properties of CVD diamond and the small thickness of the plate. Therefore, the resonance between the Lamb modes and the driving force (XFEL pulses) is not expected.

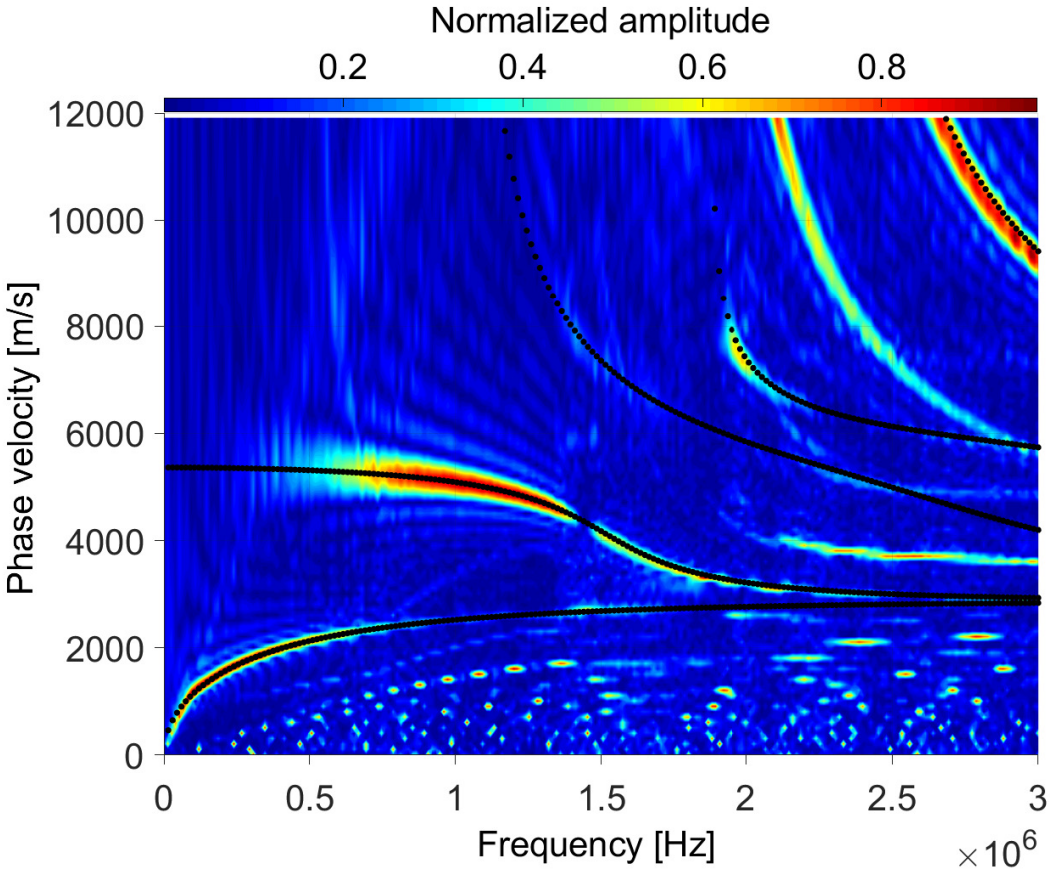

Figure 3.10: The dispersion relation of 1.5-mm-thick aluminum plate [77]. The black dots show the GUIGUW results, while the contour displays our simulation results.

Although the dominant Lamb modes are A_0 and S_0 modes, one should be reminded that, there is another mode that could potentially undermine the stability of the monochromator: S_1 mode. The reason is that, in this branch, there exists a mode with zero group velocity. In other words, this mode is not propagating and the vibrational energy will build up locally if the energy deposited by XFEL pulses is accumulated. Given that the quality factor (Q factor) of diamond is very high [81], this parasitic oscillation will not be dissipated if no external damping mechanism is implemented.

3.2.3 Zero group velocity (ZGV) mode

The ZGV modes denote the Lamb modes that has a finite phase velocity but a zero group velocity. This phenomenon could exist in S_1 mode with material Poisson ration $\sigma < 0.45$, in A_2 mode with $\sigma < 0.31$, and in other modes (S_3, S_4, S_5 and A_5 modes) [82]. At the ZGV point, two waves with opposite propagating direction interfere with each other and lead to local confinement of the energy [76], similar to standing waves. For Bragg optics, this could be a concern as the strain oscillation will remain locally and introduce pulse-to-pulse variation if its frequency is different from the repetition rate, even without considering the XFEL arrival time jittering. If the strain os-

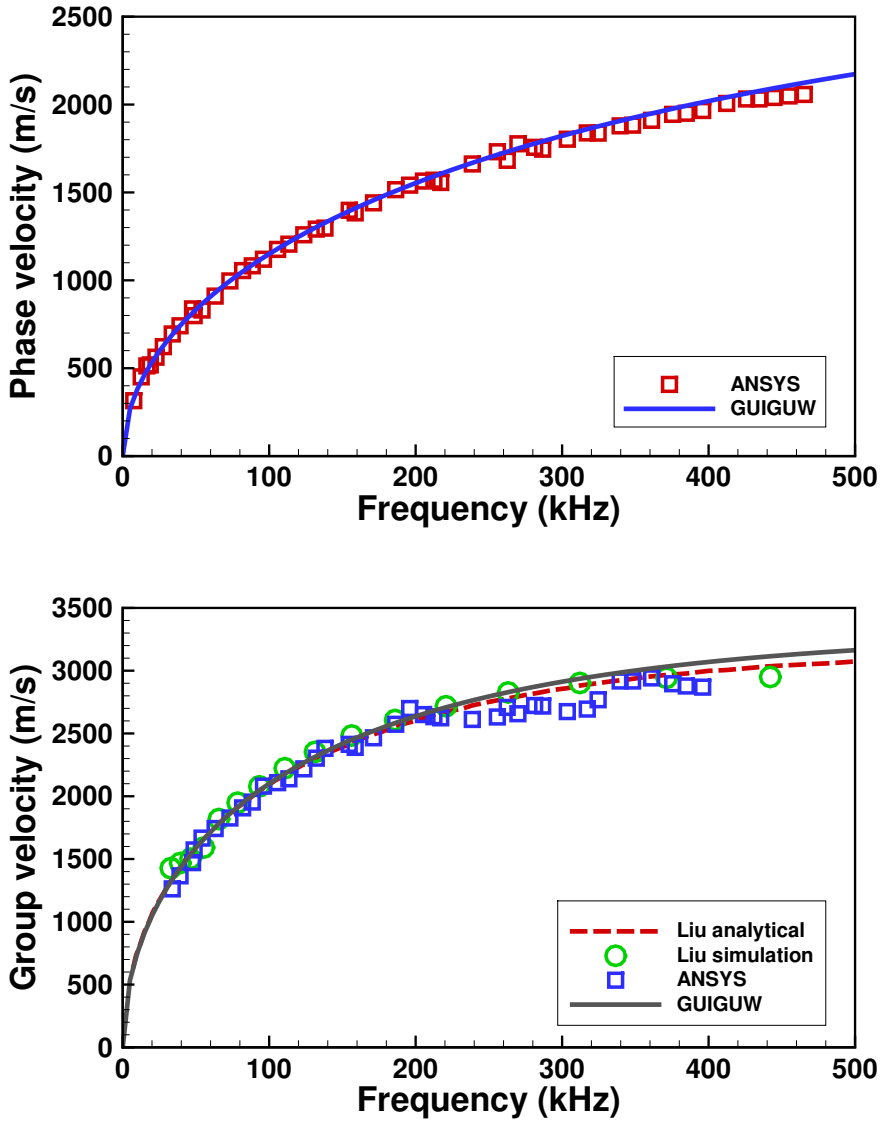

Figure 3.11: The dispersion relation of 1.5-mm-thick aluminum plate [77] for both phase velocity (top figure) and group velocity (bottom figure).

cillation frequency is close to the repetition rate, it is expected to be even worse since the resonance condition is satisfied. Therefore, it is important to avoid the coincidence of the repetition rate and the frequency of the ZGV mode.

An experimental observation of ZGV mode in 0.49-mm-thick Duralumin plate is shown in Fig. 3.14. This signal is extracted from the displacement history of the experimental measurement.

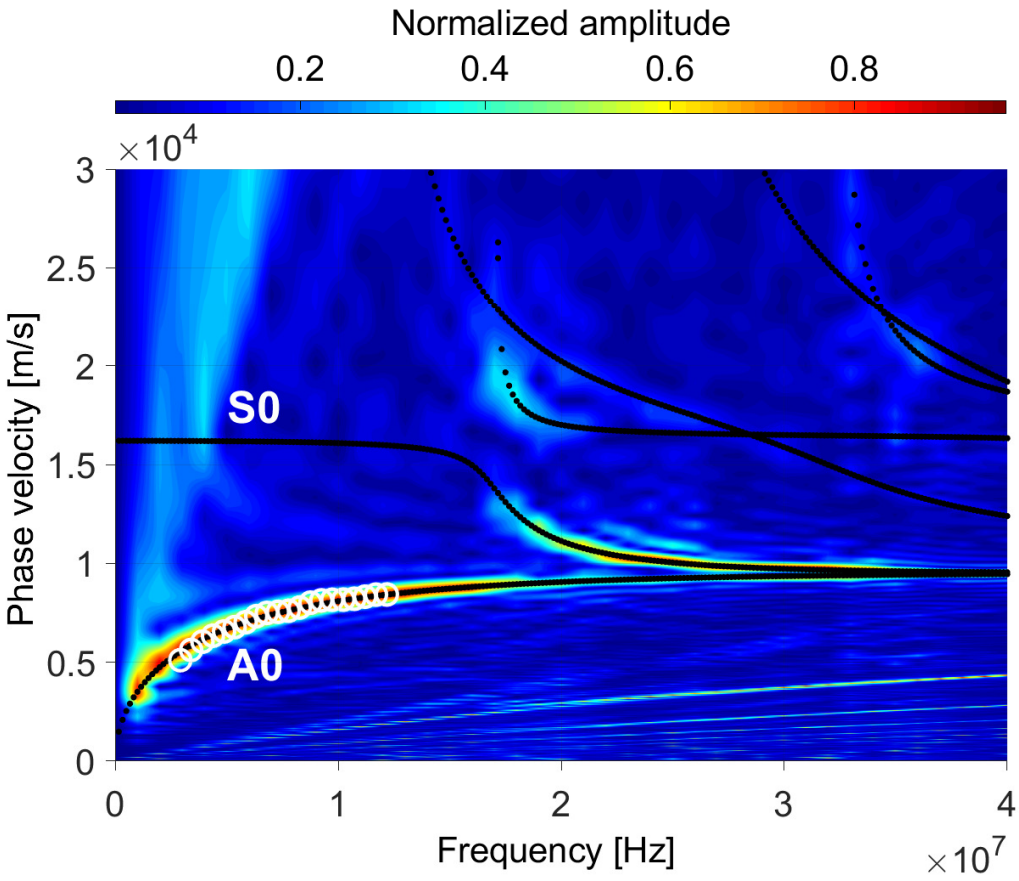

Figure 3.12: The dispersion relation of 0.46-mm-thick CVD diamond plate [80]. The contour represents the simulation results by ANSYS, the black dots show the results by GUIGUW, and the white circles display the experimental results.

Based on this figure, a quality factor, or Q factor, is estimated by

$$Q \equiv \frac{f}{\Delta f}, \tag{3.6}$$

where Δf is the half-power bandwidth (430 Hz) determined from Fig. 3.15, which is the spectrum of the signal in Fig. 3.14, and f is the frequency of the ZGV mode. Meanwhile, the finite element simulation is also performed and the results (5.76 MHz) are shown in Fig. 3.15 to agree very well with the experimental measurements (5.86 MHz).

An additional cross-check between the results by GUIGUW and the finite element analysis on 460-μm-thick CVD diamond plate is provided in Fig. 3.16 also for validation purpose. The spectrum peaks at 17.38 MHz, which is very close to the point with vertical slope at 17.19 MHz determined from the phase velocity graph from GUIGUW.

On the other hand, unfortunately, the amplitude of the ZGV mode cannot be validated, as it depends on the stimulation source (laser source) parameters including the laser penetration depth,

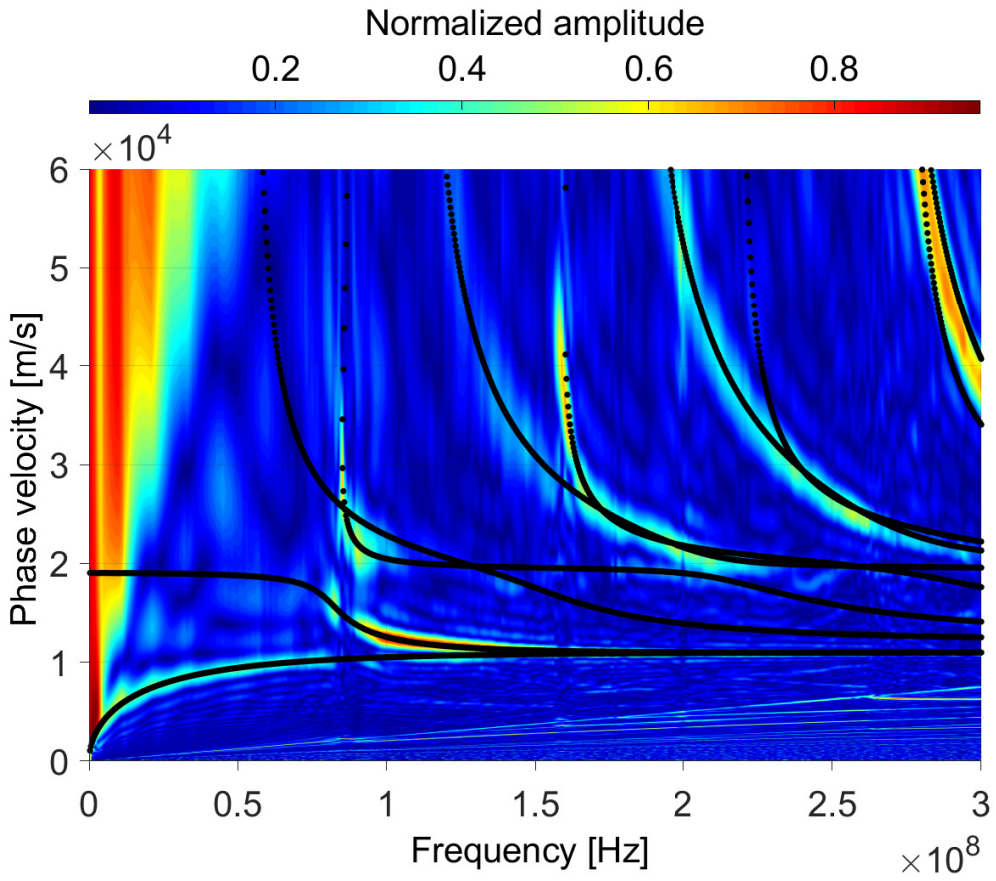

Figure 3.13: The dispersion relation of 110-μm-thick CVD diamond monochromator. The contour denotes the simulation results, while the black dots represent the theoretical results by GUIGUW.

spot size, pulse energy and duration, and material absorptance. These parameters, however, are not all included in the reference.

After validation, the analysis is performed for our 110-μm-thick diamond monochromator to find out the corresponding lowest ZGV mode. As illustrated by Fig. 3.17, the peak on spectrum corresponding to the lowest ZGV mode can be found to locate at 85.2 MHz by GUIGUW and 84.97 MHz by finite element analysis. Compared to the frequency of typical dominant modes (A_0 and S_0), the lowest ZGV mode (S_1-ZGV mode) frequency is significantly higher. The huge difference between the S_1 ZGV mode and the repetition rate of the XFEL pulses should not allow the resonance condition.

Therefore, the Lamb wave dispersion relation and ZGV modes are obtained through both the theoretical and numerical tools.

To successfully capture the behavior of ZGV with frequency of around 85 MHz, a time step size of no larger than 1.17×10^{-8} s is required. On the other hand, the mesh size is required to be at most half of the shortest wavelength, which is about 0.05 mm. However, there exists another restriction on mesh size due to the small XFEL spot size (about 30 μm), and the time step size should be reduced accordingly to prevent the strain waves from propagating across more than one

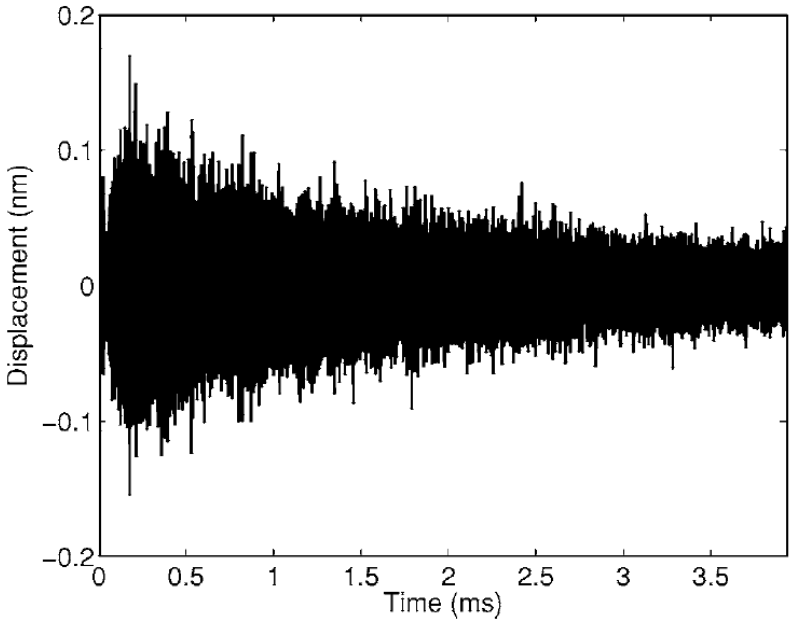

Figure 3.14: The experimental signal for S_1 ZGV mode on 0.49-mm-thick Duralumin plate up to 4 ms [76]. A calculated Q factor of 13700 indicates a very slow dissipation.

mesh. For example, if the mesh size in the laser spot is selected as 5 μm and the highest wave speed under consideration is selected as 20 km/s, then the time step size can be calculated as 2.5×10^{-10} s, assuming Courant-Friedrichs-Lewy (CFL) number is unity. In fact, COMSOL recommends a CFL of 0.1 for the default second order, quadratic mesh elements.

These harsh requirements on time step size and mesh size lead to huge computational load, especially in 3D situation as our previous quasi-static simulation. We first conduct simulation for a 2D axial symmetric situation to estimate the amplitude of the transient strain waves as compared to the quasi-static strain component.

3.2.4 Case study: axisymmetric

In order to quickly estimate the impacts of the transient strain waves, we consider the soft X-ray with central photon energy of 4.5 keV. At this photon energy, the crystal absorption of the XFEL is strong, allowing large thermal load or in other words, large strain wave amplitude. For higher photon energy, the excitation from thermal load is comparatively weaker so that the strain wave impacts are expected to be less significant.

To allow Bragg condition, we now use (1 1 1) atomic plane instead of (0 0 4) orientation. For 2D axisymmetric case, Eq. (3.1) should be modified as

$$\Delta U_T = U_{T0} \exp\left[-\left(\frac{r}{a}\right)^2 - \frac{z}{L}\right], \tag{3.7}$$

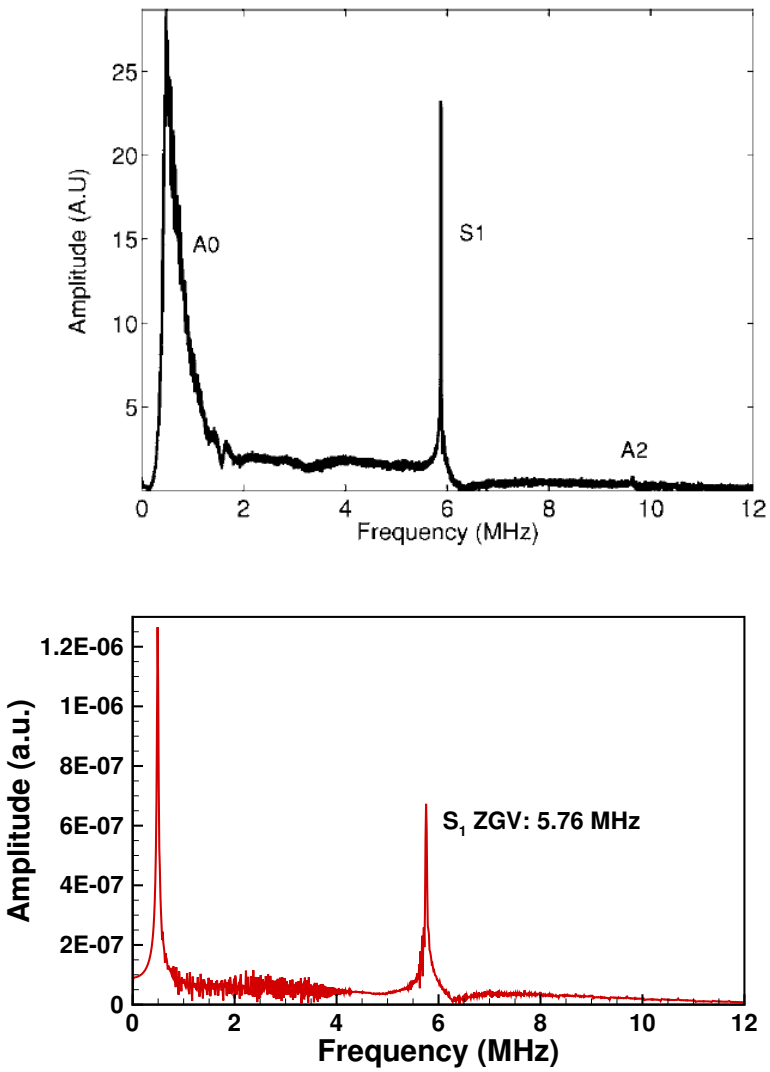

Figure 3.15: The spectrum of the experimental signal in reference [76]. The left figure shows the experimental results, while the right figure shows the results by finite element analysis using ANSYS.

with

$$U_{T0} = \frac{AI_0}{\pi a^2 L\,[1 - \exp(-h/L)]}, \tag{3.8}$$

where $I_0 = 100\,\mu\text{J}$ is pulse energy, $a = 20\sqrt{2}\,\mu\text{m}$ is spot size on the crystal surface, L is the absorption length in thickness z direction, $A = 0.7876$ is the absorptance calculated from diffraction module, and $h = 110\,\mu\text{m}$ is the thickness of the crystal. The domain size is 2 mm in radial direction. The simulation is conducted up to 1 μs.

The radial strain profile at the top surface of the monochromator at 1 μs is plotted in Fig.

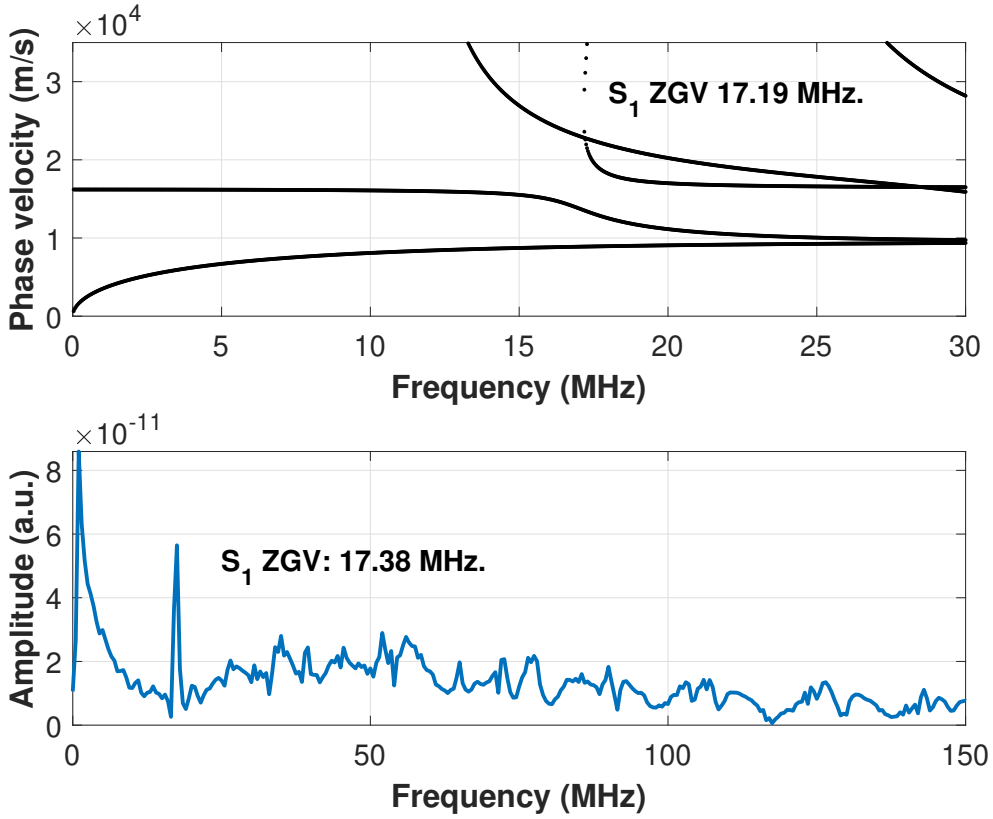

Figure 3.16: An additional comparative validation between the results from GUIGUW and finite element analysis on 460-μm-thick CVD diamond plate.

3.18. From the top figure to the bottom figure, the curve stands for total strain in z direction, elastic strain in z direction and thermal strain in z direction. The total strain is the superposition of the elastic strain and thermal strain. In this case, the thermal strain component is still one order of magnitude larger than the elastic strain at 1 μs, therefore the total strain behaves almost identically as the thermal strain. The elastic strain impacts, which is the transient wave effects discussed in this chapter, is negligible and only results in small disturbance around the thermal strain.

In addition to the transient strain profiles, the quasi-static strain profiles at the top surface are also shown in Fig. 3.18 as the red lines. The maximal amplitude of the quasi-static total strain is comparable to that of the transient total strain. The strain gradient within the laser spot is also similar according to the top figure in Fig. 3.18. In transient strain waves, the typical wavelength can be observed in the middle figure of Fig. 3.18 as around 100 μm level, which is why no rapid change or large gradient is expected in the laser spot.

In the future, we will be performing similar comparative study for other photon energy in 2D axisymmetric situations to confirm that transient strain waves influence is secondary and quasi-static strain field is enough to represent the total disturbance of the Bragg diffraction.

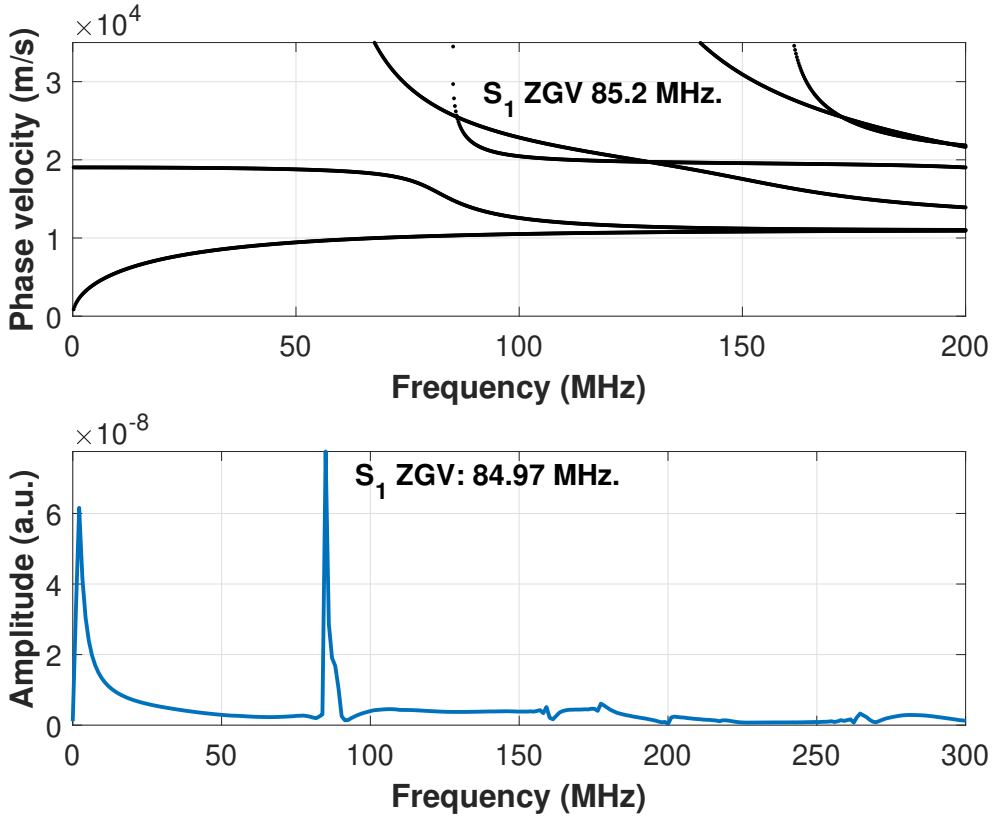

Figure 3.17: The phase velocity dispersion (top figure) and the center displacement signal spectrum for the 110-μm-thick CVD diamond plate monochromator.

3.2.5 Summary

We study the transient strain wave effects in thin diamond plate monochromator. We employ GUIGUW as our theoretical tool and finite element analysis by ANSYS and COMSOL as our numerical tool. The Lamb wave dispersions calculated by both theoretical and numerical tool are compared to both analytical and experimental results in literatures for validation. The S_1-ZGV Lamb mode is also captured by both our theoretical and numerical tools. Due to superior mechanical properties of diamond, the Lamb modes are generally of much higher frequency than the repetition rate, suggesting the exclusion of resonance condition. Based on the knowledge of Lamb wave dispersion, the finite element analysis parameters are determined. The simulation results show that the transient strain wave impacts are secondary to the quasi-static strain field, supporting our hypothesis in our previous chapters.

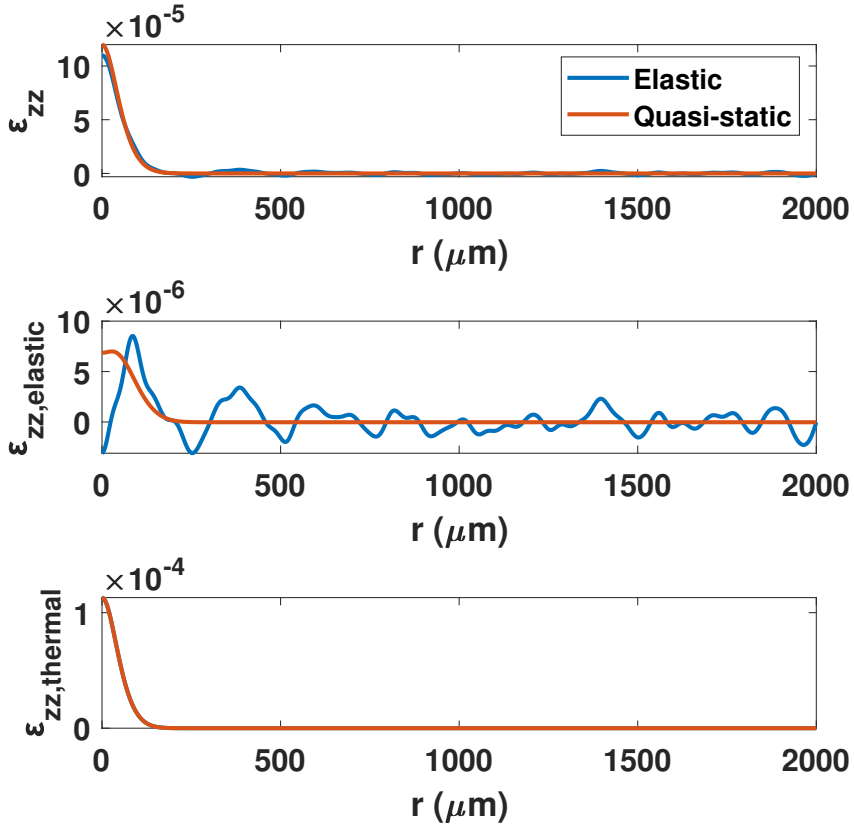

Figure 3.18: The radial strain profile at the monochromator top surface at 1 μs. The blue line stands for the transient case, while the red line represents the quasi-static case.

3.3 Thermal load on beamline monochromator

3.3.1 X-ray-matter interactions

X-ray optics has been serving the proceeding of explorations in many fundamental and practical fields for many decades [83]. Due to their high frequency and photon energy, X-rays interact with materials in a very different manner from that of visible lights. Instead of being redirected, X-rays tends to penetrate and finally absorbed by most materials [84]. Therefore, X-ray optics are usually very different from ordinary optics. There are many categories of X-ray optics, such as refractive lenses [85], Fresnel zone plates [86], Kirkpatrick-Baez mirror [87] and monochromators [88, 89]. Monochromator is one most commonly used crystal optics based on Bragg diffraction [17], as most hard X-ray beamlines at synchrotron radiation facilities require a monochromator to select a particular X-ray energy [47]. A typical four-bounce monochromator consists of two pairs of crystals with parallel surfaces, as shown in Fig. 3.19. The performance of monochromator is critical as it determines the quality of the photon beam, such as its spectrum, peak intensity, beam divergence and wavefront.

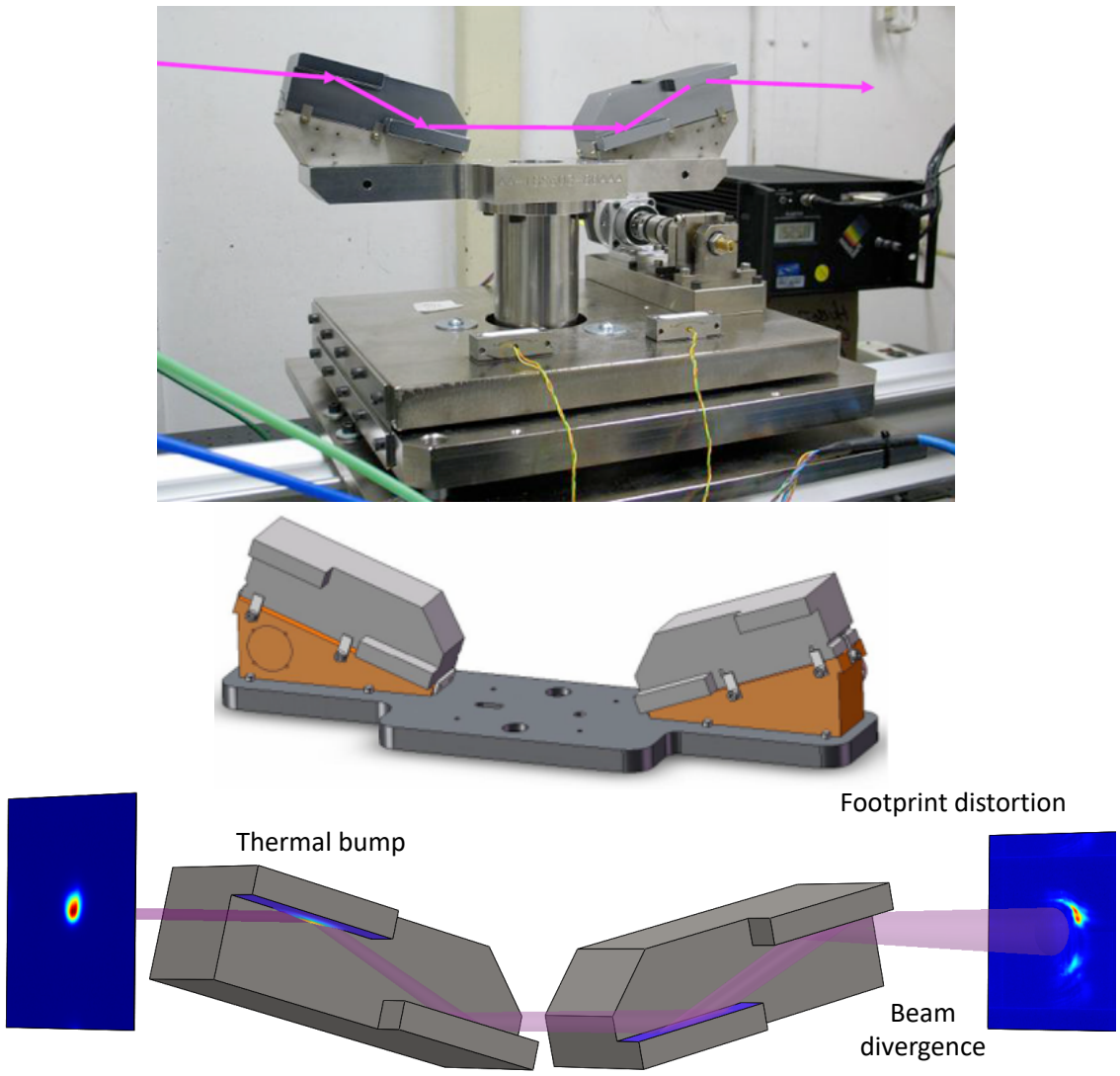

Figure 3.19: (a) A photo of the monochromator [89] in SLAC national accelerator laboratory. (b) The silicon monochromator used in this study. (c) An illustration of deformed monochromator under thermal load. Beam intensity is significantly reduced while beam divergence increases.

To enable more advancement in various scientific explorations, high-brightness X-ray source is crucial. This motivation, together with other driving forces, leads to the development of the free-electron lasers (FELs) [37, 38, 62, 90–92]. The FELs, unlike conventional lasers, employ the free electrons that are not bounded within discrete energy states in a gain medium. X-ray FELs (XFELs) has many outstanding properties, such as extremely high brightness, ultra-short pulse length, narrow bandwidth and good transverse coherence. These superior properties, however, challenge monochromators due to stronger and more localized thermal load.

Thermal load refers to the thermally induced deformation and strain on the optics. It originates from the X-ray-matter interactions. Thermal load can lead to two effects: gross bending and

mapping distortion . Gross bending is resulted by different thermal expansion across the optics thickness (due to temperature gradient). Mapping distortion, on the other hand, is the local swelling due to direct expansion of the heated material normal to the heated surface which leads to a distortion which maps the power density distribution [2]. For monochromator that consists of two pairs of parallel crystal mirrors, thermal load mostly falls on the first crystal surface. This could cause severe mismatch in lattice spacing between the surfaces [3]. As a result, the highly collimated photon beam will diverge with certain energy spread, and other surfaces cannot simultaneously reflect all the X-ray reflected by the first crystal [47]. Accordingly, the transmitted beam brightness and coherence through the monochromator cannot be preserved.

Different techniques have been implemented to relieve thermal load, such as cooling. However, very high thermal power density (due to unprecedentedly high brightness) challenge the existing techniques. For instance, the thermal power density can be calculated as about $3\times10^{11}\,\mathrm{W/mm^2}$, given the typical values: absorbed pulse energy of 1 mJ, spot size of 150 μm and pulse length of 50 fs. This is several orders of magnitude higher than the typical thermal load in modern storage rings. Furthermore, in pump-probe experiment with very short delay time [93], cooling effects are very limited. In fact, a quantitative characterization of the thermal load effects in FELs has not been reported yet.

In this work, we report the first quantitative analysis of the thermal load effects on monochromator. We study two X-ray FEL pulses, generated by two electron bunches, sequentially passing through a four-bounce silicon (1 1 1) monochromator at room temperature with a delay time of 23.8 ns. The distorted photon beam footprint with thermal load is captured in both theoretical calculation and experimental measurements with great agreement. The transmitted photon beam spectrum under thermal load, or effectively the rocking curves of the monochromator, is also characterized in the analysis for quantitative evaluations of the brightness reduction due to thermal load.

3.3.2 Thermal load

When photon beam is diffracted on thick crystal, it can be split into two components: reflection and absorption. The absorption component introduces thermal load through the interactions between the photon and bounded electrons in the crystal. The bounded electrons, after absorbing energy from photons, are excited from valence band to conduction band. This photon-electron interaction process happens very quickly with a time scale of femtoseconds. The hot excited electrons then spread out the energy through electron-electron scattering and electron-lattice scattering. Within a time scale of tens of picoseconds, the electron and lattice reach a local equilibrium. This whole heating process, compared to the delay time between the two pulses (23.8 ns), can be well approximated as an instantaneous energy deposition into the crystal with certain spatial distribution (see Method). With the instantaneous energy deposition as initial condition, the heat transfer and elastic response of the crystal can be described by the classic thermoelasticity equation. On the other hand, the thermal diffuse time is calculated as 0.41 s, and the elastic wave propagation time to reach the boundary is 0.71 μs. Both characteristic time are very large compared to delay time of 23.8 ns, suggesting the implementation of the symmetric boundary condition to reduce computational load. We perform finite element analysis with temperature-dependent thermal properties to quantitatively analyze the deformation, surface slope and strain on the crystal. The results are highly localized due to the small delay time, as shown in Fig. 3.20.

Figure 3.20 a zoom-in view of the thermal bump on the whole crystal domain. The incident

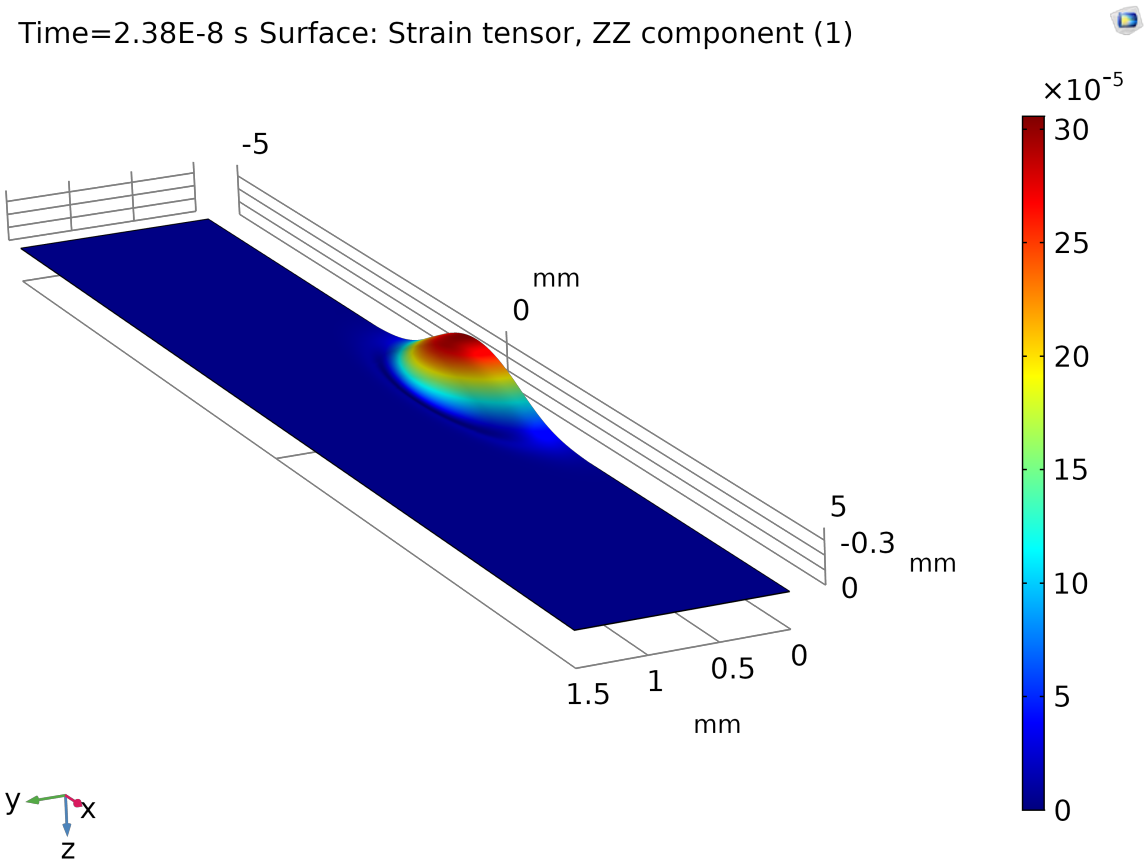

Figure 3.20: An example of the thermal response at a delay time of 23.8 ns on the first crystal surface. The incident pulse energy is 1 mJ, the footprint size is 150 µm in rms, as measured in experiments.

photon beam properties are specified as follow: central photon energy is 8.1936 keV, bandwidth is 20 eV (FWHM), pulse energy is 1 mJ, footprint size is 150 µm in rms (353 µm in FWHM), as measured in experiment. In total, 93.9% of the incident pulse energy is absorbed by the first crystal. This absorbed energy leads to a maximal instantaneous temperature rise of 57.70 K from initial temperature of 300 K. After 23.8 ns, the maximal temperature rise is still 54.11 K. The value of strain ε_{zz} (z is thickness direction) is displayed by the color bar in Fig. 3.20 with a maximum value of 3.07×10^{-4}. The surface displacement in z direction is magnified with a factor for better visibility of the thermal bump. The actual value of the surface displacement is about tens of nanometers (maximum of about 6.03 nm). When the incident pulse is attenuated by a solid attenuator, the incident pulse energy decreases to 0.1 mJ. Accordingly, the instantaneous center temperature rise is only 5.98 K. After 23.8 ns, the center temperature rise is 5.51 K. The strain is about 3×10^{-5} within the footprint. In general, all effects are scaled approximately to one tenth.

3.3.3 Footprint distortion

Both non-uniform local deformation and strain result in the footprint distortion, or beam spatial intensity distribution distortion. The footprint distortion is also known as mapping error. The non-uniform local deformation leads to the non-zero local surface slope, which further leads to the focusing or diverging of the local rays depending on the local concavity or convexity. The local strain, on the other hand, results in the shift of reflected rays spectrum and thus the absorption of these rays on other surfaces, also contributing to the distortion of the beam spatial intensity distribution.

The redirection effects (either focusing or diverging) can be explained by the concavity of the deformed surface. The deformed surface, or the thermal bump shown in Fig. 3.20, is convex near the top and concave near the bottom. Consequently, the rays incident at the top are diverged and decreased in intensity when reaching the screen, while the rays incident at the bottom are focused and increased in intensity. Outside the range of the thermal bump, however, the crystal surface is unaffected. When two pulses are spatially aligned, the trailing pulse is incident right on the thermal bump. The high intensity rays near the beam center are diverged, while the low intensity rays away from the beam center are focused. This phenomenon leads to a hollow shape footprint with a large radius. Besides the footprint distortion, different rays also have different optical path length and thus different phase. This undermines the coherence of the beam.

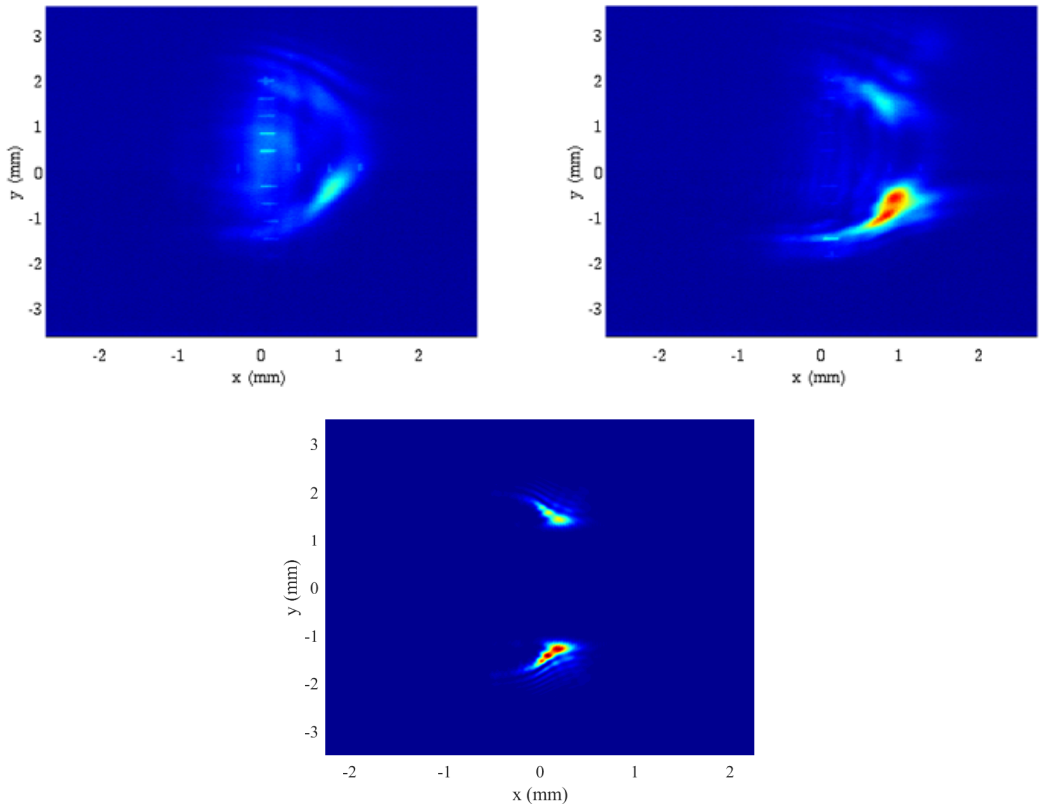

Figure 3.21: Distorted footprint of XFEL after passing through the monochromator. The first two figures are experimental measurement, while the last figure is the simulation results.

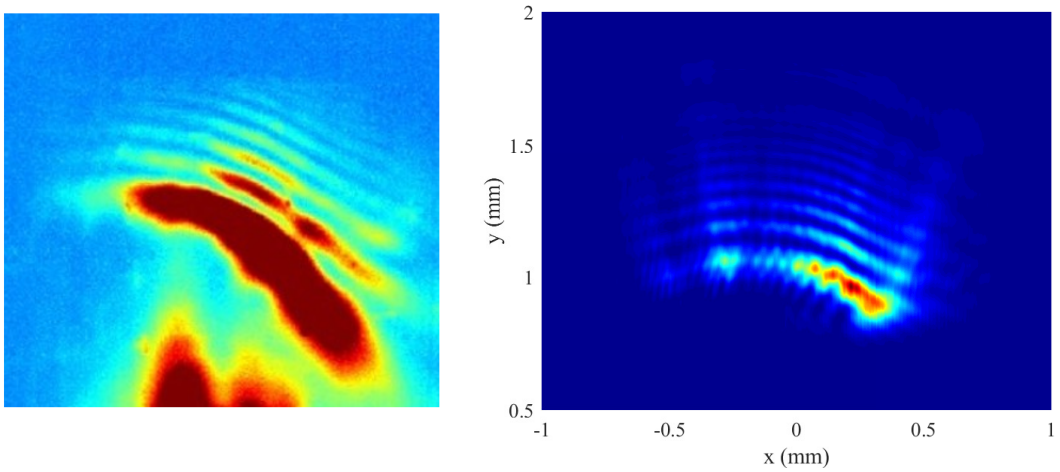

Figure 3.22: Zoom-in view of the distorted footprint. Several fringes can be clearly observed around the crescent footprint. A crescent shape with a diameter of about 4 mm can be observed in both experiments and simulations.

In experiment, there often exists an offset between the centers of two pulse due to the random nature of electron beams, as shown in the top left figure in Fig. 3.21. Because of the offset, a complete hollow shape footprint was not observed on the screen. Instead, an incomplete hollow shape (crescent shape) was captured, as displayed in the top right figure in Fig. 3.21. The effects of thermal load, in the attenuated case, are not significant, because both the strain and surface slope error are smaller than the rocking curve width (about 1.4×10^{-4}) and beam divergence (about 1.63 urad), respectively. However, in the non-attenuated case, the footprint becomes crescent shape with a diameter of approximately 4 mm. In simulation, a crescent shape of distorted footprint with almost the same radius is obtained, suggesting a good agreement with the experimental measurements. The offset used in simulation is about 2.5 times of the rms for incident pulse intensity distribution, as estimated from the attenuated experimental measurement. One should be reminded that, even though the exact value of the offset does affect the actual intensity of the output pulse, the radius of the distorted footprint remains unchanged. Consequently, in terms of the crescent footprint radius, the offset is not a deterministic parameter.

In addition to the overall crescent shape, several fringes can be observed both from experiments and simulation around the distorted footprint, as shown in Fig. 3.22. This is due to the interference between the redirected rays. Different optical path length, phase shift due to the crystal and possibly frequency among the redirected rays collectively create the fringes.

3.3.4 Peak intensity reduction

The peak intensity of the output beam from the monochromator is significantly reduced due to the thermal distortion of the rocking curve of the first crystal. At different locations of the first crystal surface, the local strain and surface slope both contribute to the shifting of the local rocking curve. Overall, for the whole first surface, the rocking curve decreases in peak value and broadened in bandwidth. Moreover, on other surfaces, even though the thermal load is negligible, the deviation of incident angle from Bragg condition still exists and leads to distortion of the rocking curve.

Therefore, the rocking curves of all four surfaces do not coincide and the peak intensity of the pulse can be significantly suppressed after passing through the monochromator with thermal load, as shown in Fig. 3.23.

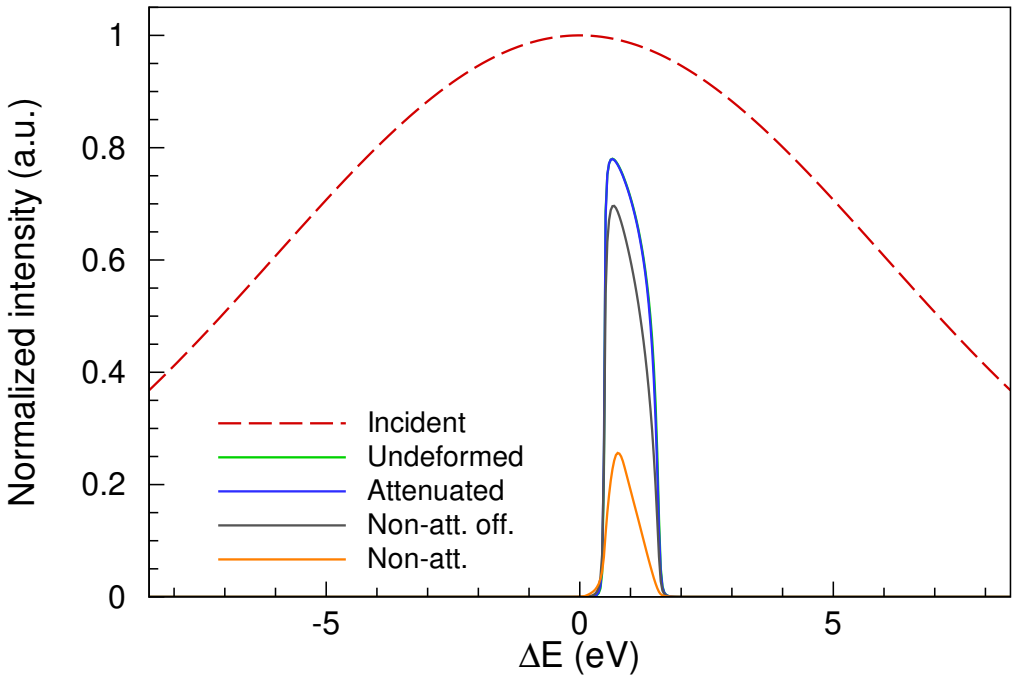

Figure 3.23: The output photon beam intensity in different situations from simulation. The dashed line shows the incident photon beam spectrum. The green line indicates the transmitted intensity when the crystal is undeformed. The blue line, which is overlapped with the green line, presents the transmitted intensity for attenuated case. The gray and orange lines stands for the non-attenuated transmitted intensity with and without the offset, respectively.

In Fig. 3.23, the peak intensity of the attenuated case well recovers to the undeformed situation, due to the mitigation of thermal load, while obvious degradation exists in the non-attenuated cases. In non-attenuated cases, the peak intensity might drop to 25% of the designed value, if two photon beams are well overlapped (orange line in Fig. 3.23). When two photon beams are offset, the peak transmitted intensity can be better preserved but still not fully recover. The main reason of the peak transmitted beam intensity reduction is the mismatch of rocking curves in four surfaces. The peak intensity of the first surface can be strongly suppressed by other surfaces if the mismatch in rocking curves exists.

3.3.5 Transverse phase difference

When reflected on the surface of the crystal, the photon beam experiences a phase shift. With thermal load, the phase shift varies in transverse direction, leading to transverse phase difference in

the output photon beam. Two factors simultaneously contribute to the transverse phase difference. The first factor is the optical path length difference due to surface deformation on the first crystal and the redirection of the rays. The second factor is the crystal response change due to thermal load. For each ray, if redirected, the response of four surfaces will all change. The transverse phase difference indicates potential degradation of transverse coherence.

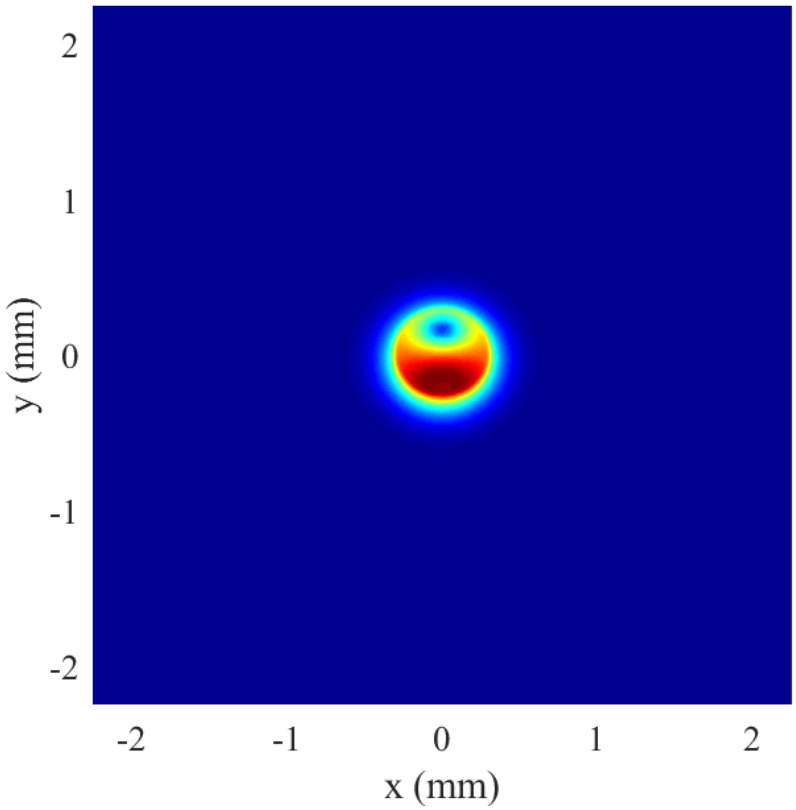

Figure 3.24: The phase shift for the most intense mode (8.1944 keV) due to Bragg reflection on the first crystal. Different phase shift can be observed at the thermal bump, leading to transverse phase difference of the output photon beam.

Figure 3.24 shows the phase change due to Bragg reflection on the first crystal. The phase change varies significantly at the thermal bump location. The phase change remains the same as unperturbed surface within a small region on the ubac slope of the thermal bump. This is because surface slope effects and strain effects are cancelled, and Bragg condition is still satisfied. However, the reflected photon frequency is different from the designed value. At other locations of the thermal bump, the surface slope and strain do not cancel out, leading to large phase difference.

In addition to the crystal response, the optical path difference between redirected rays is also contributing to the transverse phase difference (not shown here). This is because the footprint is already strongly distorted and interference happens, as shown in Figs. 3.21 and 3.22.

3.3.6 Discussion

In all the experimentally recorded pictures, the first shot does not appear. This is due to the spiky nature of SASE. The incident SASE is relatively broad band and very spiky in spectrum, even if its pulse energy is stable. Compared to SASE bandwidth, the rocking curve of the monochromator is very narrow. Within this narrow bandwidth, if there happens to be no modes with high intensity, there will be no transmitted pulse. However, due to the existing of other modes, the thermal load will still be deposited into the crystal. The absence of the first pulse actually enable a clean capture of the second pulse with thermal distortion. The deposited heat flux is about $10^4\,\mathrm{W/m^2}$. This flux, compared to the self-seeding situation, is still low, as the flux in self-seeding monochromator is about five times larger.

To mitigate the thermal load effects, several methods can be employed. Reducing the dose of the first pulse is one option, as applied in this study, but it may lead to insufficient number of photons. Furthermore, replacing silicon with CVD diamond has also been proven capable in mitigating thermal load effects [47]. Another option is implementing cooling method. Recently, EuXFEL has been developing cryogenic cooling for the silicon two-bounce reflective monochromator in beamline [94, 95]. The reported results indicate minor bandbroadening effects. Instead, peak intensity suppression is the major issue, as addressed in this study. At cryogenic temperature such as 100 K, there exists a zero-expansion point for silicon at around 120 K. Additional advantage of operating at cryogenic temperature is much better thermal diffusivity. However, other potential issues may emerge. We will discuss more in Chapter 5.

3.3.7 Methods

3.3.7.1 Experiment

Here, the experimental setup and procedure are described. A schematic of the experimental setup is shown in Fig. 3.25. The experiment took advantage of the two-bunch mode developed by Decker et al. [96–98] in Linac Coherent Light Source (LCLS) of SLAC national accelerator laboratory. The two-bunch mode provide two XFEL pulses with nanosecond separation by combining two laser systems [97]. With tunable pulse pairs, the experimental setup is presented in Fig. 3.25.

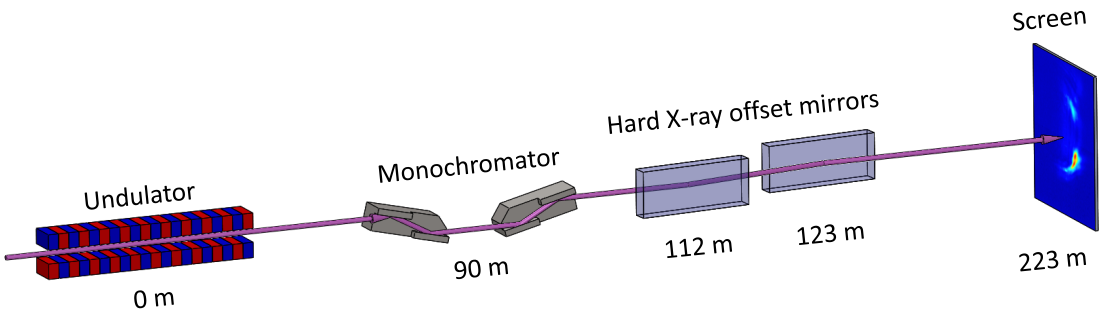

Figure 3.25: Schematic of the experiment. The actual experiment was performed with the two slits fully opened and no focusing. Instead, one screen was installed at 100 m downstream of the second hard X-ray offset mirror to record the footprint.

In experiment, the monochromator in used is a silicon four-bounce reflective monochroma-

tor with (1 1 1) orientation [89]. The monochromator is located at about 90 m downstream to the undulator section. After transmitted through the monochromator, both pulses are offset from the undulator axis by a pair of hard X-ray offset mirrors (HOMS mirrors) [99] located at 112 and 123 m downstream to the monochromator. A screen at 100 m downstream to the second mirror is placed to record the footprint.

3.3.7.2 Photon beam propagation simulation

The photon beam has a central photon energy of 8.1936 keV and a bandwidth of 20 eV in FWHM. The photon beam (modeled as a bunch of discretized rays) exits the undulator and propagates as a Gaussian beam in free space before it enters the monochromator at $z = 90$ m (assuming $z = 0$ m at beam waist). During propagation, the photon beam develops certain angular divergence. The angular divergence of the photon beam can be calculated by Eq. (3.9)

$$\frac{dw}{dz} = \frac{z/z_R^2}{\sqrt{1 + z^2/z_R^2}} w_0, \tag{3.9}$$

where $z_R = 16.76$ m is the Rayleigh range, and $w_0 = 20\sqrt{2}$ µm is the beam waist size. Consequently, the beam divergence dw/dz is calculated as 1.66 μrad at the entrance of the monochromator. The propagation and reflection of the photon beam inside the monochromator is modeled by geometric ray tracing method due to the small size of the monochromator compared to propagation length $z = 90$ m. After the photon beam exits the monochromator, it continues propagating in free space until it reaches the next component, such as a screen or a mirror. The propagation process in free space [100, 101] is modeled by an in-house Python code.

3.3.7.3 Thermal load modeling

Thermal load is simulated by finite element analysis using the commercial software COMSOL. Only the first crystal is considered since other crystals absorb negligible energy (less than 1.85% of the first one). The computational domain is 60 mm in length, 12 mm in width and 10 mm in thickness. The first pulse deposits energy density ΔU_T with spatial dependence of

$$\Delta U_T = \frac{AI_0}{\pi r_x r_y L \sin\theta_B} \exp\left[-\left(\frac{x - z\cot\theta_B}{r_x}\right)^2 - \left(\frac{y}{r_y}\right)^2 - \left(\frac{z}{L\sin\theta_B}\right)^2\right], \tag{3.10}$$

where A is the absorptance, I_0 is the pulse energy, r_x and r_y are the footprint size in x and y direction on crystal surface respectively, L is the absorption length, and z denotes the direction in crystal thickness direction. Eq. (3.10) is specified as the initial condition for the transient heat transfer simulation. For boundary conditions, all other surfaces are considered thermally insulated. The temperature-dependent thermal and mechanical properties are specified according to literature [53]. The transient heat transfer simulation is conducted up to 23.8 ns, then exported to a quasi-static mechanical simulation to evaluate the thermal load (surface deformation and strain) when the second pulse arrives.

3.3.7.4 Rocking curve calculation

The rocking curve for a single reflection at Bragg condition without any disturbance is calculated through the response function method by Shvyd'ko and Lindberg [52]. When there exists local disturbance (due to beam divergence and thermal load), the rocking curve for single reflection is calculated following the process by Bushuev [50] based on the local deviational parameter:

$$\alpha = 2\sin(2\theta_B)\left[\delta\theta + (\Omega/\omega_0 + \varepsilon)\tan\theta_B\right], \tag{3.11}$$

where θ_B is Bragg angle, $\delta\theta$ is the incident angle deviation from Bragg angle, $\varepsilon \equiv \delta d/d$ is the strain or relative interplanar distance change, and $\Omega \equiv \omega - \omega_0$ is the deviation of photon angular frequency ω from photon central angular frequency ω_0. For the first crystal, the deformation and strain at each ray location on the top surface is imported from thermal load modeling because the extinction length is very short (6.3043 nm at TER). For other crystals without strain, only $\delta\theta$ is considered. The overall rocking curve for each ray is obtained by convoluting the rocking curves of all four reflections.

3.4 Summary

In this chapter, we discussed the thermal load effects in pump-probe situations. Our numerical results indicate that, the first XFEL pulse initiates a thermal bump with non-uniform strain. This thermal bump affects the properties of the second pulse: the central photon energy shifts, the bandwidth is broadened and the seeding efficiency for self-seeding application reduces. For ordinary multi-bounce reflective monochromator in beamline, the first XFEL pulse initiates a thermal bump with non-uniform strain. This thermal bump affects the properties of the second pulse: the footprint and wavefront is distorted, and the peak intensity is suppressed. On the other hand, the impacts of transient elastic waves are also checked in pump-probe situations. These impacts are secondary to the quasi-static strain induced by thermal load.

Chapter 4

Thermal load in multi-pulse situations

In this chapter, we study more complicated situations where multiple pulses are incident. At high repetition rate, the delay time between the leading pulse and the trailing pulse is shorter than the required relaxation time for heat dissipation. Consequently, the thermal load accumulates and the output pulse properties change pulse by pulse, until a quasi-steady state is reached. We first discuss the thermal load from the first shot to a finite number of shots, as in the pulse train mode. Then we study the quasi-steady state behavior of the transmissive monochromator and estimate the critical operating parameters such as the repetition rate.

4.1 Dynamic thermal load in pulse train mode

In practical operation for XFEL facilities, multiple pulses will hit the crystal optics, bringing about the accumulation of the thermal load. One operating mode, the machine generates a certain number of pulses with high repetition rate come as a train, then rest for a certain period, and repeat. This is the pulse train mode. A representative of the pulse train mode machine is the European XFEL one, which is currently the machine with the highest repetition rate (4.54 MHz). In this mode, a quasi-steady state may not be reached so that the thermal load becomes dynamic and varies from pulse to pulse. In this section, we show the accumulation of the thermal load and suggesting tuning method to mitigate it.

4.1.1 Background: thermal load mitigations

The Free-electron laser (FEL) opens the door to a new frontier of high-intensity X-ray experiments in various research fields, e.g., physics, chemistry [41], life [42] and material sciences [43]. Combined with ultra-short duration, refined resolution, and high photon flux, hard X-ray FELs have become powerful tools to capture simultaneous information on atomic structure and dynamics, which have been exemplified by the successful operation of various X-ray FEL sources [37–40], e.g., Linac Coherent Light Source (LCLS). The process of X-ray generation in these machines is based on self-amplified spontaneous emission (SASE) [9], in which the electron beam spontaneous emission is amplified during the continuous interaction while the electron beam traveling through the undulators. The X-rays produced in the SASE process are transversely coherent, however, due to the stochastic nature of this process, one cannot fully utilize the electron beam to generate photons all in a narrow bandwidth [102–104].

One efficient way to improve the X-ray temporal properties is the self-seeding technique, which has been demonstrated experimentally at LCLS [6]. With an inserted monochromator in the undulator system, the SASE FEL spectrum is filtered and a narrow bandwidth wake seed is generated. Then, the narrow bandwidth seed will be amplified in the later undulator segments. In this way, the self-seeding scheme improves the FEL spectrum-brightness dramatically. Naturally, the "seed" property has a strong dependence on the monochromator properties, e.g., the material, the atomic reflection layer, inner strain field (bending, temperature field, etc.). Next generation FEL facilities, like European XFEL, LCLS-II [40, 105], are employing superconducting technology to improve the repetition rate (X-ray pulse per second) to MHz level, to speed up the scientific discoveries utilizing the FEL pulses. Alongside these advances, these high repetition rate machines will bring new challenges on the thermal management of the self-seeding monochromator. Due to the ultra short duration of FEL pulses, the self-seeding monochromator would be heated up instantaneously. This sudden temperature change will induce local strain and elastic waves. For a low repetition machine, there is enough time for the monochromator to recover. But for the high repetition machines, there is not enough time for the monochromator to recover before the next FEL pulse. Strain and surface slope field induced by this thermal effect would lead to seed property degradation, e.g. central photon energy shift, bandwidth broadening and seed pulse energy reduction.

In regards to this issue, studies on thermal load reduction and cooling has been carried out [14, 106]. In addition to thermal load reduction, it is also suggested that tuning the monochromator with a pitch oscillator [14] can achieve better tolerance of the temperature increase. The implementation of the pitch oscillator actually raises a further question: how should the pitch angle of the monochromator be adjusted to yield better protection against the seed quality degradation? In this study, we provide some implications from the simulation perspective for the self-seeding operation in a pulse train mode, where the crystal periodically receives a train of pulses at a high repetition rate and relaxes for some time [14]. We show the dynamic change of the seed quality including the transient behavior of the seed central photon energy shift and seeding efficiency reduction when a quasi-steady state is not reached. We accordingly address how the monochromator pitch angle should be adjusted and the pros and cons of this tuning method.

4.1.2 Simulation method

In this section, we are briefly presenting the simulation details. The simulation tool can be divided into three interconnected modules: diffraction, thermal and mechanical. The diffraction module was developed as a in-house MATLAB script based on Shvyd'ko and Lindberg's response function method [52]. The thermal and mechanical modules were based on commercial finite element analysis software COMSOL. During simulation process, the diffraction module was implemented first to obtain the seed quality and the absorptance of the crystal, while the latter was imported as an input into the thermal and mechanical module, where the quasi-static strain and displacement field was simulated and exported back to diffraction module to access the seed quality of the next XFEL pulse. A more comprehensive description of the simulation method can be found in our previous work.

To evaluate the thermal load effects on hard X-ray self-seeding, the SASE central photon energy is selected as 8.3 keV with 3 μJ pulse energy, 1.2×10^{-3} relative bandwidth, 40 μm (FWHM) spot size and 4.54 MHz repetition rate [14]. The diamond crystal monochromator is in (4 0 0) atomic

plane with geometry specified in reference [107]. At the clamped edge of the crystal, the temperature is assumed to remain at environment temperature of 300 K due to cooling of the base holder. The cooling due to radiation emission from the crystal is neglected due to low crystal temperature. In total, 1000 pulses are simulated and spontaneous radiation is not included and left for future investigation.

4.1.3 Dynamic thermal load

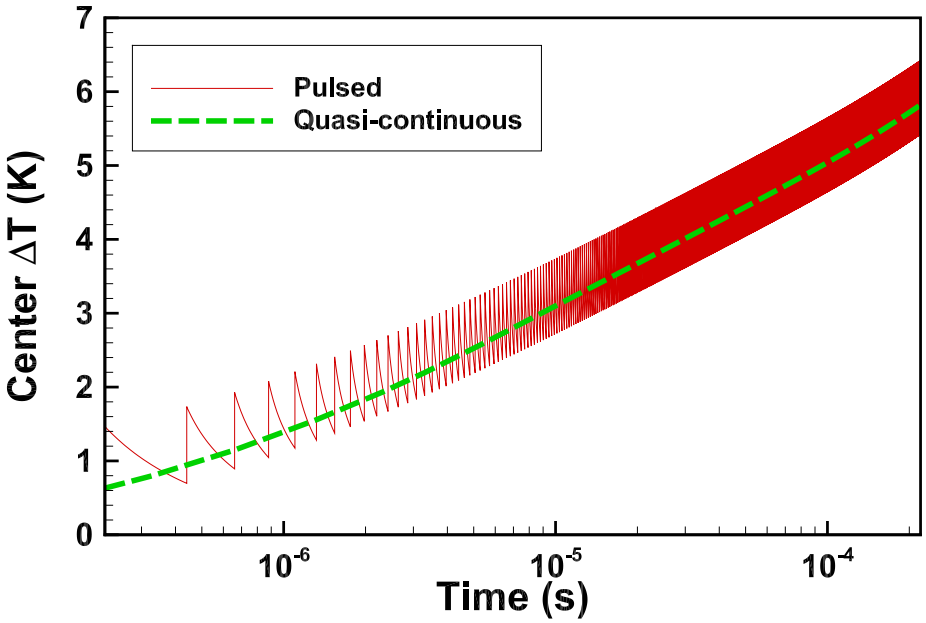

Figure 4.1: Temperature rise history at the center of the SASE spot. The red line represent the pulsed simulation results, while the thick dash green line shows the quasi-continuous results where the SASE pulse energy is averaged over time as indicated in reference [14].

Figure 4.1 presents the temperature rise at the center of the SASE spot. Following the same terminology in reference [14], the pulsed results and quasi-continuous results (for validation only) are plotted and compared. Both curves capture the accumulated thermal load as more pulses arrive, and both curves indicate that, a quasi-steady state, where pulse-to-pulse variation diminishes, has not been reached after 1000 pulses. Therefore, the thermal load is dynamic and varies with time, or number of pulses.

Similar to the spot center temperature increase behavior, the temperature gradient and strain gradient within the FEL footprint also varies with number of pulses, as displayed by Fig. 4.2. In this figure, each curve is marked with one number. This means that this curve represents the residual temperature or strain after the corresponding number of pulses. For example, 5 indicates the residual temperature or strain right before the 6^{th} pulse arrives. Here the elastic strain component is secondary to the thermal strain so that the strain profiles share a very similar behavior to the

temperature profiles. One can also notice that the variation of both the temperature and strain increases with number of pulses.

Therefore, as indicated by both Fig. 4.1 and 4.2, the thermal load is dynamic and varies with time, or number of pulses.

4.1.4 Dynamic seed quality

Accordingly, the seed quality is dynamic and varies from pulse to pulse as showed in Fig. 4.3. Both the normalized seed central photon energy and the seeding efficiency (the pulse energy ratio between the incident SASE and the seed) decrease as more pulses passing through the crystal. After 1000 shots, the seed central energy shifts outside the half Darwin width (half of the relative bandwidth 1.36×10^{-5} [14]), and the seeding efficiency decreases to about 70% of its original value (when the crystal is not deformed). The seed bandwidth is not affected and thus is not discussed in this study.

The decrease of the seed central photon energy is due to the lattice thermal expansion (strain $\varepsilon > 0$), as explained by the differential form of Bragg condition

$$-\frac{\delta E}{E} = \frac{\delta d}{d} + \cot\theta\delta\theta. \tag{4.1}$$

If strain $\varepsilon \equiv \delta a/a = \delta d/d > 0$, then $\delta E/E < 0$ and the central photon energy decreases.

On the other hand, the reduction of the seeding efficiency is attributed to the non-uniformity of the strain (ε) and surface slope ($\delta\theta$) field within the SASE footprint. A more explicit explanation based on Eq. (4.1) is that, $\delta E/E$ varies for different locations inside the spot if the strain and surface slope field is non-uniform; therefore, the overall rocking curve, which is a weighted average of all different locations, will be broadened, leading to the reduction of the seed quality.

4.1.5 Dynamic thermal load in pulse train mode

Based on the curves in Fig. 4.3, the tuning process can be employed if one is able to vary the angle between the crystal and the XFEL. By introducing a pitch angle change, $\delta\theta_{tuning}$, we can rewrite Eq. (4.1) and set it to be zero:

$$-\frac{\delta E}{E} = \frac{\delta d}{d} + \cot\theta(\delta\theta + \delta\theta_{\text{tuning}}) = 0. \tag{4.2}$$

By solving Eq. (4.2), we obtain the required pitch angle change ($\delta\theta_{\text{tuning}}$) and corresponding angular speed of the motor (ω_{tuning}) to keep the seed central photon energy from shifting, as plotted in Fig. 4.4. The pitch angle should be adjusted smaller in an approximately exponential manner, which requires the motor to provide angular speed also in an exponential manner.

With tuning, the seed quality is re-evaluated and plotted in Fig. 4.3 as the blue triangle and violet diamond line. The seed central photon energy shift is successfully eliminated, as indicated by the flat blue curve on the top. However, the seeding efficiency does not recover to its original value and still behaves in the same pattern as without tuning. This is because tuning the crystal pitch angle does not refrain the non-uniformity of the strain and surface slope field within the SASE footprint. We plan to carry out further study to mitigate this issue.

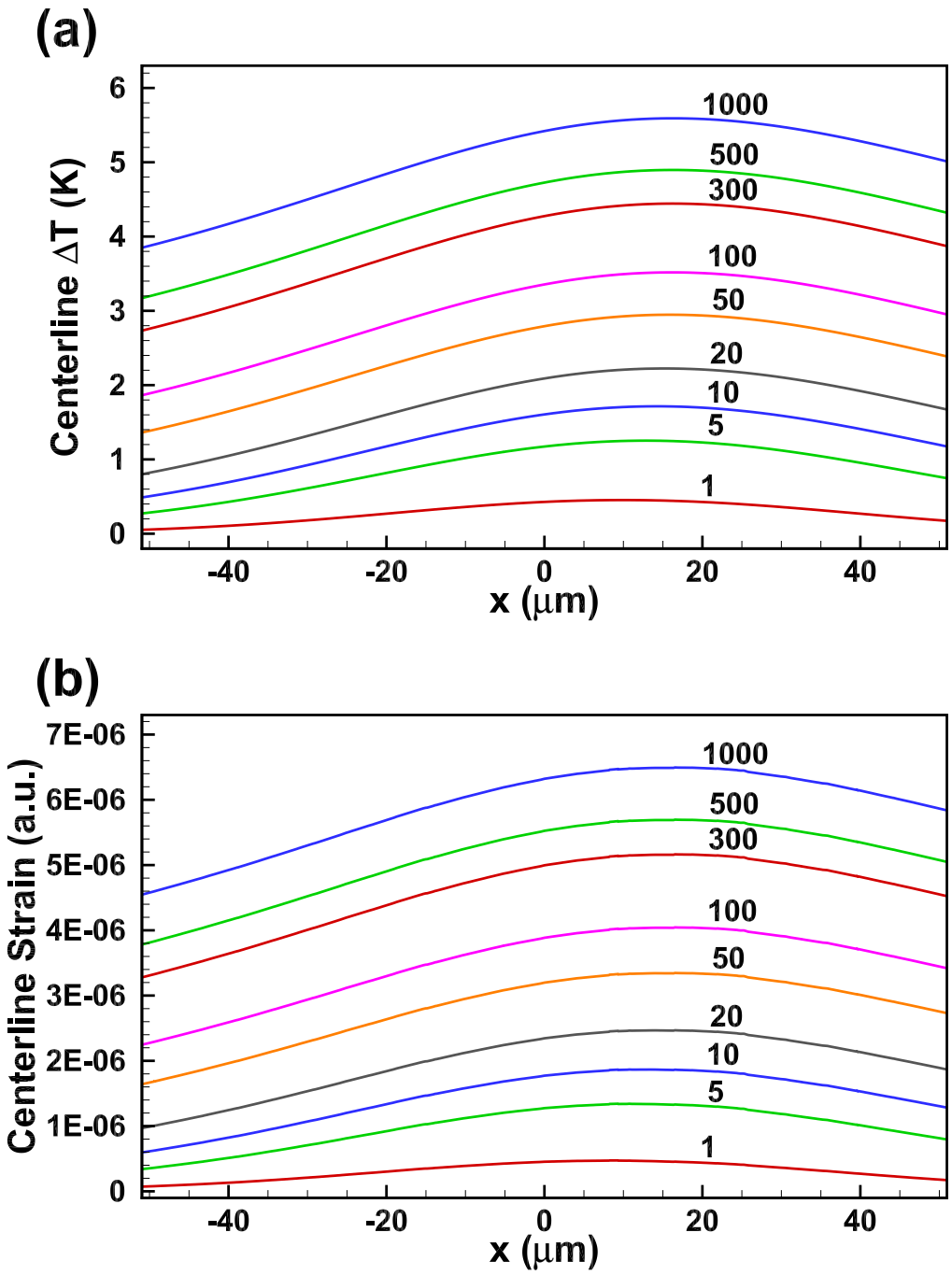

Figure 4.2: (a) Temperature rise and (b) total strain (*zz* component) at the crystal surface centerline in *x* direction (the direction parallel to the projected optical axis on the crystal surface). The number marked above each corresponding curve represents the number of the trailing pulse.

The elimination of the seed central photon energy shift is very important and beneficial to

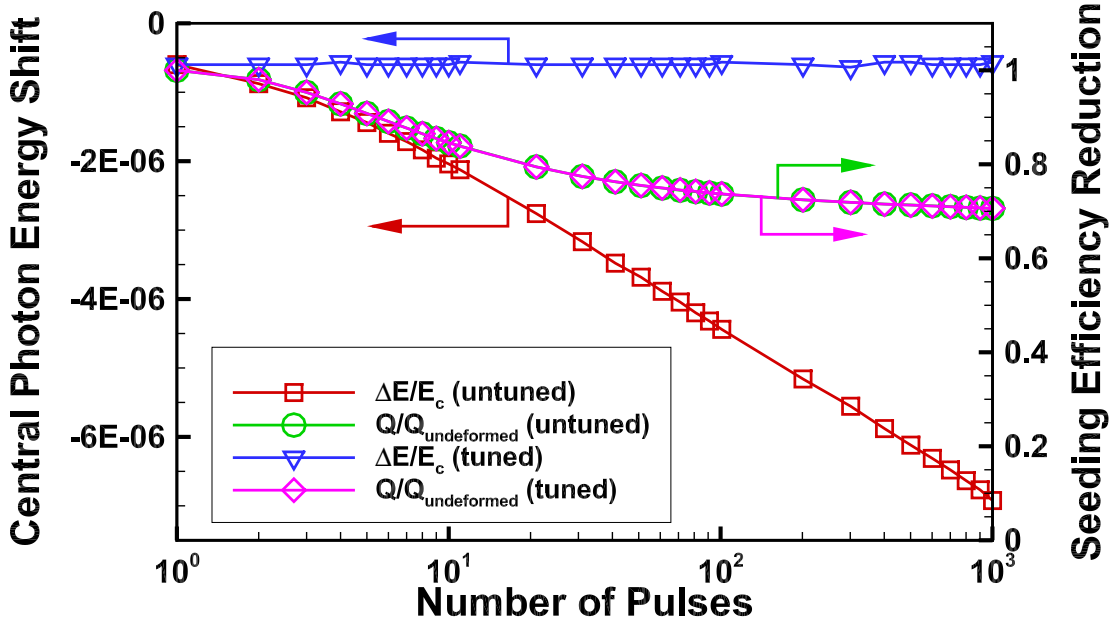

Figure 4.3: The seed quality degradation history due to dynamic thermal load. The red square and green circle lines display the seed quality history without tuning (the crystal monochromator is fixed), while the blue triangular and violet diamond lines show the seed quality history with tuning (the crystal monochromator pitch angle is changing following the tuning curve).

many photon science experiments. It is also very important for cascade systems with multiple monochromators: if the rocking curves mismatch between different monochromators, there could be significantly increased thermal load on the downstream monochromator, or there could be no detectable seed generated from the downstream monochromators. On the other hand, the seeding efficiency reduction could also be an severe issue since the self seeding could not work if the seed cannot remain dominant over the noise.

4.2 Thermal load at quasi-steady state

In this section, we study the quasi-steady state thermal load for the machine with uniformly distributed pulses, such as the machine in SLAC national accelerator laboratory. In this uniform pulse mode, a quasi-steady state can be achieved if cooling scheme is implemented. In terms of tuning, uniform pulse mode is easier to tune compared to pulse train mode, if thermal load can be predicted correctly. Also, the critical operation parameters, such as the repetition rate, can be accordingly determined.

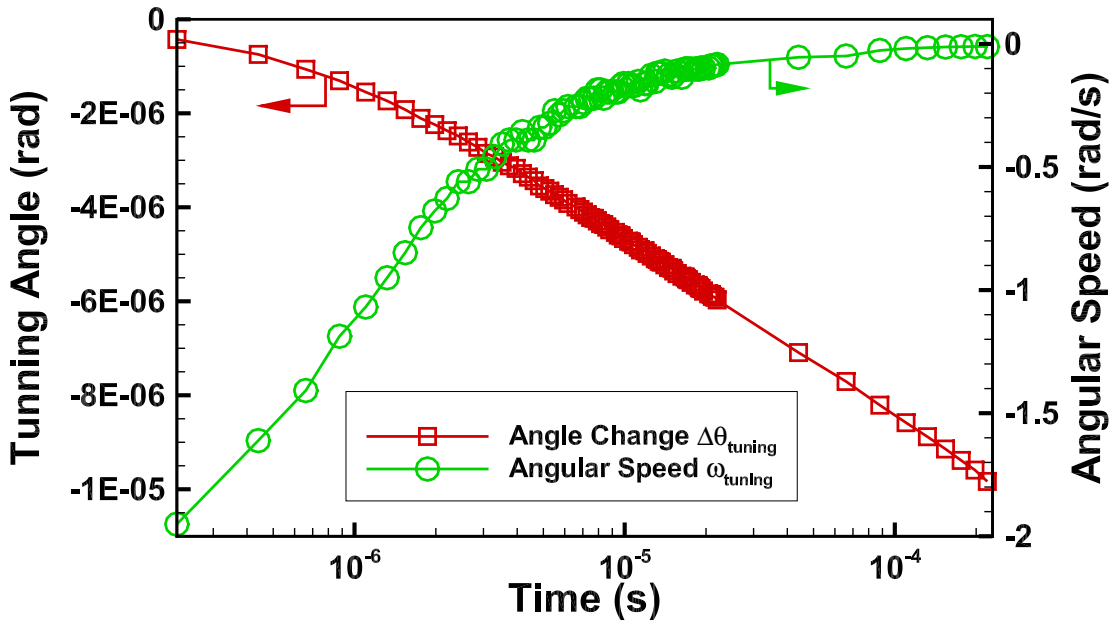

Figure 4.4: The tuning pitch angle change and corresponding angular speed for the motor with time. The red square line is the tuning pitch angle change, while the green circle line is the angular speed.

4.2.1 Background

Compared to pulse train mode, uniform pulse mode machine is more common in many facilities such as SLAC [37], PAL-XFEL [39] and SACLA [38]. For LCLS-II-HE project [108], a high repetition rate (kHz to MHz) XFEL is targeted. Compared to existing setups which usually run at repetition rate on the order of 100 Hz, this is a dramatic boost. While this dramatic boost of repetition rate offers many advantages and unlock new possibility, it also brings about the significant power density increase at the order of 10^2 to 10^4 in terms of thermal load. Both beamline optics and self-seeding monochromator should be designed to perform under the extreme thermal load. To mitigate the extreme thermal load effects at high repetition rate, several approaches are needed simultaneously.

Cooling design The absorbed energy by crystal from the photon beam needs to be extracted out of the crystal. For X-ray optics working in beamline, the power density is relatively lower than that for self-seeding monochromator. Therefore, the existing cooling techniques could still be applicable for these monochromators. For example, cryo-cooled monochromator has been designed [94] and tested [95].

However, more challenges for cooling design emerge when self-seeding monochromator is considered. The self-seeding monochromator is typically a thin CVD diamond plate [6, 106]. To provide cooling for such a thin plate, a clamping mechanism has to be implemented to obtain adequate heat transfer area and tight contact. Unfortunately, this clamping will introduce strong strain due to the imperfection of the surfaces. The strain due to clamping

could also lead to degradation of the seed properties, just as the thermal strain does. One existing solution is to cut the thin plate to refrain the strain due to clamping [106], sacrificing the heat transfer performance. This conflict is one major challenge in the cooling design for self-seeding monochromator. Other challenges also exist, such as the restrictions on material selection due to safety concern, and the required clearance at monochromator surface for the transmittance of the photon beam.

On the other hand, the active cooling mechanism is necessary. In LCLS hard X-ray self-seeding operation, there is no active cooling mechanism applied to the thin crystal monochromator. The monochromator is in trapezoidal shape. When installed, it is gently inserted into and holder and sealed at the bottom to prevent the crystal from sliding out of the holder [109]. A nearly strain-free condition can be achieved to maintain crystal performance. In this case, the cooling mechanism is passive radiative cooling. At a repetition rate of 120 Hz, radiative cooling works well and LCLS hard X-ray self-seeding was a big success. When high repetition rate pulses are considered, the radiative cooling is inadequate due to the low emittance of diamond. The temperature might be approaching the graphitization limit (around 1400 K) if no active cooling is employed.

Geometry design In addition to cooling mechanism, another critical factor is the thermal resistance between the laser spot and the cooling area of the monochromator. Once the material of the monochromator has been selected, this factor is determined by the monochromator geometry. In the monochromator design with two strain-free cut [94], the thermal path between the laser spot and cooling area (the clamping area in this case) is lengthened by about three times. This is a trade-off: with the clamping, heat transfer through the contact area between the monochromator and the holder can be improved significantly; on the other hand, the crystal has to be cut to maintain a strain-free condition at the laser spot, which actually undermines the heat transfer. These two conflicting factors imply the necessity to optimize the geometry design.

Vibration suppression One more challenge is the conflicting requirements between the hard thermal contact and the soft vibration damping mechanism. To avoid the development of the transient elastic waves, especially the ZGV modes, damping mechanism may need to be employed. The damping machanism usually requires a soft contact between the target and the holder. This is also contradictory to the requirement by cooling.

In addition to XFEL pulses, another vibration source is the cooling device. The vibration from the cooling device has been an issue even in beamline optics cooling field, where the monochromator is bulky and heavy compared to the self-seeding monochromator and its holder. Significant vibration disturbance can still be observed during the experiment for beamline monochromator. It is also a unavoidable challenge in cooling design for self-seeding monochromator.

Therefore, efforts and explorations are still in great need to resolve the conflicting requirements. Here, we present preliminary monochromator design and compare this design to some existing designs. For SASE beam at 9.5 keV, we simulate the thermal response and seeding performance of these monochromators. Based on the simulated seeding performance, the critical repetition rate for both photon energy can be determined given the practical parameters from the real LCLS-II

machine, such as the electron beam length and shot noise level. Furthermore, we also provide the seed quality prediction at cryogenic temperatures to offer some guidance for the cooling design.

4.2.2 Simulation procedure

The simulation package for this study is the same as presented in previous sections. The diffraction component is first employed to provide the absorptance, which is then fed into the thermal and mechanical module in COMSOL to obtain the deformation and strain field for the upcoming pulse. The properties of the upcoming pulse is evaluated by diffraction module with the simulated residual deformation and strain field.

However, to reach a quasi-steady state, thousands of pulses should be simulated. Fortunately, the absorptance for each pulse remains nearly constant, because the SASE bandwidth is typically 100-fold of the crystal Darwin width. Accordingly, the diffraction calculation can be skipped for intermediate pulses before the quasi-steady state. To further relieve the computational load and accelerate the converging process, the simulation is divided into fours steps:

1. A steady state thermal simulation is carried out with the quasi-continuous heat source defined similar to last section.

2. A transient thermal simulation with periodic pulse heat source is performed with the initial temperature field imported from the previous step on a coarse mesh.

3. A transient thermal simulation the same as in the previous step but with a refined mesh.

4. A quasi-static solid mechanics simulation based on the temperature field imported from the previous step.

The first two steps are implemented to reach the quasi-steady state with minimal computational time, while the latter two steps are developed to capture the detailed strain and deformation field within the laser spot. The final strain and deformation fields around the laser spot are exported from COMSOL to the diffraction module for seed quality evaluation. To simulate more realistic seeding process, a stochastic spiky SASE is generated according to the statistical characteristics observed in GENESIS simulation. On the other hand, an electron beam of 100 fs with energy jittering is considered. Due to its random nature, only a fraction of electron beam can interact with the generated seed. Therefore, an effective electron beam length is introduced to represent the part that can interact and amplify the seed. This value is assumed to be 30 fs. All these imperfection lead to the reduction of the seeding efficiency from high value of 2.5×10^{-3} to the level of 4×10^{-4}. The chicane delay is set at 25 fs, which is a typical value for hard X-ray self-seeding. In total, 10000 rounds are simulated, and the averaged seed properties are reported with error bars representing 95% confidence interval.

The parameters used in simulation are listed in Table 4.1. Other parameters are obtained based on both FEL simulation by GENESIS [110] and practical experimental experience. The signal-to-noise ratio is selected as 100 to enable the domination of the seed over the noise in the second undulator segment.

The boundary conditions in use are shown in Fig. 4.5. Two highlighted surfaces, on the top and bottom, are assumed to have fixed temperature. Even though with practical cooling scheme the boundary conditions may be different, the fixed temperature still helps to decouple and simplify

Table 4.1: Simulation parameters for quasi-steady state thermal load study.

Parameter	Value	Unit
Photon energy	9.5	keV
Pulse length	100	fs
Pulse energy	16.42	µJ
Relative bandwidth (FWHM)	8.525×10^{-4}	1
Spot size (FWHM)	44.0	µm
Absorptance	0.09	1
Shot noise	1.34	kW
Critical seed power	134	kW

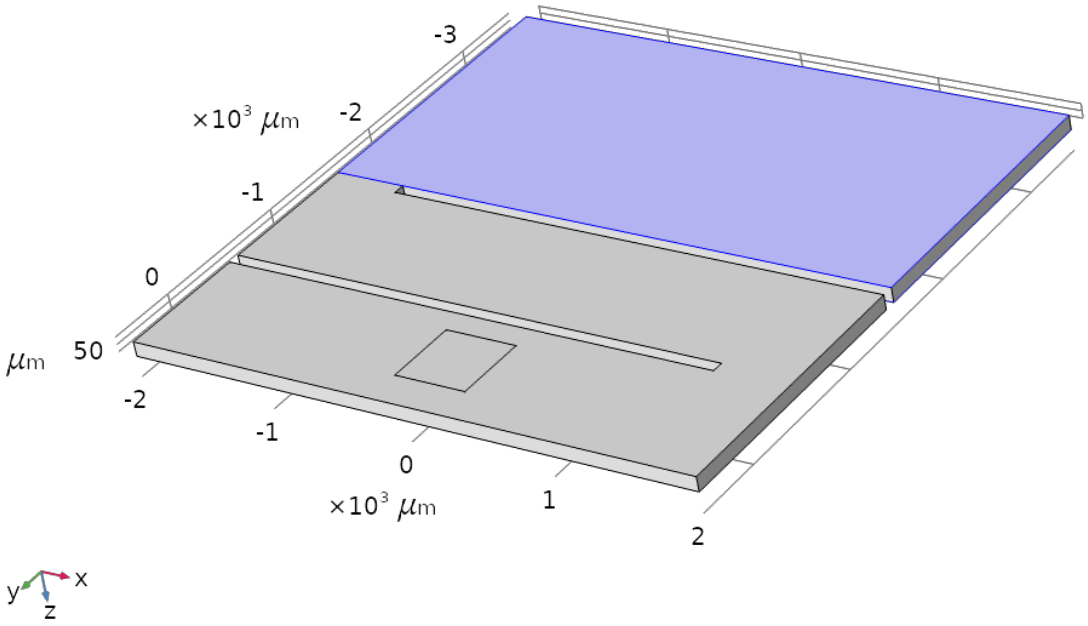

Figure 4.5: Example of computational domain and boundary condition for cut monochromator. Constant temperature boundary conditions are implemented at the highlighted surfaces (top and bottom). Other surfaces are thermally insulated. The square area at the tip indicates the laser spot, where the mesh will be refined to obtain accurate results.

the study: an optimized target temperature can first be determined, cooling scheme can then be developed accordingly. In mechanical simulation, these surfaces are fixed due to clamping, and other surfaces are free.

4.2.3 Monochromator geometric designs

The thermal resistance between the laser spot and the cooling area is one most important part in the cooling thermal circuit. For existing designs based on thin plate geometry, this thermal resistance is large, because of the small thickness, or the small cross-section area for heat transfer. It is also this small thickness that limit the crystal's ability to resist clamping, even if diamond has the highest hardness of any natural material. Additional issues suppressing the heat transfer will also show up if we operating the crystal at cryogenic temperature: the nondiffusive heat transfer phenomena. The nondiffusive heat transfer will lead to the significant reduction of the effective thermal conductivity, especially in thin films as opposed to bulk materials. For instance, experimental measurements [30, 111] of CVD thin film thermal conductivityare showed in Fig. 4.6. In multiple experiments [30,111,112], CVD diamond thin film of different thickness were studied, and the measured thermal conductivity all follow the same trend at low temperature.

Consequently, one straightforward idea is to increase the thickness of the crystal monochromator wherever possible. Three distinct improvements can be obtained: 1) larger heat transfer cross-section area, 2) higher thermal conductivity at cryogenic temperature and 3) higher stiffness and resistance to the clamping strain. Following this direction, we propose to add a thick base to the plate monochromator, as shown in Fig. 4.7. The thick base, when attached to the monochromator, is functioning as a cooler as well as a strain-free mounting point. Compared to implementing an external metal heat sink, attaching the thick base can significantly reduce the thermal resistance between the hot spot and the heat sink. It also, on the other hand, provide strong resistance to the strain generated by clamping due to its large thickness. Moreover, the large thickness also improves the effective thermal conductivity for the base and thus the cooling capacity.

We analyze all three designs and compare their performance for different incident SASE photon energy at different cooling temperature. However, it should be highlighted that, the performance for plate monochromator is only shown for a reference, because it is not compatible with clamping method shown in Fig. 4.5. The strain due to clamping may destroy the seeding condition according to the experimental experience from LCLS.

4.2.4 Thermal load evolution

The spot center thermal load of all three monochromator designs at room temperature (300 K) is shown in Fig. 4.8 for 9.5 keV. The XFEL repetition rate is 1 MHz. Other parameters can be found in Table 4.1. For 9.5 keV, the Darwin width is about 10^{-5}, which is 10 folds narrower than that of 4.5 keV (about 10^{-4}), indicating a much more strict tolerance. Even though much stronger absorption is expected for 4.5 keV beam, the rocking curve is wide and the shot noise is about four times smaller than that of 9.5 keV. One practical example for this setup is a water-cooled self-seeding system operating at room temperature. At room temperature, no noticeable difference can be observed between the thermal conductivity of thin film diamond and bulk diamond. They are both about 2000 $\mathrm{Wm^{-1}K^{-1}}$. Therefore, the different responses of the three monochromators are due to the different geometric designs. Different geometric designs yield different thermal path lengths between the spot center and cooling area. The thermal path length of plate monochromator is close to that of trapezoidal monochromator, but the trapezoidal monochromator is expected to perform better due to larger heat dissipation cross-section. The thermal path for cut monochromator is much longer than the other two, so a significantly higher temperature rise is expected and observed.

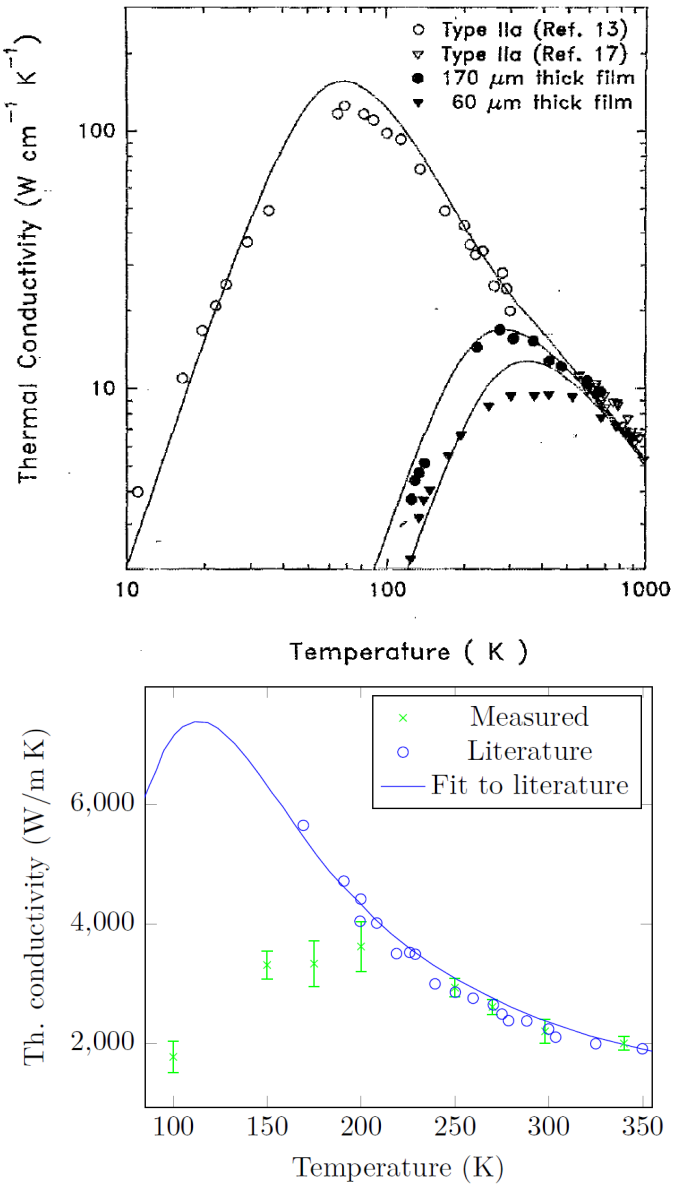

Figure 4.6: Experimentally measured thermal conductivity for bulk type IIa diamond and thin film of 60 μm and 170 μm thick [111] and 300 μm thick [30]. Similar trend with significant reduction (10-fold or more) from bulk value can be observed.

At quasi-steady state, the thermal response of the crystal is periodic in time as shown in Fig. 4.8. In both Fig. 4.8 (a) and (b), the vertical axis is broken to enable better contrast between the three curves. Three periods of temperature cycling for different monochromator are shown. The cut monochromator, due to its long thermal path length, has much higher temperature rise among the three. The residual temperature rise at the arrival time of the upcoming pulse remains at 86.11 K, as compared to 9.75 K for plate monochromator and 7.21 K for trapezoidal monochro-

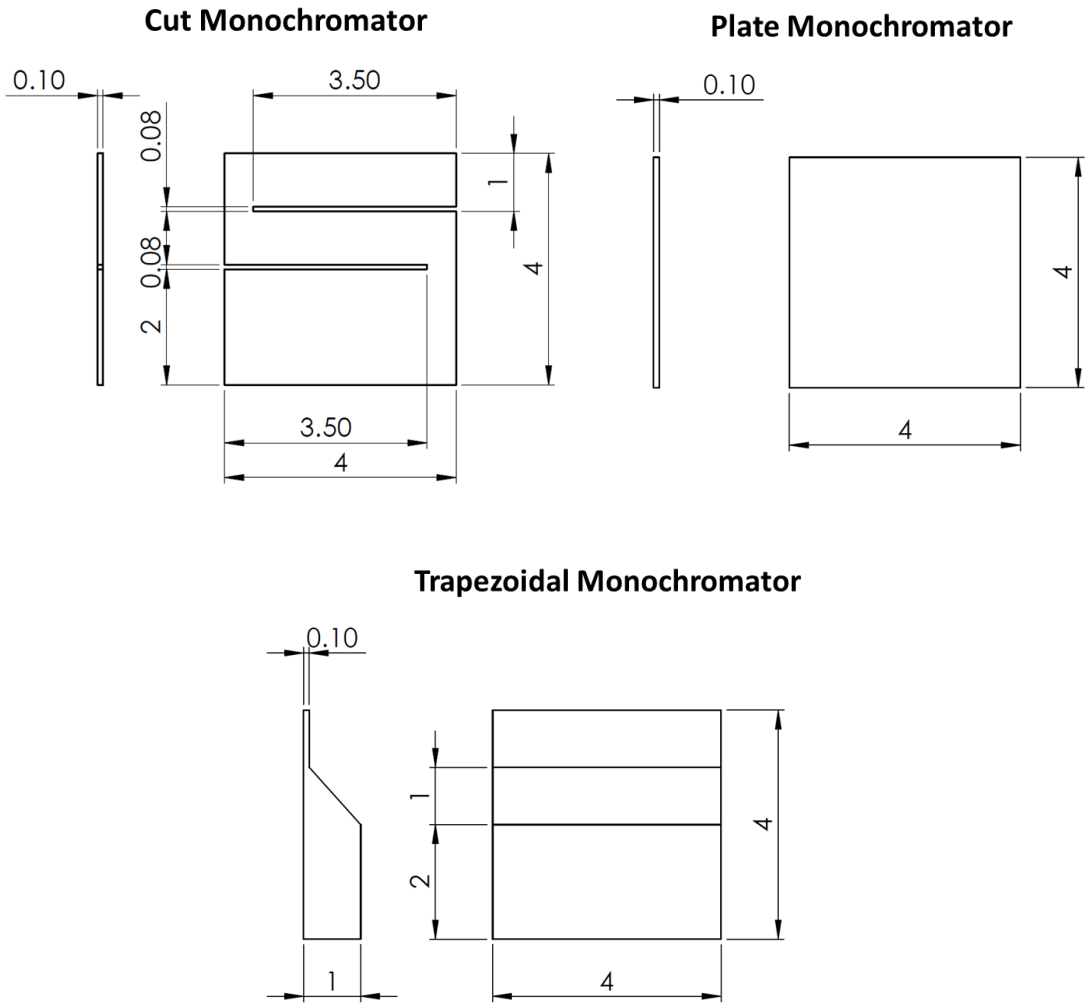

Figure 4.7: Three different geometric design of self-seeding monochromator. The cut monochromator has two strain-relief cuts to refrain the strain from the clamping part. The plate monochromator is simply a thin plate. The trapezoidal monochromator has a thick base with a thin tip of the same thickness as previous two (100 μm).

mator. The residual thermal strain for cut and plate monochromators both exceeds 10^{-5}, while trapezoidal monochromator is able to keep a strain level below 10^{-5}. Compared to the Darwin width of about 10^{-5}, no significant central photon energy shift is expected for plate and trapezoidal monochromator, but a residual thermal strain of 1.13×10^{-4} indicates a significant shift of rocking curve should be observed for cut monochromator. Even if the shift can be tuned as shown in the previous chapters, large strain gradient may exist within the beam footprint. This is detrimental to the self-seeding process. Therefore, it is necessary to operate the system at low temperature where the thermal diffusivity can be greatly improved as suggested by Fig. 4.9.

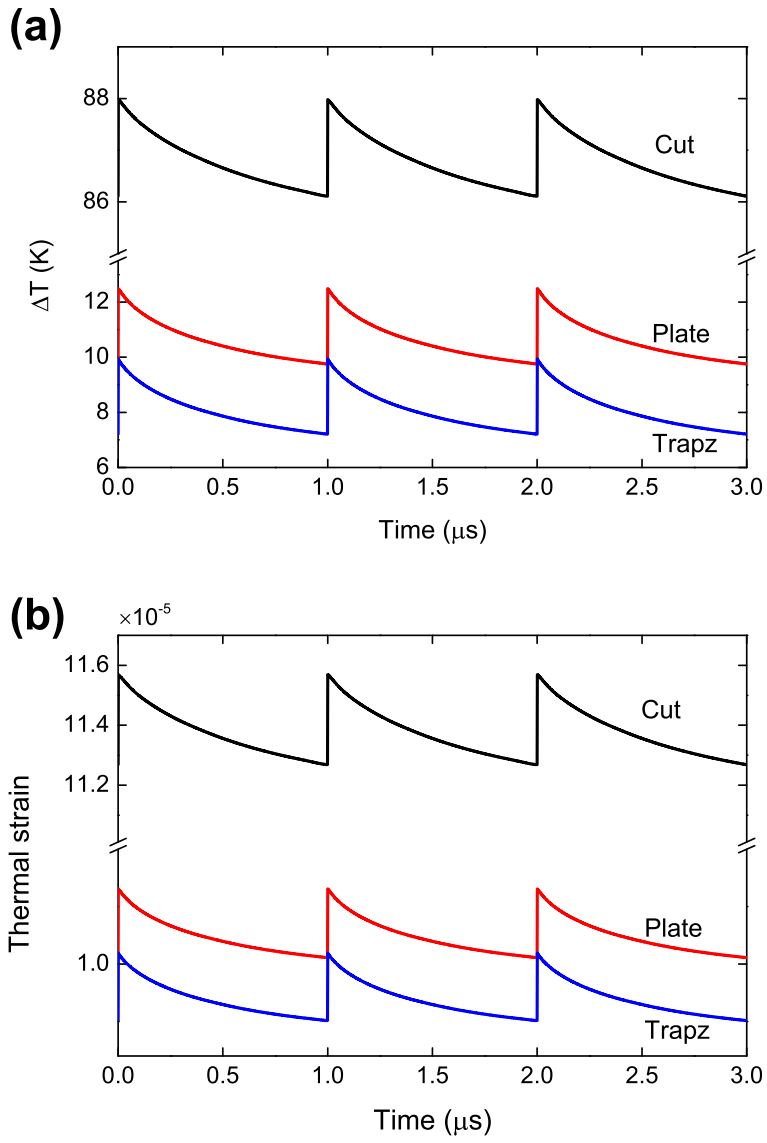

Figure 4.8: The spot center (a) temperature rise and (b) thermal strain history at quasi-steady state at room temperature (300 K) for three pulses. The black, red and blue line stand for cut, plate and trapezoidal monochromator, respectively. The XFEL beam is 9.5 keV at a repetition rate of 1 MHz.

All three curves of thermal diffusivity (bulk and thin film values) and thermal expansion coefficient are displayed in Fig. 4.9. The thermal diffusivity of both bulk and thin film CVD diamond decrease monotonically with temperature, indicating less efficient thermal dissipation at higher tem-

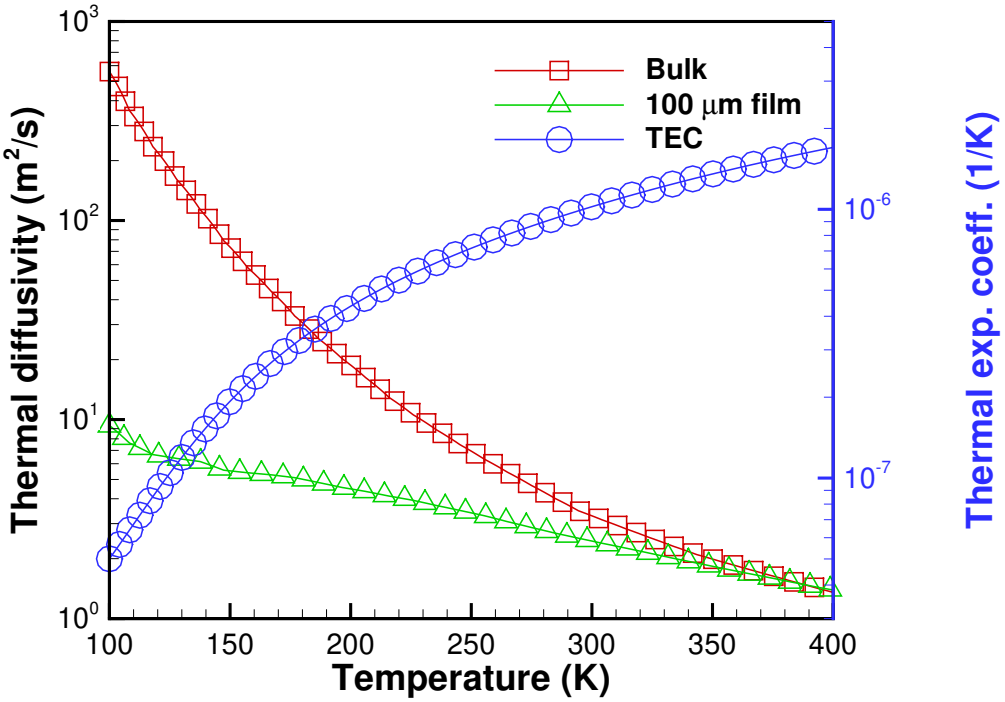

Figure 4.9: The temperature dependent thermal diffusivity and thermal expansion coefficient (TEC) of CVD diamond. The red square line represents the thermal diffusivity of bulk CVD diamond, and the green triangular lines stands for the interpolated 100-μm-thick CVD diamond film. The thin film value is obtained by linear interpolation of the 170-μm-thick sample and 60-μm-thick sample in reference [111]. The blue circle line corresponding to the right vertical axis shows the TEC of CVD diamond [113].

perature. Meanwhile, thermal expansion coefficient of CVD diamond is also monotonic [113]:

$$\alpha_T = \sum_{j=1}^{3} \frac{X_j \theta_j^2 \exp\left(\theta_j/T\right)}{T^2 \left[\exp\left(\theta_j/T\right) - 1\right]^2}, \tag{4.3}$$

where $\theta_1 = 200\,\mathrm{K}$, $\theta_2 = 880\,\mathrm{K}$, $\theta_3 = 2137.5\,\mathrm{K}$, $X_1 = 0.4369 \times 10^{-7}\,\mathrm{K}^{-1}$, $X_2 = 15.7867 \times 10^{-7}\,\mathrm{K}^{-1}$, $X_3 = 42.5598 \times 10^{-7}\,\mathrm{K}^{-1}$. The increased thermal diffusivity at low temperature indicates a much faster recovery of the crystal between pulses, while the decreased thermal expansion coefficient suggests a smaller induced strain if the temperature rise is preserved. Assuming operating at 100 K, the thermal diffusivity increases from $3.28\,\mathrm{m^2 s^{-1}}$ to $560.31\,\mathrm{m^2 s^{-1}}$ for bulk material and $9.33\,\mathrm{m^2 s^{-1}}$ for thin film. The TEC decreases from $1.02 \times 10^{-6}\,\mathrm{K}^{-1}$ to $5.01 \times 10^{-8}\,\mathrm{K}^{-1}$. Both properties can be improved by about an order of magnitude or more.

However, one should be careful when evaluating the monochromator performance at low temperature. If bulk thermal conductivity is used, as in other engineering applications, the monochromator thermal performance can be severely over-predicted, as indicated by Fig. 4.10. In this figure,

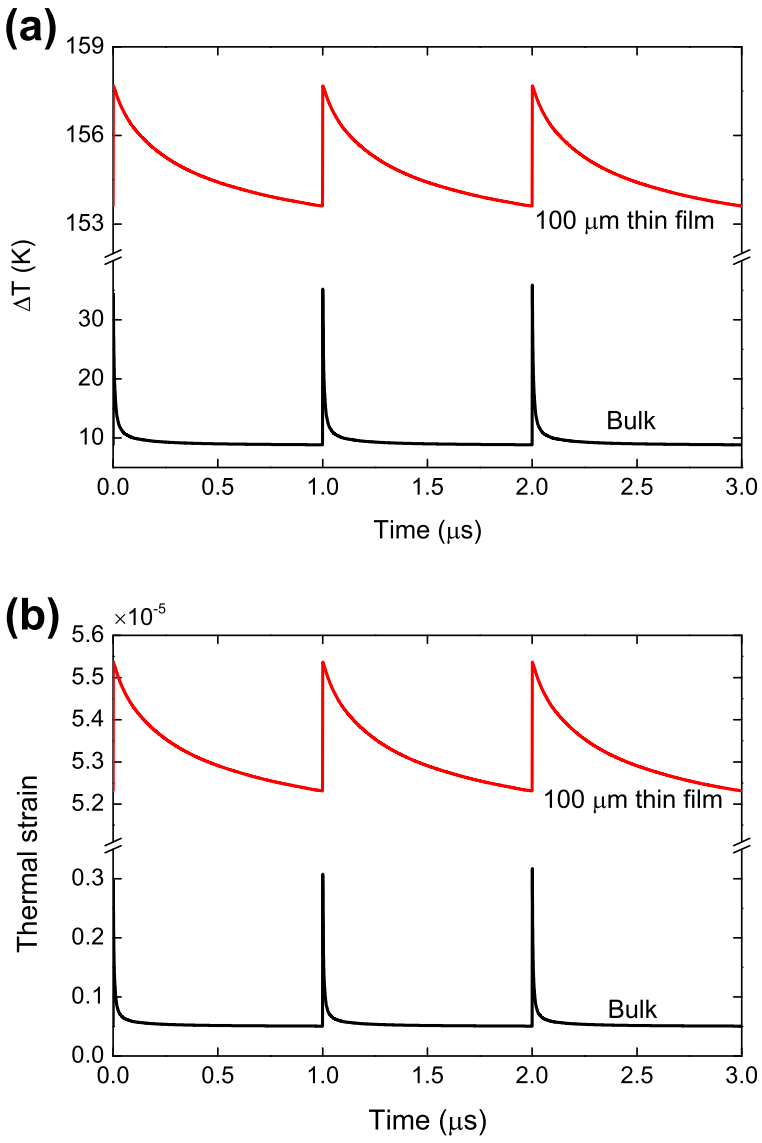

Figure 4.10: The cut monochromator spot center (a) temperature rise and (b) thermal strain history at quasi-steady state at cryogenic temperature (100 K) for three pulses. The black line indicates the calculation using bulk diamond thermal conductivity, while the red line represents the calculation using the thin film thermal conductivity. The XFEL beam is 9.5 keV at a repetition rate of 1 MHz.

the quasi-steady thermal response of cut monochromator for 9.5 keV at 1 MHz repetition rate and 100 K is shown. When bulk thermal conductivity is used, the instantaneous temperature rise due to the incident photon beam is larger compared to that at 300 K, but the crystal is able to quickly recover to the status with very little strain (about 5.06×10^{-7}). However, the recovery behavior of the cut monochromator is significantly undermined with thin film thermal conductivity. The slow decay curve between pulses suggests insufficient recovery time. At the arrival time of the upcoming

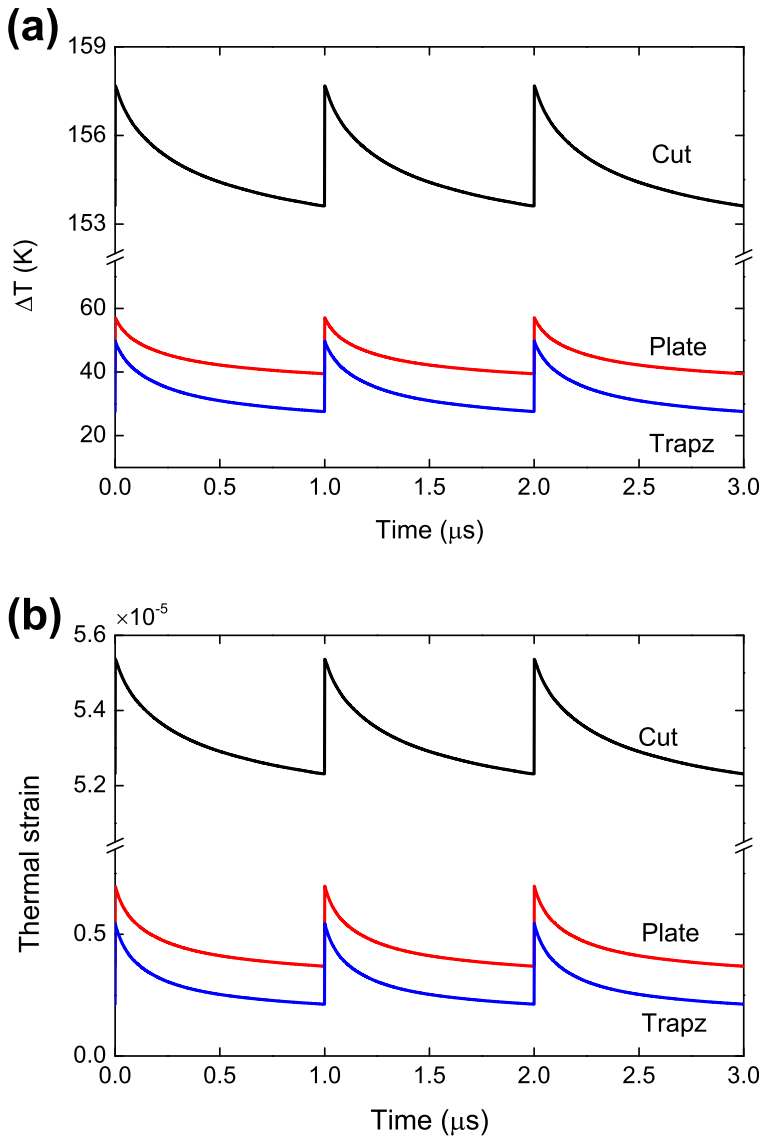

Figure 4.11: The spot center temperature rise history at quasi-steady state at cryogenic temperature (100 K) for three pulses. The XFEL beam is 9.5 keV at a repetition rate of 1 MHz. Effective thin film thermal conductivity is used.

pulse, the spot center temperature rise is 153.62 K. Compared to 8.84 K using bulk thermal conductivity, this is more than 10 folds. The spot center residual thermal strain is 5.23×10^{-5}, 100 folds higher than that in the bulk case. This huge difference is attributed to not only the reduced thermal conductivity, but also the temperature dependence of the properties: inefficiency heat dissipation leads to high temperature, while high temperature results in even lower thermal diffusivity and worse heat dissipation. In extreme cases, a thermal runaway might be triggered. The reduction of thermal conductivity for thin film materials is attributed to the nondiffusive heat transfer phe-

nomena. Furthermore, a heating spot size dependent thermal conductivity has also been measured in multiple experimental works [114–116]. These effects will be discussed later in chapter 5.

Therefore, the effective thin film thermal conductivity is necessary to be considered in the study. The suppressed effective thermal conductivity in thin film materials is generally observed in multiple materials, such as diamond, silicon and GaAs. The suppression is due to the emerging nondiffusive effects, which has also been observed in smaller length scale at room temperature. More discussions and preparations will be given in chapter 5.

Figure 4.11 shows the thermal load comparison between three monochromators at 100 K. Compared to 300 K, the cut monochromator performance is not significantly improved, as the residual thermal strain remains at the level of 5×10^{-5}. The limited improvement is due to the long thermal path and temperature dependence of thermal properties, as explained in previous paragraphs. The plate and trapezoidal monochromators are able to recover more quickly. They both show residual spot center thermal strain of lower than 5×10^{-6}, indicating a negligible shift in rocking curve. The efficient heat dissipation, on the other hand, can also relax the strain gradient within the beam footprint and mitigate the rocking curve distortion due to thermal load, as will be shown in the following subsection.

4.2.5 Rocking curve distortion under thermal load

The maximal thermal strain within the footprint shown in last subsection serves only as an indicator of how much central photon energy shift is expected. To directly access the distortion of the rocking curve and its impacts on seeding performance, the rocking curves at repetition rate of 1 MHz at room temperature are presented in Fig. 4.12. The distorted rocking curves are calculated based on the simulated residual strain and deformation field, as described in simulation procedure session. One typical shot in time domain is also shown to illustrate the thermal load effect on the seed power for cut monochromator in Fig. 4.12(c). The distortion of rocking is not as significant as that shown in Chapter 3, due to the minimized incident SASE dose (16.42 μJ vs. 100 μJ in Chapter 3). However, some distortion effects are still obvious. For example, the reflectance curve on perfect crystal should tilt towards the left near the top. On the contrary, the reflectance of cut monochromator tilts towards the opposite direction at the top. The reflectance curves for other two monochromators shifts to the left and loses the spikes due to multiple reflection within the crystal. Overall, they still remain very similar to the undeformed on in terms of shape. The minor distortion indicates that the strain gradient is not very severe within the laser footprint for plate and trapezoidal monochromators.

The most direct and important effect from thermal distortion of the rocking curve is the seed power reduction: when seed has inadequate power and cannot effectively dominate the shot noise, other modes with different frequency will grow, broadening the bandwidth of the output beam and undermining or even destroying the coherence. In the end, the output becomes SASE again. The seed power in time domain is plotted in Fig. 4.12(c) for cut monochromator at 1 MHz and 300 K. A significant power reduction can be observed in seed bumps that follow the spiky SASE (0 – 100 fs in Fig. 4.12(c)). At this repetition rate and temperature, the seed power cannot remain well dominant over the shot noise. The seed power is reduced from 237 kW to 96.56 kW, while the requirement is 134 kW (100 times of the shot noise). In this case, the seeding functioning is questionable since some strong modes of shot noise may have comparable power as the seed does. Effectively, all these modes can be growing in the second segment of undulator (if not tuned to suppress undesired

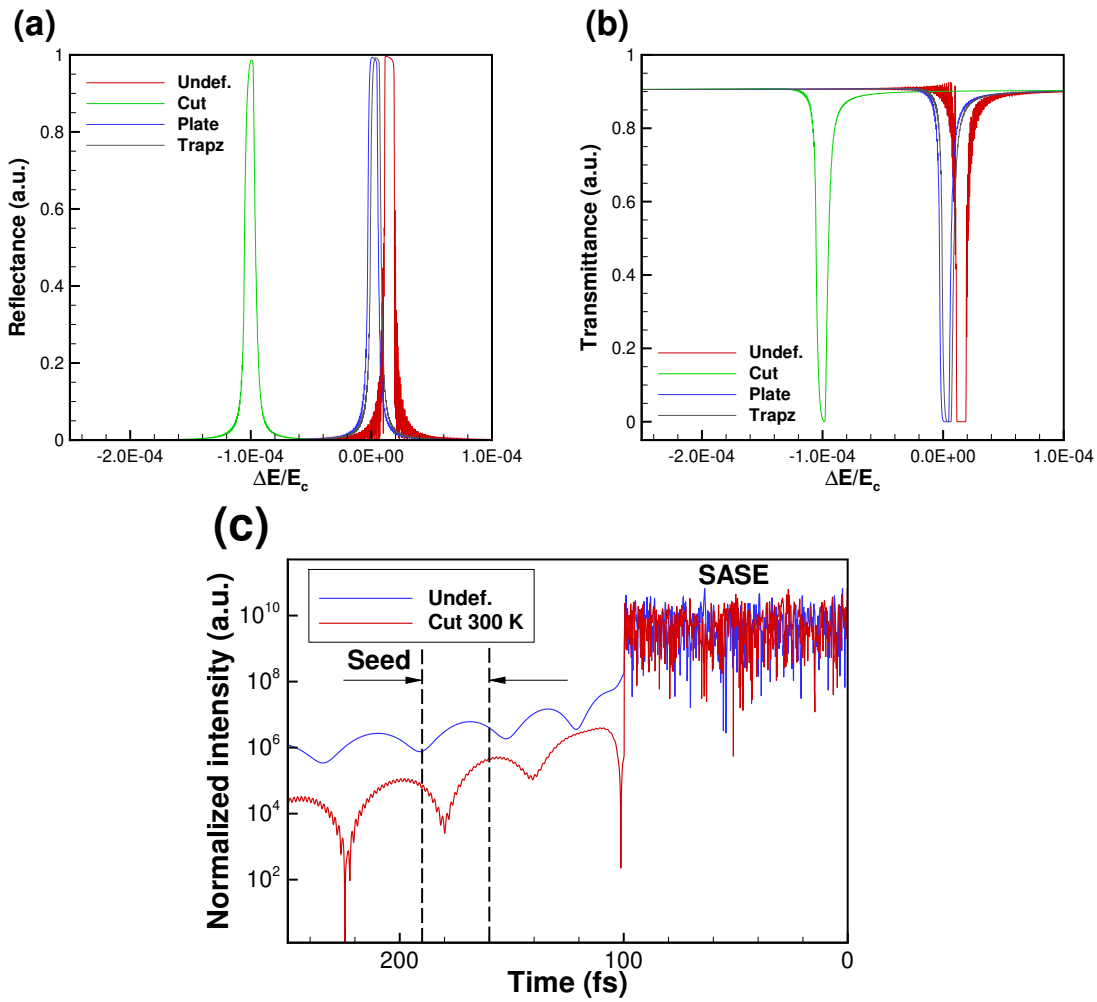

Figure 4.12: (a) Reflectance and (b) transmittance curves for three monochromators at 9.5 keV, 1 MHz and 300 K. The undeformed one is plotted using red line as reference. One typical transmitted pulse for cut monochromator is visualized in (c). The seed power is reduced significantly due to the distortion.

modes), and finally the output beam bandwidth can be broadened.

In addition to the seed power reduction, fine spikes can be observed in the seed bumps, indicating there even exist multiple modes in the seed, rather than one single mode as designed. To illustrate this, the seed spectrum for 10 typical shots are plotted in Fig. 4.13. Some seeds even have two modes with approximately the same power. When magnified in the second undulator session, they both may grow, resulting in the increase of bandwidth by a factor of about two. This undermines the brightness and longitudinal coherence of the beam.

Compared to room temperature of 300 K, the thermal load at 100 K can be dissipated much more efficiently. The rocking curves for both plate and trapezoidal monochromator are almost overlapped with the undeformed one, as incidated by Fig. 4.14. The seed power is approximately preserved at about 200 kW as compared to original value of 237 kW. The central photon energy

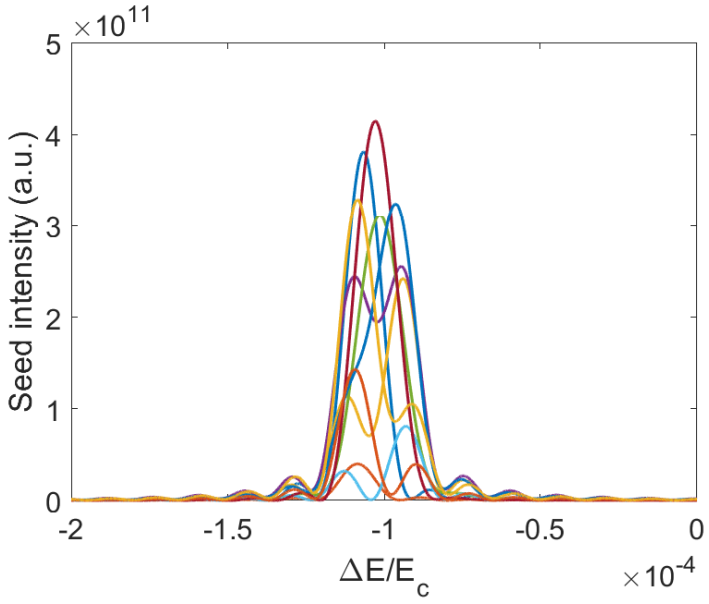

Figure 4.13: Seed spectrum for 10 pulses at 9.5 keV, 1 MHz and 300 K. More than one modes can be clearly observed as multiple peaks in the seed, leading to significant broadening effects in the output pulse.

shift is maintained at about 1×10^{-5}, as compared to original value of 1.5×10^{-5}. One should be reminded that certain detuning exists [117] between the exact Bragg condition and the crystal response. On the other hand, the rocking curve for cut monochromator is also not significantly distorted but shifted by about 4×10^{-5}. However, even without distortion, the central photon energy shift, if unaware, can also induce detrimental effects in final output seeded photon beam from two aspects:

Spectrum mismatch between SASE and rocking curve The spectrum mismatch between SASE and the rocking curve of the crystal leads to seed power reduction. When the central photon energy of SASE and rocking curve are well aligned, the seed is generated by the most intense modes of SASE, allowing the optimal seed power. If mismatched, the seed is not generated from the most intense modes and will decrease in power.

Resonance energy mismatch between electron beam and seed After seed is generated, it enters the second segment of undulator and co-propagates with the electron beam. During propagation, they interact with each other if the resonance condition is satisfied. However, if their energy is mismatched, the seed will not be amplified significantly, and SASE will again grow. Typically, this phenomenon happens together with the spectrum mismatch between SASE and rocking curve, as SASE is generated by the electron beam. The combined effects cause significant quality degradation of the output seeded beam.

Consequently, certain tuning to align SASE beam, electron beam and the rocking curve of the crystal is necessary. Fortunately, for machine that operates at uniformed pulse mode, the tuning is not dynamic and can be done by carefully re-orienting the crystal at quasi-steady state. In the next subsection, we summarize the seed quality and provide the re-orienting angle for tuning.

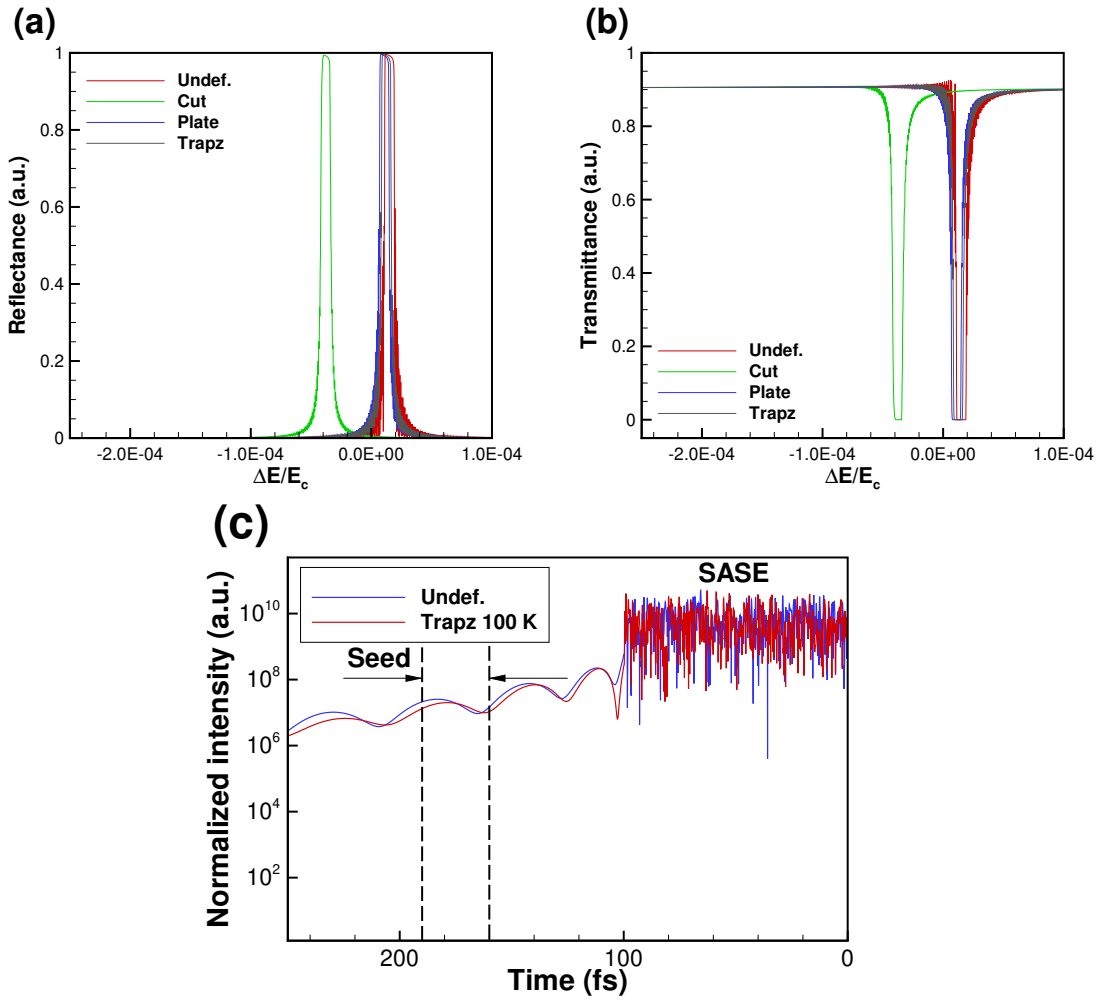

Figure 4.14: (a) Reflectance and (b) transmittance curves for three monochromators at 9.5 keV, 1 MHz and 100 K. The undeformed one is plotted using red line as reference. One typical transmitted pulse for cut monochromator is visualized in (c). The seed power is successfully preserved.

4.2.6 Seed quality & tuning

The seed central photon energy shift is plotted in Fig. 4.15. The left vertical axis shows the relative photon energy shift normalized by $E_c = 9.5\,\text{keV}$, while the right vertical axis is the corresponding tuning angle $\Delta\theta_{\text{tuning}}$ calculated by Eq. 4.2. In total, 10000 pulses of random spiky SASE are simulated. No significant change in both mean and standard deviation of the central energy shift was observed when further increasing the number of rounds. The central photon energy jittering of SASE is one RMS value of its bandwidth (about 3.6×10^{-4}). For seeding with undeformed crystal, this jittering lowers the seeding efficiency from about 6.5×10^{-4} to 4.3×10^{-4} due to the spectrum mismatch between SASE and rocking curve. The seed central photon energy also shows jittering behavior, which is visualized by the error bars in Fig. 4.15. The jittering is about 4.5×10^{-6}, or about one half to one third of the seed bandwidth. One case that stands out is the cut monochromator case

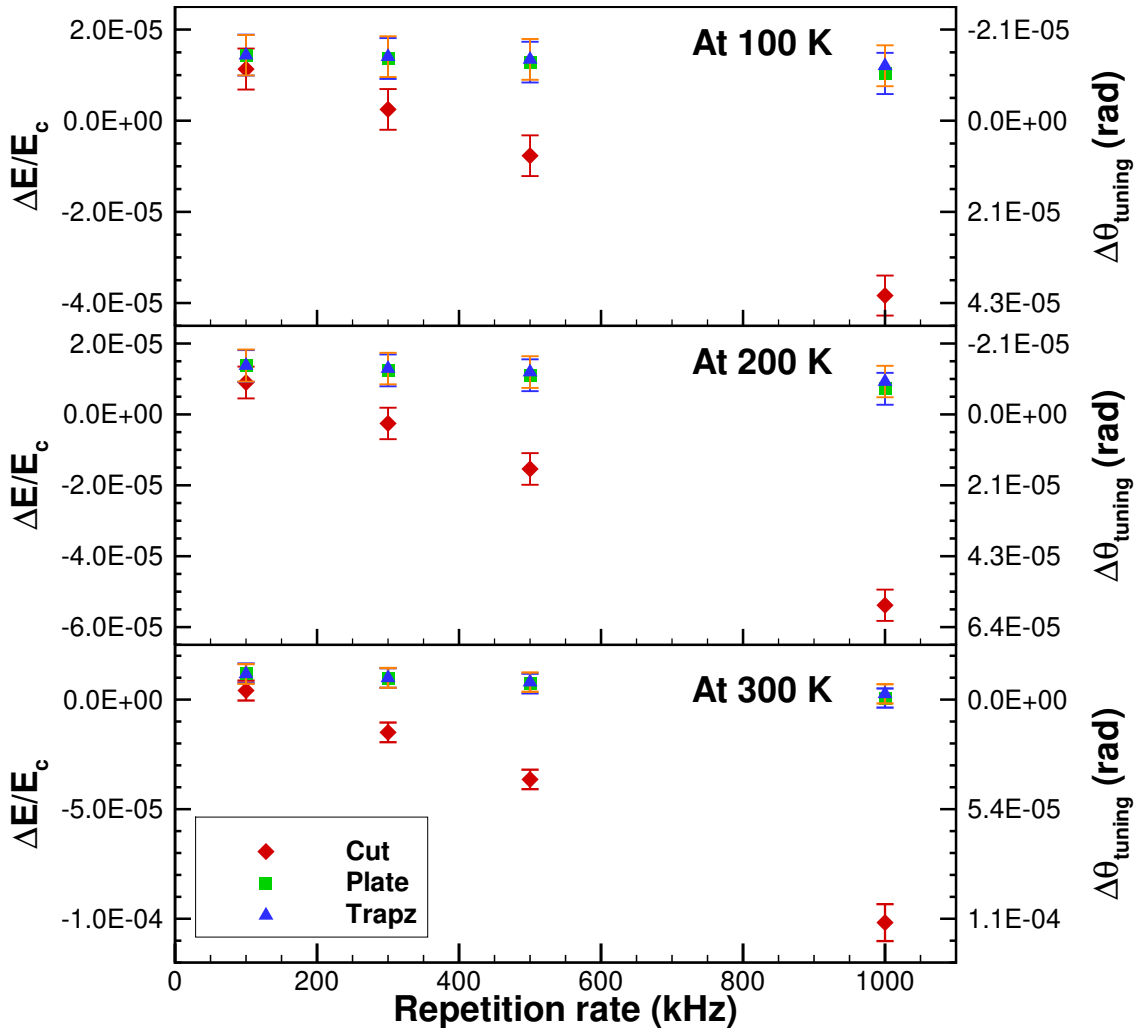

Figure 4.15: The central photon energy shift of the seed at 9.5 keV for different repetition rate and temperature. The parameters are given in Table 4.1. The error bar represents the standard deviation of central photon energy shift.

at 1 MHz and 300 K. The central photon energy jittering is twice of those in other cases, indicating that two modes with comparable amplitude are contained in the seed. The central photon energy shift of the seed for all cases follows the shift of the rocking curve, as expected. Considering the pitch angle and roll angle stability (10 μrad) of the crystal for LCLS [109] as an example, the energy shift is tunable. Minor difference (about 10^{-7} level) can be ignored compared to the seed bandwidth (about 10^{-5} level). Similar to the tuning in pulse train mode, re-orienting the crystal following the curve in Fig. 4.15 (right vertical axis) can maintain the central photon energy at 9.5 keV.

The seed power results are plotted in Fig. 4.16. The error bar is not displayed due to large fluctuation of the seeding efficiency. The large fluctuation of the seed power is due to the stochastic nature of the electron beam and SASE, but it could be overridden by thermal load in some cases. For example, the averaged seed power is reduced to lower than 50 kW at 1 MHz and 300 K. With even

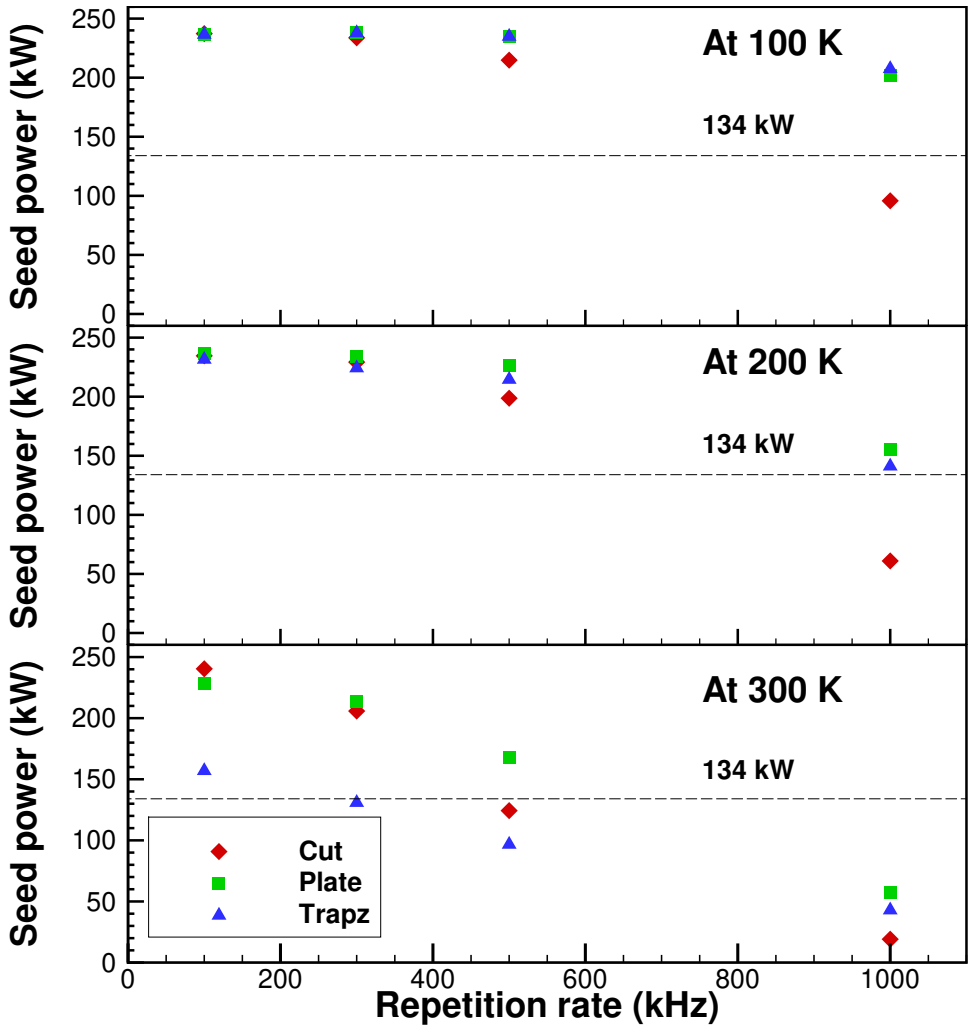

Figure 4.16: The seed power at 9.5 keV for different repetition rate and temperature. The parameters are given in Table 4.1. The black dashed line indicates the critical seed power determined by 100 times of shot noise.

100% error bar, it still cannot reach the critical level of 134 kW to dominate the shot noise. One counter-intuitive observation at this temperature is the performance of the trapezoidal monochromator. The seed power by trapezoidal monochromator remains at relatively low value at repetiton rate from 100 kHz to 1 MHz, even if it has much better thermal performance as shown in previous subsections. This phenomenon is caused by the thermal expansion of the thick base and transition part. Due to their large thickness, strong thermal stress is generated when heated. Non-uniform thermal stress is generated along x direction (Fig. 4.5) and leads to the bending of the thin tip. The bending results in the elastic strain gradient in the laser footprint. This is very similar to the clamping issue of the plate monochromator: when clamped, due to imperfection of the clamping surface, non-uniform strain is generated and propagate to the working area, affecting the seeding performance. Fortunately, this effect is significantly mitigated since heat conduction becomes much

more efficient in thick parts of trapezoidal monochromator at cryogenic temperature.

At cryogenic temperatures, the seed power of plate and trapezoidal monochromators does not show obvious reduction until at high repetition rates. At 200 K, the seed power is close to the criterion, while at 100 K it is well above the criterion. For cut monochromator, the inefficient thermal dissipation results in a large temperature increase within the footprint (close to room temperature), but its long thermal path also effectively mitigates the strain gradient within the footprint. This feature preserves the seed power at relatively low repetition rates but not high repetition rate, since the advantages of superior thermal properties vanishes as the temperature approaching room temperature.

Critical repetition rates at different temperature for different monochromator designed can then be determined by Fig. 4.16. A quantitative estimation is accessible once finer parametric sweeps are conducted.

4.3 Summary

In this chapter, we consider the thermal load effects in multi-pulse situations for self-seeded XFEL. In pulse train mode, the thermal load varies pulse-by-pulse, due to the accumulation of the residual heat. Accordingly, the seeding behavior is also dynamic, resulting in challenges for tuning as well as spectrum alignment in two stage self-seeding scheme. Furthermore, the quasi-steady monochromator performance in uniform pulse mode has also been investigated, with the stochastic characteristics of the input SASE and electron beam. We show the seed quality for different designs of monochromators at different environment temperatures. These seed quality curves are directly applicable for tuning the operation and can be potentially integrated into the feedback control system.

Chapter 5

Towards cryogenic operation: nondiffusive heat transfer

Operating the optics at cryogenic temperatures, as compared to room temperature, is expected to improve the resistance of the crystal optics to thermal load [118]. This is because of the thermal properties of the crystal becomes more favorable: 1) thermal diffusivity significantly increases and 2) thermal expansion coefficient significantly decreases. The former one indicates a superior capacity to dissipate heat, while the latter one suggests a much less severe strain and deformation. However, there are several potential issues that may cause discrepancy if unaware: 1) thermal conductivity reduction due to nondiffusive heat transfer; 2) size-dependent heat dissipation; 3) wave-like thermal transport behavior.

In this chapter, we explore the potential problems and solutions to these issues. To characterize the first two potential issues, we apply a simplified nondiffusive model, the two-parameter heat conduction model, while we propose another simplified model for wave-like thermal transport.

5.1 Background: failure of thermal diffusion model

Heat conduction traditionally is believed due to the random collisions and diffusion of particles. the kinetic and potential energy, jointly known as internal energy, is gradually dissipating and finally leading to thermodynamic equilibrium. This equilibrium process is characterized by the inhomogeneity of the energy distribution: larger difference in internal energy results in higher energy dissipation rate for two fixed locations in certain material. However, for different materials, the heat conduction rate also varies, even though the same difference exists in temperature, which is defined as a sign of internal energy. Notably, the first empirical relationship between the heat conduction rate in a material and the temperature gradient in the direction of energy flow is formulated by Jean Baptiste Joseph baron Fourier, who concluded that "the heat flux resulting from thermal conduction is negatively proportional to the magnitude of the temperature gradient and opposite to it in sign" [119]. Mathematically, it can be expressed as

$$\vec{q} = -\kappa \nabla T, \tag{5.1}$$

where $\vec{q}$ denotes the heat flux vector, T represents temperature, and κ is the proportionality constant, defined as the thermal conductivity of the material of interest. In this study, the bold font always denotes a vector quantity. This law, combined with energy conservation, offers solutions to most macroscopic heat conduction problems. Specifically, the thermal conductivity remains roughly a constant for given bulk materials within a certain range of temperature. By this definition, heat conduction is sometimes referred to as "heat diffusion" since it behaves just as mass diffusion.

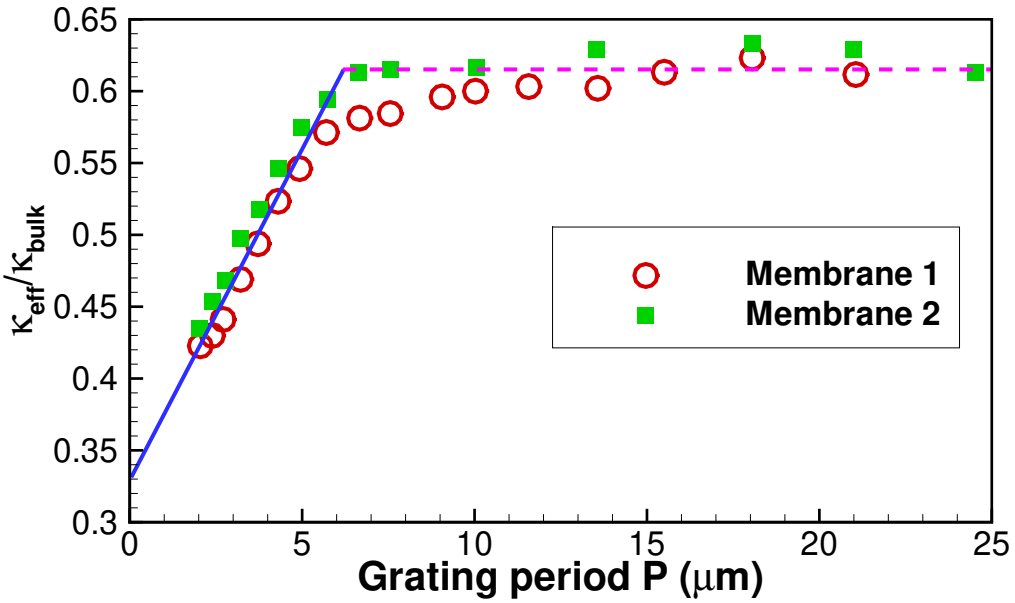

Figure 5.1: An illustrative figure of the size-dependent thermal conductivity found in the one-dimensional transient thermal grating experiments.

In macroscopy and at relatively high temperature (i.e., room temperature), the collisions between particles are intense and continuously taking place. One ideal case is to assume the collisions happen everywhere at any moment, which is the diffusive assumption. It is due to the validity of this diffusive assumption that the analysis through Fourier's law serves macroscopic engineering calculations and predictions with satisfactory precisions. Unfortunately, this assumption does not unconditionally hold. Discrepancies between Fourier's law predictions and experiments were found in the miniaturization technology. For example, as shown in Fig. 5.1, the measured effective thermal conductivity (ETC) shows dependence on the system characteristic length L_c (either the system size or thermal transport characteristic length) instead of remaining as a constant defined by Fourier's law. Moreover, when L_c approaches the phonon mean free path (MFP), which is defined as the free distance a phonon travels without collision, phonon transport is not diffusive anymore, or even becomes ballistic. The Knudsen number is defined to characterize the heat transport regime: $\mathrm{Kn} = \Lambda/L_c$, where Λ is the phonon MFP. When $\mathrm{Kn} \gg 1$, phonons travel ballistically with few collisions; while $\mathrm{Kn} \ll 1$, the diffusive assumption holds since phonons propagate diffusively, experiencing scattering at any moment. Between these two extreme cases, for example $\mathrm{Kn} \sim 1$, the size-dependent ETC can be obtained from measurements. Therefore, it is the decrease in collisions

intensity between the heat carriers that leads to the failure of the diffusive assumption, and finally results in the breakdown of Fourier's law. Fortunately, some simplified nondiffusive models are available to describe the thermal transport in this regime, such as the two-parameter heat conduction model.

5.2 Two-Parameter Heat Conduction model (TPHC)

The governing equation for this scale is Boltzmann transport equation (BTE), which requires the knowledge of phonon dispersion obtained either from experiment or first principle calculation. Moreover, solving the BTE is typically computationally expensive. We present a simplified nondiffusive model, the two-parameter heat conduction (TPHC) model, to capture the nondiffusive heat transfer characteristics. Integrated with this model, the nondiffusive heat transfer could potentially be included and more reliable estimation should be accessible.

5.2.1 Nondiffusive models

The traditional macroscale heat conduction model, Fourier's law, fails to describe thermal transport in meso/nanoscale [120–123]. This failure happens due to the invalidity of diffusive assumption in this scale, the key assumption on which Fourier's law is based. Physically, it happens when the characteristic thermal transport length in nanosystems is comparable to or even larger than the mean free path (MFP) of phonons (major heat carrier in dielectric materials) [124]. In these situations, nondiffusive heat transfer emerges, introducing new phenomena in this scale, such as size-dependent thermal conductivity [125] and interface resistivity [116, 126, 127].

To study nondiffusive heat transfer, nanothermometry techniques are developed. Among different nanothermometry techniques, time-domain thermoreflectance (TDTR) [116, 126, 127] and metallic grating probed by diffracted signal of soft X-ray [128, 129] are two experimental tools to capture the nondiffusive heat transfer phenomena. Unfortunately, these two experimental tools introduce thermal interface, which is also been shown to depend on the characteristic length of the system. To eliminate the impact from size-dependent thermal interface and study the nondiffusive effects inside the materials alone, a transient thermal grating (TTG) method was proposed [125, 130, 131]. It was found in TTG experiments that there is grating size-dependent heat transfer in silicon thin films at room temperature [125].

On the other hand, the modeling of nondiffusive heat transfer is also indispensable not only to extract the physics behind the nondiffusive phenomena observed in experiments, but also to analyze the experimental data. Physically, the phonon Boltzmann transport equation (BTE) can describe nondiffusive heat transfer, but it is computationally very expensive to apply [132]. Many other simplified nondiffusive models, including Cattaneo-Vernotte model [133, 134], Guyer-Krumhansl model [135], C and F process model [136], ballistic-diffusive model [137], two-channel model [138], were also proposed. Unfortunately, these nondiffusive models are still not widely used due to insufficient experimental justifications, and Fourier's law is still implemented in experimental data analysis and engineering design despite of the possibility that it may break down, which exposes the devices to the risk of thermal failure.

5.2.2 Two-Parameter Heat Conduction model

Recently, a two-parameter heat conduction (TPHC) model has been proposed by Ma [139], which has been successful in explaining TTG experiments [125] and TDTR experiments [114]. Based on this model, a nondimensional parameter is defined to characterize the applicability of Fourier's law. First, we briefly describe the TPHC model. A more detailed description of this model is given in Ma's paper [139]. The key concept of this model is the nonequilibrium absolute temperature β in nondiffusive heat transfer, defined as $\beta = E/c_v$. E here is internal energy and c_v is the volumetric specific heat. β is related to the equilibrium local temperature T through a relaxation process

$$\frac{\partial \beta}{\partial t} = -\frac{\beta - T}{\tau_B}, \tag{5.2}$$

where τB is the relaxation time. Meanwhile, this τB is also the characteristic time in ballistic heat transport.

With the definition of β, the three-dimensional (3D) TPHC model is given as [139, 140]

$$c_v \frac{\partial \beta}{\partial t} + \nabla \cdot \vec{q} = Q, \tag{5.3}$$

$$\vec{q} = -\kappa \nabla \beta + \frac{\Lambda_D \Lambda_B}{9} \left[\nabla^2 \vec{q} + 2\nabla \left(\nabla \cdot \vec{q} \right) \right], \tag{5.4}$$

where c_v is volumetric specific heat, κ is thermal conductivity. The parameter $\Lambda_B = c\tau_B$ in Eq. (5.4) is called nondiffusive phonon mean free path (MFP), where c is the speed of sound. Another characteristic length in Eq. (5.4) is diffusive phonon MFP $\Lambda_D = c\tau_D$, where τ_D is the diffusive phonon relaxation time. This τ_D, according to kinetic theory on diffusive heat conduction, is related to thermal conductivity $\kappa = c_v c^2 \tau_D/3$. Accordingly, $\Lambda_D = 3\kappa/c_v c$. Both Λ_D and Λ_B are assumed to be material properties that are independent of heat conditions. Thus, there are two independent parameters in Eq. (5.4): thermal conductivity κ and nondiffusive phonon MFP Λ_B, so this model is called two-parameter heat conduction (TPHC) model.

One simplified form assuming the heat flux is irrotational can be obtained by taking the divergence of both sides of Eq. (5.4) and plugging Eq. (5.3) in to yield

$$c_v \frac{\partial \beta}{\partial t} = \kappa \nabla^2 \beta + \frac{\Lambda_D \Lambda_B}{3} c_v \frac{\partial}{\partial t} \left(\nabla^2 \beta \right) + Q - \frac{\Lambda_D \Lambda_B}{3} \nabla^2 Q. \tag{5.5}$$

5.2.3 Nondimensional parameter ζ

The terms with coefficient $\Lambda_D \Lambda_B/3$ account for the nondiffusive effects. Therefore, an appropriate form of the nondimensional parameter that characterizes nondiffusive heat transfer can be expressed as

$$\zeta = \frac{\Lambda_D \Lambda_B}{3 L_c^2}, \tag{5.6}$$

where L_c is the characteristic length of the system of interest.

For very small ζ, the nondiffusive effects become negligible, and Fourier's law is applicable for thermal analysis. As system characteristic length L_c shrinks, ζ grows larger and the nondiffusive phenomena play increasingly important role in heat transfer. Up to the point where ζ becomes larger than the critical value, Fourier's law fails. This critical value should be according to the accuracy requirement from the projects. Here, we take $\zeta_c = 0.01$ as an example. Thus, the applicability of Fourier's law is evaluated by ζ.

This parameter is instructive for engineering projects where Fourier's law is commonly preferred due to its simplicity and integration in commercial softwares. A quick calculation on ζ can be performed to evaluate the applicability of Fourier's law before the possibly large-scale simulation is run. Based on the calculated ζ, we can determine whether the simulation is to run or the result is to be trusted. Specifically, in some cases, an effective thermal conductivity (ETC) can be estimated with ζ considered, as will be illustrated in the following part about the transient thermal grating (TTG).

5.2.4 1D transient thermal grating

In the TTG experiments conducted by Johnson et al. [125, 141, 142], there is spatially sinusoidal heating pattern (called thermal grating) in the in-plane (parallel to sample surface) direction on the sample material due to two concurrent interfering pulsed-lasers. This micro-sized thermal grating is adjustable in periodicity so that the change of temperature field resulted by the size-dependent heat transfer can be detected by a probe laser as diffracted signal. The sample used in TTG can be thin film of less than 1 μm thick, or substrate of several micrometers thick. In the thin film cases [125], the heat transfer is one-dimensional (1D); in the substrate cases [142], two-dimensional (2D) thermal transport has to be considered.

First, we reinterpret the 1D-TTG [125] study based on our previous study [139]. In this case, $\Lambda_B = 7.1$ μm has been fitted by Ma [139] for the 400-nm-thick silicon thin film. Another parameter $\Lambda_D = 26$ nm can be calculated according to the measured diffusive ETC $\kappa_{\text{diff}} = 92\,\text{Wm}^{-1}\text{K}^{-1}$. To calculate ζ using Eq. (5.6), the characteristic length (L_c) of 1D-TTG system is set to be the reciprocal of wavenumber $L_c = 1/\lambda = L/2\pi$, where L is the spatial period of the thermal grating. Thus, each ζ value corresponds to one grating period size. On the other hand, the size-dependent ETC in 1D-TTG can be calculated by assuming a solution which is periodic in space and exponentially decaying in time, for example $\beta = \beta_0 \exp(i\lambda x - \gamma t)$. γ here is the thermal decay rate. Hence, the ETC can be solved as

$$\kappa_{\text{eff}} = \frac{\kappa}{1 + \Lambda_D \Lambda_B \lambda^2/3} = \frac{\kappa}{1+\zeta}. \tag{5.7}$$

Based on this equation, Fig. 5.2 shows the dependence of $\kappa_{\text{eff}}/\kappa$ on ζ.

In Fig. 5.2, the results by the TPHC model agree with the experimental results very well. Stronger nondiffusive effects, characterized by a larger value of ζ, lead to a lower ETC according to Eq. (5.7). Similarly, when ζ is smaller than the critical value 0.01, negligible nondiffusive effects allow the validity of Fourier's law with an ETC adequately close to the diffusive thermal conductivity $\kappa_{\text{eff}} = 0.99\kappa_{\text{diff}}$. In addition, $L = 15.59$ μm can be calculated based on $\zeta_c = 0.01$ as the critical period for Fourier's law to be applicable in data analysis of this 1D-TTG experiment.

However, a discrepancy between measured diffusive thermal conductivity $\kappa_{\text{diff}} = 92\,\text{Wm}^{-1}\text{K}^{-1}$ for thin film here and bulk value $\kappa = 148\,\text{Wm}^{-1}\text{K}^{-1}$ may still be caused by the nondiffusive phe-

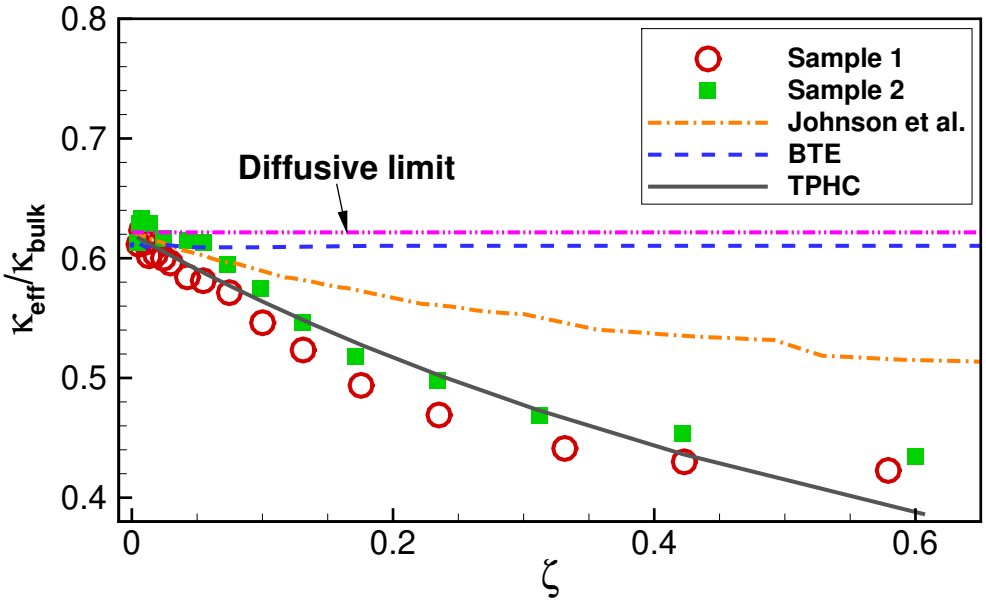

Figure 5.2: The size-dependent ETC changes with ζ calculated by Eq. (5.6). The diffusive ETC is measured [125] as $\kappa_{\text{diff}} = 92\,\text{Wm}^{-1}\text{K}^{-1}$ when $\zeta \to 0$ and plotted using violet line as a reference. The results based on a two-fluid model [125] and BTE [143] are also shown for comparison.

nomena. In other word, the "diffusive" here only denotes the vanishing of nondiffusive effects from in-plane thermal transport. The nondiffusive effects from the cross-plane (normal to the sample surface) direction is still likely to trigger the deviation of ETC from the bulk value, suggesting the need for a 2D extension of ζ.

5.2.5 2D transient thermal grating

To extend ζ into 2D, we study 2D-TTG cases. As introduced previously, 2D-TTG is very similar to 1D-TTG. In the experiment, a sample substrate, rather than a sample thin film, is heated by two concurrent interfering lasers. It then acquires a periodic thermal grating pattern in the in-plane direction. Different from 1D-TTG where the laser penetration is almost uniform, the temperature rises due to heating decays exponentially in the cross-plane direction due to finite laser penetration. The thermal decay of the sample is probed by another laser and the diffracted signal is obtained. To model the heating and thermal decay processes, we assume the laser heating process can be modeled as a source term in which is a Dirac delta function in time with spatial periodicity in the in-plane x direction and exponential decay in the cross-plane y direction can be introduced. Thus, the source term in Eq. (5.5) is given as

$$Q(t,x,y) = Q_0 \exp(i\lambda x - \beta_1 |y|)\,\delta(t), \tag{5.8}$$

where Q_0 is the amplitude, and β_1 is the absorption coefficient for the pump beam in the solid.

To obtain the analytical solution, we perform Fourier transform on both sides of Eq. (5.5)

with the source term given in Eq. (5.8), the solution in frequency domain can be written as follows:

$$\Delta\hat{\beta}\left(\eta,\xi_x,\xi_y\right)=\frac{\hat{Q}\left(\eta,\xi_x,\xi_y\right)}{ic_v\eta+\kappa_{\text{eff}}\left(\xi\right)\xi^2}, \tag{5.9}$$

where $\hat{Q}\left(\eta,\xi_x,\xi_y\right)$ corresponds to the source term $Q\left(t,x,y\right)$ in frequency domain, $\xi=\sqrt{\xi_x^2+\xi_y^2}$ is the magnitude of spatial frequency, and η accounts for temporal frequency. The ETC in Eq. (5.9) is expressed by

$$\kappa_{\text{eff}}\left(\xi\right)=\kappa/\left(1+\frac{\Lambda_B\Lambda_D}{3}\xi^2\right). \tag{5.10}$$

Minnich [144] stated that the optical signal $H\left(t,x\right)$ probed in 2D-TTG experiment is a weighted average of the temperature over cross-plane direction. Accordingly, the experimental signal can be calculated in frequency domain with Eq. (5.9), and inversely transformed back to time and space domain. The final solution can be formulated as

$$H\left(t,x\right)=A\exp\left(i\lambda x\right)\int_0^\infty\frac{\exp\left[-\kappa(\xi)\xi^2t/c_v\right]}{\left(\beta_1^2+\xi_y^2\right)\left(\beta_2^2+\xi_y^2\right)}d\xi_y, \tag{5.11}$$

where A is a constant amplitude, $\xi=\sqrt{\lambda^2+\xi_y^2}$, and β_2 is the absorption coefficient of the probe laser. For detailed derivation please check our other studies [145, 146]. The integral in Eq. (5.11) can be obtained by standard numerical integration techniques.

According to Eqs. (5.10) and (5.11), the ETC $\kappa\left(\xi\right)$ cannot be explicitly formulated as in 1D-TTG. Minnich reported similar results [144]. In Eq. (5.11), the multiexponential behavior leads to seemingly anisotropy in ETC under the framework of Fourier's law, indicating the breakdown of Fourier's law since the solution is no more unique.

Although the explicit ETC does not exist in 2D-TTG, the nondiffusive effects are still able to be characterized by ζ if the characteristic length in the cross-plane direction is considered. The characteristic length in x direction is still $1/\lambda$ due to the sinusoidal heating, while the characteristic length in y direction can be the penetration depth (β_1^{-1}) of the heating laser. Thus, ζ can be written as

$$\zeta=\zeta_x+\zeta_y=\frac{\Lambda_D\Lambda_B}{3L_{c,x}^2}+\frac{\Lambda_D\Lambda_B}{3L_{c,y}^2}=\frac{\Lambda_D\Lambda_B}{3\left(L/2\pi\right)^2}+\frac{\Lambda_D\Lambda_B}{3\left(1/\beta_1\right)^2}. \tag{5.12}$$

Here, the overall characteristic length is $L_c^{-2}=L_{c,x}^{-2}+L_{c,y}^{-2}$.

Eq. (5.12) includes the nondiffusive effects from both in-plane direction and cross-plane direction. This may explain the ETC in 1D-TTG as well. Instead of the penetration depth of the pump laser in 2D-TTG, the thickness of the thin film is the appropriate $L_{c,y}$, which is 400 nm [125]. Plug it into Eq. (5.12) to obtain $\zeta=\zeta_x+\zeta_y=\zeta_y=0.618$ for diffusive cases (large grating period) and bulk thermal conductivity $\kappa=148\,\text{Wm}^{-1}\text{K}^{-1}$. Accordingly, $\kappa_{\text{eff}}=\kappa/\left(1+\zeta\right)=91.45\,\text{Wm}^{-1}\text{K}^{-1}$, which is very close to the measured diffusive ETC $\kappa_{\text{diff}}=92\,\text{Wm}^{-1}\text{K}^{-1}$ for the thin film.

To characterize the nondiffusive effects in 2D-TTG, we compare the signal calculated by Eq. (5.11) and other results (Fig. 5.3). Fig. 5.3(a) shows the comparison with experimental results

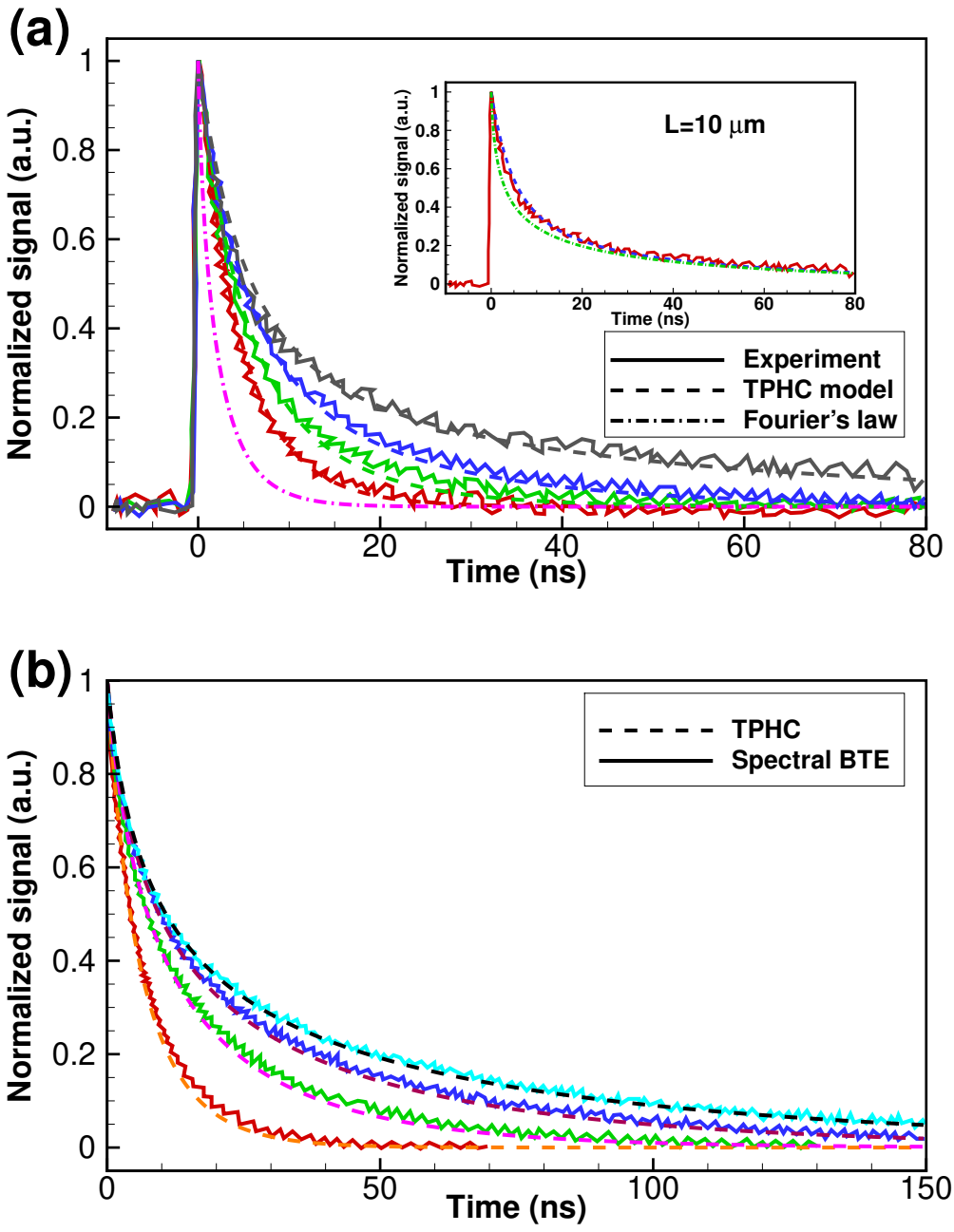

Figure 5.3: Comparison between the normalized signal calculated by TPHC model using Eq. (5.11) and (a) experimental results by Johnson et al. [142] on GaAs sample (ζ = 3.73, 3.35, 3.20, 3.11, corresponding to L = 2.05 μm, 3.2 μm, 4.9 μm and 10 μm, respectively, from low to high); (b) theoretical results obtained calculated using full-spectral Boltzmann transport equation by Minnich [144] on silicon (ζ=0.41, 0.33, 0.31, 0.30, corresponding to L = 5.75 μm, 10.5 μm, 15.25 μm and 20 μm, respectively, from low to high).

by Johnson et al. on GaAs substrate. The material properties can be found in our previous work [139]. In this figure, a small window specifically highlights the comparison among the results for $L = 10\,\mu\text{m}$ obtained by experiments, the TPHC model and Fourier's law, where the TPHC model matches the experiment well while Fourier's law deviates from both. Here, the nondiffusive effects are still significant and cause Fourier's law to fail despite $\zeta_x = 0.0274$ indicating weak nondiffusive effects from the in-plane direction. These effects mainly come from the cross-plane direction since $\zeta_y = 2.71$ ($\beta_1 = \beta_2 = 160\,\text{nm}^{-1}$), further suggesting the observation of nondiffusive heat transfer for even larger grating periods. On the other hand, for smallest grating period $L = 2.05\,\mu\text{m}$, Fourier's law severely overpredicts the thermal decay rate due to the nondiffusive effects from both in-plane and cross-plane direction.

Similar trend is observed in Fig. 5.3(b) that displays the BTE results by Minnich [144] with phonon dispersion calculated from *ab initio* simulation. This consistency with BTE results further validates the TPHC model as well as ζ. However, in this case, the nondiffusive heat transfer is still found even for the largest grating period $L = 20\,\mu\text{m}$ based on the calculation of $\zeta = 0.30$ using Eq. (5.12) with $\Lambda_B = 7.1\,\mu\text{m}$, $\Lambda_D = 41.8\,\text{nm}$, as reported by Minnich using an anisotropic ETC $\kappa_x = 0.85\kappa$ and $\kappa_y = 0.73\kappa$.

To show the effect of ζ in full range from nondiffusive region to diffusive limit, we consider an artificial 2D-TTG case on sapphire, as shown in Fig. 5.4. The 2D-TTG experiment on sapphire has not been reported so far, possibly due to the transparency of sapphire. However, the metallic grating similar to 2D-TTG was reported by Siemens et al. [128] and has been studied in our other work [147, 148], where material properties of sapphire can be found, including $\Lambda_D = 4.24\,\text{nm}$ and $\Lambda_B = 1.6\,\mu\text{m}$. Although the transparency of sapphire leaves the penetration depth undetermined, it implies a very large penetration depth (i.e. $\gg 0.5\,\mu\text{m}$). Here, we take $\beta_1 = \beta_2 = \beta = 0.5\,\mu\text{m}$.

To quantify this difference, we applied a simple definition to describe how different two curves are. We use Eq. 5.13 to calculate the average difference δ between two curves.

$$\delta = \frac{1}{n}\sum_{k=1}^{n}\left|1 - \frac{H_F(t_k, x=0)}{H_T(t_k, x=0)}\right|, \tag{5.13}$$

where the subscript F represents Fourier's law, T represents the TPHC model. Ideally, this average difference δ is 0 if two curves are identical. However, it is approaching 0 if the tails of two calculated signals are considered. Consequently, we choose a criteria 0.01. That is, we only consider part of the curve where the signal is larger than 0.01 and use this segment to calculate the average difference. On the other hand, this difference also depends on the number of discretized time steps selected for calculation, or equivalently, resolution. We have already tested different resolutions to assure that the result is independent of resolution.

The result of this parametric study is shown in Fig. 5.4(b). In a wide range of optical depth, the average difference δ remains unchanged for all four cases, indicating that in this given range, optical depth is not an important factor for nondiffusive heat transfer. However, this depth weighs more when it approaches the size of grating period, and results in the increase of δ. This increase marks nondiffusive behavior, suggesting that optical depth could be a representative length in cross-plane direction characterizing nondiffusive heat transfer. We will conduct further study in the future.

Similar prediction can also be applied on the time-domain thermoreflectance (TDTR) experiments, where the characteristic length is the radius of the heating laser. For example, in Al/Si system [114], $\Lambda_D = 41.8\,\text{nm}$ and $\Lambda_B = 7.1\,\mu\text{m}$. By setting $\zeta = 0.01$, we can calculate the critical

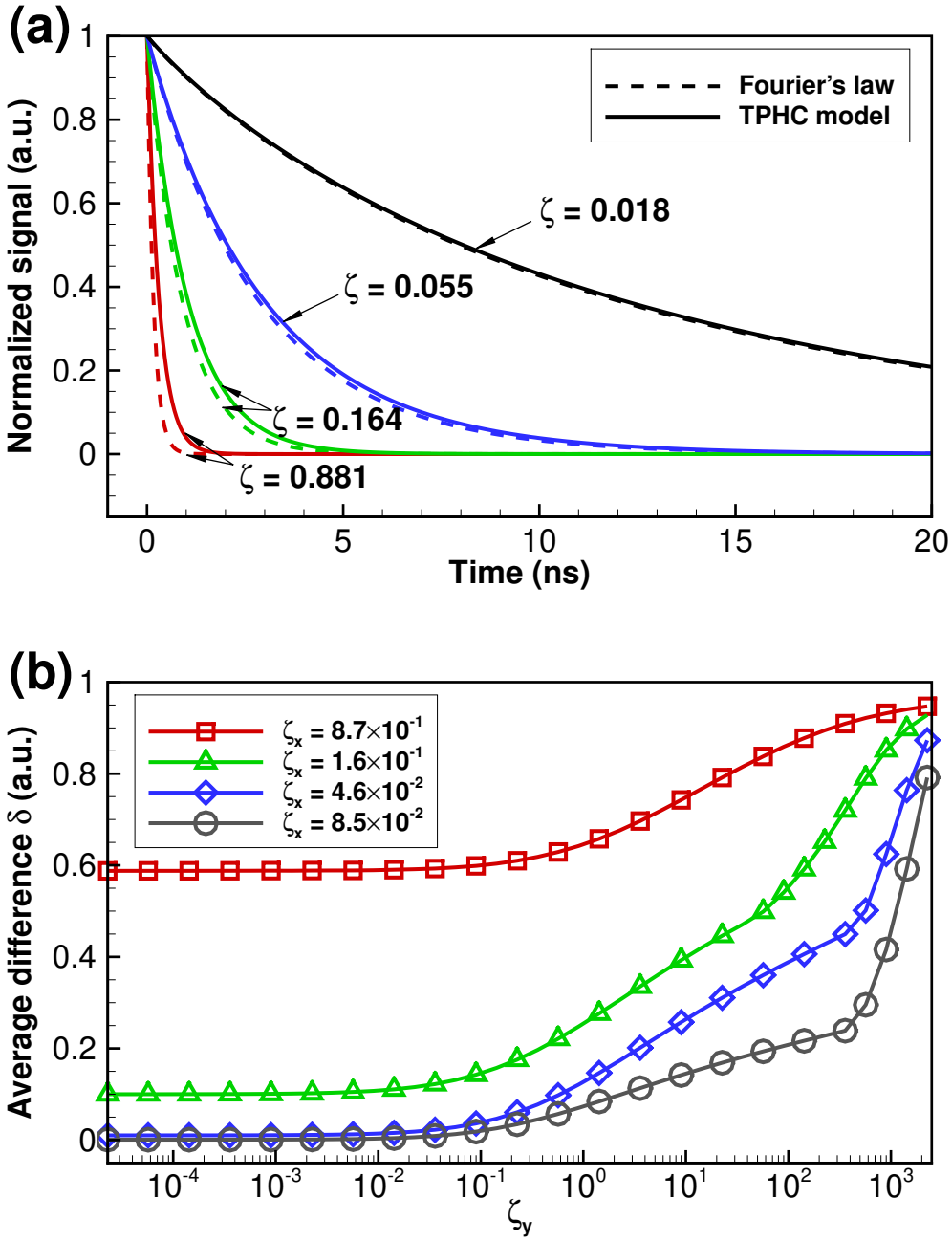

Figure 5.4: (a) Comparison between the 2D-TTG signals calculated by TPHC model and Fourier's law on sapphire (ζ = 0.881, 0.164, 0.055, 0.018, corresponding to L = 0.32 μm, 0.76 μm, 1.4 μm and 3.24 μm, respectively, from low to high). (b) The average difference δ between the result by Fourier's law and TPHC model, calculated using Eq. 5.13. Both ζ_x and ζ_y components introduce nondiffusive effects.

diameter of the heating laser $D = 6.29\,\mu m$. Comparable value of the critical pump laser diameter has been reported by solving the BTE [115], where the ETC starts to deviate from the value obtained by using very large pump laser diameter. However, it is challenging, though desirable, to validate this criterion with experimental observation, since the interface conductance also contributes to the size-dependent thermal transport.

5.2.6 Conclusions

In conclusion, the nondimensional parameter ζ is capable of capturing the breakdown of Fourier's law. By introducing both in-plane direction and cross-plane direction components, ζ can handle multidimensional situations. Based on this parameter, once a criterion is appropriately selected according to requirements (like 0.01 in sapphire 2D-TTG case), the applicability of Fourier's law can be examined, offering information in model selection in an engineering design process.

5.3 Wave-like thermal transport

Another unusual thermal transport in small scales or cryogenic temperature is the wave-like thermal transport behavior. Phenomenologically, a temperature pulse is generated at one end of a crystal at cryogenic temperature, and it could be detected also as a temperature pulse on the other side of the crystal. Its contribution to thermal load release is still unknown but worth further investigation. Here, we derive a simplified model to describe this phenomenon.

5.3.1 History of thermal waves

The development of nanotechnologies for microelectronics and thermoelectric devices raises significant research interests in micro/nanoscale heat transfer [121–123], especially for insulators and semiconductors. In these materials, phonons are the dominant energy carriers for thermal transport processes. The phonon transport behavior in macroscale is diffusive and can be captured by Fourier's law, the traditional heat conduction model. However, in micro/nanoscale, Fourier's law is found to break down in many studies [115, 128, 142] due to the emerging nondiffusive heat transfer phenomena that challenge the diffusive assumption. The nondiffusive heat transfer not only exposes the incomplete understanding of heat transfer physics, but also leads to practical issues in engineering fields, such as the thermal management of electronics [149].

Some earliest considerations of nondiffusive heat transfer trace back to the work by Tisza [150] and by Landau [151]. Inspired by these studies, Peshkov reported experimental observations of wave-like transport of heat in liquid Helium II [152]. The wave-like transport was termed by Landau as "second sound". Later, to resolve the infinite propagating speed of temperature in Fourier's law, Cattaneo [133] and Vernotte [134] proposed the model known as Maxwell-Cattaneo-Vernotte (MCV) model. The MCV model essentially introduces a hyperbolic generalization that impose a finite material-dependent propagating speed. This model, also known as hyperbolic heat equation, stimulated the experimental exploration of second sound. However, the experimental attempts to observe the second sound in crystals were not successful until the appropriate window condition was specified by Guyer and Krumhansl [135]. When window condition is satisfied, wave-like transport, or thermal waves, has been observed experimentally in crystalline helium He_4 [153], sodium fluorid [154–156], bismuth [157], sodium iodide and lithium fluoride [155] at low temperatures

(below around 15 K). In these experiments, three transport regimes have been identified: (1) ballistic regime (2) diffusive regime and (3) transitional regime. In ballistic regime, clear temperature pulses can be observed, indicating the direct evidence of ballistic heat transfer. In diffusive regime, Fourier's law becomes valid since the diffusive approximation is satisfied. In transitional regime, second sound, a unique phenomenon, can be identified.

Since the experimental discovery of wave-like heat transfer, various theoretical models were proposed to understand the thermal waves. One category of these models are thermodynamics based and can be classified as extended thermodynamics or N-field-theory [158]. The extended thermodynamics can qualitatively reproduce the heat pulse experimental results [158]. The MCV model and Guyer-Krumhansl (GK) model are compatible with extended thermodynamics. However, the extended thermodynamics fails to obtain correct phase velocity of ballistic phonons, which should be Debye velocity, unless more than 30 variables are used [158]. This drawback results in heavy computational load. Also, there is no easy physical interpretation of high order variables and parameters in this type of theory. Further developments incorporating entropy inequality and non-equilibrium thermodynamics lead to many nondiffusive models [159]. Under this framework, in addition to MCV model and GK model, other models like Jeffreys-type model [160], are also shown as special cases. Jeffreys-type model gains its name because the kernel is analogous to the stress and strain rate model in liquids proposed by Jeffreys. Jeffreyss-type model decomposes the thermal conductivity into two parts: the effective thermal conductivity and elastic conductivity. Another interesting theory by Green and Naghdi [161] is based on the definition of a unique internal variable, the thermal displacement rate. Their theory indicates the existence of a heat conduction without dissipation. Other models, such as the second viscosity by Rogers [162] and hybrid phonon gas model [163] introduce complex viscosity without straightforward physical meanings. The theory of non-equilibrium thermodynamics by Kovács and Ván [164] is able to quantitatively reproduce the heat pulse experiments results. However, in general, large number of parameters in these models do not yield easy and clear physical interpretations.

In recent years, nondiffusive heat transfer are also found in micro/nanostructure experiments at room temperature. Many researchers believe that the nondiffusive heat transfer arising in micro/nanoscale is caused by the ballistic heat transfer, because phonons tend to travel ballistically without scattering when the system size is comparable or smaller than the phonon mean free paths (MFPs). This idea gives rise to many Boltzmann transport equation (BTE) based nondiffusive models [139, 165]. Some of them categorize phonons into two groups: the ballistic phonons and diffusive phonons [137, 138, 166]. However, there has been no report on the reproduction of heat pulse experiments using these models. In addition, many of these models, such as Ballistic-diffusive model [137], two-channel model [138], dual phase lag model [167] actually still apply the concept of thermal conductivity for ballistic photons. In the case of additional ballistic heat transfer, the thermal transport should become more efficient, as the energy carried by phonons can directly be transported to other locations. This consideration intuitively leads to a higher effective thermal conductivity. Unfortunately, the experimentally measured effective thermal conductivity was often found decreasing with the system size. On the other hand, no clear study has either explicitly related the nondiffusive heat transfer to the ballistic heat transfer or reported a direct observation of ballistic heat transfer at room temperature.

To further understand the nondiffusive heat transfer and provide some simple but clear insights, we still focus on the thermal waves at cryogenic temperatures from a wave propagation perspective by using a simple wave-diffusive model. In this model, the phonons are categorized

into two groups: the low frequency ballistic phonons with strong wave-like behavior, and the high frequency diffusive phonons with Fourier-like behavior. For ballistic phonons, a wave equation is employed and the concept of thermal conductivity is total removed. For diffusive phonons, the parabolic heat conduction of Fourier's law is still in use due to its advantages over hyperbolic-type of heat equation [159]. Compared to the non-equalibrium thermodynamics based models, only two parameters with clear physical meanings are involved in this simple model, while a quantitative reproduction of thermal waves experiments can be successfully achieved. In this study, we first derive the wave-diffusive model, then compare the results from this wave-diffusive model against the published experimental signals. The good agreement in the comparison confirms the validity of this model and indicates the possibility to understand the nondiffusive heat transfer phenomena at room temperature from new perspectives.

5.3.2 Wave-diffusive model

In this section, without the loss of generality, we first derive the one-dimensional (1D) form of wave-diffusive model for thermal wave experiments. In thermal wave experiments, the heat transfer can be approximated as 1D [168]. However, a three-dimensional (3D) form can be obtained similarly.

The schematic of thermal wave experiments is shown in Fig. 5.5. In thermal wave experiments, the sample is a high-purity cubic crystal. The high purity is critical to minimize the resistive scatterings due to imperfections such as substitutional defect. The side length and thickness of the crystal are usually several millimeters. On one sample surface, a thin zig-zag shape Manganin heater is evaporated on one face of the sample. This heater generates a pulse heating with duration of sub-microsecond. On the opposing face of the sample, a lead detector is evaporated [155] to record the temperature change of the other surface. It is expected that, if the ballistic phonons can be preserved during the propagation, a pulse signal of similar shape should be captured on the detector side.

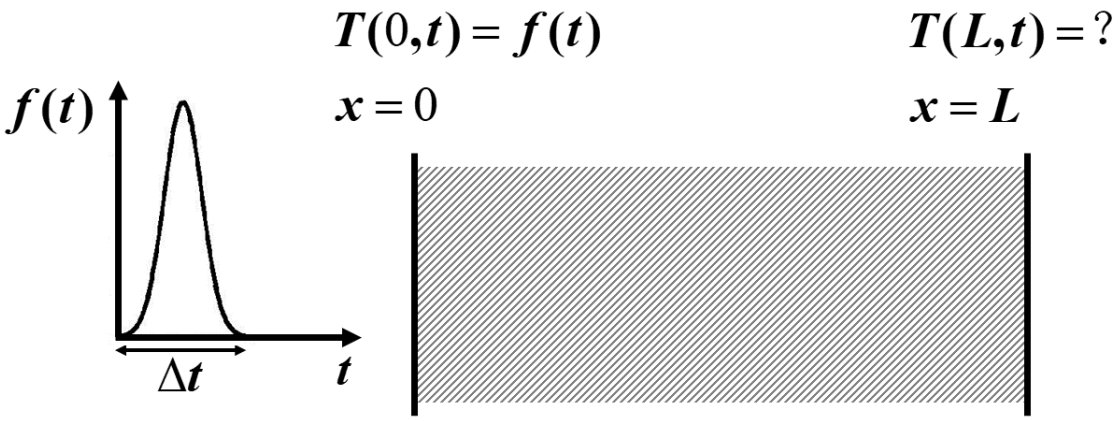

Figure 5.5: Schematic of the physical situation of the thermal wave experiments. The heater is evaporated on one surface of the high-purity crystal sample to generate a pulse heating input, while the detector is evaporated on the opposing surface of the sample to record the temperature change.

5.3.2.1 Governing equation

For this 1D situation, we start with the energy conservation equation without source term

$$\frac{\partial E}{\partial t} + \frac{\partial q}{\partial x} = 0. \tag{5.14}$$

We assume that the energy can be divided into two parts carried by two categories of phonons: the ballistic phonons and diffusive phonons

$$E = E^b + E^d, \tag{5.15}$$

where the superscript b and d refer to ballistic and diffusive, respectively. Similarly, the energy flux can also be divided into two categories as

$$q = q^b + q^d. \tag{5.16}$$

We can now rewrite the governing equation Eq. (5.14)

$$\begin{cases} \frac{\partial E^b}{\partial t} + \frac{\partial q^b}{\partial x} = -\Delta E' \\ \frac{\partial E^d}{\partial t} + \frac{\partial q^d}{\partial x} = \Delta E' \end{cases}, \tag{5.17}$$

where the source term $\Delta E'$ represents the energy conversion between the ballistic and diffusive components.

For ballistic part we have

$$q^b = cE^b, \tag{5.18}$$

where c refers to ballistic phonon phase velocity.

On the other hand, for diffusive part, the Fourier's law can be written as

$$q^d = -\kappa \frac{\partial T}{\partial x} = -\frac{\kappa}{c_v} \frac{\partial E^d}{\partial x}, \tag{5.19}$$

where κ is thermal conductivity and c_v is volumetric specific heat. These two thermal properties are assumed not space-dependent in this case.

Substituting Eqs. (5.18) and (5.19) into Eq. (5.17) yields the governing equation

$$\begin{cases} \frac{\partial E^b}{\partial t} + c\frac{\partial E^b}{\partial x} = -\Delta E' \\ \frac{\partial E^d}{\partial t} - \frac{\kappa}{c_v}\frac{\partial^2 E^d}{\partial x^2} = \Delta E' \end{cases}, \tag{5.20}$$

The upper equation for ballistic heat transfer component in Eq. (5.20) indicates wave behaviors of energy transport when compared to 1D general wave equation, which is

$$u_t + cu_x = \alpha u_{xx} + \beta u_{xxx}. \tag{5.21}$$

We can solve this wave equation by conducting Fourier decomposition

$$u(x,t) = A\exp(at)\exp(ikx). \tag{5.22}$$

Substituting Eq. (5.22) into Eq. (5.21) yields

$$a = -\left(c+\beta k^2\right)(ik) - \alpha k^2. \tag{5.23}$$

Therefore, the general solution of the wave equation takes the form of

$$u(x,t) = A\exp\left(-\alpha k^2 t\right)\exp\left\{ik\left[x-\left(c+\beta k^2\right)t\right]\right\}. \tag{5.24}$$

Applying this solution to ballistic heat transfer part in Eq. (5.20) without dispersion ($\beta = 0$), we get damping wave solutions

$$E^b(x,t) = A\exp\left(-\alpha k^2 t\right)\exp\left[ik(x-ct)\right]. \tag{5.25}$$

A damping relaxation time, τ_w, can accordingly be defined as

$$\tau_w = 1/\alpha k^2. \tag{5.26}$$

This relaxation time quantifies the energy conversion rate from the wave component to diffusive component. It is a measure of the resultant relaxation time, in which all different scattering mechanisms are involved. For example, following the hybrid phonon gas (HPG) model by Ma [168], it can be written as

$$\frac{1}{\tau_w} = \frac{1}{3\tau_N} + \frac{5}{6\tau_R}, \tag{5.27}$$

where τ_R and τ_N are relaxation time for R-process and N-process, respectively. In this study, we keep τ_w as a free parameters to avoid the complication to deal with different scattering mechanisms, which is out of the scope here.

For input heating with waveform $E^b(0,t) = f(t)$, the solution is

$$E^b(x,t) = f(t-x/c)\exp\left(-\alpha k^2 t\right). \tag{5.28}$$

The damping of ballistic phonons is due to the interactions with diffusive phonons that convert the ballistic phonons to diffusive phonons. To quantify this energy conversion rate $\Delta E'$, we take derivative of energy carried by ballistic phonon in Eq. (5.28), i.e.,

$$\frac{\partial E^b(x,t)}{\partial t} = f'\left(t-\frac{x}{c}\right)\exp\left(-\alpha k^2 t\right) - \frac{E^b(x,t)}{\tau_w}, \tag{5.29}$$

$$\frac{\partial E^b(x,t)}{\partial x} = -\frac{1}{c}f'\left(t-\frac{x}{c}\right)\exp\left(-\alpha k^2 t\right). \tag{5.30}$$

Obviously, the solution can satisfy the governing equation (5.20) with $\beta = 0$. From Eqs. (5.29) and

(5.30), the quantity of energy conversion rate is

$$\Delta E' = \frac{E^b(x,t)}{\tau_w}. \tag{5.31}$$

Consequently, the governing equation Eq. (5.20) can be rewritten as

$$\begin{cases} \frac{\partial E^b}{\partial t} + c\frac{\partial E^b}{\partial x} = -\frac{E^b(x,t)}{\tau_w} \\ \frac{\partial E^d}{\partial t} - \frac{\kappa}{c_v}\frac{\partial^2 E^d}{\partial x^2} = \frac{E^b(x,t)}{\tau_w} \end{cases}. \tag{5.32}$$

This is the governing equation for the wave-diffusive model in heat pulse situations. If thermal conductivity is known as in most experimental cases, the only free parameter is the relaxation time for wave component τ_w. However, one may realize that a clean analytical form of wave component may not always be accessible.

5.3.2.2 Initial & boundary conditions

For boundary condition of ballistic heat transfer at $x = 0$, we can either specify pulsed E^b or $q^b = cE^b$, both will give the same solution. Here, we assume a Gaussian pulse

$$E^b(0,t) = f(t) = \exp\left[-\left(\frac{t-t_c}{\sqrt{2}\sigma_t}\right)^2\right]. \tag{5.33}$$

For diffusive component, two boundary conditions are needed. On both the heater and detector sides, the boundary is considered as a thermal interface due to the energy loss from the sample to the detector: at heater side $x = 0$, we specify

$$q^d = h\left(E^d_\infty - E^d|_{x=0}\right)/c_v, \tag{5.34}$$

while at detector side $x = L$, we specify

$$q^d = h\left(E^d|_{x=L} - E^d_\infty\right)/c_v. \tag{5.35}$$

The interface conductance h of this thermal interface has no interference with the major physical features of the thermal wave signals [145].

During heating process, we assume that when phonons are initially excited, they are all ballistic since they have not participated in any scattering event associated with propagation. Similar assumption was also implemented in the extended thermodynamics [158]. Therefore, only ballistic phonons are excited at the boundary $x = 0$. This assumption equivalently defines the initial condition ($E^d = 0$ everywhere) for the diffusive heat transfer. As time evolves, the energy carried by ballistic phonons will be gradually transferred to diffusive phonons through phonon-phonon interactions. Eventually, we will find that heat can be dissipated through both side of the crystal.

5.3.2.3 Numerical method

When solving wave-diffusive model in thermal wave experiments, we normalize the variables using the form of $\phi^* = \phi/\phi_0$, where ϕ is general variable and phi_0 is the reference value for nor-

malization. In thermal wave experiments, we select the crystal size L as the length scale, L/c as the time scale. Accordingly, the governing equation can be writen as

$$\frac{\partial E^{d*}}{\partial t^*} - \kappa^* \frac{\partial^2 E^{d*}}{\partial x^{*2}} = \frac{E^{b*}}{\tau_w^*}, \tag{5.36}$$

where E^b can be obtain by Eq. (5.28), and $\kappa^* = \kappa/c_v cL$ is nondimensional thermal conductivity. Accordingly, the normalized initial condition is

$$E^{d*} = 0, \tag{5.37}$$

and boundary conditions are

$$\frac{\partial E^{d*}}{\partial x^*}|_{x^*=0} = -\frac{hL}{\kappa}\left(E_\infty^{d*} - E^{d*}|_{x^*=0}\right), \tag{5.38}$$

$$\frac{\partial E^{d*}}{\partial x^*}|_{x^*=1} = -\frac{hL}{\kappa}\left(E^{d*}|_{x^*=1} - E_\infty^{d*}\right). \tag{5.39}$$

The normalized governing equation with initial and boundary condition, Eqs. (5.36)-(5.38), is then solved by simple finite difference method. A central difference scheme is used for spatial derivative, and Crank-Nicolson scheme is used for time evolution. Accordingly, the discretized governing equation and auxiliary conditions are given as

$$\begin{aligned} E_j^{d*,n+1} - E_j^{d*,n} =& \frac{\kappa^* \Delta t^*}{2\Delta x^{*2}}\left(E_{j+1}^{d*,n+1} - 2E_j^{d*,n+1} + E_{j-1}^{d*,n+1}\right) \\ &+ \frac{\kappa^* \Delta t^*}{2\Delta x^{*2}}\left(E_{j+1}^{d*,n} - 2E_j^{d*,n} + E_{j-1}^{d*,n}\right) \\ &+ \frac{1}{\tau_w^*}\frac{E_j^{b*,n+1} + E_j^{b*,n}}{2}\Delta t^*, \end{aligned} \tag{5.40}$$

$$\begin{aligned} E_2^{d*,n+1} - E_1^{d*,n+1} + E_2^{d*,n} - E_1^{d*,n} \\ = -\frac{hL\Delta x^*}{\kappa}\left(2E_\infty^{d*} - E_1^{d*,n+1} - E_1^{d*,n}\right), \end{aligned} \tag{5.41}$$

$$\begin{aligned} E_J^{d*,n+1} - E_{J-1}^{d*,n+1} + E_J^{d*,n} - E_{J-1}^{d*,n} \\ = -\frac{hL\Delta x^*}{\kappa}\left(E_J^{d*,n+1} + E_J^{d*,n} - 2E_\infty^{d*}\right), \end{aligned} \tag{5.42}$$

$$E_j^{d*,1} = 0, \tag{5.43}$$

where J is the total number of grid in the domain, n and j are time and space step indices, respectively. The discretized equation can then be easily solved using a band solver. The results for all cases are checked and confirmed grid-independent.

5.3.3 Results

Before comparing the numerical results with the experiments, we briefly state the material properties. The specific heat of NaF crystal is obtained through literature [169]

$$c_v = 234 N_A k_B \left(T/\Theta_D\right)^3, \tag{5.44}$$

where N_A is Avogadro constant, k_B is Boltzmann constant, $\Theta_D = 466\,\mathrm{K}$ is Debye temperature. The density of NaF is $2866\,\mathrm{kg/m^3}$ [164]. The longitudinal wave speed ($c_l = 6051\,\mathrm{m/s}$) and transverse wave speed ($c_t = 3186\,\mathrm{m/s}$) are also specified in literatures [154, 156]. The thermal conductivity, which the key parameter, is obtained from the corresponding studies as will be shown later. We assume that thermal conductivity is the same for both longitudinal and transverse modes, though different polarization modes should have different scattering mechanisms and thus different thermal conductivity. Since in most cases the two polarization peaks are well separated, the relaxation time τ_w can be fitted individually from the corresponding peak. Here, we compare and discuss the results in the three regimes as specified in the introduction section: ballistic regime, diffusive regime and transitional regime.

5.3.3.1 Ballistic regime

Typically, when the environmental temperature is lower than 10 K, strong ballistic transport can be observed in NaF crystal of relatively high purity. Figure 5.6 shows a comparison between the experimental results at 9.6 K by Jackson et al. [154] and wave-diffusive results. Different from diffusive heat transfer, the temperature signal recorded by the detector clearly depicts two separate peaks corresponding to two polarization modes of phonons: longitudinal and transverse. Excellent agreement can be observed in the comparison between the experimental results and our simulation results.

There is certain delay time (roughly $0.2\,\mu\mathrm{s}$) for the heating pulse peak. The delay can be calculated from the arrival time of the peaks in experiment. The delay time remains the same for both polarization modes. The heating pulse duration (FHWM) is fitted as $0.25\,\mu\mathrm{s}$ from this ballistic transport case. This value, as indicated by McNelly et al. [155], falls into the range of 0.1 to $1.0\,\mu\mathrm{s}$ in practical experiments. The arrival time of these two separate peaks coincides with the theoretical arrival time for the two polarized waves in the sample. The waveforms of these two separated peaks also suggest minor dissipation during propagation, indicating that the scattering effect is weak at this temperature in the bulk sample. The fitted τ_{wl} is $1.25\,\mu\mathrm{s}$ for longitudinal mode and τ_{wt} is $4.51\,\mu\mathrm{s}$ for transverse mode based on the measured thermal conductivity of $8857.93\,\mathrm{Wm^{-1}K^{-1}}$ (curve B of Fig. 3 in Ref. [156]). One reference relaxation time $\tau_R = 1.56\,\mu\mathrm{s}$ reported by Ma [168] is comparable to our fitted τ_w. This value is calculated based on the assumption that boundary scattering (due to the Casimir limit [170]) is dominant over the scatterings in the bulk. In this regime, the result is not very sensitive to τ_w.

5.3.3.2 Diffusive regime

When the temperature is high enough (i.e., 25.5 K), the diffusive transport dominates the heat transfer and first sound peak is quickly dissipated. Rogers et al. [162], on the other hand, reported the thermal wave experiment results close to the other limit: diffusive transport. They provided not

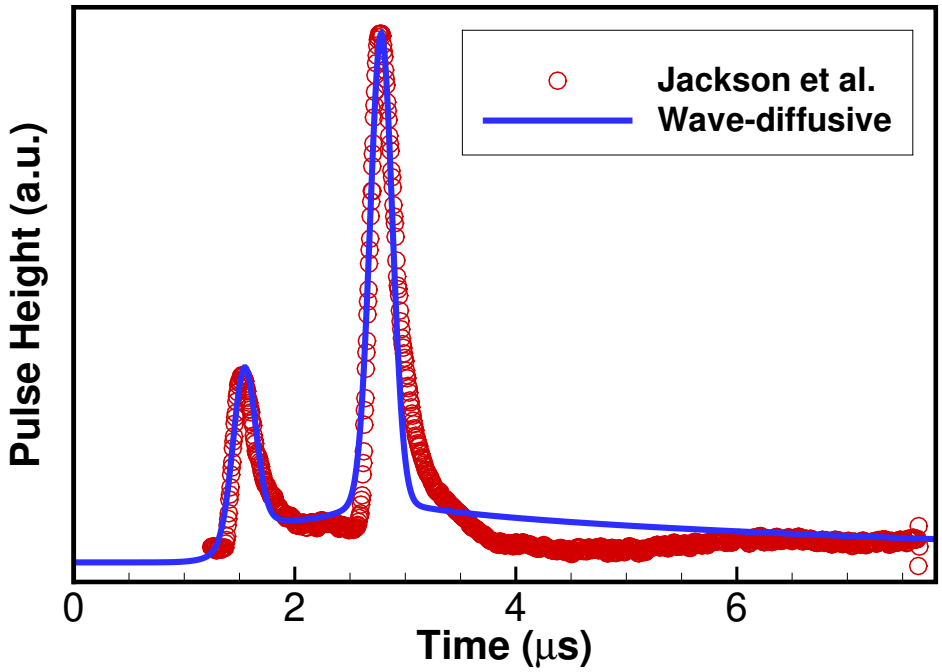

Figure 5.6: Thermal wave signals at 9.6 K in ballistic transfer regime by Jackson et al. [154] (solid line) and wave-diffusive model (dashed line). The sample size in the thermal wave propagation direction is 8.3 mm.

only the experimental data but also a computational model for simulating the thermal wave. The two results are both plotted in Fig. 5.7, along with the thermal wave calculated from the wave-diffusive model.

The wave-diffusive model also predicts a correct trend of the thermal wave in diffusive regime. In this diffusive case, a thermal conductivity of 3536.99 $\mathrm{Wm^{-1}K^{-1}}$ can be directly extracted by from the curve in Fig. 11 of the work by Rogers et al. [162] with linear interpolation. The extracted relaxation time is $\tau_{wl} = 0.027\,\mu\mathrm{s}$ for longitudinal mode and $\tau_{wt} = 0.096\,\mu\mathrm{s}$ for transverse mode. However, here, one may notice that both numerical results almost exceed the upper noise bound at the tail. Actually, Ma [168] reported similar trend of the tail behavior. This minor discrepancy is most possibly due to the energy loss through the interface between the sample and the detector. The detector receives and absorbs a small amount of energy, equivalently cooling down the backside of the sample cube. In the ballistic case, such cooling effect is secondary because of the short duration time (less than 10 μs) monitored. However, as the duration of the experiment observation increases, this cooling effect introduces differences. To qualitatively capture this and better model the practical situation, minor heat loss (non-zero interface conductance h) is assumed at the detector side surface, to physically reproduce the heat transfer through the interface to the detector. An order-of-magnitude estimation yields an average interface conductance $h = 6 \times 10^5\ \mathrm{Wm^{-2}K^{-1}}$ considering typical heat pulse experiment parameters [155]: heating pulse average power of 150 W,

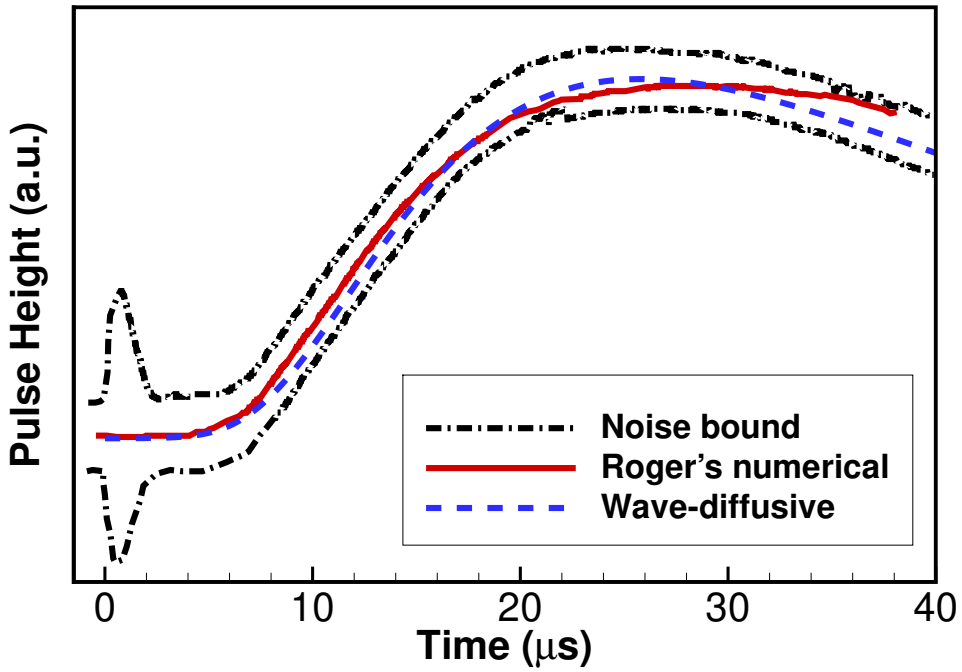

Figure 5.7: Thermal wave signals in diffusive transfer regime by Rogers et al. [162] from experiments (dashed-dot lines) and his model (dashed line), and the wave-diffusive model (solid line). The sample size in the thermal wave propagation direction is 4.3 mm.

duration of 1 μs, repetition rate of 1 kHz, sample cross-section of 5 mm × 5 mm and average temperature rise of 0.01 K.

5.3.3.3 Transition between the ballistic and diffusive thermal transport

When the temperature falls between the ballistic and diffusive limit, a transition of waveform takes place, as observed by McNelly et al. [155] and Jackson and Walker [156]. The results are shown in Fig. 5.8. The signal amplitude is normalized. McNelly et al. pointed out that, it is not meaningful to compare the pulse amplitudes for different traces, because the amplifier gain was increased with increasing temperature.

At different environmental temperatures, thermal wave propagation behaves differently. A smooth transition from the ballistic heat transfer to the diffusive heat transfer can be observed as the environmental temperature increases. At 7.8 K for this NaF sample, ballistic transport is captured as two clear separate peaks with little dissipation, like the signal in Fig. 5.6. At around 11 K to 12 K, the diffusive component emerges, causing the broadening of the temperature pulses, though the ballistic component can still be observed as two peaks with the same arrival time. This implies that the transport is not purely ballistic since more and more phonons are delayed possibly due to the collision or scattering of multiple kinds. Nevertheless, the intensity of scattering is still not high enough to justify the diffusive assumption for all phonons. Consequently, both ballistic

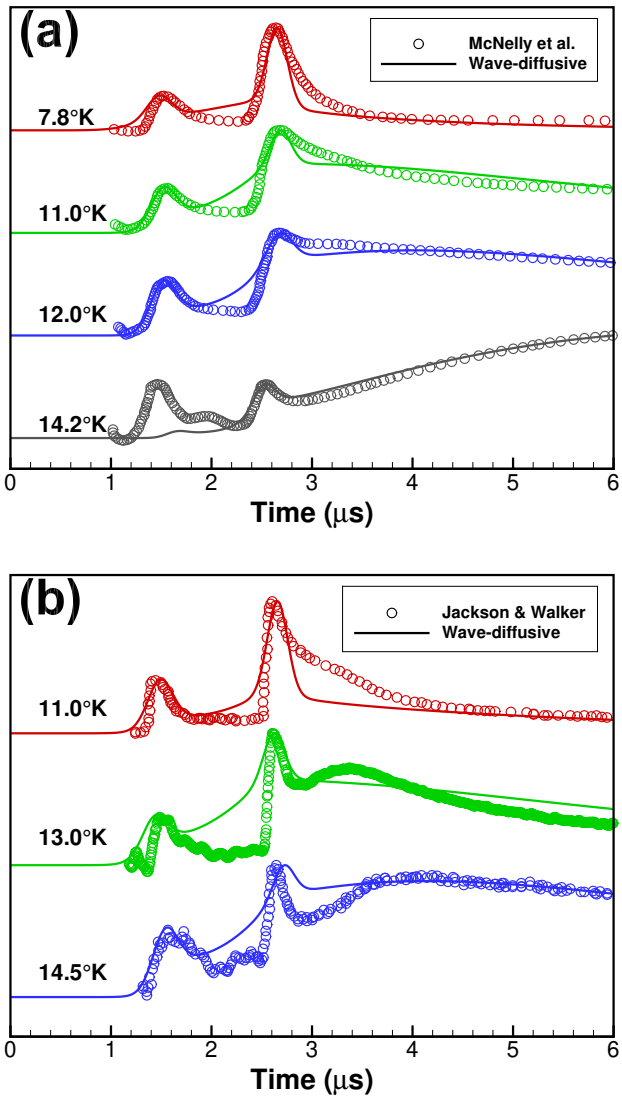

Figure 5.8: Thermal wave signals in transitional regime by (a) McNelly et al. [155] and (b) Jackson and Walker [156] at different environmental temperature. The circle represents the experimental signal, and solid line shows the result by wave-diffusive model. The sample size in the thermal wave propagation direction is (a) 7.8 mm and (b) 7.9 mm.

Table 5.1: Measured thermal conductivity and extracted τ_w for different experimental cases and the corresponding thermal transport regime.

Experiment	Temperature	Long. τ_{wl}	Trans. τ_{wt}	Therm. cond. κ	Regime
Ref. [154]	9.6 K	1.25 µs	4.51 µs	8858 $Wm^{-1}K^{-1}$	Ballistic
Ref. [155]	7.8 K	0.52 µs	0.75 µs	5267 $Wm^{-1}K^{-1}$	Ballistic
Ref. [155]	11.0 K	0.46 µs	0.47 µs	6981 $Wm^{-1}K^{-1}$	Transitional
Ref. [155]	12.0 K	0.38 µs	0.46 µs	7000 $Wm^{-1}K^{-1}$	Transitional
Ref. [155]	14.2 K	0.21 µs	0.38 µs	6320 $Wm^{-1}K^{-1}$	Diffusive
Ref. [156]	11.0 K	0.71 µs	0.93 µs	9124 $Wm^{-1}K^{-1}$	Ballistic
Ref. [156]	13.0 K	0.46 µs	0.57 µs	13032 $Wm^{-1}K^{-1}$	Transitional
Ref. [156]	14.5 K	0.45 µs	0.48 µs	14561 $Wm^{-1}K^{-1}$	Transitional
Ref. [162]	25.5 K	0.027 µs	0.096 µs	3537 $Wm^{-1}K^{-1}$	Diffusive

and diffusive transport contribute to the heat transfer in this transitional regime. Additionally, in this regime, another new and interesting feature, the second sound, can be observed as the third peak in the signal. The second sound is believed to exist when the momentum-conserving phonon collisions (N-processes) becomes significant compared to the momentum-destroying collisions (R-process). Hence, the phonons travel collectively as a temperature pulse, known as second sound, with varying speed depending on the scattering intensity. Mathematically, in wave-diffusive model, strong N-process triggers an efficient conversion of energy from the ballistic component to the diffusive component, as indicated by Eq. (5.26). This effect does introduce a diffusive-like tail due to the energy conversion.

The extracted parameters are summarized in Table 5.1. The thermal conductivity for each case is found in the corresponding studies.

5.4 Discussions

In existing experiments, the transition between ballistic propagation and diffusive propagation was observed by tuning the environmental temperature. Effectively, the relaxation time for scattering also varies, and different transport regimes can be reached. However, according to the wave-diffusive model, this transition is also expected to happen inside the crystal sample, even at high temperature. In other words, the ballistic propagation should still be observable within certain distance from the heater in diffusive regime. Based on the ballistic component solution given by Eq. (5.28), a characteristic length L_c similar to the "penetration" length of the ballistic phonons can be defined as

$$L_c = -\ln(0.01)\frac{c}{\tau_w}. \tag{5.45}$$

This L_c indicates the propagation distance at which the ballistic component decays to 1% of its original value. A different factor can also be selected depending on the requirements to replace the factor, $-\ln(0.01)$, in Eq. (5.45). An example calculation for this 14.5 K case yields a characteristic length of 9 mm, as compared to the actual sample size of 7.9 mm. This suggests that, a diffusive-like signal can be captured if the sample size increase to 9 mm. The corresponding time scale t_0 for

normalization is given by

$$t_0 = \frac{L_c}{c} = -\ln(0.01)\tau_w. \tag{5.46}$$

With the estimated propagation characteristic length and time, we study the full propagation process in a virtual crystal sample. This virtual crystal sample shares the same properties as the one shown in the bottom curve of Fig. 5.8(b) at 14.5 K, but its size is 12.47 mm instead of 7.9 mm using longitudinal speed. The propagation process is visualized by the temperature rise profiles at different selected moments in Fig. 5.9(a) and the history of temperature rise signal at different locations in Fig. 5.9(b). In Fig. 5.9, the input heat pulse decays in amplitude as propagating, while leaves a diffusive tail on its path. The decay behavior is exponential, as suggested by Eq. (5.28). The decayed signal vanishes at the other end of the domain when normalized length is 1, indicating the validity of the length window provided by Eq. (5.45). The diffusive tail in the signal is resulted by the dissipated energy from ballistic component. On the other hand, the signal taken at different locations also indicates a transition process within the virtual crystal sample. At normalized length of 0.1, the longitudinal peak and transverse peak cannot be distinguished due to the width of the heating pulse. But they are separated after normalized length of 0.2. At normalized length of 1, the signal becomes very flat and two first sound peaks can barely be recognized. The direct comparison of signals at different locations also suggest that, even if the normalized signal in diffusive regime seems significant, but it should be small in amplitude when compared to the ballistic component.

On the other hand, in this study, unfortunately, different scattering mechanisms are not well accounted due to the simplification. This is probably the reason why second sound cannot be well described here. The purity of the crystal applied in the experiment is sufficiently high so that different scattering mechanisms are necessary to be considered. If so, the simplified relaxation time assumption fails. In fact, the attempt to distinguish different scattering mechanisms and to extract relaxation time for specific scattering has been made for many years. However, no well recognized method has been reported. For example, the N-process mean free path in NaF at low temperature can be extracted by thermal conductivity data [156] and by direct analysis of heat pulse experiment [162], but the two methods fail to converge with about 10 fold difference between them. Moreover, in high temperature cases, the phonon dispersion relation should also be considered to replace simplified gray assumption.

5.4.1 Conclusions

We proposed a simple wave-diffusive model to provide new perspectives for nondiffusive heat transfer phenomena. We used this model to interpret the thermal wave experiments at cryogenic temperatures. The thermal wave signals in all three transport regimes, namely ballistic regime, transitional regime and diffusive regime, have been successfully reproduced. The relaxation time of wave component τ_w offers meaningful insights for the explanation of the transition mechanisms between different transport regimes. The wave and diffusive component dominates the thermal transport in ballistic and diffusive regime respectively, while the energy conversion characterized by τ_w enables a successful reconstruction of the phenomena in the transitional regime. The wave-diffusive model is therefore proved applicable for thermal wave experiments at cryogenic temperatures, where the wave-like behavior of thermal transport is significant. This study suggests the possibility to characterize the ballistic transfer regime from the perspective of waves, showing its

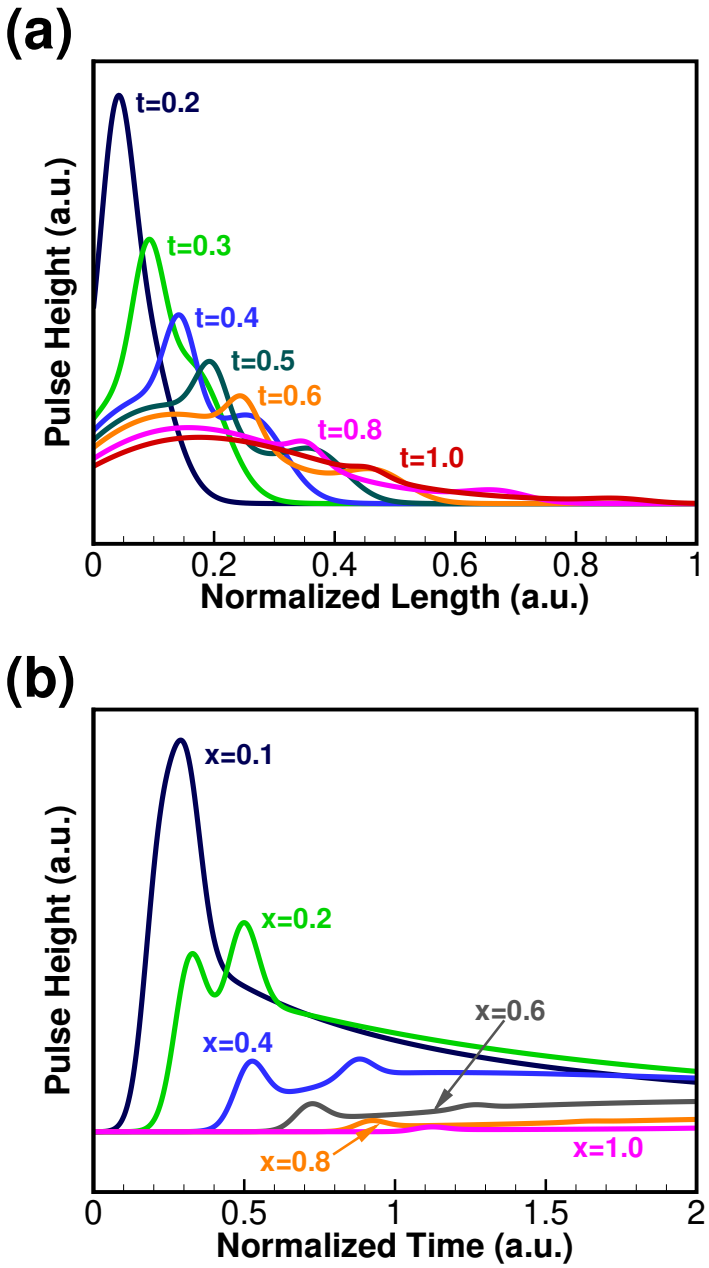

Figure 5.9: (a) The profiles at different moments and (b) the history at different locations inside the sample with same properties of the sample in Fig. 5.8(b). The crystal length is 12.47 mm, the environmental temperature is 14.5 K, thermal conductivity is 14561 $\mathrm{Wm^{-1}K^{-1}}$ and $\tau_{wl} = 0.45\,\mu\mathrm{s}$ for longitudinal mode and $\tau_{wt} = 0.48\,\mu\mathrm{s}$. The length is normalized by L_c given in Eq. (5.45), and time is normalized by t_0 given in Eq. (5.46).

potential to provide new insights for nondiffusive heat transfer experiments above cryogenic temperatures and even at room temperature.

5.5 Summary

In sum, we consider the nondiffusive heat transfer phenomena at cryogenic temperature. We employ simplified nondiffusive heat transfer model to investigate the impacts due to the failure of traditional diffusive assumption. However, due to the complexity of the diamond thin film and lack of existing data, the experimental work is still needed to validate the results by nondiffusive models and evaluate the practical performance of the optics at that temperature.

Chapter 6

Summary and Future Work

6.1 Concluding Remarks

Thermal load is an important issue limiting performance of the optics for high-brightness high-repetition-rate X-ray free-electron laser. Due to the extreme high photon flux with low beam divergence, severe power density induces highly localized non-uniform thermal deformation and strain in the optics, especially crystal monochromators. As identified in chapter 1, the overall objective of this dissertation is to characterize the thermal load effects on crystal optics performance at high repetition rate, and provide general design principle for the optics and operation conditions.

Accordingly, after analyzing all relevant physical processes, an analytical model was developed to qualitatively and semi-quantitatively understand how thermal load results in the distortion of the crystal response under Bragg condition. Based on the analytical model, different factors were decomposed and general design directions were listed. The results indicate that, the thermal distortion of the rocking curves consists of two effects: 1) the tunable central photon energy shift due to the overall temperature increase and 2) the untunable rocking curve distortion due to the strain gradient within the footprint.

More realistic numerical simulation were performed for different situations based on the coupled photo-thermal-mechanical simulation tool developed in this study. In pump-probe situations, the dominant component is the untunable part. Depending on SASE parameters, strong distortion of rocking curves due to thermal load was observed. For transmissive monochromator for self-seeding applications, the thermally induced strain field results in severe reduction of the seed power, even to the extent that the seed cannot dominate the shot noise and self-seeding fails. For beamline multi-bounce monochromator, similar distortion was also observed, but it leads to a peak intensity suppression for the output photon beam. This is because of the spectrum mismatch between different crystal surface, implying the existence of similar issue in multi-stage Bragg diffraction systems. In addition, the wavefront of the output beam was also distorted by the thermal bump. The wavefront distortion, or transverse coherence degradation, introduces additional error for applications such as coherent X-ray diffractive imaging and X-ray holography. The footprint shape and location deviate from design status, as observed both experimentally and numerically. Fringes appear, indicating the interference within the photon beam and complicating the data analysis on the user side. All these effects were characterized through the developed photo-thermal-mechanical simulation tool.

Further investigations were performed for multi-pulse situations, where the thermal load was

accumulating pulse-by-pulse until a quasi-steady state depending on system configuration. Both tunable component and untunable component of thermal load contribute to the changes of the crystal rocking curve. For pulse train mode, the thermal load varies pulse-by-pulse, or dynamically, so that the tuning should be accordingly dynamic to enable the minimization of thermal load effects. In multi-stage system where multiple crystal monochromator were considered, the dynamic thermal load could result in the spectrum mismatch issues, if the thermal load on each crystal is unequal for each pulse. In uniform pulse situation where a quasi-steady state will finally be reached, the tuning guideline is also provided and the critical operating parameters can be determined according to the selected criteria. Different geometric design of the monochromator were studied and compared with realistic random incident SASE pulses. The results suggest that cryogenic cooling is necessary at high repetition rate for all designed monochromators. At present, frontier research on hard X-ray self-seeding project in SLAC national accelerator laboratory is on-going and experiments have been scheduled.

At cryogenic temperatures where new challenge by nondiffusive heat transfer may emerge, potential tools were also prepared and preliminary explorations were conducted. Based on two-parameter heat conduction (TPHC) model, a nondimensional criterion was selected to provide quick identification on the necessity of applying nondiffusive thermal transport models. In more extreme cases where ballistic heat transfer can be observed, a simplified wave-diffusive model was proposed to model the transport process. In addition to tackling the potential challenge that X-ray optics may be faced with at cryogenic temperature, the wave-diffusive model also offers more insights for fundamentals of thermal transport from new perspectives.

6.2 Future Work

Based on the results and understanding provided by this dissertation, one most important and planned study in the near future is the experimental characterization of crystal behavior under thermal load. This includes the design of cryo-cooling system for self-seeding crystal monochromator at high brightness and high repetition rate, and the validation for the simulation package developed in this dissertation. In addition, more possible directions have been open for future work. We here address some aspects of future study.

6.2.1 Feedback control based on thermal load

As indicated in this dissertation, the central photon energy shift can be compensated through re-orienting the monochromator. In current practical operation, the tuning process is still mostly achieved by manual control. This poses significant difficulty on tuning processes at dynamic situations (pulse train mode) or multi-crystal cases (XFELO). When properties of the incident photon beam are measured from upstream diagnostic devices, the thermal load can be determined by simulation and the tuning parameters can be fed into the control system to automatically re-orienting the crystal. This can lead to significant simplifications on the control and tuning for many applications.

6.2.2 Ring heater for thermal load gradient compensation

One major challenge in mitigating thermal load is mitigating the thermally induced strain gradient. As described by the analytical model, this part cannot be compensated by re-orienting the

crystal. Although cooling is an effective and promising solution for applications that working at quasi-steady state, it does not work for situations where the crystal has very limited time to relax. In this case, one very challenging but possible solution is the implementation of a ring heater (such as a ring shape infrared laser) synchronized with the incident pulse. In this way, the thermal power distribution becomes even on the crystal surface and the gradient effects can be strongly suppressed.

6.2.3 Surface morphology detection

In the study for beamline monochromator, the footprint and wavefront are distorted by the thermal bump on crystal surface. The output beam is still to some extent coherent but distorted. In fact, the actual shape information has been "mapped" in the output beam. With recent development of the wavefront sensor, it becomes possible to detect extremely small and fine structures or fast dynamics with XFEL.

Bibliography

[1] M. Hart, L. Berman, X-ray optics for synchrotron radiation: Perfect crystals, mirrors and multilayers, Acta Crystallographica Section A: Foundations of Crystallography 54 (6) (1998) 850–858. doi:10.1107/S0108767398011283.

[2] M. R. Howells, Some fundamentals of cooled mirrors for synchrotron radiation beam lines, Optical Engineering 35 (4). doi:10.1117/1.600607.

[3] C. S. Rogers, D. M. Mills, W. K. Lee, P. B. Fernandez, T. Graber, Experimental results with cryogenically cooled thin silicon crystal x-ray monochromators on high heat flux beamlines, in: High Heat Flux Engineering III, Vol. 2855, International Society for Optics and Photonics, 1996, pp. 170–179. doi:10.1117/12.259830.

[4] T. L. Bergman, F. P. Incropera, D. P. DeWitt, A. S. Lavine, Fundamentals of Heat and Mass Transfer, John Wiley & Sons, 2011.

[5] E. Seddon, J. Clarke, D. Dunning, C. Masciovecchio, C. Milne, F. Parmigiani, D. Rugg, J. Spence, N. Thompson, K. Ueda, et al., Short-wavelength free-electron laser sources and science: a review, Reports on Progress in Physics 80 (11) (2017) 115901.

[6] J. Amann, W. Berg, V. Blank, F.-J. Decker, Y. Ding, P. Emma, Y. Feng, J. Frisch, D. Fritz, J. Hastings, Z. Huang, J. Krzywinski, R. Lindberg, H. Loos, A. Lutman, H.-D. Nuhn, D. Ratner, J. Rzepiela, D. Shu, Y. Shvyd'ko, S. Spampinati, S. Stoupin, S. Terentyev, E. Trakhtenberg, D. Walz, J. Welch, J. Wu, A. Zholents, D. Zhu, Demonstration of self-seeding in a hard x-ray free-electron laser, Nature Photonics 6 (10) (2012) 693–698. doi:10.1038/nphoton.2012.180.

[7] Free-electron laser, page Version ID: 923932611 (Oct. 2019).

[8] C. Pellegrini, A. Marinelli, S. Reiche, The physics of x-ray free-electron lasers, Reviews of Modern Physics 88 (1) (2016) 015006. doi:10.1103/RevModPhys.88.015006.

[9] R. Bonifacio, C. Pellegrini, L. M. Narducci, Collective instabilities and high-gain regime in a free electron laser, Optics Communications 50 (6) (1984) 373–378. doi:10.1016/0030-4018(84)90105-6.

[10] C. Pellegrini, The history of x-ray free-electron lasers, The European Physical Journal H 37 (5) (2012) 659–708. doi:10.1140/epjh/e2012-20064-5.

[11] C. Feng, H.-X. Deng, Review of fully coherent free-electron lasers, Nuclear Science and Techniques 29 (11) (2018) 160. doi:10.1007/s41365-018-0490-1.

[12] G. Geloni, V. Kocharyan, E. Saldin, A novel self-seeding scheme for hard X-ray FELs, Journal of Modern Optics 58 (16) (2011) 1391–1403. doi:10.1080/09500340.2011.586473.

[13] G. Geloni, V. Kocharyan, E. Saldin, Production of transform-limited x-ray pulses through self-seeding at the european x-ray fel, arXiv:1109.5112 [physics]ArXiv: 1109.5112.

[14] S. Liu, W. Decking, V. Kocharyan, E. Saldin, S. Serkez, R. Shayduk, H. Sinn, G. Geloni, Preparing for high-repetition rate hard x-ray self-seeding at the european x-ray free electron laser: Challenges and opportunities, Physical Review Accelerators and Beams 22 (6) (2019) 060704.

[15] Y. V. Shvyd'ko, S. Stoupin, A. Cunsolo, A. H. Said, X. Huang, High-reflectivity high-resolution x-ray crystal optics with diamonds, Nature Physics 6 (3) (2010) 196–199. doi:10.1038/nphys1506.

[16] K.-J. Kim, et al., An Oscillator Configuration for Full Realization of Hard X-ray Free Electron Laser, in: Proceedings, 7th International Particle Accelerator Conference (IPAC 2016): Busan, Korea, May 8-13, 2016, 2016, p. MOPOW039. doi:10.18429/JACoW-IPAC2016-MOPOW039.

[17] W. H. Bragg, W. L. Bragg, The reflection of x-rays by crystals, Proceedings of the Royal Society of London. Series A, Containing Papers of a Mathematical and Physical Character 88 (605) (1913) 428–438. doi:10.1098/rspa.1913.0040.

[18] Bragg condition for the constructive interference of waves, https://www.didaktik.physik.uni-muenchen.de/elektronenbahnen/index.php.

[19] C. G. Darwin, Xxxiv. the theory of x-ray reflexion, The London, Edinburgh, and Dublin Philosophical Magazine and Journal of Science 27 (158) (1914) 315–333.

[20] P. P. Ewald, Zur begründung der kristalloptik, Annalen der Physik 359 (23) (1917) 519–556.

[21] M. v. Laue, Die dynamische theorie der röntgenstrahlinterferenzen in neuer form, in: Ergebnisse der exakten naturwissenschaften, Springer, 1931, pp. 133–158.

[22] W. H. Zachariasen, E. L. Hill, The theory of x-ray diffraction in crystals, The Journal of Physical Chemistry 50 (3) (1946) 289–290. doi:10.1021/j150447a024.

[23] R. W. James, The optical principles of the diffraction of X-rays, G.Bell and Sons, London, 1954.

[24] R. James, The dynamical theory of x-ray diffraction, in: Solid State Physics, Vol. 15, Elsevier, 1963, pp. 53–220.

[25] A. Authier, Étude de la transmission anormale des rayons x dans des cristaux de silicium. i. cas des cristaux parfaits, Bulletin de Minéralogie 84 (1) (1961) 51–89.

[26] B. W. Batterman, H. Cole, Dynamical diffraction of x rays by perfect crystals, Reviews of modern physics 36 (3) (1964) 681.

[27] S. Takagi, A dynamical theory of diffraction for a distorted crystal, Journal of the Physical Society of Japan 26 (5) (1969) 1239–1253.

[28] D. Taupin, Théorie dynamique de la diffraction des rayons x par les cristaux déformés, Bulletin de Minéralogie 87 (4) (1964) 469–511.

[29] J. Gronkowski, Propagation of x-rays in distorted crystals under dynamical diffraction, Physics Reports 206 (1) (1991) 1–41. doi:10.1016/0370-1573(91)90086-2.

[30] C. Maag, Influence of pulsed heat load on the performance of diamond bragg mirrors for an xfel-oscillator, Ph.D. thesis, Universitat Hamburg (2018).

[31] E. Konorova, S. Kozlov, V. Vavilov, Ionization currents in diamonds during irradiation with 500 to 1000-kev electrons, Soviet Phys.-Solid State (Engl. Transl.) 8.

[32] M. Kozák, F. Trojánek, P. Malỳ, Optical study of carrier diffusion and recombination in cvd diamond, physica status solidi (a) 210 (10) (2013) 2008–2015.

[33] A. H. Chin, R. W. Schoenlein, T. E. Glover, P. Balling, W. P. Leemans, C. V. Shank, Ultrafast Structural Dynamics in InSb Probed by Time-Resolved X-Ray Diffraction, Physical Review Letters 83 (2) (1999) 336–339. doi:10.1103/PhysRevLett.83.336.

[34] C. Thomsen, H. T. Grahn, H. J. Maris, J. Tauc, Surface generation and detection of phonons by picosecond light pulses, Physical Review B 34 (6) (1986) 4129–4138. doi:10.1103/PhysRevB.34.4129.

[35] S. Stoupin, A. M. March, H. Wen, D. A. Walko, Y. Li, E. M. Dufresne, S. A. Stepanov, K.-J. Kim, Y. V. Shvyd'ko, V. D. Blank, S. A. Terentyev, Direct observation of dynamics of thermal expansion using pump-probe high-energy-resolution x-ray diffraction, Physical Review B 86 (5) (2012) 054301. doi:10.1103/PhysRevB.86.054301.

[36] S. Zhang, W. Dai, H. Wang, R. V. Melnik, A finite difference method for studying thermal deformation in a 3d thin film exposed to ultrashort pulsed lasers, International journal of heat and mass transfer 51 (7-8) (2008) 1979–1995.

[37] P. Emma, R. Akre, J. Arthur, R. Bionta, C. Bostedt, J. Bozek, A. Brachmann, P. Bucksbaum, R. Coffee, F.-J. Decker, Y. Ding, D. Dowell, S. Edstrom, A. Fisher, J. Frisch, S. Gilevich, J. Hastings, G. Hays, P. Hering, Z. Huang, R. Iverson, H. Loos, M. Messerschmidt, A. Miahnahri, S. Moeller, H.-D. Nuhn, G. Pile, D. Ratner, J. Rzepiela, D. Schultz, T. Smith, P. Stefan, H. Tompkins, J. Turner, J. Welch, W. White, J. Wu, G. Yocky, J. Galayda, First lasing and operation of an ångstrom-wavelength free-electron laser, Nature Photonics 4 (9) (2010) 641–647. doi:10.1038/nphoton.2010.176.

[38] T. Ishikawa, H. Aoyagi, T. Asaka, Y. Asano, N. Azumi, T. Bizen, H. Ego, K. Fukami, T. Fukui, Y. Furukawa, S. Goto, H. Hanaki, T. Hara, T. Hasegawa, T. Hatsui, A. Higashiya, T. Hirono, N. Hosoda, M. Ishii, T. Inagaki, Y. Inubushi, T. Itoga, Y. Joti, M. Kago, T. Kameshima, H. Kimura, Y. Kirihara, A. Kiyomichi, T. Kobayashi, C. Kondo, T. Kudo, H. Maesaka, X. M. Maréchal, T. Masuda, S. Matsubara, T. Matsumoto, T. Matsushita, S. Matsui, M. Nagasono, N. Nariyama, H. Ohashi, T. Ohata, T. Ohshima, S. Ono, Y. Otake, C. Saji, T. Sakurai, T. Sato, K. Sawada, T. Seike, K. Shirasawa, T. Sugimoto, S. Suzuki, S. Takahashi, H. Takebe, K. Takeshita, K. Tamasaku, H. Tanaka, R. Tanaka, T. Tanaka, T. Togashi, K. Togawa, A. Tokuhisa, H. Tomizawa, K. Tono, S. Wu, M. Yabashi, M. Yamaga, A. Yamashita, K. Yanagida, C. Zhang, T. Shintake, H. Kitamura, N. Kumagai, A compact x-ray free-electron laser emitting in the sub-ångström region, Nature Photonics 6 (8) (2012) 540–544. doi:10.1038/nphoton.2012.141.

[39] H.-S. Kang, C.-K. Min, H. Heo, C. Kim, H. Yang, G. Kim, I. Nam, S. Y. Baek, H.-J. Choi, G. Mun, B. R. Park, Y. J. Suh, D. C. Shin, J. Hu, J. Hong, S. Jung, S.-H. Kim, K. Kim, D. Na, S. S. Park, Y. J. Park, J.-H. Han, Y. G. Jung, S. H. Jeong, H. G. Lee, S. Lee, S. Lee, W.-W. Lee, B. Oh, H. S. Suh, Y. W. Parc, S.-J. Park, M. H. Kim, N.-S. Jung, Y.-C. Kim, M.-S. Lee, B.-H. Lee, C.-W. Sung, I.-S. Mok, J.-M. Yang, C.-S. Lee, H. Shin, J. H. Kim, Y. Kim, J. H. Lee, S.-Y. Park, J. Kim, J. Park, I. Eom, S. Rah, S. Kim, K. H. Nam, J. Park, J. Park, S. Kim, S. Kwon, S. H. Park, K. S. Kim, H. Hyun, S. N. Kim, S. Kim, S.-m. Hwang, M. J. Kim, C.-y. Lim, C.-J. Yu, B.-S. Kim, T.-H. Kang, K.-W. Kim, S.-H. Kim, H.-S. Lee, H.-S. Lee, K.-H. Park, T.-Y. Koo, D.-E. Kim, I. S. Ko, Hard X-ray free-electron laser with femtosecond-scale timing jitter, Nature Photonics 11 (11) (2017) 708–713. doi:10.1038/s41566-017-0029-8.

[40] M. Scholz, FEL Performance Achieved at European XFEL, in: Proceedings, 9th International Particle Accelerator Conference (IPAC 2018): Vancouver, BC Canada, April 29-May 4, 2018, 2018, p. MOZGBD2. doi:10.18429/JACoW-IPAC2018-MOZGBD2.

[41] W. Zhang, R. Alonso-Mori, U. Bergmann, C. Bressler, M. Chollet, A. Galler, W. Gawelda, R. G. Hadt, R. W. Hartsock, T. Kroll, K. S. Kjær, K. Kubiček, H. T. Lemke, H. W. Liang, D. A. Meyer, M. M. Nielsen, C. Purser, J. S. Robinson, E. I. Solomon, Z. Sun, D. Sokaras, T. B. van Driel, G. Vankó, T.-C. Weng, D. Zhu, K. J. Gaffney, Tracking excited-state charge and spin dynamics in iron coordination complexes, Nature 509 (7500) (2014) 345–348. doi:10.1038/nature13252.

[42] M. M. Seibert, T. Ekeberg, F. R. Maia, M. Svenda, J. Andreasson, O. Jönsson, D. Odić, B. Iwan, A. Rocker, D. Westphal, et al., Single mimivirus particles intercepted and imaged with an x-ray laser, Nature 470 (7332) (2011) 78–81.

[43] D. Milathianaki, S. Boutet, G. Williams, A. Higginbotham, D. Ratner, A. Gleason, M. Messerschmidt, M. M. Seibert, D. Swift, P. Hering, et al., Femtosecond visualization of lattice dynamics in shock-compressed matter, Science 342 (6155) (2013) 220–223.

[44] I. A. Vartanyants, A. Singer, A. P. Mancuso, O. M. Yefanov, A. Sakdinawat, Y. Liu, E. Bang, G. J. Williams, G. Cadenazzi, B. Abbey, et al., Coherence properties of individual femtosecond pulses of an x-ray free-electron laser, Physical review letters 107 (14) (2011) 144801.

[45] C. Gutt, P. Wochner, B. Fischer, H. Conrad, M. Castro-Colin, S. Lee, F. Lehmkühler, I. Steinke, M. Sprung, W. Roseker, et al., Single shot spatial and temporal coherence properties of the slac linac coherent light source in the hard x-ray regime, Physical Review Letters 108 (2) (2012) 024801.

[46] M. Ware, A. Natan, J. Glownia, J. Cryan, P. Bucksbaum, Filming nuclear dynamics of iodine using x-ray diffraction at the lcls, Bulletin of the American Physical Society 62.

[47] D. H. Bilderback, A. K. Freund, G. S. Knapp, D. M. Mills, The historical development of cryogenically cooled monochromators for third-generation synchrotron radiation sources, Journal of Synchrotron Radiation 7 (2) (2000) 53–60. doi:10.1107/S0909049500000650.

[48] L. Zhang, W. Lee, M. Wulff, L. Eybert, Performance prediction of cryogenically cooled silicon crystal monochromator, AIP Conference Proceedings 705 (1) (2004) 623–626. doi:10.1063/1.1757873.

[49] P. Rauer, I. Bahns, W. Hillert, J. Roßbach, W. Decking, H. Sinn, Integration of an xfelo at the european xfel facility, Proceedings of the 39th International Free-Electron Laser Conference PROCEEDING-2020-014.

[50] V. A. Bushuev, Effect of the thermal heating of a crystal on the diffraction of pulses of a free-electron X-ray laser, Bulletin of the Russian Academy of Sciences: Physics 77 (1) (2013) 15–20. doi:10.3103/S1062873813010061.

[51] V. A. Bushuev, Influence of thermal self-action on the diffraction of high-power X-ray pulses, Journal of Surface Investigation. X-ray, Synchrotron and Neutron Techniques 10 (6) (2016) 1179–1186. doi:10.1134/S1027451016050487.

[52] Y. Shvyd'ko, R. Lindberg, Spatiotemporal response of crystals in x-ray Bragg diffraction, Physical Review Special Topics - Accelerators and Beams 15 (10) (2012) 100702. doi:10.1103/PhysRevSTAB.15.100702.

[53] M. S. Shur, Handbook Series on Semiconductor Parameters, World Scientific, 1996.

[54] W. Ackermann, G. Asova, V. Ayvazyan, A. Azima, N. Baboi, J. Bähr, V. Balandin, B. Beutner, A. Brandt, A. Bolzmann, R. Brinkmann, O. I. Brovko, M. Castellano, P. Castro, L. Catani, E. Chiadroni, S. Choroba, A. Cianchi, J. T. Costello, D. Cubaynes, J. Dardis, W. Decking, H. Delsim-Hashemi, A. Delserieys, G. D. Pirro, M. Dohlus, S. Düsterer, A. Eckhardt, H. T. Edwards, B. Faatz, J. Feldhaus, K. Flöttmann, J. Frisch, L. Fröhlich, T. Garvey, U. Gensch, C. Gerth, M. Görler, N. Golubeva, H.-J. Grabosch, M. Grecki, O. Grimm, K. Hacker, U. Hahn, J. H. Han, K. Honkavaara, T. Hott, M. Hüning, Y. Ivanisenko, E. Jaeschke, W. Jalmuzna, T. Jezynski, R. Kammering, V. Katalev, K. Kavanagh, E. T. Kennedy, S. Khodyachykh, K. Klose, V. Kocharyan, M. Körfer, M. Kollewe, W. Koprek, S. Korepanov, D. Kostin, M. Krassilnikov, G. Kube, M. Kuhlmann, C. L. S. Lewis, L. Lilje, T. Limberg, D. Lipka, F. Löhl, H. Luna, M. Luong, M. Martins, M. Meyer, P. Michelato,

V. Miltchev, W. D. Möller, L. Monaco, W. F. O. Müller, O. Napieralski, O. Napoly, P. Nicolosi, D. Nölle, T. Nuñez, A. Oppelt, C. Pagani, R. Paparella, N. Pchalek, J. Pedregosa-Gutierrez, B. Petersen, B. Petrosyan, G. Petrosyan, L. Petrosyan, J. Pflüger, E. Plönjes, L. Poletto, K. Pozniak, E. Prat, D. Proch, P. Pucyk, P. Radcliffe, H. Redlin, K. Rehlich, M. Richter, M. Roehrs, J. Roensch, R. Romaniuk, M. Ross, J. Rossbach, V. Rybnikov, M. Sachwitz, E. L. Saldin, W. Sandner, H. Schlarb, B. Schmidt, M. Schmitz, P. Schmüser, J. R. Schneider, E. A. Schneidmiller, S. Schnepp, S. Schreiber, M. Seidel, D. Sertore, A. V. Shabunov, C. Simon, S. Simrock, E. Sombrowski, A. A. Sorokin, P. Spanknebel, R. Spesyvtsev, L. Staykov, B. Steffen, F. Stephan, F. Stulle, H. Thom, K. Tiedtke, M. Tischer, S. Toleikis, R. Treusch, D. Trines, I. Tsakov, E. Vogel, T. Weiland, H. Weise, M. Wellhöfer, M. Wendt, I. Will, A. Winter, K. Wittenburg, W. Wurth, P. Yeates, M. V. Yurkov, I. Zagorodnov, K. Zapfe, Operation of a free-electron laser from the extreme ultraviolet to the water window, Nature Photonics 1 (6) (2007) 336–342. doi:10.1038/nphoton.2007.76.

[55] A. M. Kondratenko, E. L. Saldin, Generation of coherent radiation by a relativistic electron beam in an ondulator, Particle Accelerators 10 (3-4) (1980) 207–216.

[56] L. H. Yu, Generation of intense uv radiation by subharmonically seeded single-pass free-electron lasers, Physical Review A 44 (8) (1991) 5178–5193. doi:10.1103/PhysRevA.44.5178.

[57] G. Stupakov, Using the beam-echo effect for generation of short-wavelength radiation, Physical Review Letters 102 (7) (2009) 074801. doi:10.1103/PhysRevLett.102.074801.

[58] B. Jia, Y. K. Wu, J. J. Bisognano, A. W. Chao, J. Wu, Influence of an imperfect energy profile on a seeded free electron laser performance, Physical Review Special Topics - Accelerators and Beams 13 (6) (2010) 060701. doi:10.1103/PhysRevSTAB.13.060701.

[59] J. Feldhaus, E. L. Saldin, J. R. Schneider, E. A. Schneidmiller, M. V. Yurkov, Possible application of x-ray optical elements for reducing the spectral bandwidth of an x-ray sase fel, Optics Communications 140 (4) (1997) 341–352. doi:10.1016/S0030-4018(97)00163-6.

[60] E. L. Saldin, E. A. Schneidmiller, Y. V. Shvyd'ko, M. V. Yurkov, X-ray FEL with a meV bandwidth, AIP Conference Proceedings 581 (1) (2001) 153–161. doi:10.1063/1.1401570.

[61] I. Inoue, T. Osaka, T. Hara, T. Tanaka, T. Inagaki, T. Fukui, S. Goto, Y. Inubushi, H. Kimura, R. Kinjo, H. Ohashi, K. Togawa, K. Tono, M. Yamaga, H. Tanaka, T. Ishikawa, M. Yabashi, Generation of narrow-band x-ray free-electron laser via reflection self-seeding, Nature Photonics 13 (5) (2019) 319–322. doi:10.1038/s41566-019-0365-y.

[62] H. Weise, W. Decking, Commissioning and First Lasing of the European XFEL, in: Proceedings, 38th International Free Electron Laser Conference, FEL2017, 2018, p. MOC03. doi:10.18429/JACoW-FEL2017-MOC03.

[63] T. Raubenheimer, LCLS-II: Status of the CW X-ray FEL Upgrade to the LCLS Facility, in: Proceedings, 37th International Free Electron Laser Conference (FEL 2015): Daejeon, Korea, August 23-28, 2015, 2015, pp. 618–624. doi:10.18429/JACoW-FEL2015-WEP014.

[64] B. Yang, S. Wang, J. Wu, Transient thermal stress wave and vibrational analyses of a thin diamond crystal for X-ray free-electron lasers under high-repetition-rate operation, Journal of Synchrotron Radiation 25 (1) (2018) 166–176. doi:10.1107/S1600577517015466.

[65] G. Marot, Cryogenic cooling of high heat load optics, Optical Engineering 34 (2) (1995) 426–432. doi:10.1117/12.195196.

[66] L. Zhang, D. Cocco, N. Kelez, D. S. Morton, V. Srinivasan, P. M. Stefan, Optimizing x-ray mirror thermal performance using matched profile cooling, Journal of Synchrotron Radiation 22 (5) (2015) 1170–1181. doi:10.1107/S1600577515013090.

[67] Z. Liu, T. Gog, S. A. Stoupin, M. H. Upton, Y. Ding, J.-H. Kim, D. M. Casa, A. H. Said, J. A. Carter, G. Navrotski, High-heat-load monochromator options for the RIXS beamline at the APS with the MBA lattice, AIP Conference Proceedings 1741 (1) (2016) 040046. doi:10.1063/1.4952918.

[68] J. Stimson, S. Diaz-Moreno, P. Docker, J. Kay, J. Sutter, M. Ward, A Thermal Exploration of Different Monochromator Crystal Designs, in: Proceedings, 9th Mechanical Engineering Design of Synchrotron Radiation Equipment and Instrumentation (MEDSI 2016): Barcelona, Spain, September 11-16, 2016, 2017, p. TUPE10. doi:10.18429/JACoW-MEDSI2016-TUPE10.

[69] O. Lugovskaya, S. Stepanov, Calculation of the polarizabilities of crystals for diffraction of x-rays of the continuous spectrum at wavelength of 0.1–10å, Sov. Phys. Crystallogr 36 (1991) 478–481.

[70] Sergey Stepanov's X-ray Server.
URL `https://x-server.gmca.aps.anl.gov/index.shtml`

[71] R. R. Lindberg, Y. V. Shvyd'ko, Time dependence of bragg forward scattering and self-seeding of hard x-ray free-electron lasers, Physical Review Special Topics - Accelerators and Beams 15 (5) (2012) 050706. doi:10.1103/PhysRevSTAB.15.050706.

[72] H. Lamb, On waves in an elastic plate, Proceedings of the Royal Society of London. Series A, Containing Papers of a Mathematical and Physical Character 93 (648) (1917) 114–128. doi:10.1098/rspa.1917.0008.

[73] M. S. Harb, F. G. Yuan, A rapid, fully non-contact, hybrid system for generating lamb wave dispersion curves, Ultrasonics 61 (2015) 62–70. doi:10.1016/j.ultras.2015.03.006.

[74] Z. Su, L. Ye, Y. Lu, Guided lamb waves for identification of damage in composite structures: A review, Journal of Sound and Vibration 295 (3) (2006) 753–780. doi:10.1016/j.jsv.2006.01.020.

[75] Bocchini Paolo, Marzani Alessandro, Viola Erasmo, Graphical user interface for guided acoustic waves, Journal of Computing in Civil Engineering 25 (3) (2011) 202–210. doi:10.1061/(ASCE)CP.1943-5487.0000081.

[76] D. Clorennec, C. Prada, D. Royer, T. W. Murray, Laser impulse generation and interferometer detection of zero group velocity lamb mode resonance, Applied Physics Letters 89 (2) (2006) 024101. doi:10.1063/1.2220010.

[77] W. Liu, J.-W. Hong, Finite element simulation of guided waves generated by laser pulses, in: Sensors and Smart Structures Technologies for Civil, Mechanical, and Aerospace Systems 2012, Vol. 8345, International Society for Optics and Photonics, 2012, p. 83450C. doi:10.1117/12.915046.

[78] E. A. Olafsdottir, S. Erlingsson, B. Bessason, Tool for analysis of multichannel analysis of surface waves (masw) field data and evaluation of shear wave velocity profiles of soils, Canadian Geotechnical Journal 55 (2) (2017) 217–233. doi:10.1139/cgj-2016-0302.

[79] C. B. Park, R. D. Miller, J. Xia, Multichannel analysis of surface waves, Geophysics 64 (3) (1999) 800–808. doi:10.1190/1.1444590.

[80] K. V. d. Rostyne, C. Glorieux, W. Gao, V. Gusev, M. Nesladek, W. Lauriks, J. Thoen, Investigation of elastic properties of cvd-diamond films using the lowest order flexural leaky lamb wave, physica status solidi (a) 172 (1) (1999) 105–111. doi:10.1002/(SICI)1521-396X(199903)172:1¡105::AID-PSSA105¿3.0.CO;2-E.

[81] R. S. Sussmann, C. J. H. Wort, C. G. Sweeney, J. L. Collins, C. N. Dodge, J. A. Savage, Optical and dielectric properties of cvd polycrystalline diamond plates, in: Window and Dome Technologies and Materials IV, Vol. 2286, International Society for Optics and Photonics, 1994, pp. 229–238. doi:10.1117/12.187344.

[82] K. Negishi, Existence of negative group velocities in lamb waves, Japanese Journal of Applied Physics 26 (S1) (1987) 171. doi:10.7567/JJAPS.26S1.171.

[83] N. Ceglio, Revolution in x-ray optics, Journal of X-ray Science and Technology 1 (1) (1989) 7–78.

[84] B. L. Henke, E. M. Gullikson, J. C. Davis, X-ray interactions: photoabsorption, scattering, transmission and reflection e= 50-30,000 ev, z= 1-92, Atomic data and nuclear data tables 54 (2).

[85] B. Lengeler, C. Schroer, M. Richwin, J. Tümmler, M. Drakopoulos, A. Snigirev, I. Snigireva, A microscope for hard x rays based on parabolic compound refractive lenses, Applied physics letters 74 (26) (1999) 3924–3926.

[86] C. David, B. Nöhammer, E. Ziegler, Wavelength tunable diffractive transmission lens for hard x rays, Applied Physics Letters 79 (8) (2001) 1088–1090.

[87] K. Yamauchi, K. Yamamura, H. Mimura, Y. Sano, A. Saito, A. Souvorov, M. Yabashi, K. Tamasaku, T. Ishikawa, Y. Mori, Nearly diffraction-limited line focusing of a hard-x-ray beam with an elliptically figured mirror, Journal of synchrotron radiation 9 (5) (2002) 313–316.

[88] M. Yabashi, H. Yamazaki, K. Tamasaku, S. Goto, K. T. Takeshita, T. Mochizuki, Y. Yoneda, Y. Furukawa, T. Ishikawa, Spring-8 standard x-ray monochromators, in: X-Ray Optics Design, Performance, and Applications, Vol. 3773, International Society for Optics and Photonics, 1999, pp. 2–13.

[89] J. Welch, A. Brachmann, F. Decker, Y. Ding, P. Emma, A. Fisher, J. Frisch, Z. Huang, R. Iverson, H. Loos, et al., Undulator k-parameter measurements at lcls, Proceedings of FEL09, Liverpool (2009) 730–733.

[90] E. Allaria, R. Appio, L. Badano, W. Barletta, S. Bassanese, S. Biedron, A. Borga, E. Busetto, D. Castronovo, P. Cinquegrana, et al., Highly coherent and stable pulses from the fermi seeded free-electron laser in the extreme ultraviolet, Nature Photonics 6 (10) (2012) 699–704.

[91] I. S. Ko, H.-S. Kang, H. Heo, C. Kim, G. Kim, C.-K. Min, H. Yang, S. Y. Baek, H.-J. Choi, G. Mun, et al., Construction and commissioning of pal-xfel facility, Applied Sciences 7 (5) (2017) 479.

[92] C. J. Milne, T. Schietinger, M. Aiba, A. Alarcon, J. Alex, A. Anghel, V. Arsov, C. Beard, P. Beaud, S. Bettoni, et al., Swissfel: the swiss x-ray free electron laser, Applied Sciences 7 (7) (2017) 720.

[93] A. Marinelli, D. Ratner, A. Lutman, J. Turner, J. Welch, F.-J. Decker, H. Loos, C. Behrens, S. Gilevich, A. Miahnahri, et al., High-intensity double-pulse x-ray free-electron laser, Nature communications 6 (1) (2015) 1–6.

[94] X. Dong, D. Shu, H. Sinn, Design of a cryo-cooled artificial channel-cut crystal monochromator for the european xfel, in: AIP Conference Proceedings, Vol. 1741, AIP Publishing LLC, 2016, p. 040027.

[95] I. Petrov, J. Anton, U. Boesenberg, M. Dommach, X. Dong, J. Eidam, J. Hallmann, K. Kazarian, S. Kearney, C. Kim, et al., Effect of heat load on cryo-cooled monochromators at the european x-ray free-electron laser: Simulations and first experimental observations, in: 39th Free Electron Laser Conf.(FEL'19), Hamburg, Germany, 26-30 August 2019, JACOW Publishing, Geneva, Switzerland, 2019, pp. 502–505.

[96] F. Decker, R. Akre, A. Brachmann, Y. Ding, D. Dowell, P. Emma, A. Fisher, J. Frisch, S. Gilevich, P. Hering, et al., A demonstration of multi-bunch operation in the lcls, in: Proceedings of the 2010 Free Electron Laser Conference, Vol. 467, 2010, pp. 467–470.

[97] F.-J. Decker, S. Gilevich, Z. Huang, H. Loos, A. Marinelli, C. Stan, J. Turner, Z. Van Hoover, S. Vetter, Two Bunches with ns-Separation with LCLS, in: Proceedings, 37th International Free Electron Laser Conference (FEL 2015): Daejeon, Korea, August 23-28, 2015, 2015, p. WEP023. doi:10.18429/JACoW-FEL2015-WEP023.

[98] F.-J. Decker, K. Bane, W. Colocho, A. Lutman, J. Sheppard, Recent Developments and Plans for Two Bunch Operation with up to 1 μs Separation at LCLS, in: Proceedings, 38th International Free Electron Laser Conference, FEL2017, 2018, p. TUP023. doi:10.18429/JACoW-FEL2017-TUP023.

[99] S. Moeller, J. Arthur, A. Brachmann, R. Coffee, F.-J. Decker, Y. Ding, D. Dowell, S. Edstrom, P. Emma, Y. Feng, et al., Photon beamlines and diagnostics at lcls, Nuclear Instruments and Methods in Physics Research Section A: Accelerators, Spectrometers, Detectors and Associated Equipment 635 (1) (2011) S6–S11.

[100] J. B. Murphy, Phase space conservation and selection rules for astigmatic mode converters, Optics communications 165 (1-3) (1999) 11–18.

[101] L. C. Andrews, R. L. Phillips, Laser beam propagation through random media; 2nd ed., PM152, SPIE, Bellingham, 2005.

[102] J. Andruszkow, B. Aune, V. Ayvazyan, N. Baboi, R. Bakker, V. Balakin, D. Barni, A. Bazhan, M. Bernard, A. Bosotti, J. C. Bourdon, W. Brefeld, R. Brinkmann, S. Buhler, J.-P. Carneiro, M. Castellano, P. Castro, L. Catani, S. Chel, Y. Cho, S. Choroba, E. R. Colby, W. Decking, P. Den Hartog, M. Desmons, M. Dohlus, D. Edwards, H. T. Edwards, B. Faatz, J. Feldhaus, M. Ferrario, M. J. Fitch, K. Flöttmann, M. Fouaidy, A. Gamp, T. Garvey, C. Gerth, M. Geitz, E. Gluskin, V. Gretchko, U. Hahn, W. H. Hartung, D. Hubert, M. Hüning, R. Ischebek, M. Jablonka, J. M. Joly, M. Juillard, T. Junquera, P. Jurkiewicz, A. Kabel, J. Kahl, H. Kaiser, T. Kamps, V. V. Katelev, J. L. Kirchgessner, M. Körfer, L. Kravchuk, G. Kreps, J. Krzywinski, T. Lokajczyk, R. Lange, B. Leblond, M. Leenen, J. Lesrel, M. Liepe, A. Liero, T. Limberg, R. Lorenz, L. H. Hua, L. F. Hai, C. Magne, M. Maslov, G. Materlik, A. Matheisen, J. Menzel, P. Michelato, W.-D. Möller, A. Mosnier, U.-C. Müller, O. Napoly, A. Novokhatski, M. Omeich, H. S. Padamsee, C. Pagani, F. Peters, B. Petersen, P. Pierini, J. Pflüger, P. Piot, B. Phung Ngoc, L. Plucinski, D. Proch, K. Rehlich, S. Reiche, D. Reschke, I. Reyzl, J. Rosenzweig, J. Rossbach, S. Roth, E. L. Saldin, W. Sandner, Z. Sanok, H. Schlarb, G. Schmidt, P. Schmüser, J. R. Schneider, E. A. Schneidmiller, H.-J. Schreiber, S. Schreiber, P. Schütt, J. Sekutowicz, L. Serafini, D. Sertore, S. Setzer, S. Simrock, B. Sonntag, B. Sparr, F. Stephan, V. A. Sytchev, S. Tazzari, F. Tazzioli, M. Tigner, M. Timm, M. Tonutti, E. Trakhtenberg, R. Treusch, D. Trines, V. Verzilov, T. Vielitz, V. Vogel, G. v. Walter, R. Wanzenberg, T. Weiland, H. Weise, J. Weisend, M. Wendt, M. Werner, M. M. White, I. Will, S. Wolff, M. V. Yurkov, K. Zapfe, P. Zhogolev, F. Zhou, First observation of self-amplified spontaneous emission in a free-electron laser at 109 nm wavelength, Physical Review Letters 85 (18) (2000) 3825–3829. doi:10.1103/PhysRevLett.85.3825.

[103] J. Wu, Y. Ding, P. Emma, Z. Huang, H. Loos, M. Messerschmidt, E. Schneidmiller, M. Yurkov, Lcls x-ray pulse duration measurement using the statistical fluctuation method, 2010, pp. 147–150, 32nd International Free Electron Laser Conference, FEL 2010 ; Conference date: 23-08-2010 Through 27-08-2010.

[104] G. Zhou, et al., Coherence Time Characterization for Self-Amplified Spontaneous Emission Free-Electron Lasers, in: Proc. 10th International Particle Accelerator Conference (IPAC'19), Melbourne, Australia, 19-24 May 2019, no. 10 in International Particle Accelerator Conference, JACoW Publishing, Geneva, Switzerland, 2019, pp. 1820–1823. doi:doi:10.18429/JACoW-IPAC2019-TUPRB062.

[105] P. Emma, J. Frisch, Z. Huang, A. Marinelli, T. Maxwell, H. Loos, Y. Nosochkov, T. Raubenheimer, J. Welch, L. Wang, et al., Linear accelerator design for the lcls-ii fel facility, in: Proc. of 36th Int. Free-Electron Laser Conf., Basel, 2014.

[106] L. Samoylova, D. Shu, X. Dong, G. Geloni, S. Karabekyan, S. Terentev, V. Blank, S. Liu, T. Wohlenberg, W. Decking, H. Sinn, Design of hard x-ray self-seeding monochromator for european xfel, AIP Conference Proceedings 2054 (1) (2019) 030016. doi:10.1063/1.5084579.

[107] X. Dong, G. Geloni, S. Karabekyan, L. Samoylova, S. Serkez, H. Hinn, W. Decking, C. Engling, N. Golubeva, V. Kocharyan, B. Krause, S. Lederer, S. Liu, A. Petrov, E. Saldin, T. Wohlenberg, D. Shu, V. D. Blank, S. Terentiev, Status of the hard x-ray self-seeding project at the european xfel (2017).

[108] T. Raubenheimer, The LCLS-II-HE, A High Energy Upgrade of the LCLS-II, in: Proceedings, 60th ICFA Advanced Beam Dynamics Workshop on Future Light Sources (FLS2018): Shanghai, China, March 5-9, 2018, 2018, p. MOP1WA02. doi:10.18429/JACoW-FLS2018-MOP1WA02.

[109] D. Shu, Y. Shvyd'ko, J. Amann, P. Emma, S. Stoupin, J. Quintana, Design of a diamond-crystal monochromator for the lcls hard x-ray self-seeding project, in: Journal of Physics: Conference Series, Vol. 425, IOP Publishing, 2013, p. 052004.

[110] S. Reiche, Genesis 1.3: a fully 3d time-dependent fel simulation code, Nuclear Instruments and Methods in Physics Research Section A: Accelerators, Spectrometers, Detectors and Associated Equipment 429 (1-3) (1999) 243–248.

[111] H. Chae, Y. Han, D. Seong, J. Kim, Y. Baik, Thermal conductivity of dc-plasma assisted chemical vapor deposited diamond films, Journal of Applied Physics 78 (11) (1995) 6849–6851. doi:10.1063/1.360447.

[112] V. Efimov, L. Mezhov-Deglin, Phonon scattering in diamond films, Physica B: Condensed Matter 263 (1999) 745–748.

[113] R. R. Reeber, K. Wang, Thermal expansion and lattice parameters of group iv semiconductors, Materials Chemistry and Physics 46 (2-3) (1996) 259–264.

[114] Y. Ma, Hotspot size-dependent thermal boundary conductance in nondiffusive heat conduction, Journal of Heat Transfer 137 (8). doi:10.1115/1.4030170.

[115] D. Ding, X. Chen, A. J. Minnich, Radial quasiballistic transport in time-domain thermoreflectance studied using Monte Carlo simulations, Applied Physics Letters 104 (14) (2014) 143104. doi:10.1063/1.4870811.

[116] A. J. Minnich, J. A. Johnson, A. J. Schmidt, K. Esfarjani, M. S. Dresselhaus, K. A. Nelson, G. Chen, Thermal conductivity spectroscopy technique to measure phonon mean free paths, Physical Review Letters 107 (9) (2011) 095901. doi:10.1103/PhysRevLett.107.095901.

[117] C. Yang, C.-Y. Tsai, G. Zhou, X. Wang, Y. Hong, E. D. Krug, A. Li, H. Deng, D. He, J. Wu, The detuning effect of crystal monochromator in self-seeding and oscillator free electron laser, Optics express 27 (9) (2019) 13229–13239.

[118] H. Sinn, Heat load estimates for xfel beamline optics, HASYLAB Annual Report.

[119] J. B. J. b. Fourier, Théorie analytique de la chaleur, F. Didot, 1822.

[120] D. G. Cahill, P. V. Braun, G. Chen, D. R. Clarke, S. Fan, K. E. Goodson, P. Keblinski, W. P. King, G. D. Mahan, A. Majumdar, H. J. Maris, S. R. Phillpot, E. Pop, L. Shi, Nanoscale thermal transport. ii. 2003–2012, Applied Physics Reviews 1 (1) (2014) 011305. doi:10.1063/1.4832615.

[121] G. J. Snyder, E. S. Toberer, Complex thermoelectric materials, in: materials for sustainable energy: a collection of peer-reviewed research and review articles from Nature Publishing Group, World Scientific, 2011, pp. 101–110.

[122] G. Chen, M. S. Dresselhaus, G. Dresselhaus, J.-P. Fleurial, T. Caillat, Recent developments in thermoelectric materials, International Materials Reviews 48 (1) (2003) 45–66. doi:10.1179/095066003225010182.

[123] W. Lu, C. M. Lieber, Nanoelectronics from the bottom up, in: Nanoscience And Technology: A Collection of Reviews from Nature Journals, World Scientific, 2010, pp. 137–146.

[124] D. G. Cahill, W. K. Ford, K. E. Goodson, G. D. Mahan, A. Majumdar, H. J. Maris, R. Merlin, S. R. Phillpot, Nanoscale thermal transport, Journal of Applied Physics 93 (2) (2002) 793–818. doi:10.1063/1.1524305.

[125] J. A. Johnson, A. A. Maznev, J. Cuffe, J. K. Eliason, A. J. Minnich, T. Kehoe, C. M. S. Torres, G. Chen, K. A. Nelson, Direct measurement of room-temperature nondiffusive thermal transport over micron distances in a silicon membrane, Physical Review Letters 110 (2) (2013) 025901. doi:10.1103/PhysRevLett.110.025901.

[126] Y. K. Koh, D. G. Cahill, Frequency dependence of the thermal conductivity of semiconductor alloys, Physical Review B 76 (7) (2007) 075207. doi:10.1103/PhysRevB.76.075207.

[127] M. Highland, B. C. Gundrum, Y. K. Koh, R. S. Averback, D. G. Cahill, V. C. Elarde, J. J. Coleman, D. A. Walko, E. C. Landahl, Ballistic-phonon heat conduction at the nanoscale as revealed by time-resolved x-ray diffraction and time-domain thermoreflectance, Physical Review B 76 (7) (2007) 075337. doi:10.1103/PhysRevB.76.075337.

[128] M. E. Siemens, Q. Li, R. Yang, K. A. Nelson, E. H. Anderson, M. M. Murnane, H. C. Kapteyn, Quasi-ballistic thermal transport from nanoscale interfaces observed using ultrafast coherent soft x-ray beams, Nature Materials 9 (1) (2010) 26–30. doi:10.1038/nmat2568.

[129] K. M. Hoogeboom-Pot, J. N. Hernandez-Charpak, X. Gu, T. D. Frazer, E. H. Anderson, W. Chao, R. W. Falcone, R. Yang, M. M. Murnane, H. C. Kapteyn, D. Nardi, A new regime

of nanoscale thermal transport: Collective diffusion increases dissipation efficiency, Proceedings of the National Academy of Sciences of the United States of America 112 (16). doi:10.1073/pnas.1503449112.

[130] H. J. Eichler, P. Günter, D. W. Pohl, Laser-induced dynamic gratings, Vol. 50, Springer, 2013.

[131] J. A. Rogers, A. A. Maznev, M. J. Banet, K. A. Nelson, Optical generation and characterization of acoustic waves in thin films: Fundamentals and applications, Annual Review of Materials Science 30 (1) (2000) 117–157. doi:10.1146/annurev.matsci.30.1.117.

[132] S. A. Ali, G. Kollu, S. Mazumder, P. Sadayappan, A. Mittal, Large-scale parallel computation of the phonon boltzmann transport equation, International Journal of Thermal Sciences 86 (2014) 341–351. doi:10.1016/j.ijthermalsci.2014.07.019.

[133] C. CATTANEO, Sur une forme de l'equation de la chaleur eliminant la paradoxe d'une propagation instantantee, Compt. Rendu 247 (1958) 431–433.

[134] P. VERNOTTE, The true heat equation, Comptes Rendus 247 (1958) 2103.

[135] R. A. Guyer, J. A. Krumhansl, Solution of the linearized phonon boltzmann equation, Physical Review 148 (2) (1966) 766–778. doi:10.1103/PhysRev.148.766.

[136] X. Zhou, K. K. Tamma, C. V. Anderson, On a new c-and f-processes heat conduction constitutive model and the associated generalized theory of dynamic thermoelasticity, Journal of Thermal Stresses 24 (6) (2001) 531–564.

[137] G. Chen, Ballistic-diffusive heat-conduction equations, Physical Review Letters 86 (11) (2001) 2297–2300. doi:10.1103/PhysRevLett.86.2297.

[138] R. B. Wilson, J. P. Feser, G. T. Hohensee, D. G. Cahill, Two-channel model for nonequilibrium thermal transport in pump-probe experiments, Physical Review B 88 (14) (2013) 144305. doi:10.1103/PhysRevB.88.144305.

[139] Y. Ma, A two-parameter nondiffusive heat conduction model for data analysis in pump-probe experiments, Journal of Applied Physics 116 (24) (2014) 243505. doi:10.1063/1.4904355.

[140] Y. Zhang, Y.-L. He, Multiscale Thermal Transport in Energy Systems, Nova Science Publishers, Incorporated, 2016.

[141] J. A. Johnson, A. A. Maznev, J. K. Eliason, A. Minnich, K. Collins, G. Chen, J. Cuffe, T. Kehoe, C. M. S. Torres, K. A. Nelson, Experimental evidence of non-diffusive thermal transport in si and gaas, MRS Online Proceedings Library Archive 1347. doi:10.1557/opl.2011.1333.

[142] J. A. Johnson, J. K. Eliason, A. A. Maznev, T. Luo, K. A. Nelson, Non-diffusive thermal transport in gaas at micron length scales, Journal of Applied Physics 118 (15) (2015) 155104. doi:10.1063/1.4933285.

[143] A. J. Minnich, Determining phonon mean free paths from observations of quasiballistic thermal transport, Physical Review Letters 109 (20) (2012) 205901. doi:10.1103/PhysRevLett.109.205901.

[144] A. J. Minnich, Multidimensional quasiballistic thermal transport in transient grating spectroscopy, Physical Review B 92 (8) (2015) 085203. doi:10.1103/PhysRevB.92.085203.

[145] Z. Qu, Multiscale nondiusive heat transfer in dielectric materials, Master's thesis, UC Merced (2016).

[146] D. Wang, Z. Qu, Y. Ma, Analytical solutions of enhanced gray boltzmann transport equation on transient thermal grating and time-domain thermoreflectance experiments, in: ASME 2017 Heat Transfer Summer Conference, American Society of Mechanical Engineers Digital Collection, 2017.

[147] Z. Qu, D. Wang, Y. Ma, Nondiffusive thermal transport and prediction of the breakdown of Fourier's law in nanograting experiments, AIP Advances 7 (1) (2017) 015108. doi:10.1063/1.4973331.

[148] Z. Qu, D. Wang, Y. Ma, Application of two-parameter non-diffusive heat conduction model to nanoscale transient grating experiments, in: ASME 2015 International Mechanical Engineering Congress and Exposition, American Society of Mechanical Engineers Digital Collection, 2015.

[149] S. V. Narumanchi, J. Y. Murthy, C. H. Amon, Boltzmann transport equation-based thermal modeling approaches for hotspots in microelectronics, Heat and mass transfer 42 (6) (2006) 478–491.

[150] L. Tisza, Transport phenomena in helium ii, Nature 141 (3577) (1938) 913–913.

[151] L. Landau, Two-fluid model of liquid helium ii, J. Phys. Ussr 5 (1) (1941) 71–90.

[152] V. Peshkov, The second sound in helium ii, Journal of Physics 8 (1944) 381–389.

[153] C. C. Ackerman, B. Bertman, H. A. Fairbank, R. Guyer, Second sound in solid helium, Physical Review Letters 16 (18) (1966) 789.

[154] H. E. Jackson, C. T. Walker, T. F. McNelly, Second sound in naf, Physical Review Letters 25 (1) (1970) 26.

[155] T. McNelly, S. Rogers, D. Channin, R. Rollefson, W. Goubau, G. Schmidt, J. Krumhansl, R. Pohl, Heat pulses in naf: onset of second sound, Physical Review Letters 24 (3) (1970) 100.

[156] H. E. Jackson, C. T. Walker, Thermal conductivity, second sound, and phonon-phonon interactions in naf, Physical Review B 3 (4) (1971) 1428.

[157] V. Narayanamurti, R. Dynes, Observation of second sound in bismuth, Physical Review Letters 28 (22) (1972) 1461.

[158] W. Dreyer, H. Struchtrup, Heat pulse experiments revisited, Continuum Mechanics and Thermodynamics 5 (1) (1993) 3–50.

[159] P. Ván, Theories and heat pulse experiments of non-fourier heat conduction, Communications in Applied and Industrial Mathematics 7 (2) (2016) 150–166.

[160] D. D. Joseph, L. Preziosi, Heat waves, Reviews of Modern Physics 61 (1) (1989) 41.

[161] A. E. Green, P. M. Naghdi, A re-examination of the basic postulates of thermomechanics, Proceedings of the Royal Society of London. Series A: Mathematical and Physical Sciences 432 (1885) (1991) 171–194.

[162] S. Rogers, Transport of heat and approach to second sound in some isotopically pure alkali-halide crystals, Physical Review B 3 (4) (1971) 1440.

[163] Y. Ma, A transient ballistic–diffusive heat conduction model for heat pulse propagation in nonmetallic crystals, International Journal of Heat and Mass Transfer 66 (2013) 592–602.

[164] R. Kovács, P. Ván, Second sound and ballistic heat conduction: Naf experiments revisited, International Journal of Heat and Mass Transfer 117 (2018) 682–690.

[165] D. Wang, Z. Qu, Y. Ma, An enhanced gray model for nondiffusive heat conduction solved by implicit lattice boltzmann method, International Journal of Heat and Mass Transfer 94 (2016) 411–418.

[166] K. T. Regner, D. P. Sellan, Z. Su, C. H. Amon, A. J. McGaughey, J. A. Malen, Broadband phonon mean free path contributions to thermal conductivity measured using frequency domain thermoreflectance, Nature communications 4 (2013) 1640.

[167] D. Tzou, Nonlocal behavior in phonon transport, International Journal of Heat and Mass Transfer 54 (1-3) (2011) 475–481.

[168] Y. Ma, A hybrid phonon gas model for transient ballistic-diffusive heat transport, Journal of Heat Transfer 135 (4) (2013) 044501.

[169] J. Harrison, G. Lombardo, P. Peressini, Specific heat of naf, Journal of Physics and Chemistry of Solids 29 (3) (1968) 557–559.

[170] H. Casimir, Note on the conduction of heat in crystals, Physica 5 (6) (1938) 495–500.